



# 1<sup>st</sup> International Conference on Microfluidic Handling Systems

## Proceedings

Chair: Dr. J.C. Lötters  
Co-chair: Prof. Dr. G.A. Urban

[www.mfhs2012.org](http://www.mfhs2012.org)  
10-12 October 2012, Enschede, The Netherlands

## Conference Chairs



Dr. Joost C. Lötters

*University of Twente, department of Transducers Science and Technology, The Netherlands*

*Bronkhorst High-Tech BV, department of R&D, The Netherlands*



Prof. Dr. Gerald Urban

*University of Freiburg, Freiburg Institute for Advanced Studies, Germany*

## Program Committee



Prof. Dr. Miko Elwenspoek

*University of Twente, department of Transducers Science and Technology, The Netherlands*



Prof. Dr. Han Gardeniers

*University of Twente, Mesoscale Chemical Systems, The Netherlands*



Dr. Wybren Jouwsma

*Bronkhorst High-Tech BV, The Netherlands*



Prof. Dr. Andreas Manz

*Korea Institute of Science and Technology (KIST), Germany*

*Saarland University, Faculty Mechatronics, Germany*



Prof. Dr. Shuichi Shoji

*Waseda University, Faculty of Science and Engineering, Japan*



Prof. Dr. Göran Stemme

*KTH Royal Institute of Technology, Microsystem Technology Lab, Sweden*



Prof. Dr. Roland Zengerle

*University of Freiburg, Laboratory for MEMS-Applications, Germany*

Conference Sponsors

UNIVERSITY OF TWENTE.

# MESA+

INSTITUTE FOR NANOTECHNOLOGY



*The Business of Science®*

## Invited Speaker 1



Dr. Mirko Lehmann  
Innovative Sensor Technology IST AG  
Wattwil, Switzerland  
a company of the Endress and Hauser group

Title: "Different flow applications require different devices and technologies"

There are various situations how and where to measure flow. The media (gas or liquid, harsh environments...), the dynamic range, the response time, life time requirements, only to name a few can vary in these situations.

For these different applications there is not one flow sensor, one device. But, there are a lot of different devices based on various technologies. Some of those different technologies are presented ranging from measuring with a sensorelement directly in liquids over measuring dynamic ranges from 0.001 m/s...100 m/s to measuring flow with living cells.

Advantages, disadvantages and histories of the development of these sensor devices are also addressed.

Mirko Lehmann, Dr. rer. nat, born 1971, studied physics, graduated with dissertation at the university of Rostock in the field of cellular sensors. From 1996 to 2007 at Micronas GmbH in Freiburg, Germany responsible for Advanced Sensors. Since 2007 at Innovative Sensor Technology IST AG in Wattwil ([www-ist-ag.com](http://www-ist-ag.com)), Switzerland a company of the Endress and Hauser group, Reinach Switzerland in the position of the Managing Director and Supervisory Board Member of the Hahn-Schickard-Gesellschaft (HSG) with the institutes IMIT in Villingen and IMAT in Stuttgart (both Germany).

Several patents, publications and projects in the field of sensorics, among other publications: co-editor of the Springer book Solid State Gas Sensors: From Operating Principle to Industrialisation (other editor: Maximilian Fleischer, Siemens)



## Invited Speaker 2



Prof. dr. Volker Hessel  
Micro Flow Chemistry and Process Technology  
University of Technology Eindhoven,  
Eindhoven, the Netherlands

Title: "From Microfluidics to Future Factories in Chemistry: Intensification at all Scales"

Prof.dr. Volker Hessel, born 1964, studied chemistry at Mainz University. He got the PhD level in the field of organic chemistry in 1993. The topic of his PhD thesis was structure-property relationships of special supra-molecular structures, micelles and lyotropic liquid crystals, constructed by so-called bi- or multi-polar amphiphiles with rigid core unit.

Since 1994 Prof.dr. Hessel is an employee of the Institut für Mikrotechnik Mainz GmbH and since 1996 he became group leader for microreaction technology. In 1999 he was appointed Head of the Microreaction Technology Department, formed at that time, meanwhile named Chemical Process Technology. His fields of research comprise micro process engineering for mixing, fine chemistry, fuel processing and heterogeneous catalysis. In 2002 Prof. Dr. Hessel was appointed Vice Director R&D at IMM and in 2007 as Director R&D at IMM.

Prof.dr. Hessel is author or co-author of more than 150 peer-reviewed publications (with 24 extended reviews) and more than 180 conference papers with regard to chemical micro process engineering, 15 book chapters, and 5 books.

In July 2005, Prof.dr. Hessel was appointed as part-time professor for the chair of **"Micro Process Engineering"** at Eindhoven University of Technology, TU/e. This professorship is under the umbrella of the Chemical Reactor Engineering group of Prof.dr.ir. Jaap Schouten in the Department of Chemical Engineering and Chemistry. Currently, Prof.dr. Hessel was appointed as honorary professor at the Technical Chemistry Department at Technical University of Darmstadt and is in this function active within the Cluster of Excellence Smart Interfaces (CSI).

Prof.dr. Hessel received the AIChE award **"Excellence in Process Development Research"** in 2007. His Hirsch number (scientific impact measure) is 25.

A.o. Prof.dr. Hessel was AIChE chair (US) **"Microprocess Engineering"** (2005-2008); elected board member of the German industrial platform IPmVT; member of the editorial boards of **"Catalysis Today"**, **"Chemical Engineering Journal"**, **"Chemical Engineering Technology"**, **"Recent Patents on Chemical Engineering"**, and **"Current Organic Chemistry"**; Topical chair at AIChE Spring conferences 2006+2007 and organising committee member of symposia held at CHISA-6, ECCE-6 (EPIC), EUChemS and WCCE-8 as well as chair of the program committees of the **"Conference on Smart Synthesis and Technologies for Organic Processes"** (SynTOP) and the **"International Conference on Microreaction Technology 10"** (IMRET-10).

## Invited Speaker 3



Dr. Ir. Tom A. van de Goor  
R&D Manager  
Liquid Phase Separations Business  
Life Science Group  
Agilent Technologies  
Waldbronn, Germany

Title: Microfluidic components driving performance in Liquid Chromatography

The microfluidic technology development has been compared to the revolution in microelectronics, where both performance and price point have benefitted from developments in the semi-conductor industry. The vision of a Lab-on-a-chip is however still far away and has shown to be technologically complex and commercially challenging.

In this presentation, examples of microfluidic products and product components will be discussed as they relate to liquid chromatography. They fall in 3 categories: 1. Miniaturization for sample limited applications; 2. Miniaturization to improve analytical performance; 3. Miniaturization to integrate functionality to reduce cost.

### EDUCATION

Ph.D. Analytical Chemistry, 12/1992  
Eindhoven University of Technology, The Netherlands  
B.S. Chemical Engineering, 12/1987  
Eindhoven University of Technology, The Netherlands

### INDUSTRY EXPERIENCE :

Agilent Technologies / Hewlett-Packard, 1992-present  
Technical management and scientific contributor at the Central Research Laboratory in Palo Alto, USA.  
Research & Product Development Management in multiple business divisions both in the US and Germany.  
Areas of Expertise: Separation Science, Chromatography & Electrophoresis, Mass Spectrometry, Ion-sources, Microfluidics, Life Science Applications, Omics, Pharmaceutical Analysis

### PUBLICATIONS

Over 35 peer reviewed publications, 3 book chapters, 10 patents, invited speaker at over 100 conference contributions (oral and poster presentations)

## Programme

### Wednesday 10 October 2012

17:00 : Registration  
18:00 : Welcome Reception  
19:00 : Demonstration / Explanation of Roulette / Black Jack  
21:00 : Closure

### Thursday 11 October 2012

08:00 : Registration  
09:00 : Welcome, announcements. Chairs: Dr. Joost Lötters, Prof. Gerald Urban  
09:15 : Invited talk 1:

#### **Different flow applications require different devices and technologies**

Mirko Lehman

Innovative Sensor Technology IST AG, Wattwil, Switzerland

Chairs: Dr. Joost Lötters, Prof. Gerald Urban

09:40 : Session 1: Sensors. Chairs: Dr. Joost Lötters, Prof. Gerald Urban

11:00 : Coffee Break / Poster / Exhibition

11:30 : Session 2: Actuators. Chairs: Prof. Roland Zengerle, Prof. Shuichi Shoji

12:50 : Lunch / Poster / Exhibition

14:00 : Session 3: Fluidic Control Systems I. Chairs: Dr. W. Jouwsma, Prof. M.C. Elwenspoek

15:20 : Coffee Break / Poster / Exhibition

15:45 : Invited talk 2:

#### **From Microfluidics to Future Factories in Chemistry: Intensification at all Scales**

Volker Hessel

Micro Flow Chemistry and Process Technology, University of Technology Eindhoven,  
Eindhoven, the Netherlands

Chairs: Prof. Han Gardeniers, Prof. Miko Elwenspoek

16:15 : Poster Session. Chairs: Prof. Miko Elwenspoek, Prof. Shuichi Shoji

18:30 : Closure of the day

19:00 : Conference dinner

20:00 : Evening lecture:

#### **Microfluidic Handling Systems: "Where to Apply Them?"**

Kees de Gooijer

Food and Nutrition Delta, the Netherlands

Chairs: Dr. Joost Lötters, Prof. Gerald Urban

## Friday 12 October 2012

08:00 : Registration

09:00 : Welcome, announcements. Chairs: Dr. Joost Lötters, Prof. Gerald Urban

09:15 : Invited talk 3:

### **Microfluidic components driving performance in Liquid Chromatography**

**Tom A. van de Goor**

Liquid Phase Separations Business, Life Science Group, Agilent Technologies,  
Waldbronn, Germany

Chairs: Dr. Joost Lötters, Prof. Gerald Urban

09:40 : **Session 4: Fluidic control systems II.** Chairs: Dr. Wybren Jouwsma, Prof. Shuichi Shoji

11:00 : Coffee Break / Poster / Exhibition

11:30 : **Session 5: Applications.** Chairs: Prof. Han Gardeniers, Prof. Roland Zengerle

12:50 : Closure of the conference, Best paper / poster award and Next Conference

13:15 : Lunch

14:30 : Optional: lab tour at MESA+ / TST labs

17:00 : Closure

Session A  
(Thursday 09:40)

**10:00 - A01 MEASURING PICOLITER-PER-MINUTE FLOW RATES BY ELECTRICAL CROSS-CORRELATION SPECTROSCOPY**

Klaus Mathwig, Shuo Kang, Dileep Mampallil and Serge G. Lemay  
MESA+ Institute for Technology, University of Twente

**10:20 - A02 SIMULATION OF THE OSCILLATORY EXCITATION OF A THERMAL FLOW SENSOR**

Diego Reyes Romero, Ali Cubukcu and Gerald Urban  
Department of Microsystems Engineering, University of Freiburg, Freiburg, Germany

**10:40 - A03 TUNABLE SENSOR RESPONSE BY VOLTAGE-CONTROL IN BIOMIMETIC HAIR FLOWSENSORS**

Harmen Droogendijk and Gijs J.M. Krijnen  
University of Twente

**11:00 - A04 COMPACT MASS FLOW METER BASED ON A MICRO CORIOLIS FLOW SENSOR**

Wouter Sparreboom<sup>1</sup>, Marcel Katerberg<sup>1</sup>, Theo Lammerink<sup>2</sup>, Ferry Postma<sup>3</sup>, Jeroen Haneveld<sup>4</sup>, Jarno Groenesteijn<sup>2</sup>, Remco Wiegerink<sup>2</sup> and Joost Lötters<sup>1</sup>  
<sup>1</sup>Bronkhorst High-Tech BV, <sup>2</sup>University of Twente, <sup>3</sup>Lionix BV, <sup>4</sup>Micronit BV



Session B  
(Thursday 11:30)

**11:30 - B01 DEVELOPMENT OF AN ACTIVE MICROMIXER USING AN EXTERNAL MECHANICAL ACTUATOR ARRAY**

Yawar Abbas, Junichi Miwa, Roland Zengerle and Felix von Stetten

IMTEK - Department of Microsystems Engineering, University of Freiburg, Germany

**11:50 - B02 ENHANCED LIQUID METAL MICRO DROPLET GENERATION BY PNEUMATIC ACTUATION BASED ON THE STARJET METHOD**

Nils Lass<sup>1</sup>, Lutz Riegger<sup>1</sup>, Andreas Ernst<sup>2</sup>, Roland Zengerle<sup>1</sup> and Peter Koltay<sup>1</sup>

<sup>1</sup>Universitt Freiburg IMTEK, <sup>2</sup>BioFluidix GmbH

**12:10 - B03 CONTROLLABLE ACTIVE MICRO DROPLETS MERGING DEVICE USING HORIZONTAL PNEUMATIC VALVES**

Afshan Jamshaid, Masaya Igaki, Donghyun Yoon, Tetsushi Sekiguchi and Shuichi Shoji

Nanosciences & Nanoengineering, Waseda University, Tokyo, Japan

**12:30 - B04 ACTIVE AND PRECISE CONTROL OF MICRODROPLET DIVISION USING HORIZONTAL PNEUMATIC VALVES IN BIFURCATING MICROCHANNEL**

Dong Hyun Yoon, Junichi Ito, Tetsushi Sekiguchi and Shuichi Shoji

Waseda University

Session C  
(Thursday 14:00)

**14:00 - C01 PRESSURE DRIVEN AND REGULATED DISPENSER FOR THE MICROLITER RANGE**

Laurent Tanguy<sup>1</sup>, Andreas Ernst<sup>2</sup>, Stefan Bammesberger<sup>1</sup>, Roland Zengerle<sup>1</sup> and Peter Koltay<sup>1</sup>

<sup>1</sup>Laboratory for MEMS Applications, IMTEK - University of Freiburg, <sup>2</sup>Biofluidix GmbH

**14:20 - C02 A CALIBRATION-FREE, DISPOSABLE, NON-CONTACT REAGENT DOSING CARTRIDGE FOR THE SUB-L RANGE**

Stefan Bammesberger, Andreas Ernst, Tanguy Laurent, Peter Koltay and Roland Zengerle  
Laboratory for MEMS Applications, IMTEK - Department of Microsystems Engineering, University of Freiburg, Germany

**14:40 - C03 ADVANCED CAPILLARY SOFT VALVES FOR FLOW CONTROL IN SELF-DRIVEN MICROFLUIDICS**

Martina Hitzbleck and Emmanuel Delamarche

IBM Research - Zurich

**15:00 - C04 A FULLY INTEGRATED ELECTROCHEMICAL PUMP FOR MICROFLUIDIC CHIP SYSTEMS**

Philipp Meyer, Slim Larbi, Sydney Hakenberg, Carsten Hermann, Gregory Dame and Gerald Urban

Laboratory for Sensors, Department for Microsystem Engineering (IMTEK), University of Freiburg

Session D  
(Friday 09:40)

**09:40 - D01 PHASEGUIDES: A PARADIGM SHIFT IN MICROFLUIDIC LIQUID HANDLING**

Paul Vulto<sup>1</sup>, Sebastiaan Trietsch<sup>1</sup>, Jos Joore<sup>2</sup> and Thomas Hankemeier<sup>1</sup>

<sup>1</sup>Leiden University, <sup>2</sup>MIMETAS

**10:00 - D02 NEW INSIGHTS GAINED FROM MAKING AND BREAKING EMULSIONS IN MICROFLUIDIC DEVICES**

Karin Schroen, Maartje Steegmans, Koen van Dijke, Thomas Krebs and Remko Boom  
Wageningen University

**10:20 - D03 WATER FLOW CALIBRATION FACILITY IN FRANCE (1 ML/H TO 10 000 ML/H)**

Christopher David<sup>1</sup>, Pierre Claudel<sup>1</sup> and Joost Lötters<sup>2</sup>

<sup>1</sup>CETIAT, <sup>2</sup>Bronkhorst High-Tech BV

**10:40 - D04 ENHANCED ENERGY CONVERSION FROM THE STREAMING POTENTIAL BY POLYMER ADDITION**

Trieu Nguyen, Yanbo Xie, Lennart J. de Vreede, Albert van Den Berg and Jan Eijkel  
MESA+ Institute for Nanotechnology, University of Twente, Enschede, the Netherlands

Session E  
(Friday 11:30)

**11:30 - E01 POLYMER MICRO FLUIDIC SYSTEMS FABRICATED BY ULTRASOUND**

Johannes Sackmann<sup>1</sup>, Katharina Burlage<sup>1</sup>, Christof Gerhardy<sup>1</sup>, Dirk Loibl<sup>2</sup>, Liangyu Cui<sup>1,3</sup> and Werner Karl Schomburg<sup>1</sup>

<sup>1</sup>RWTH Aachen University, KEmikro, Aachen, <sup>2</sup>Herrmann Ultraschalltechnik GmbH&Co.KG, Karlsbad, <sup>3</sup>Tianjin University, Tianjin, P.R. China

**11:50 - E02 MICROBEADS FOR SAMPLING AND MIXING IN A COMPLEX SAMPLE**

Drew Owen<sup>1</sup>, Wenbin Mao<sup>1</sup>, Alexander Alexeev<sup>1</sup>, Jenifer Cannon<sup>2</sup> and Peter Hesketh<sup>1</sup>

<sup>1</sup>Georgia Institute of Technology, <sup>2</sup>University of Georgia

**12:10 - E03 HIGH EFFICIENCY ENERGY CONVERSION FROM LIQUID JET FLOW**

Yanbo Xie, Lennart J. de Vreede, Trieu Nguyen, Hans L. de Boer, Ad Sprenkels, Albert van Den Berg and Jan Eijkel

MESA+ Institute for Nanotechnology, University of Twente, Enschede, the Netherlands

**12:30 - E04 REALIZATION OF A MINIATURIZED MASS SPECTROMETER BASED ON A MICROFLUIDIC DEVICE**

Winfred Kuipers<sup>1</sup>, Michael Deilmann<sup>1</sup>, Michael Gerding<sup>1</sup>, Thorsten Neumann<sup>1</sup>, Michael Vogt<sup>1</sup>, Gregor Quiring<sup>2</sup>, Regulo Miguel Ramirez Wong<sup>2</sup>, Maria Reinhardt-Szyba<sup>2</sup>, Henning Wehrs<sup>2</sup> and Jörg Müller<sup>2</sup>

<sup>1</sup>KROHNE Messtechnik GmbH, Duisburg, Germany, <sup>2</sup>Hamburg University of Technology, Hamburg, Germany

**P01 DETERMINATION OF THERMAL GAS PROPERTIES AND FLOW SPEED USING THERMAL FLOW SENSORS**

Christoph Hepp<sup>1</sup>, Florian Krogmann<sup>1</sup> and Gerald Urban<sup>2</sup>

<sup>1</sup>Innovative Sensor Technology IST AG, <sup>2</sup>University of Freiburg

**P02 ONLINE LIQUID CALIBRATION TECHNOLOGIES**

Dong Liang<sup>1</sup>, Muniyogeshbabu Thanikhatla Govindaiah<sup>2</sup>, Laurent Tanguy<sup>2</sup>, Andreas Ernst<sup>2,3</sup>, Roland Zengerle<sup>1,2,4</sup> and Peter Koltay<sup>2,3</sup>

<sup>1</sup>HSG-IMIT, <sup>2</sup>IMTEK, <sup>3</sup>Biofluidix GmbH, <sup>4</sup>BIOSS

**P03 A MICRO-THERMAL FLOW SENSOR FOR SHUNT BLOCKAGE DETECTION IN PATIENTS WITH HYDROCEPHALUS**

Fred Hamlin, Andrew Gallant and Christopher Reay

School Of Engineering And Computing Sciences, Durham University, Durham, United Kingdom

**P04 STANDARDS FOR LOW TO ULTRA-LOW FLOW RATES FOR DRUG DELIVERY APPLICATIONS**

Peter Lucas<sup>1</sup>, I.J. Nielsen<sup>2</sup> and C. Melvad<sup>2</sup>

<sup>1</sup>Dutch Metrology Institute (VSL), Delft, Netherlands<sup>2</sup>Danish Technology Institute, Aarhus, Denmark

**P05 MICRO CORIOLIS MASS FLOW SENSOR FOR CHEMICAL MICRO-PROPULSION SYSTEMS**

Remco Wiegerink<sup>1</sup>, Theo Lammerink<sup>1</sup>, Jarno Groenesteijn<sup>1</sup>, Marcel Dijkstra and Joost Lötters<sup>1,2</sup>

<sup>1</sup>MESA+ Institute for Nanotechnology, <sup>2</sup>Bronkhorst High-Tech

**P06 CMOS MEMS BASED MICROFLUIDIC SYSTEM FOR CYTOMETRY AT 5 GHZ**

Subhajit Guha<sup>1,2</sup>, Klaus Schmalz<sup>1</sup>, Christian Wenger<sup>1</sup>, Wolfgang Krautschneider<sup>2</sup> and Chafik Meliani<sup>1</sup>

<sup>1</sup>IHP Microelectronics, Frankfurt (Oder), Germany, <sup>2</sup>Hamburg University of Technology, Hamburg, Germany

**P07 COMPARISON OF TWO TYPES OF HYBRID MICROFLUIDIC VALVES FOR COMPLEX MICROFLUIDIC FLOWPATH CONFIGURATIONS**

Albert Prak<sup>1</sup>, Theo Veenstra<sup>1</sup>, Frederik Schreuder<sup>1</sup>, Floris Falke<sup>1</sup> and Guus Borst<sup>2</sup>

<sup>1</sup>LioniX BV, <sup>2</sup>Dutch Space

**P08 STRUCTURE CONTROLLED POLYMERIC MICROLENS FABRICATION USING MULTIPHASE DROPLET ASSEMBLY**

Kenta Hasegawa, Dong Hyun Yoon, Asahi Nakahara, Tetsushi Sekiguchi and Shuichi Shoji

Major in Nanoscience and Nanoengineering, Waseda University, Tokyo, Japan



**P09 PASSIVE VALVE BASED MICROFLUIDIC STRUCTURE FOR ME-  
TERING**

Michael Suppan, Sylvia R Scheicher, Heinz Pichler, Markus Rumpler, Valentin Satzinger,  
Martin Hajnsek and Stefan Köstler

JOANNEUM RESEARCH, MATERIALS - Institute of Surface Technologies and Pho-  
tonics, Graz, Austria

**P10 SIMPLIFIED MICROFLUIDIC-BASED SYSTEM TO GENERATE DOU-  
BLE EMULSION MICRO DROPLETS FOR BIOMEDICAL APPLICATIONS**

Rui Sekine, Haruka Okada, Takashi Sakurai, Yoon Donghyun, Ryo Iizuka, Tetsushi  
Sekiguchi, Takashi Funatsu and Shuichi Shoji

Major in Nanoscience and Nanoengineering, Waseda University, Tokyo, Japan

**P12 A MICROFLUIDIC INTERPOSER BASED ON A THREE DIMEN-  
SIONAL MOLDED SUBSTRATE TECHNOLOGY**

Thomas Leneke, Marc-Peter Schmidt, Sören Hirsch and Bertram Schmidt

Institute of Micro and Sensor Systems, Otto-von-Guericke-University, Magdeburg, Ger-  
many

**P13 POLYMER-BASED MICRO FLOW SENSOR WITH ALTERNATIVE  
ELECTRONIC SIGNAL INTERFACES FOR LOW AND HIGH FLOW RATES**

Thomas Schönstein

Innovative Sensor Technology IST AG

**P14 WAFER-THROUGH ACCESS TRENCHES FOR SURFACE CHANNEL  
TECHNOLOGY**

J. Groenesteijn<sup>1</sup>, M. J. De Boer<sup>1</sup>, T.S.J. Lammerink<sup>1</sup>, J.C. Lötters<sup>2</sup> and R.J. Wiegerink<sup>1</sup>

<sup>1</sup>MESA+ Institute for Nanotechnology, University of Twente, Enschede, The Netherlands,

<sup>2</sup>Bronkhorst High-Tech BV, Ruurlo, The Netherlands

**P15 PRECISE FLUID HANDLING SYSTEM BASED ON PRESSURE REG-  
ULATION**

Charles-André Kieffer<sup>1</sup>, Stéphane Ritty<sup>1</sup>, Thomas Boudot<sup>1</sup>, Nicolas Petit<sup>2</sup>, Jérémie Weber<sup>1</sup>  
and Anne Le Nel<sup>1</sup>

<sup>1</sup>Fluigent, <sup>2</sup>CAS

**P16 NOVEL GRAVIMETIC CALIBRATION METHOD FOR NANO LITER  
LIQUID HANDLING DEVICES**

Dong Liang<sup>1</sup>, Laurent Tanguy<sup>2</sup>, Andreas Ernst<sup>1,3</sup>, Roland Zengerle<sup>1,2,4</sup> and Peter Koltay<sup>1,3</sup>

<sup>1</sup>HSG-IMIT, <sup>2</sup>IMTEK, <sup>3</sup>BioFluidix GmbH, <sup>4</sup>BIOS

**P18 TOWARDS A MICROVALVE FOR PROPORTIONAL CONTROL OF  
MASS FLOW**

M.S. Groen<sup>1</sup>, D.M. Brouwer<sup>2</sup>, J.C. Lötters<sup>3</sup> and R.J. Wiegerink<sup>1</sup>

<sup>1</sup>MESA+ Research Institute, University of Twente, Enschede, The Netherlands, <sup>2</sup>DEMCON  
Advanced Mechatronics, Oldenzaal, The Netherlands, <sup>3</sup>Bronkhorst High-Tech BV, Ru-  
urlo, The Netherlands

**P19 PROBING RED BLOOD CELL DYNAMICS**

René C.H. van der Burgt, Patrick D. Anderson and Frans N. van de Vosse

Eindhoven University of Technology

**P20 A LOW-COST, NORMALLY CLOSED, SOLENOID VALVE FOR NON-CONTACT DISPENSING IN THE SUB-L RANGE**

Stefan Bammesberger, Sabrina Kartmann, Tanguy Laurent, Dong Liang, Klaus Mutschler, Andreas Ernst, Peter Koltay and Roland Zengerle

Laboratory for MEMS Applications, IMTEK - Department of Microsystems Engineering, University of Freiburg, Germany

**P21 A MICROFLUIDIC PASSIVE BATCH MIXING CHIP FOR RECOMBINASE POLYMERASE AMPLIFICATION UTILIZING PHASEGUIDE TECHNOLOGY**

Sydney Hakenberg, Matthias Hügler, Gregory Dame and Gerald Urban

Laboratory for Sensors, Department for Microsystem Engineering (IMTEK), University of Freiburg

**P22 FLOW STOPPING USING A 3D-STRUCTURED MICROFLUIDIC T-JUNCTION**

Tsung-Ju Chen<sup>1</sup>, Fan-Gang Tseng<sup>1</sup> and Ching-Chang Chieng<sup>2</sup>

<sup>1</sup>Institute of NanoEngineering and MicroSystems, National Tsing Hua University, HsinChu, Taiwan(R.O.C.), <sup>2</sup>Department of Mechanical and Biomedical Engineering, City University of Hong Kong, Hong Kong, China

**P23 THE APPLICATION OF MICRO-AND NANOFLUIDICS IN WOBBE INDEX METERS**

Albert Mouris<sup>1</sup>, Remco Wiegerink<sup>2</sup>, Joost Lötters<sup>3</sup>, Marco Pap<sup>2</sup> and Theo Lammerink<sup>2</sup>

<sup>1</sup>Hobre Instruments BV, Purmerend, The Netherlands, <sup>2</sup>University of Twente, Enschede, The Netherlands, <sup>3</sup>Bronkhorst High-Tech BV, Ruurlo, The Netherlands

**P24 MICROREACTORTECHNOLOGY: REAL-TIME FLOW MEASUREMENTS IN ORGANIC SYNTHESIS**

Bas van Den Broek, Pieter Nieuwland and Kaspar Koch

Future Chemistry

**P25 PRESSURE DROP REDUCTION IN CONICAL CHANNEL MICROEVAPORATORS**

Cor Rops<sup>1</sup>, Giaco Oosterbaan<sup>1</sup> and Cees van der Geld<sup>2</sup>

<sup>1</sup>TNO, Eindhoven, The Netherlands, <sup>2</sup> Eindhoven University of Technology, Eindhoven, The Netherlands

**P26 TOWARDS SINGLE CELL LEVEL HEAT SHOCK PROTEIN EXPRESSION BY MEANS OF HYDRODYNAMIC TRAPPING AND LOCAL HEATING**

Maurizio R. Gullo<sup>1</sup>, Ryohei Ueno<sup>2</sup>, Yuan Pang<sup>2</sup>, Nobuyuki Takama<sup>2</sup>, Yasuyuki Sakai<sup>2</sup>, Beomjoon Kim<sup>2</sup> and Jürgen Brugger<sup>1</sup>

<sup>1</sup>Microsystems Laboratory, EPFL, Lausanne, Switzerland, <sup>2</sup>Institute of Industrial Science, The University of Tokyo, Tokyo, Japan



## PUSHING THE LIMITS OF ELECTRICAL DETECTION OF ULTRALOW FLOWS IN NANOFLUIDIC CHANNELS

*K. Mathwig, S. Kang, D. Mampallil and S.G. Lemay*

MESA+ Institute for Nanotechnology, University of Twente, Enschede, The Netherlands

### ABSTRACT

This paper presents improvements in flow detection by electrical cross-correlation spectroscopy. This new technique detects molecular number fluctuations of electrochemically active analyte molecules as they are transported by liquid flow through a nanochannel. These fluctuations are used as a marker of liquid flow as their time of flight in between two consecutive transducers is determined, thereby allowing for the measurement of liquid flow rates in the picoliter-per-minute regime. Here we show an enhanced record-low sensitivity below 1 pL/min by capitalizing on improved electrical instrumentation, an optimized sensor geometry and a smaller channel cross section.

### KEYWORDS

Flow detection, electrochemical sensor, nanofluidics, cross-correlation, nanochannel, redox cycling

### INTRODUCTION

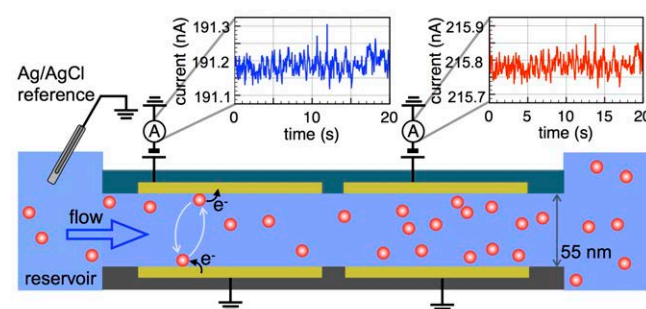
Microfabricated flow sensors are used in a wide range of commercial and research applications, their importance being reflected in the vast number of different types of sensors and measurement concepts [1,2]. Also in nanofluidic systems, the flow rate is a desirable property to quantify, e.g. when measuring liquid slip or investigating the transport of macromolecules through nanochannels [3].

Our group has recently introduced electrochemical cross-correlation spectroscopy as an all-electrical method to detect ultralow picoliter-per-minute flow rates in nanofluidic channels [4]. The basis of this method is nanogap sensors [5], in which electrochemical active molecules undergo redox cycling between two closely spaced electrodes embedded in opposite walls of a nanochannel. The molecules travel back and forth by diffusion and are repeatedly oxidized and reduced at the electrodes, thereby shuttling electrons across the channel and generating an electrical current. This current is directly proportional to the number of molecules in the nanogap sensor. Since the molecules undergo random thermal Brownian motion, their number fluctuates considerably in time in the small femtoliter detection volume – an effect that is reflected in corresponding fluctuations of the electrical current.

To measure liquid flow we detect the time of flight of this diffusion noise in between two

consecutive transducers, as shown in Figure 1. The fluctuations are measured by recording current-time traces at the top electrodes of both sensors. The time of flight is then extracted by cross correlation analysis of these traces.

Here, we report a tenfold improvement in the sensitivity of this method and discuss its limits.



*Figure 1: Schematic of the experimental setup. Fluctuations in the number density of electroactive molecules are used as tracers of liquid flow as water is transported through a nanochannel. The fluctuations are detected electrically by redox cycling and their time of flight between the detectors – or, equivalently, the flow velocity – are then determined by cross correlation analysis of current-time traces (curves in the insets are a schematic illustration).*

### DEVICE FABRICATION

Nanogap devices were fabricated as described previously [6] on an oxidized 4-inch silicon wafer. 20 nm thick Pt bottom electrodes were deposited by electron beam evaporation and patterned by a lift-off process. The nanochannel was defined as a 55 nm thick Cr layer also deposited and defined by electron beam deposition and photolithography, respectively. After deposition of a 100 nm thick Pt top electrode, the whole structure was buried in a passivating SiN layer deposited by chemical vapor deposition. At both ends of the nanochannel, access holes were etched into the passivation layer by reactive ion etching. Schematic cross sections of the device are shown in Figure 2. It consists of a 202  $\mu\text{m}$  long, 5  $\mu\text{m}$  wide and 55 nm high nanochannel. The electrode pairs at the channel floor and ceiling are 100  $\mu\text{m}$  long and are separated by a 2  $\mu\text{m}$  wide gap.

Liquid flow is generated in the nanochannel by a syringe pump (Harvard Apparatus Pump 11 Pico Plus Elite). Since ultralow flow rates cannot be driven directly, the pump flow is reduced via Parallel Flow

Control [7]. Tubing is connected to the nanofluidic device via an additional layer in polydimethylsiloxane (PDMS), which was formed by molding on an SU-8/silicon master and bonded to the SiN surface after surface activation in an oxygen plasma. In this layer, four 200  $\mu\text{m}$  long, 5  $\mu\text{m}$  wide and 3  $\mu\text{m}$  high microchannels connect both access holes of the nanochannel. The flow is then divided in between the parallel nano- and microchannels according to the ratio of their hydraulic resistances. Since the resistances change cubically with the channel height the nanochannel flow rate is reduced by a factor of approximately 400 000 with respect to the syringe pump flow rate. A micrograph of the device is shown in Figure 3.

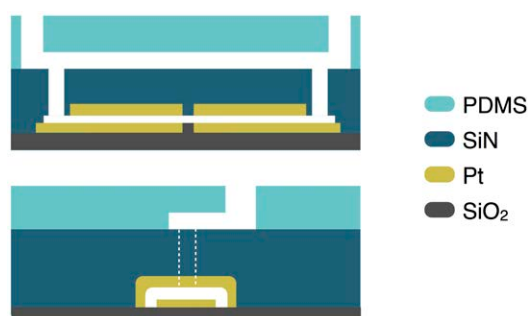


Figure 2: Schematic cross section of the device along the longitudinal (top) and lateral axis (bottom).

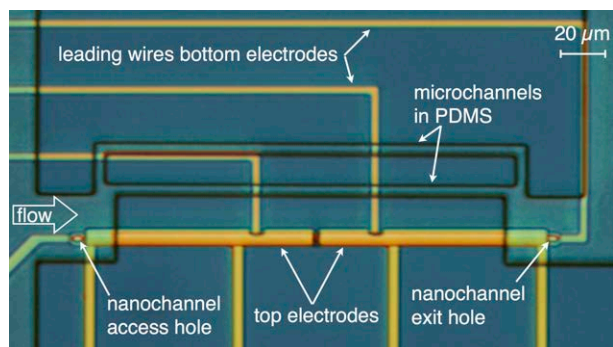


Figure 3: Top view micrograph of a 202  $\mu\text{m}$  long nanofluidic device bonded to a PDMS microchannel layer (only two out of four microchannels running in parallel to the device are shown).

## EXPERIMENTAL

Ferrocenedimethanol ( $\text{Fc}(\text{MeOH})_2$  from Acros, diffusion coefficient  $D = 6.7 \cdot 10^{-10} \text{ m}^2/\text{s}$ ) was chosen as redox-active species and prepared as a 1 mM solution in Milli-Q water with 0.1 M KCl (Sigma-Aldrich) added as background electrolyte together with 5 mM  $\text{H}_2\text{SO}_4$  (Sigma-Aldrich) to prevent electrode degradation. Directly before a measurement, the Cr sacrificial layer was removed and the nanochannel was formed by purging the microchannels with a chromium etchant solution

(Selectipur, BASF). The redox active solution was then driven through the channel with varying syringe pump flow rates of up to 60  $\mu\text{L}/\text{h}$ .

Both the bottom and top electrodes of the device were connected to a CH Instruments 842B bipotentiostat. Both top electrodes were biased at an oxidizing potential of 0.45 V while the bottom electrodes were short-circuited to a Ag/AgCl reference electrode that was connected by tubing downstream of the device (reducing potential). The whole setup except for the bipotentiostat was shielded from interference in a Faraday cage. Current-time traces of up to 600 s length were recorded at 10 ms sampling intervals at both top electrodes. We used high pass filtering to remove slow instrumental drift (see below).

## RESULTS AND DISCUSSION

The times of flight of molecular number concentrations were extracted from the detected current-time traces by cross-correlation analysis [4]: the traces  $I_{1,2}(t)$  exhibit diffusion noise  $\delta I(t) = I(t) - \langle I(t) \rangle$ , from which a normalized cross-correlation function  $G(\tau)$  is evaluated:

$$G(\tau) = \langle \delta I_1(t) \delta I_2(t + \tau) \rangle / \langle \delta I_{1,2}^2 \rangle.$$

$G(\tau)$  peaks at the time  $\tau_{\text{peak}}$ , which is – in a first approximation – identical to the time of flight of  $\text{Fc}(\text{MeOH})_2$  molecules from the center of the first transducer to the center of the second one located 102  $\mu\text{m}$  downstream. In Figure 4 cross-correlation functions are shown as a function of the syringe pump flow rate.

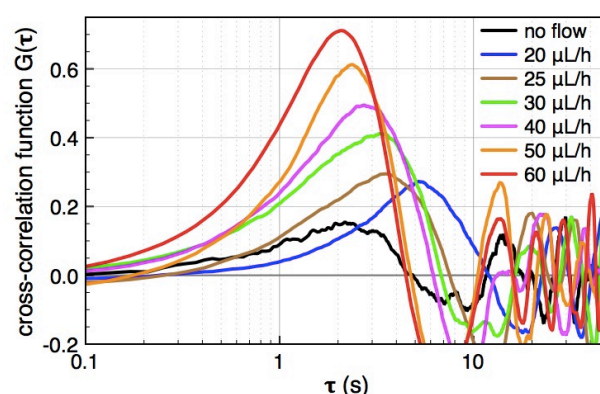


Figure 4: Cross-correlation functions for different syringe pump flow rates determined from current-time traces recorded at both 100  $\mu\text{m}$  long top electrodes of a 202  $\mu\text{m}$  long nanofluidic device.

The curves are defined exclusively by longitudinal advection and diffusion. The increasing influence of diffusion for decreasing flow rates leads to peak broadening and loss of correlation. It prohibits the



detection of times of flight longer than approximately 8 s because the number fluctuations decay entirely during the flight.

The liquid flow rate in the nanochannel was determined by multiplying the center-to-center distance  $\Delta x$  of the transducers with the channel cross section and dividing by  $\tau_{\text{Peak}}$ . It is shown in Figure 5 as a function of pump flow (orange diamonds).

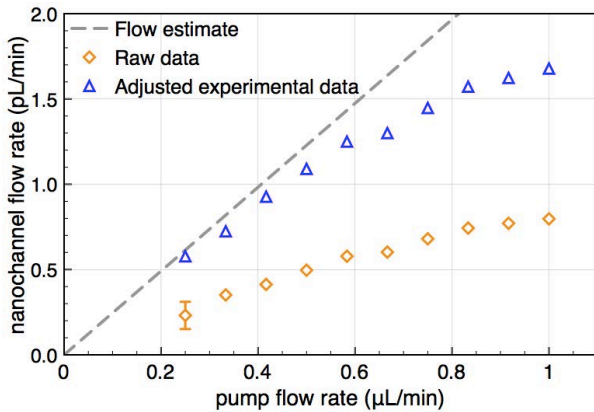


Figure 6: Nanofluidic flow rates as a function of syringe flow. The adjusted experimental data points are corrected for the shift of the peak times as well as for dynamic adsorption. The dashed line's slope corresponds to the ratio of the micro- and nanochannels' resistances of  $1/400\,000$ .

However, two effects need to be accounted for for a more accurate flow detection.

First, due to the high surface-to-volume ratio of the nanochannel of  $2 \cdot 10^7 \text{ m}^{-1}$ , the  $\text{Fc}(\text{MeOH})_2$  molecules undergo pronounced dynamic reversible adsorption at the electrodes and nanochannel walls, which slows down their average transport with respect to the fluid. We estimate the relative number of adsorbed molecules  $N_{\text{ads}}/N_{\text{tot}}$  by stochastic chronoamperometry [8]. Its magnitude exhibits considerable scatter but amounts approximately to  $N_{\text{ads}}/N_{\text{tot}} = 0.5$ , i.e., the molecules are slowed down to 50% of the mean liquid flow velocity.

Secondly, the increasing influence of diffusion shifts the cross-correlation peak time  $\tau_{\text{Peak}}$  away from the actual times of flight for slow flow rates. This shift is determined from the known analytical cross-correlation function [4] and is shown in Figure 6 for the molecular diffusion coefficient  $D = 6.7 \cdot 10^{-10} \text{ m}^2/\text{s}$  (green curve) and an adjusted effective  $D_{\text{eff}} = 0.5 D$ , which takes into account the reduction of diffusive transport by the dynamic adsorption.

Nanochannel flow rates adjusted for both effects are shown as blue triangles in Figure 6. (The nonlinear decrease in nanochannel flow for higher pump flow rates is caused by PDMS bulging at high pressures

[9].) We are able to detect flow rates below  $1 \text{ pL}/\text{min}$ , which is a factor of ten smaller compared to our previous measurements [4].

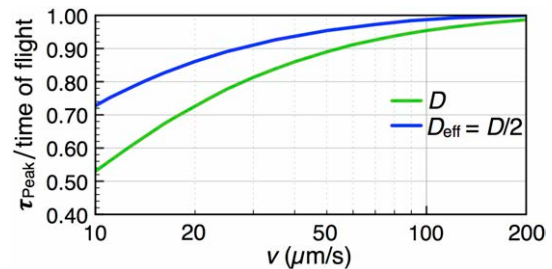


Figure 6: Analytically determined deviation of the cross-correlation function's peak time  $\tau_{\text{Peak}}$  from the time of flight as a function of flow velocity. The blue curve is corrected for an effectively slower diffusion of the molecules due to dynamic adsorption. Experimental flow rates range from  $15 \text{ μm}/\text{s}$  to  $50 \text{ μm}/\text{s}$ .

This increase in sensitivity is achieved for three reason:

- 1) The nanochannel has a height of  $55 \text{ nm}$  instead of  $130 \text{ nm}$ , thereby simply reducing the flow rate for the same average flow velocity.

- 2) The length of each electrode is increased from  $50 \text{ μm}$  to  $100 \text{ μm}$ . The correlation or fluctuation in a longer plug of fluid is measured, thereby directly increasing the signal strength. Also, in a longer plug it takes more time for the fluctuations to decay by diffusion.

- 3) Since our method relies on the detection of purely stochastic noise, sensitivity is increased by sampling longer traces or employing faster sampling rates. Our previous instrumentation (Keithley 6430 sub-femtoamp source meters) limited the current-time traces to a length of  $25 \text{ s}$  at a fast  $100 \text{ s}^{-1}$  acquisition rate. The instrumentation used here allowed extending the measurement period to up to  $600 \text{ s}$  at the same sampling interval.

Diffusion sets the limit of the slowest resolvable velocity in the nanochannel to  $v \geq 2D/\Delta x$ . However, for our current setup, the sensitivity is ultimately limited by instrumental drift of the measured current of about  $0.5\%$  or  $1 \text{ nA}$  peak-to-peak, most likely caused by temperature drift. This external noise occurs at time scales of up to several  $10$ 's of  $\text{mHz}$  and can be reduced by high-pass filtering ( $4^{\text{th}}$  order Butterworth filter) with a  $f = 100 \text{ mHz}$  cutoff frequency. The drift essentially prohibits detection of slower flow rates with corresponding times of flight longer than about  $10 \text{ s}$ . For longer times, the diffusion noise is lost in the instrumental drift, which occurs at the same time scales but exhibits a larger amplitude.

## CONCLUSION AND OUTLOOK

We have used all-electrical cross-correlation spectroscopy of mesoscopic number fluctuations to detect record-low liquid flow rates below 1 pL/min in electrochemical nanogap sensors. This is comparable to the sensitivity achieved by the related method of determining the autocorrelation function of a single current-time trace as a function of flow in a 100  $\mu\text{m}$  long and 50 nm high sensor [10].

We emphasize that the determined nanochannel flow rates are subject to error due to uncertainties in channel height,  $\tau_{\text{Peak}}$ , and adsorption. Thus, while detection in the sub-picoliter-per-minute range is possible, we do not claim a precision measurement in this regime.

Our method is the direct electrical analogue to optical fluorescence correlation spectroscopy [11]. Therefore we envision its application not exclusively for flow detection but as a tool to investigate properties of smallest quantities of analyte molecules such as adsorption, concentration or electrochemical reaction kinetics.

## ACKNOWLEDGEMENT

We gratefully acknowledge financial support from the Netherlands Organization for Scientific Research (NWO) and the European Research Council (ERC).

## REFERENCES

- [1] J.T.W. Kuo, L. Yu, E. Meng, "Micro-machined Thermal Flow Sensors—A Review", *Micromachines*, Vol.3, pp.550-573, 2012.
- [2] S. Silvestri, E. Schena, "Micromachined Flow Sensors in Biomedical Applications", *Micromachines*, Vol.3, pp.225-243, 2012.
- [3] K.J.A. Westin, C.-H. Choi, K.S. Breuer, "A novel system for measuring liquid flow rates with nanoliter per minute resolution", *Exp. Fluids*, vol.34, pp.635-642, 2003.
- [4] K. Mathwig, D. Mampallil, S. Kang, S.G. Lemay, "Electrical Cross-Correlation Spectroscopy: Measuring Picoliter-per-Minute Flows in Nano-channels", *Phys. Rev. Lett.*, vol.109, pp.118302, 2012.
- [5] M.A.G. Zevenbergen, B.L. Wolfrum, W.D. Goluch, P.S. Singh, S.G. Lemay, "Fast electron-transfer kinetics probed in nanofluidic channels", *J. Am. Chem. Soc.*, vol.131, pp.11471-11477, 2009.
- [6] S. Kang, K. Mathwig, S.G. Lemay, "Response time of nanofluidic electrochemical sensors", *Lab Chip*, vol.12, pp.1262-1267, 2012.
- [7] H. Liang, W.J. Nam, S.J. Fonash, "A novel parallel flow control (PFC) system for syringe-driven nanofluidics", *NSTI Nanotechnology Conference and Trade Show, Technical Proceedings, Boston, USA*, 2008, vol. 3, pp. 281-283.
- [8] P.S. Sing, H.-S. M. Chan, S. Kang, S.G. Lemay, "Stochastic amperometric fluctuations as a probe for dynamic adsorption in nanofluidic electrochemical systems", *J. Am. Chem. Soc.*, vol.133, pp. 18289–18295, 2011.
- [9] T. Gervais, J. El-Ali, A. Günther, K.F. Jensen, "Flow-induced deformation of shallow microfluidic channels", *Lab Chip*, vol.6, pp.500-507, 2006.
- [10] K. Mathwig, D. Mampallil, S. Kang, S.G. Lemay, "Detection of Sub-Picoliter-per-Minute Flows by Electrochemical Autocorrelation Spectroscopy", *Proceedings of the 16th International Conference on Miniaturized Systems for Chemistry and Life Sciences (MicroTAS), Okinawa, Japan*, Oct. 28 -Nov. 1, 2012, in press.
- [11] D. Magde, W.W. Webb, E.L. Elson, "Fluorescence Correlation Spectroscopy. III. Uniform Translation and Laminar Flow", *Biopolymers*, vol.17, pp. 361-376, 1978.

## CONTACT

\* S.G. Lemay, S.G.Lemay@utwente.nl

## 1. Sensors

# SIMULATION OF THE OSCILLATORY EXCITATION OF A THERMAL FLOW SENSOR

*D.F. Reyes-Romero<sup>1</sup>, A.S. Cubukcu<sup>1</sup> and G.A. Urban<sup>2</sup>*

<sup>1</sup>University of Freiburg, Department of Microsystems Engineering, Freiburg, Germany

<sup>2</sup>University of Freiburg, Freiburg Institute for Advanced Studies, Freiburg, Germany

## ABSTRACT

This contribution presents a method to determine the thermal conductivity of gases under flow in a micro-fluidic channel by using high frequency thermal excitation (200 Hz). Results are obtained by using finite element method simulations. The ultimate goal is to measure all thermal properties in order to achieve gas independent flow measurement.

## KEYWORDS

Thermal flow sensor; Frequency; Sinusoidal excitation

## INTRODUCTION

Micromachined thermal flow sensors have been widely used during the last years. Their small size and cheap production costs make them suitable for applications where price and space are the major constraints. Any thermal flow sensor features at least a heat source and a temperature sensor.

Depending on the measuring principle, the heater and the temperature probe can be the same element (anemometric principle) [1], two independent elements (calorimetric and time-of-flight principles) [1] or an array of multiple heaters and temperature probes [1, 2]. In order to maximize the heat transfer from the heat source to the moving medium, the heater and the temperature probes are usually placed on thermally insulating structures such as bridges or membranes. A common problem among all types of thermal sensors is that their measuring characteristic is strongly affected by the thermal properties of the flowing medium. Therefore, such sensors need to be calibrated for a specific fluid before any measurement takes place. If the fluid is changed, then these sensors need to be recalibrated or compensated given that the new fluid or its thermal properties are known.

The sensor presented in this contribution features a thin membrane and operates using the calorimetric flowing principle. Its main difference from similar sensors is the heater-thermistor structure that is placed right in the middle of its surface. Calorimetric flow sensors usually use continuous heat generation. Research has been done on sensors that feature oscillating heat generation. It has been shown that a thermal sensor under oscillatory excitation is able to measure the thermal conductivity and the thermal diffusivity of gases and liquids [2], which brings the possibility of applying autocalibration procedures if

the fluid changes. However, the major drawback is that flow speed must be known before hand.

Autocalibration is still an open problem with regard to thermal flow sensor. In this contribution we also explore an approach that exploits the central heater-thermistor structure under oscillatory heat generation in order to measure the thermal properties of the flowing medium at any flow rate, in particular the thermal conductivity. Constant heat generation is simultaneously applied in order to measure the actual flow. Analysis and results are obtained by means of finite element simulations.

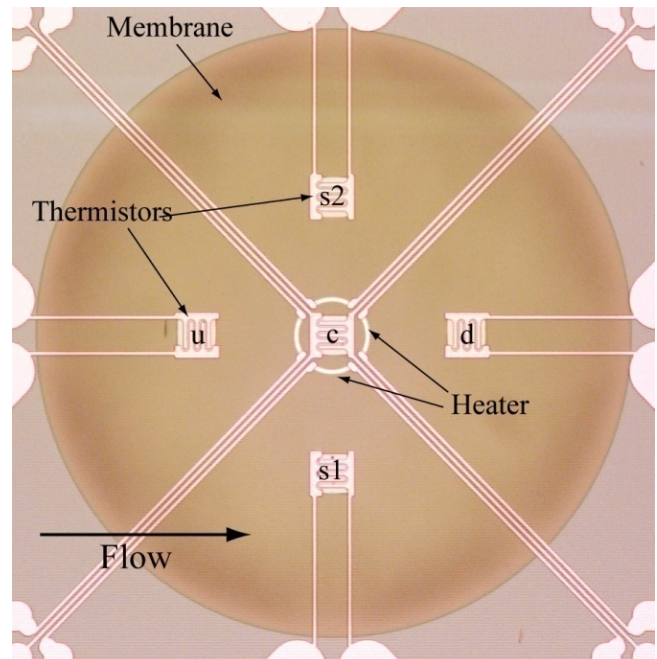


Figure 1: Top view of the sensor's membrane. The labels c, u, d, s1 and s2, mark the position of the thermistor according to the flow direction, that is, central, upstream, downstream and side thermistors.

## SENSOR DESCRIPTION

The simulated sensor has already been fabricated and reported in a previous contribution [3]. It consists of a silicon chip whose dimensions are  $12.7 \times 12.7 \times 0.5 \text{ mm}^3$ . It supports a 1-mm-diameter, insulating membrane made out of  $\text{SiO}_2$  and silicon nitride. Like typical calorimetric flow sensors [1, 2], a chromium heater is placed at the center of the membrane whilst several temperature sensors are placed around it. An additional silicon nitride passivation layer is deposited all over.



Table 1. Thermal conductivities at 20°C of the gases used in the simulations [5, 6]. 0.5He-0.5Ne represents a molar composition of 50%-50%.

Gas	Thermal Conductivity, $k$ (mW/(m K))
Helium	153.5
Air	25.87
CO <sub>2</sub>	16.25
Argon	17.49
Hydrogen	189.8
Neon	49
Xenon	5.37
0.5He-0.5Ne	86.63

Flow measurement is based on the temperature difference between two different points, usually located up- and downstream with respect to the heating element. The temperature probes are germanium thermistors, which are arranged concentrically around the heater, as shown in Figure 1. They are patterned in a square shape (75  $\mu\text{m} \times 75 \mu\text{m}$ ). An additional thermistor (labeled 'c' in Fig. 1) is placed right at the center of the membrane within the heating element. Germanium was selected due to its high temperature coefficient of resistance (TCR) and its relatively high resistance [4]. Thermistors exhibit a final typical resistance of 150 k $\Omega$ , which requires a reduced polarization power (in the order of microwatts).

The heater is divided in four circular arcs in order to allow the interconnection of the central thermistor. The mean radius of the heater is 60.5  $\mu\text{m}$ . The heater was fabricated by depositing chromium, which selected due to its very low TCR.

## SIMULATION MODEL

The sensor's operation in thermal domain is simulated in COMSOL Multiphysics. A micro-fluidic channel is located just above the sensor's surface. The channel has a height  $H = 330 \mu\text{m}$  and a width  $W = 1.5 \mu\text{m}$ . Gas flows through the channel under laminar conditions at constant average flow speed, which is varied from 0.001 to 1 m/s.

The flow field itself is not solved by the simulation model but provided as an analytical input, thus reducing the simulation time. Several common gases were used as the flowing medium (see Table 1). Assuming a fully developed flow profile, the velocity field inside the channel is independent of the gas type and approximated as

$$u(x,y,z) = 36u_0 z(H-z)(W^2/4 - y^2) / (WH)^2, \quad (1)$$

where  $x$ ,  $y$  and  $z$  are the rectangular coordinates and  $u_0$  is the average flow speed. The flow profile described by Eq. (1) does not correspond to the exact analytical solution of the Navier-Stokes equations. However, it offers a good approximation given the high aspect ratio of the channel.

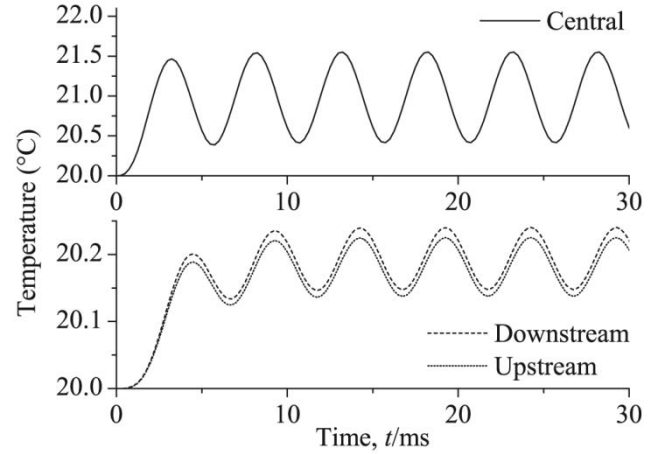


Figure 2. Simulated thermistor temperatures for helium flowing at an average flow speed of 0.1 m/s.

The membrane and the structures placed thereon are all modeled as a single circular shell, which was divided into several regions. These regions model the thermistors, the heater and the metal contacts. Equivalent thermal properties are calculated for each region based on the materials of the stacked layers. The space below the membrane is modeled as an entirely static gas. The gas above and below the membrane is the same. A sinusoidal power generation signal is applied to the heater. Its amplitude, mean value and frequency are 0.5 mW, 0.5 mW and 200 Hz, respectively. The final time of each simulation is long enough to guarantee that the temperature at the thermistors agrees with

$$T_i(t) = |T_i| \sin(2\pi ft + \varphi_i) + T_{i,0}, \quad (2)$$

where  $i$  is the thermistor index (as shown in Figure 1),  $f$  is the frequency,  $t$  is the time,  $|T_i|$  is the temperature amplitude,  $\varphi_i$  is the phase (with respect to input power signal) and  $T_{i,0}$  is the average temperature. Figure 2 presents an exemplary simulation for helium in which after 15 ms the temperature signals can be described by Eq. (2). From this figure it also becomes clear that two independent temperature fields develop in steady state: A constant or DC temperature, which only depends on the average heating power; and an oscillatory or AC component that is solely driven by the oscillatory component of the heat generation. The independency between these two components holds as long as the DC overtemperature produced by the DC heat generation does not change the thermal properties

of the gas.

## RESULTS AND DISCUSSION

Figure 3 depicts the simulation result for  $|T_c|$  (central thermistor). This magnitude appears to be barely dependent on the flow rate regardless the gas. From 0.001 to 1 m/s, all gases show a reduction in the amplitude. However, this reduction is less than 0.5%. This behavior is only observed for the central thermistor. The simulated temperature oscillations at all other thermistors are strongly dependent on the flow rate. Their phase shifts and average temperatures are also affected by the flow rate for all gases in the investigated speed range.

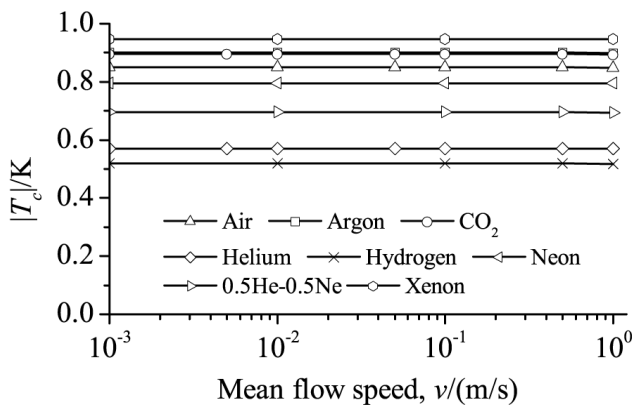


Figure 3: Amplitude of the simulated temperature oscillations at the central thermistor ('c' in Figure 1) for different gases.

Results in Fig. 3 can be explained by the combination of two factors: the high operation frequency, and the short separation between the central thermistor and the heater.

First, the average distance from the heater to the central thermistor is about 16  $\mu\text{m}$ , which is 10 times smaller to the distance to any other thermistor. Hence, much of the heat flux that reaches the central thermistor occurs directly through the membrane. However, an important contribution to this heat flux also occurs through the gas, very close to the surface of the membrane, where the no-slip condition keeps the flow velocity close to zero regardless the average flow speed inside the flow channel. This means that heat conduction is the dominant mechanism that transports heat to the central thermistor. Consequently, the average flow speed must be quite large in order to take heat away and reduce the amplitude of the oscillations. Given the large distance between the heater and all the other thermistors, the influence of the forced convection (hence, the flow speed) on their temperature is more significant.

Secondly, when the heat generation oscillates at high frequencies, thermal systems behave like a low

pass filter. Furthermore, the attenuation factor grows as the distance from the heat source increases. As a consequence of this, the oscillatory thermal boundary layer over the membrane becomes narrower as the frequency increases. If this AC thermal boundary layer is sufficiently small, it does not get affected or modulated by the flow speed because of the no-slip condition at the surface of the membrane. As a result, at high frequencies the heat transport between the heater and the central thermistor is almost entirely driven by conduction.

The simulated gases cover a wide range of thermal conductivity, density and specific heat capacity. The smallest amplitude  $|T_c|$  among all gases corresponds to hydrogen whereas the largest corresponds to xenon. This amplitude increases for gases with lower thermal conductivity (see Fig. 3 and Table 1).

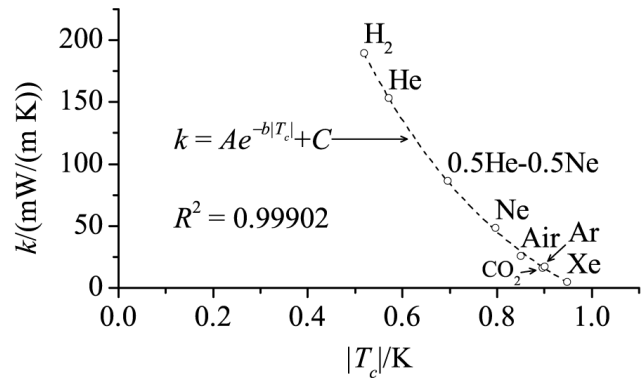


Figure 4: Correlation between the thermal conductivity  $k$  and  $|T_c|_{v=0.001 \text{ m/s}}$  at 20°C. Estimated parameters are  $A=1134 \text{ mW/(m·K)}$ ,  $b=2.811 \text{ K}^{-1}$  and  $C=-74.48 \text{ mW/(m·K)}$  (see Eq. (3)).

Although the number of simulated gases might not reach enough statistical significance, results suggest that the amplitude of the temperature oscillations at the central thermistor is exclusively correlated to the gas thermal conductivity. This relation seems to be given by

$$k = A \cdot \exp(-b \cdot |T_c|) + C, \quad (3)$$

where  $A$ ,  $b$  and  $C$  are fitting parameters and  $k$  is the thermal conductivity of the gas. Figure 4 depicts the resulting curve after fitting Eq. (3) to the simulation results.

The regression shows a high statistical significance confirming that the amplitude of the thermal oscillations at the central thermistor is highly correlated to thermal conductivity of the gas. The thickness of the AC thermal boundary layer might also explain this dependency.

Besides the thermal conductivity, the specific heat



capacity ( $c_p$ ) and the density of the gases ( $\rho$ ) are the relevant thermal properties taken into the account in the simulations. The product of these two magnitudes ( $c_p \cdot \rho$ ), known as the volumetric heat capacity, defines the amount of heat needed to increase the temperature of a given volume of material. As previously discussed, under AC excitation the oscillatory boundary layer has a small thickness, these means that the amount of gas that gets warmed and cooled on each cycle becomes smaller at higher frequencies.

As a consequence, the volumetric heat capacity of the membrane dominates. Since the density and the specific heat capacity in solids is much larger than in gases and the thickness of the AC thermal boundary layer is small, changes in the volumetric heat capacity of the gas does not have a major impact on the amplitude of the temperature oscillations at the central thermistor  $\cdot |T_c|$ .

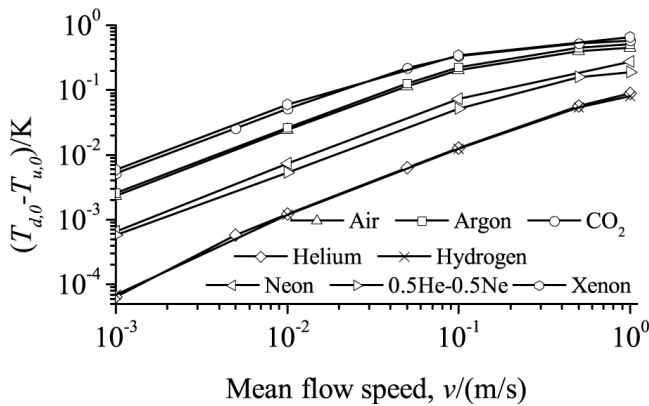


Figure 5: Simulated difference between the average temperatures down- and upstream for different gases.

## CONCLUSIONS

By means of thermal simulations, it has been shown that a thermal flow sensor that features a central thermistor enclosed in a heater is able to determine the thermal conductivity of real common gases under flow conditions.

This potential thermal conductivity measurement can be achieved by analyzing the AC component of thermal oscillations. It is important to keep the maximum DC overtemperature in the gas from being too large. This condition is necessary to maintain the thermal properties of the gas as uniform as possible. Regions with a large DC overtemperature may have different thermal conductivity, which affects correlation described by Eq. (3). Nonetheless, the presented results do take into account the dependency of the gases' thermal properties on the temperature.

Figure 3 suggests that the thermal conductivity can still be determined at average flow speeds as high as 1 m/s. Given the cross section of the channel, this means that a flow rate of about 30 ml/min is still

suitable for the method presented in this contribution. Nevertheless, adjusting the cross-sectional area can increase the flow rate range.

Fluid independent flow measurement is still a challenge. It requires the determination of the volumetric heat capacity or the thermal diffusivity. In such a case, the DC component of the temperature at the up- and downstream locations can be used to measure the flow rate. Figure 5 shows that the difference between the average temperature downstream and upstream increases monotonically for the analyzed flow speed range. In fact, this relationship appears to be linear for flow speeds up to 0.1 m/s.

Figure 5 also shows the minimum flow speed that could be measured by the real sensor. The resolution of germanium thermistors is limited by noise to 0.1 mK [4]. This implies that for gases with high thermal conductivity such as hydrogen and helium the minimum detectable flow speed is 0.001 m/s.

## REFERENCES

- [1] M. Elwenspoek. "Thermal flow micro sensors". *Semiconductor Conference, 1999. CAS '99 Proceedings. 1999 International*, 1999, pp. 423-435 vol.422.
- [2] R. Beigelbeck, F. Kohl, S. Cerimovic, A. Talic, F. Keplinger, and B. Jakoby. "Thermal property determination of laminar-flowing fluids utilizing the frequency response of a calorimetric flow sensor". *Sensors, 2008, IEEE, Lecce, Italy*, 2008, pp. 518-521.
- [3] A. S. Cubukcu, E. Zernickel, U. Buerklin, and G. A. Urban, "A 2D thermal flow sensor with sub-mW power consumption", *Sensors and Actuators A: Physical*, Vol. (2), pp. 449-456, 2010.
- [4] G. Urban, A. Jachimowicz, F. Kohl, H. Kuttner, F. Olcaytug, H. Kamper, F. Pittner, E. Mann-Buxbaum, T. Schalkhammer, O. Prohaska, and M. Schönauer, "High-resolution thin-film temperature sensor arrays for medical applications", *Sensors and Actuators A: Physical*, Vol. (1-3), pp. 650-654, 1989.
- [5] D. R. Lide, ed. *CRC Handbook of Chemistry and Physics*. 90th ed. 2009, CRC Press/Taylor and Francis: Boca Raton. 2804.
- [6] J. Kestin, K. Knierim, E. A. Mason, B. Najafi, S. T. Ro, and M. Waldman, "Equilibrium and Transport Properties of the Noble Gases and Their Mixtures at Low Density", *Journal of Physical and Chemical Reference Data*, Vol. (1), pp. 229-303, 1984.

## CONTACT

\* G.A. Urban, urban@imtek.de

# TUNABLE SENSOR RESPONSE BY VOLTAGE-CONTROL IN BIOMIMETIC HAIR FLOW SENSORS

*H. Droogendijk and G. J. M. Krijnen*

MESA<sup>+</sup> Institute for Nanotechnology, University of Twente, The Netherlands

## ABSTRACT

We report improvements in detection limit and responsivity of biomimetic hair flow sensors by electrostatic spring-softening (ESS). Applying a DC-bias voltage to our capacitive flow sensors mediates large (80% and more) voltage-controlled electro-mechanical amplification of the flow signal for frequencies below the sensor's resonance. Application of an AC-bias voltage proves that tunable filtering and selective gain up to 20 dB can be achieved. Further, the quality and reliability of low frequency flow measurements can be improved using an AC-bias voltage.

**KEYWORDS** Flow sensor, Electrostatic Spring Softening, Hair, Cricket, Biomimetics

## INTRODUCTION

Inspired by crickets and their perception of flow phenomena (Fig. 1), MEMS hair flow sensors have been developed in our group [1]. Improvement of fabrication methodologies (Fig. 2) has led to better performance, making it possible to detect flow velocities in the sub-mm/s range [2].

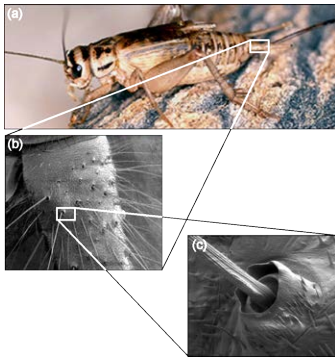


Figure 1: Flow sensing by crickets (SEM pictures courtesy of Jérôme Casas, Université de Tours).

To further increase the sensitivity and enhance the mechanical transfer of these sensors, we demonstrate the use of Electrostatic Spring Softening (ESS). Previously, ESS was demonstrated for electrostatically actuated flow sensors [3]. Here, we show that ESS is applicable to adaptively change the electro-mechanical properties of the

system for oscillating air flow perception.

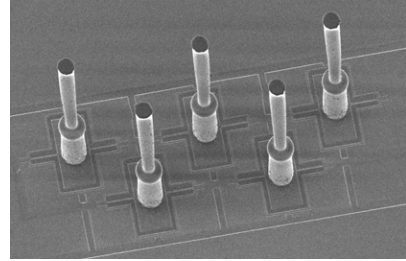


Figure 2: MEMS hair flow sensors.

## THEORY AND MODELLING

The motion of a flow susceptible hair is described by a second order mechanical system, wherein a harmonic air-flow causes the hair to periodically rotate due to a drag torque  $T(t)$  caused by viscous forces [4]. The system's response is governed by its moment of inertia  $J$ , torsional resistance  $R$  and torsional stiffness  $S$ :

$$J \frac{d^2\theta(t)}{dt^2} + R \frac{d\theta(t)}{dt} + S\theta(t) = T_0 \cos(\omega t) \quad (1)$$

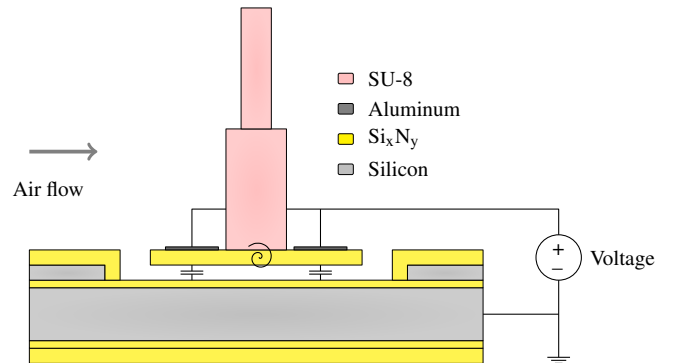


Figure 3: Controlling the torsional stiffness by applying DC voltages to the sensor's capacitances.

In our MEMS hair-flow sensory system, the torsional stiffness  $S$  is controlled using a bias voltage on the sensor membrane electrodes (Figure 3). By symmetrically supplying voltages to the electrodes of the sensor, the electrostatic transduction nature of the system is exploited to obtain ESS, without actually mechanically driving the sensor.

To model the system's behavior under application of symmetric bias voltages, we consider the electrostatically induced torque and stiffness which can be calculated from the first and second derivative of the energy in the capacitor with respect to  $\theta$  respectively.

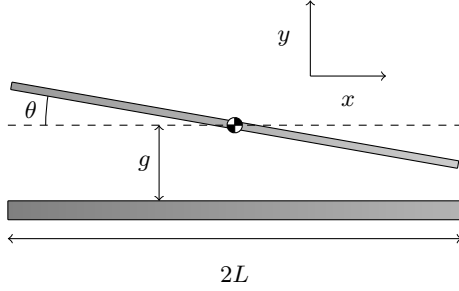


Figure 4: Geometry of the angle-dependent rectangular capacitor.

Due to the small angles  $\theta$  encountered in practice and since the gap is much smaller than both the width  $w$  and length of the plates  $2L$ , the capacitor is treated as a parallel plate geometry (Figure 4). The sensor operates in air, for which the relative electric permittivity is assumed to be equal to 1. Additionally, the two silicon-nitride layers with thicknesses  $t_1$  and  $t_2$ , and relative permittivity  $\epsilon_r$  increase the gap-distance, leading to an effective gap  $g_{\text{eff}}$ :

$$g_{\text{eff}} = g + \frac{t_1}{\epsilon_r} + \frac{t_2}{\epsilon_r} \quad (2)$$

The angle dependent capacitance  $C(\theta)$  for the rotational sensor using the parallel plate approximation is given by:

$$C(\theta) = \epsilon_0 w \frac{\cos(\theta)}{\sin(\theta)} \ln \left( \frac{g_{\text{eff}} + L \sin(\theta)}{g_{\text{eff}} - L \sin(\theta)} \right) \quad (3)$$

Transduction principles are used to find the electrostatic spring softening by an angle-dependent and voltage-controlled capacitor. For this, we use Legendre's transform for the co-energy  $E'$  of the system, since the capacitor is so-called voltage-controlled:

$$E'(\theta, u) = \frac{1}{2} S_0 \theta^2 - \frac{1}{2} u^2 C(\theta) \quad (4)$$

where  $S_0$  is the intrinsic material-based stiffness. The effective stiffness is found by differentiating

twice with respect to the rotational angle  $\theta$  and keeping the voltage  $u$  constant:

$$S(u, \theta) = \left. \frac{\partial^2 E'}{\partial \theta^2} \right|_u = S_0 - \frac{1}{2} u^2 \frac{\partial^2 C(\theta)}{\partial \theta^2} \quad (5)$$

Hence on applying a bias voltage  $u$  the total torsional stiffness  $S$  becomes:

$$S(u, \theta) = S_0 - \eta u^2 \quad \text{with} \quad \eta \approx \frac{2\epsilon_0 w L^3}{3g_{\text{eff}}^3} \quad (6)$$

These expressions state that the total torsional stiffness  $S$  contains both the intrinsic material-based stiffness  $S_0$  and a voltage-dependent stiffness, allowing for electrostatic control of the system's response.

## RESULTS

ESS-experiments using optics for measuring the sensor's response are performed using the experimental setup shown in figure 5. A waveform generator (Agilent 33220A-001) is used for generating a sinusoidal signal at a frequency  $f_a$  that is supplied to an amplifier. This amplifier drives a loudspeaker (Visaton WS 17 E) to generate the oscillating air-flow. Another voltage source is used to supply the bias voltage to the top electrodes. The bottom electrode is grounded as is the measurement setup. The sensor rotational angle  $\theta$  is derived from Laser Doppler Vibrometry using a Polytec MSA-400.

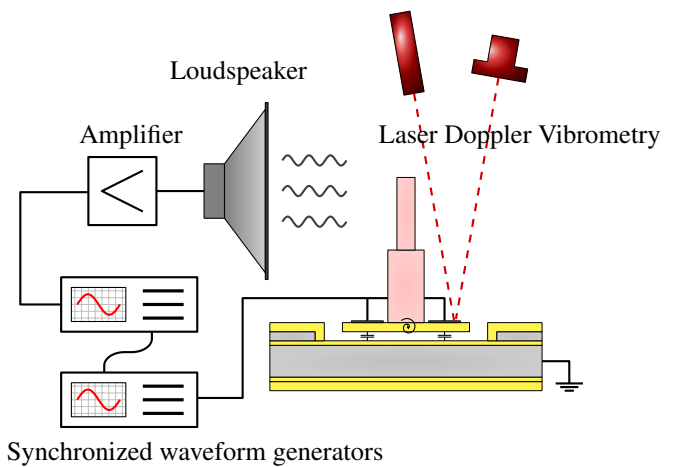


Figure 5: Measurement setup for determining the membrane displacement of the hair flow sensor.

### DC-biasing

First, a DC-bias voltage was used to control the system's torsional stiffness. The mechanical transfer was determined for flow frequencies from 100 to 1000 Hz with and without the application of a DC-bias voltage. During this measurement, a DC-bias voltage  $U_{dc}$  of 2.5 V was used, giving an increase in sensitivity of about 80% for frequencies within the sensor's bandwidth. Also lowering of the resonance frequency  $\omega_r$  is observed (about 20%). Overall, measurements are in good agreement with modeling and it is shown clearly that DC-biasing leads to a larger sensitivity below the sensor's resonance frequency (Fig. 6) [5].

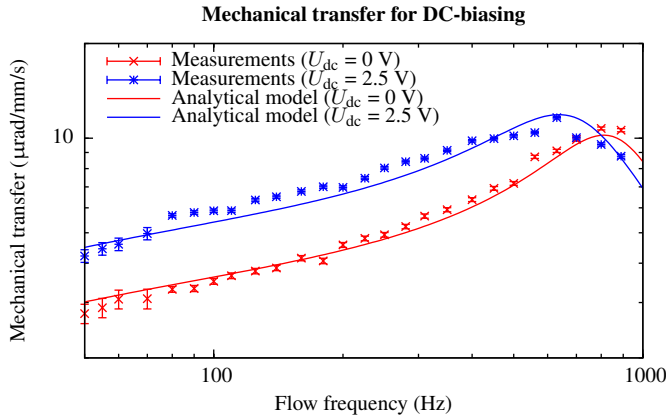


Figure 6: Enhancing the mechanical transfer of the hair flow sensor by applying a DC-bias voltage.

### Parametric amplification

To improve the performance of these sensors even further and implement adaptive filtering, we make use of non-resonant parametric amplification (PA). Parametric amplification is a mechanism based on modulation of one or more system parameters, in order to control the system behavior. This leads to complex interactions between the modulating signals in which amplitude, frequency and phase play important roles [6]. In this work, we obtain the conditions for PA by changing the DC-bias voltage to an AC-bias voltage (also called pump signal), which is another way of exploiting ESS.

Parametric amplification can give selective gain or attenuation, depending on the pump frequency  $f_p$  and pump phase  $\phi_p$ . Equal frequencies for flow and pump ( $f_p = f_a$ ) give coherency in torque and spring softening, for which the pump phase determines whether the system will show

relative amplification or attenuation. Therefore, it is possible to realize a very sharp band pass/stop filter, depending on the pump settings.

Setting the frequency of the AC-bias voltage to 150 Hz, its amplitude to 5 V and the pump phase to the value producing maximum gain, and supplying an oscillating air flow consisting of three frequency components (135 Hz, 150 Hz and 165 Hz), filtering and selective gain of the flow signal are demonstrated. The presence of a bias-signal, through the action of non-resonant PA, increases the frequency-matched signal by 20 dB, whereas the other two components are only amplified by 8–9 dB, resulting in selective gain of the flow signal [7].

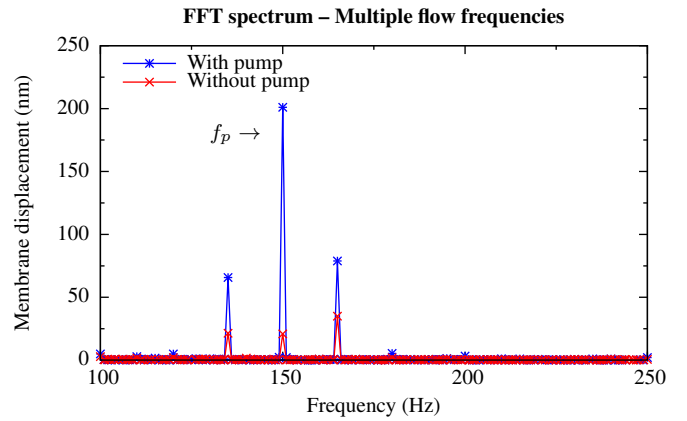


Figure 7: Measured gain of about 20 dB for the flow frequency component at 150 Hz determined by FFT. The AC-bias voltage is fixed at  $f_p=150$  Hz with an amplitude of 5 V.

### EMAM

We also implemented ESS by setting the AC-bias voltage frequency considerably higher than the frequency of the air flow. As a result, the system's spring-stiffness is electromechanically modulated, which results in Electro Mechanical Amplitude Modulation (EMAM). Experimentally, generating a periodic flow at 30 Hz and setting the AC-bias voltage frequency to 300 Hz, the flow is modulated and the flow information is upconverted to higher frequencies [9].

The incoming air flow signal is recovered by demodulation (using synchronous detection) of the measured rotational angle. Without EMAM, a noisy relationship between the flow amplitude and the resulting output voltage is observed. Also,



large, undesired, fluctuations are observed (Fig. 8). However, with EMAM, a clear linear relationship is observed for flow velocity amplitudes above 5 mm/s, showing that the measurement quality of low frequency flows too can be improved by ESS.

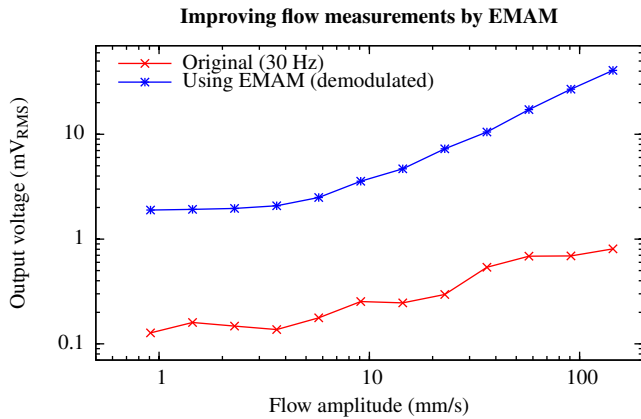


Figure 8: Improvement of the quality of the measured RMS-voltage values at low frequency signals using EMAM. In case of EMAM, a clear linear relationship between flow and output voltage is observed above the system's noise level ( $> 5$  mm/s).

## CONCLUSIONS

Applying a DC-bias voltage to our hair flow sensors mediates large (80% and more) voltage-controlled electro-mechanical amplification of the flow signal for frequencies below the sensor's resonance. Application of an AC-bias voltage proves that tunable filtering and frequency and phase selective gain up to 20 dB can be achieved. Further, the quality and reliability of low frequency flow measurements can be improved using higher frequency modulating AC-bias voltages.

## ACKNOWLEDGEMENTS

The authors would like to thank STW/NWO for funding this research in the framework of the Vici project *BioEARS*.

## REFERENCES

[1] M. A. Dijkstra, J. J. J. van Baar, R. J. Wiegerink, T. S. J. Lammerink, J. H. de Boer and G. J. M. Krijnen, "Artificial sensory hairs based on the flow sensitive receptor hairs of crickets", *J. Micromech. Eng.*, Vol. 15, pp. S132–S138, 2005.

- [2] C. M. Bruinink, R. K. Jaganatharaja, M. J. de Boer, J. W. Berenschot, M. L. Kolster, T. S. J. Lammerink, R. J. Wiegerink and G. J. M. Krijnen, "Advancements in technology and design of biomimetic flow-sensor arrays", *Proc., MEMS 2009 Conf., Sorrento, Italy*, Jan. 25–29, 2009, pp. 152–155.
- [3] J. Floris, N. Izadi, R. K. Jaganatharaja, R. J. Wiegerink, T. S. J. Lammerink and G. J. M. Krijnen, "Adaptation for frequency focusing and increased sensitivity in biomimetic flow sensors using electrostatic spring softening", *Proc., Transducers 2007 Conf., Lyon, France*, Jun. 10–14, 2007, pp. 1267–1270.
- [4] T. Shimozawa, T. Kumagai and Y. Baba, "Structural scaling and functional design of the wind-receptor hairs of a cricket", *J. Comp. Physiol. A*, Vol. 183, pp. 171–186, 1998.
- [5] H. Droogendijk, C. M. Bruinink, R. G. P. Sanders and G. J. M. Krijnen, "Improving the performance of biomimetic hair-flow sensors by electrostatic spring softening", *J. Micromech. Eng.*, Vol. 22, 065026, 2012.
- [6] D. Rugar and P. Grütter, "Mechanical Parametric Amplification and Thermomechanical Noise Squeezing", *Phys. Rev. Lett.*, Vol. 67, pp. 699–702, 1991.
- [7] H. Droogendijk, C. M. Bruinink, R. G. P. Sanders and G. J. M. Krijnen, "Non-resonant parametric amplification in biomimetic hair flow sensors: Selective gain and tunable filtering.", *Appl. Phys. Lett.*, Vol. 99, 213503, 2011.
- [8] M. J. Thompson and D. A. Horsley, "Parametrically Amplified Z-Axis Lorentz Force Magnetometer", *J. Micromech. Eng.*, Vol. 20, pp. 702–710, 2011.
- [9] H. Droogendijk, C. M. Bruinink, R. G. P. Sanders and G. J. M. Krijnen, "Application of electro mechanical stiffness modulation in biomimetic hair flow sensors", *Proc., MEMS 2012 Conf., Paris, France*, Jan. 29 – Feb. 2, 2012, pp. 531–534.

## CONTACT

\* H. Droogendijk, h.droogendijk@utwente.nl

## 1. Sensors

**COMPACT MASS FLOW METER BASED ON A MICRO CORIOLIS FLOW SENSOR**

W. Sparreboom<sup>1\*</sup>, M. Katerberg<sup>1</sup>, T.S.J. Lammerink<sup>2</sup>, F.M. Postma<sup>3</sup>, J. Haneveld<sup>4</sup>,  
J. Groenesteijn<sup>2</sup>, R.J. Wiegerink<sup>2</sup> and J.C. Lötters<sup>1,2</sup>

<sup>1</sup>Bronkhorst High-Tech BV, Ruurlo, The Netherlands

<sup>2</sup>University of Twente, Transducers Science and Technology, Enschede, The Netherlands

<sup>3</sup>Lionix BV, Enschede, The Netherlands

<sup>4</sup>Micronit BV, Enschede, The Netherlands

**ABSTRACT**

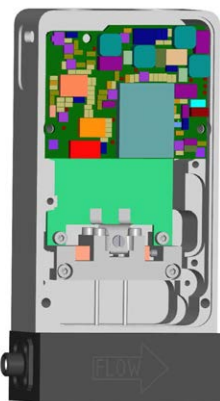
In this paper we present a compact ready-to-use micro Coriolis mass flow meter. The full scale flow is 2 g/h (for water at a pressure drop of 2 bar). It has a zero stability of 2 mg/h and an accuracy of 0.5% reading. The temperature drift between 10 and 50 °C is below 1 mg/h/°C. The meter is robust, has standard fluidic connections and can be read out by a PC or laptop via USB. Its performance was tested for several common gases (helium, nitrogen, argon and air) and liquids (water and IPA).

**KEYWORDS**

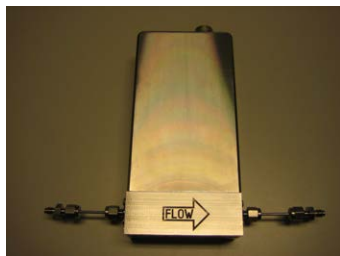
Mass flow meter, Coriolis, Microfluidic

**INTRODUCTION**

Microfluidic systems have gained a lot of interest in the last decade in a wide area of applications [1]. Examples of such can be found in the analytical field, (bio)-chemistry, medical and industry. These fields require in-line measurement and control over mass transport. Since often mixtures of varying composition are found, a true mass flow sensor is wanted. Haneveld et al. presented such a mass flow sensor based on the measurement of the Coriolis effect [2].



1a)



1b)

Figure 1: Micro Coriolis mass flow sensor integrated into a robust housing using a custom-made chip holder. 1/16" stainless steel tubes are connected to the chip. 1a) First design; 1b) realization.

However, to be useful in the field, the sensor should be packaged and have a simple and robust (electric and fluidic) connection to the outside world.

**MASS FLOW METER DESCRIPTION****Novelty**

Here we present packaging of a micro Coriolis mass flow sensor into a stainless steel housing (figure 1). Several experiments were performed to characterize the behavior of the meter. The meter is ready-to-use by integrating interface electronics and standard fluidic connections. The electrical connection is a standard Bronkhorst High-Tech connection that can be connected to a pc or laptop via USB. The fluidic connections in the current design are 1/16" Swagelok connectors.

**Sensor structure and operating principle**

The functioning of the Coriolis mass flow meter is described using figure 2. By Lorentz actuation the tube is brought into resonance. The movement is an alternating rotational displacement of 1 to 10  $\mu\text{m}$  around the x-axis (torsion mode). A flow running through the section of the tube that is indicated by  $L$  causes an alternating force in the z-direction around the y-axis (swing mode). This force is called Coriolis force and causes a displacement of the tube roughly between 1 and 100 nm.

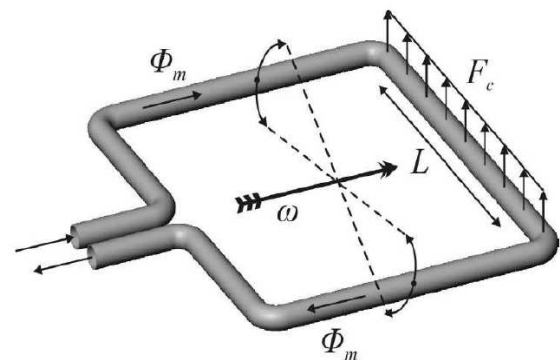


Figure 2. Rectangle-shaped Coriolis flow sensor. The tube is brought into resonance by Lorentz actuation at an angular velocity,  $\omega$ , the displacement at the corners of the tube is between 1 and 10  $\mu\text{m}$ ;  $F_c$  indicates the Coriolis force as a result of mass flow  $\phi_m$  through the part of the tube indicated by  $L$ , this force causes a displacement roughly between 1 and 100 nm.

### Chip and packaging

The chip is fabricated using surface micromachining techniques. Details can be found in [3]. To protect the relatively fragile Coriolis tube a glass cover is glued on top of the chip. The combination is then glued to a PCB after which wirebonds are made to connect the chip electrically. In figure 3 a photograph of the chip and PCB can be found.

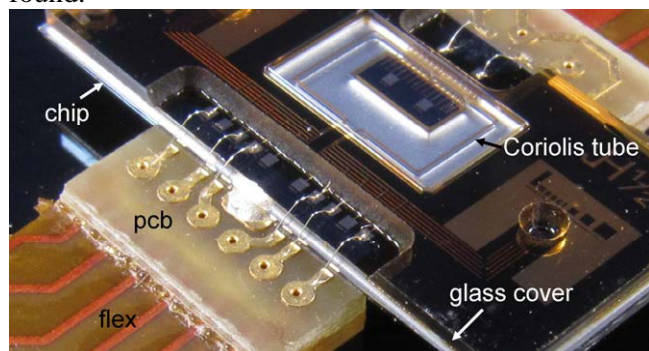


Figure 3: Micro Coriolis chip glued to a PCB. Electrical connections to the PCB are made with wirebonds.

### Chip holder and fluidic connections

To robustly interface the sensor chip to the “macro” world, we placed the chip into a stainless steel chip holder (figure 4). This holder forms a steady base to connect the chip fluidically using stainless steel nuts and Tefzel ferrules that connect two 1/16” stainless steel tubes with the chip.

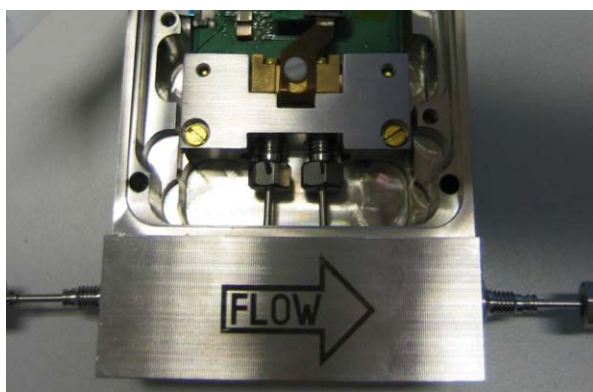


Figure 4: Micro Coriolis mass flow sensor integrated into a robust housing using a custom-made chip holder. 1/16” stainless steel tubes are connected to the chip via a Tefzel ferrule. In the top part the interface electronics are partly visible.

### Electronics

It is apparent that the displacement by the Coriolis force is extremely small. This places strong demands on the detection part which is done using electrostatic comb structures [3]. Here displacement of the tube causes a change in capacitance that is transformed into

a voltage change. This is detected by a digital signal processor (DSP) via several analog to digital (ADCs) and digital to analog converters (DACs). The chip and the ADCs and DACs are interfaced via a charge amplifier.

## EXPERIMENTAL RESULTS

### Pressure tests

Several tests were performed. A helium pressure test was done at the Bronkhorst High-Tech production facility. This showed that the Coriolis mass flow meter could withstand a maximum pressure of 40 bar.

### Temperature drift

The influence of ambient temperature on the zero stability was tested by placing the meter inside a climate chamber (Vötsch VC4018). The relative humidity was kept constant at 20%. A temperature sweep was made between 10 and 50 °C in steps of 5 °C. Between steps the temperature was kept constant for two hours. Results of this experiment are given in figure 5. This shows a temperature drift between 10 and 50 °C below 1 mg/h/°C.

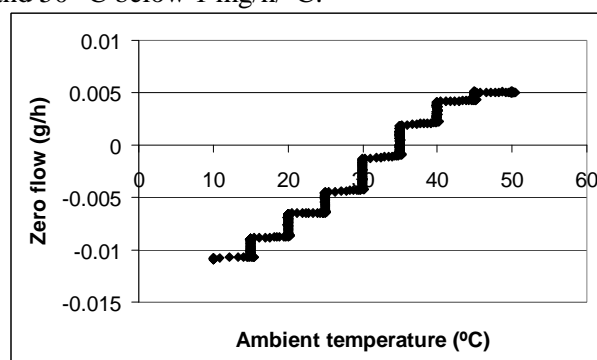


Figure 5: Measured temperature drift of the Coriolis mass flow meter. The meter was placed inside a climate chamber (Vötsch VC4018). The temperature was swept between 10 and 50 °C in steps of 5 °C every 2 hours.

### Mass flow of water

We tested the Coriolis mass flow meter for several liquids (water, IPA) in a temperature controlled environment. In this room the temperature was kept between 20 and 25 °C. Here we present the results with water.

In figure 6 a schematic overview of the setup is given. The mass flow measurements were done by comparing the read-out value of the meter with a weighing scale (Mettler Toledo AX205). A pressure difference across the meter was generated by pressurizing a 300 ml water tank with helium. After this tank a 2 µm peek filter unit (Upchurch Scientific A-355 with a A-700 filter frit) was placed. To prevent interference by air bubbles, the water was degassed



in-line by a Systec mini vacuum degasser. The Coriolis mass flow meter was used to control the mass flow rate by driving a normally closed valve (Bronkhorst top-mount valve) that was placed in front of the Coriolis mass flow meter. Between the valve and the meter again a  $2\text{ }\mu\text{m}$  filter was placed. This second filter prevents particles, that possibly originate from the metal valve, to enter the Coriolis mass flow meter. Via a piece of peek tubing the water was passed towards a 200 ml glass beaker placed on the weighing scale. The beaker was prefilled with water and topped by a layer of oil to prevent evaporation of water during the measurement. Each point represents a measurement over a period of 4 minutes. The result for the mass flow measurement of water is presented in figure 7. For water the meter shows a zero stability of  $2\text{ mg/h}$  and an accuracy of 0.5% reading. The full flow of  $2\text{ g/h}$  is reached at an approximate pressure of 2 bar.

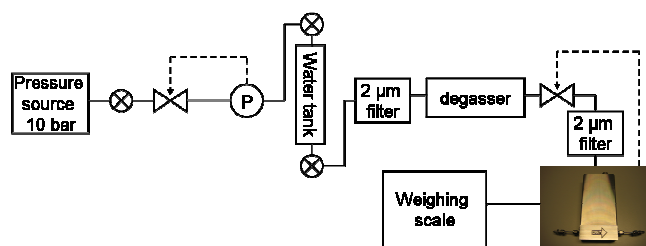


Figure 6: Schematic overview of the setup used for the water mass flow measurements. A water tank is pressurized by helium. The helium pressure is controlled using pressure meter P. The water is filtered directly after the tank and again between the valve and the Coriolis mass flow meter. A degasser removes air from the water. As a reference an AX205 weighing scale was used.

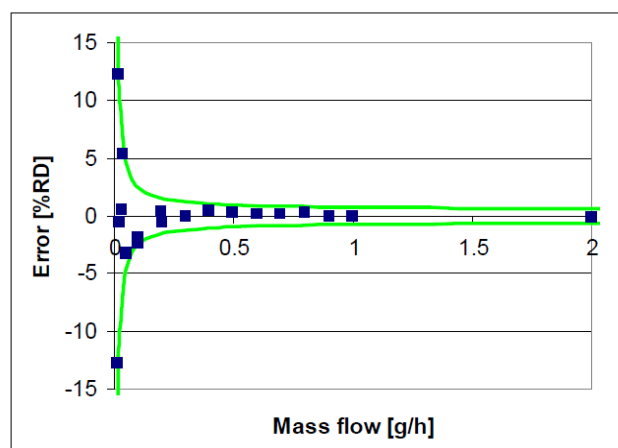


Figure 7: Measured water mass flow vs. Mettler Toledo (AX205 weighing scale). The envelope represents a zero stability of  $2\text{ mg/h}$  and an accuracy of 0.5% reading. The pressure drop across the Coriolis mass flow meter was approximately 2 bar.

For IPA the same zero stability and accuracy was found. Because IPA mixes with oil, we were not able to reliably use the weighing scale for mass flow measurements of IPA. For this purpose we drove mass flow by a syringe pump using calibrated  $100\text{ }\mu\text{l}$  syringes.

### Mass flow of air

We tested the Coriolis mass flow meter for several common gases (He,  $\text{N}_2$ , Ar and air) in a temperature controlled environment. Since the meter was designed for an approximate 1 bar pressure drop at  $1\text{ g/h}$  mass flow of water, the pressure drop for  $1\text{ g/h}$  gas mass flow is expected to be higher. Again the temperature was kept between 20 and  $25\text{ }^\circ\text{C}$ . Here we present the results obtained with air. In figure 8 a schematic overview of the setup is given.

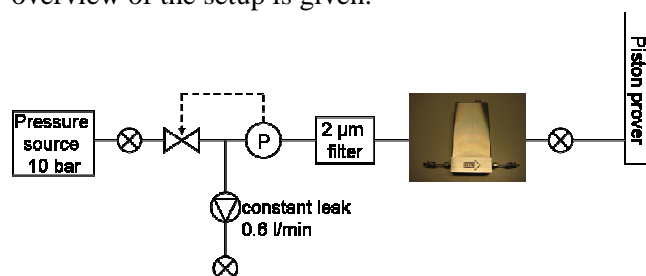


Figure 8: Schematic overview of the setup used for the air mass flow measurements. Air was pressurized at 10 bar. Pressure meter P controls the pressure before the Coriolis mass flow meter. A constant leak of  $0.6\text{ l/min}$  is necessary for the valve to operate reliably. The filter is placed in front of the Coriolis mass flow meter to prevent clogging. A piston prover is used as a reference.

As a reference we used a piston prover ( $0.1\text{ l/min}$ ). A well-defined pressure difference across the Coriolis mass flow meter was generated by a pressure controller (Bronkhorst EL-press). The maximum pressure difference we could apply across the Coriolis mass flow meter was 8 bar. As a consequence we could not reach the nominal flow rate of  $1\text{ g/h}$ . For the valve to operate reliably we generated a constant leak of  $0.6\text{ l/min}$  with a thermal flow controller (Bronkhorst EL-flow). This was necessary since the volume flow through the micro Coriolis meter is extremely small. Between the pressure controller and the Coriolis mass flow meter we placed  $2\text{ }\mu\text{m}$  filter (Upchurch Scientific A-355 with a A-700 filter frit) to prevent clogging. The meter was directly connected to the piston prover. For each measurement point we did at least three runs. In these runs we let the piston prover pass between the same two detection points. The result for the mass flow measurement of air is presented in figure 9. For air the meter shows a zero stability of  $2\text{ mg/h}$  and an accuracy of 0.5% reading.

The same zero stability and accuracy were found for nitrogen, helium and argon.

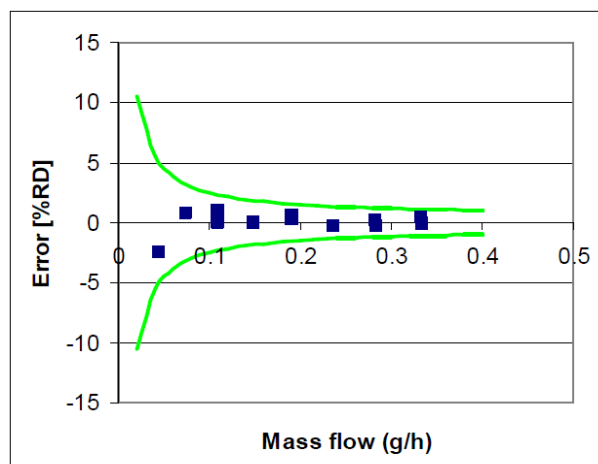


Figure 9: Measured air mass flow vs. piston prover. The envelope represents a zero stability of 2 mg/h and an accuracy of 0.5% reading. The pressure drop across the Coriolis mass flow meter was approximately 8 bar.

## CONCLUSION

We presented a compact and ready-to-use micro Coriolis mass flow meter in a stainless steel housing. It has a full scale mass flow of 2 g/h and accuracy of 0.5 % reading. Its zero stability is 2 mg/h. The meter can withstand 40 bar and operates well in an ambient temperature range between 10 and 50°C. Its temperature drift is below 1 mg/h/°C. It measures mass flow of both liquids and gasses. We tested the meter for water, IPA, helium, argon, nitrogen and air. The meter was designed to have a 1 bar pressure drop at 1 g/h water mass flow. Since our current gas setup was limited to 8 bar pressure drop across the Coriolis mass flow meter, the mass flow meter is characterized for air up to ~0.35 g/h.

## ACKNOWLEDGEMENT

This project was funded by MicroNed and Nanonext. We thank Gijs Ratering for assistance with the water measurements. Rik de Boer and Eddie van Hattum are thanked for assistance with the gas measurements and helpful discussions.

## CONTACT

\* W. Sparreboom, w.sparreboom@bronkhorst.com

## REFERENCES

- [1] G.M. Whitesides, "The origins and the future of microfluidics", *Nature* 442, pp. 368-373, 2006
- [2] Haneveld, J. and Lammerink, T.S.J. and Dijkstra, M.A. and Droogendijk, H. and de Boer, M.J. and Wiegerink, R.J., "Highly sensitive micro coriolis mass flow sensor", *MEMS 2008 Tucson - 21<sup>st</sup> IEEE International Conference on Micro Electro Mechanical Systems, 13-17, Tucson, AZ, United States*, pp. 920-923, IEEE Computer Society, 2008.
- [3] J. Haneveld, T.S.J. Lammerink, M.J. de Boer, R.G.P. Sanders, A Mehendale, J.C. Lötters, M. Dijkstra, R.J. Wiegerink, "Modeling, design, fabrication and characterization of a micro Coriolis mass flow sensor", *Journal of Micromechanics and Microengineering*, 2010.

## DEVELOPMENT OF AN ACTIVE MICROMIXER USING AN EXTERNAL MECHANICAL ACTUATOR ARRAY

Y. Abbas<sup>1</sup>, J. Miwa<sup>2</sup>, R. Zengerle<sup>1,2,3</sup> and F. von. Stetten<sup>1,2</sup>

<sup>1</sup> Laboratory for MEMS Applications, IMTEK - Department of Microsystems Engineering, University of Freiburg, Georges-Koehler-Allee 103, 79110 Freiburg, Germany

<sup>2</sup> HSG-IMIT - Institut für Mikro- und Informationstechnik, Villingen-Schwenningen, Germany

<sup>3</sup> BIOS - Centre for Biological Signalling Studies, University of Freiburg, Germany

### ABSTRACT

We present an active continuous-flow micromixer based on channel-wall deflection in a polydimethylsiloxane (PDMS) chip using Braille display pins. The chip design comprises a main micro-channel connected to a series of side channels with dead ends aligned on the Braille pins. Computer-controlled deflection of the side-channel walls induces chaotic advection in the main-channel, which substantially accelerates mixing in low-Reynolds number flow. Several influencing parameters such as the number of cross-channels, actuation frequency, side-channel width, actuation sequence, and flow rate velocities have been investigated. Sufficient mixing of fluids could be achieved within seconds (~500 ms). Finally, continuous dilution of yeast cell sample by a ratio down to 1:10 is successfully demonstrated.

### KEYWORDS

Active micro-mixer, mixing index, chaotic advection, channel wall deflection, PDMS chip, and cell sample dilution.

### INTRODUCTION

Mixing of fluids in micro-channels is challenging due to stable laminar flow. The speed of mixing is limited by molecular diffusion, and is inversely proportional to the size of the fluid molecule or particle to be mixed [1]. Typically, for relatively large biomolecules such as cells, mixing can take as long as hours in microchannels. An efficient method for mixing enhancement in microchannels is needed for biomedical applications such as cell counting, enzyme assays, screening assays, cell lysis, protein folding, and biological analytical assay [2].

One method for efficient microscale mixing is chaotic advection [3], which involves local stretching and folding of the fluid streams and the resulting significant reduction in the effective diffusion length. The key to effective mixing lies in producing strong stretching and folding [4].

Active mixers generally provide efficient mixing with enhanced control over the process and independence of flow conditions [5]. Several active mixers based on chaotic advection have been reported where efficient mixing was observed in subseconds [3-5]. Tabeling *et al.* [3] reported a cross-channel

micromixer which exploit chaotic motion in the main channel due to the pressure perturbation at side channels. Such structures with robust and compact pressure-perturbation sources can be used for rapid mixing in microscale continuous flow.

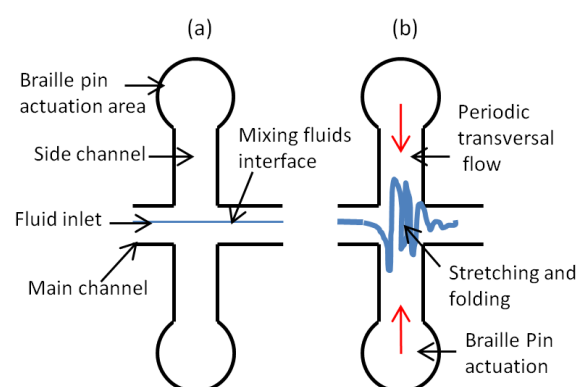


Fig. 1: Schematic of a cross-channel mixer and principle of pressure perturbation. (a) At no actuation, flow in main channel is laminar. (b) After pin actuation stretching and folding of fluid interface occur in main channel.

In this work we present a PDMS active micromixer that creates chaotic advection in cross-channel structures. The main microchannel is connected to a series of side channels with dead ends that are aligned to Braille display pins. The side channel walls deform as the Braille pins underneath deflect, creating transverse flow at the mixing fluid interface in the main channel. By operating the Braille pins in a periodic sequence, the fluid undergoes local stretching and folding, which leads to rapid fluid mixing. Fig. 1 depicts the principle of chaotic advection in the main channel due to pressure perturbation in the side channels.

## MATERIALS AND METHODS

### Chip Fabrication

The microfluidic chip is composed of polydimethylsiloxane (PDMS) fabricated using standard soft lithography procedures [6]. Fig. 2 shows the schematic of the chip fabrication process. The master mould structure was fabricated on a 4-inch silicon wafer patterning multilayered photoresist (AZ9260, Microchemicals GmbH). The patterned 100-μm thick

structures were reflowed at 120 °C for 2 hours to obtain round channel cross sections. The PDMS channel structures were made by pouring Sylgard 184 (Dow Corning Corp., mixture ratio of curing agent to prepolymer 1:10) onto the mould and baking in an oven at 70 °C for 2 hours. A 100 µm thick PDMS membrane was spun on another silicon wafer and cured in the same oven to form the deformable wall. The two PDMS layers were permanently bonded after surface activation in oxygen plasma. Fig. 3a shows the PDMS chip after fabrication. The microfluidic channel width is 200 µm, and the dead-end chambers for Braille-pin actuation has a diameter of 1.5 mm.

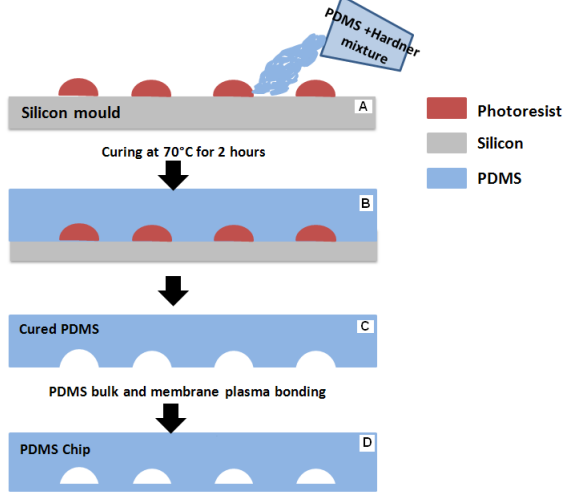


Fig. 2: PDMS chip fabrication steps

### Braille Pin Actuator

The commercial Braille display (KGS Corp.) used in the current study provided an 8 × 8 array of 1.3-mm diameter pins that are each connected to piezoelectric bimorphs. These pins each deliver a force of 0.1 N for membrane deflection of up to 700 µm. The force corresponds to approx. 280 kPa pressure at the PDMS chambers when the chip is aligned and clamped on the Braille display (Fig. 3b). The resonance frequency of each piezoelectric element is 10 Hz. The pin actuation is controlled by an in-house developed computer program connected through an electronic interface circuit.

### Experimental Setup

The schematic of experimental setup is illustrated in Fig. 4. The PDMS chip is placed over the grid of the Braille display pin, in such a way that the lower PDMS membrane is in direct contact with the Braille display pins. To pump the fluid through the chip at a predetermined flow rate, a neMESYS syringe pump (Cetoni GmbH) was used. A high-speed camera (pco. 1200, PCO AG) was used to acquire instantaneous images of the fluid mixing inside the fluid channels. A 12x objective lens (Navitar Inc.) was attached to the high-speed camera to magnify the image.

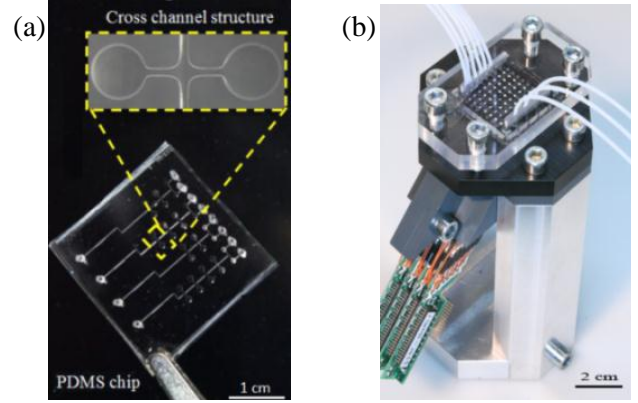


Fig. 3: (a) Cross-channel structures in the PDMS chip. Braille pins deflect the membrane at the circular areas of the cross-channel. (b) PDMS chip with integrated cross channel on a commercially available Braille pin actuator.

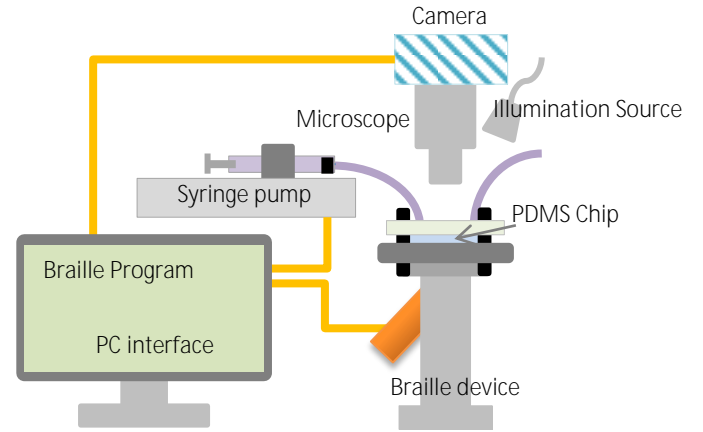


Fig. 4: Schematic of complete experimental setup

### Mixing quantification

The efficiency of the Braille-actuated micromixer is evaluated by image analysis of instantaneous images of two water streams, one of which is colored with ink. The performance is quantified using a mixing index (MI) defined as the standard deviation of the pixel intensity values of an instantaneous image from a reference image at time  $t$ . In the current study, the reference is defined as the image where the fluid is homogenized or completely mixed [5]. The expression for MI is given in eq. 1.

$$MI = \sqrt{\frac{1}{N} \sum_{n=1}^N \left( \frac{I(t,n) - I_{avg}}{I_{avg}} \right)^2} \quad (1)$$

Where  $N$  is number of pixels and  $I$  is the optical intensity. Mixing index value of 1 and 0 indicates laminar flow and completely mixed state, respectively. Many of the literature considered 0.1 mixing index as an arbitrary value to define well mixed fluids [5]. Mixing time is therefore defined as the time to reach mixing index value of 0.1.



## RESULT AND DISCUSSION

### Qualitative Analysis

The snapshots of fluid interface at the cross channel indicates the stretching and folding behavior of the fluid interface in the main channel during pin actuation are shown in Fig. 5. This image sequence indicates that the Braille-actuated micromixer induces chaotic advection and consequently enhances fluid mixing. The Braille pin displaces  $3\ \mu\text{l}$  of fluid during each actuation step.

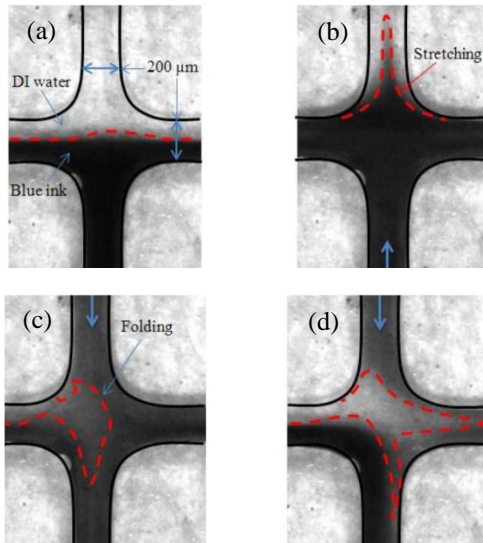


Fig. 5: Snapshots of the cross-channel structure (Top view) during Braille actuation at an interval of 200 ms. (a) Before actuation. (b) Lower Braille pin is actuated and induces transversal flow causing stretching of the fluid interface. (c), (d) Upper pin is actuated, causing the folding of the stretched interface. The stretching and folding of the interface is a key fluidic behaviour in chaotic advection (Total flow rate in channel is  $0.4\ \mu\text{L/s}$ ).

### Quantitative Analysis

Fig. 6 illustrates the effect of pin-actuation frequency on the mixing efficiency. At lower frequencies ( $<1\ \text{Hz}$ ) mixing is not efficient due to weak perturbation; in this case the actuation time is more than the residence time of the fluid element in the mixing structure. At higher frequencies ( $>10\ \text{Hz}$ ) mixing efficiency is low due to unstable actuation (practical limitations). Therefore the optimal for mixing performance is observed at  $10\ \text{Hz}$ .

Fig. 7 depicts the dependency of mixing efficiency on the total flow rate of fluids inside the main channel. The mixing efficiency decreases as flow rate increases due to the fact that the residence time of the fluid in the channel is decreased and fluid elements undergo less perturbation before they leave the mixing chamber. Although the Reynolds number at  $2\ \mu\text{l/s}$  is relatively high ( $\sim 20$ ), it is not high enough to enhance

mixing by turbulence. Thus for velocities higher than  $0.4\ \mu\text{l/s}$ , higher number of Braille pins ( $>4$ ) are required for efficient mixing.

Fig. 8 depicts the effect of fluid viscosity on the mixing index. Fluids with different viscosities were prepared by diluting glycerol at different percentages in DI water. The mixing index increases (decreasing mixing efficiency) with the increase in the fluid viscosity, which is natural since viscosity is inversely proportional to the diffusion constant. Still, for wide range of viscosities (up to  $50\ \text{mPa}\cdot\text{s}$ ), the mixing index is within the sufficient range.

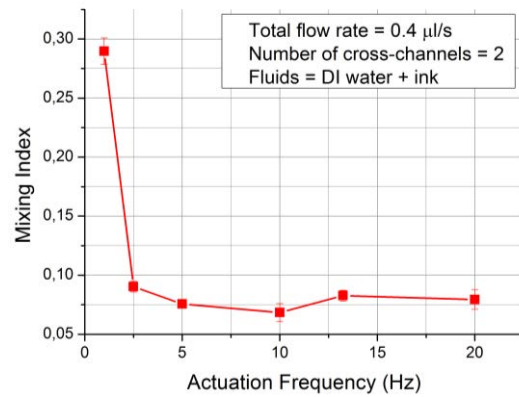


Fig. 6: Mixing index response of cross-channel mixer for different actuation frequencies.

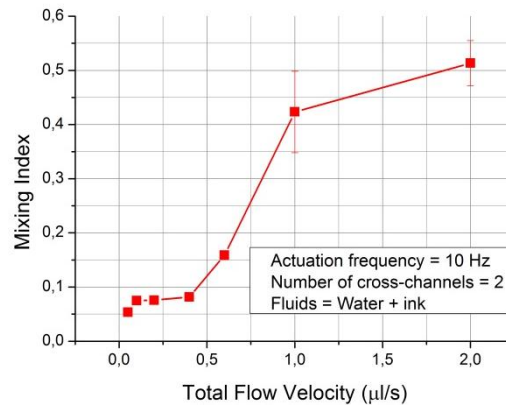


Fig. 7: Mixing index response at different fluid velocities at the chip inlet.

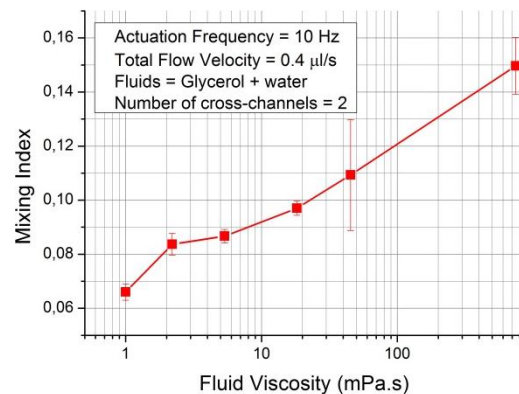


Fig. 8: Effect of fluid viscosity on the mixing index of the cross-channel mixer

The transient response of the mixing index at optimal conditions defined through the above-mentioned parameter studies is shown in Fig. 9. Here the mixing time is on the order of 100 ms, and homogeneous mixing is sustained for as long as the experiment was conducted.

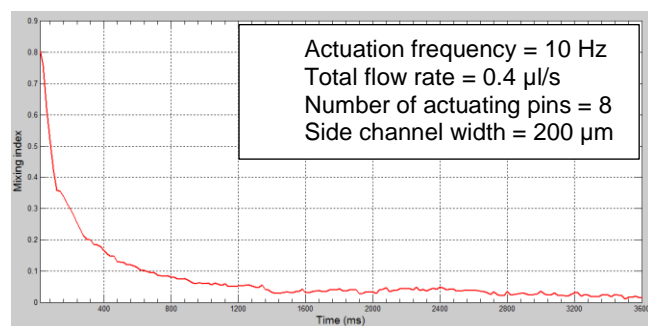


Fig. 9: Transient response of the mixing index for optimal process and design parameters.

Finally, dilution experiments of continuous-flow cell samples was performed. The cell sample was of wild yeast type (*S. cerevisiae*) in a buffer solution YNB medium. The photographs of cell dilution near the outlet channel over the Braille pin is given in Fig. 10. The total flow rate is 0.4  $\mu\text{L/s}$ , and the flow rate ratio is 1:10 (cell sample : DI water). Initially at  $t = 0$  no mixing is observed and all cells flow in the lower part of the channel in the image. After 2 s the cells are dispersed throughout the width of the channel and diluted. The shear stress in the cross-channel due to the main channel and the induced side flow is roughly calculated to be on the order of  $\sim 102$  Pa. In this range, shear-stress does not affect the viability of yeast cells [7].

## CONCLUSION

We demonstrated a novel approach for mixing enhancement by membrane actuation using mechanical actuator array. It is shown that rapid mixing of cell/particle flow can be achieved across a wide range of flow parameters using a cost-effective configuration with easily replaceable PDMS microfluidic chips.

Chaotic advection in the main channel is demonstrated by the generation of periodic stretching and folding. Development of strong stretching and folding trajectories is decisive in efficient mixing. Sufficient mixing of continuously flowing fluids was achieved within half a second. Several influencing parameters of the mixing setup have been studied. It is found that parameters like flow rate ratio and fluid viscosity have no significant effect on mixing for a wide range. The successful demonstration of cell sample dilution proved the feasibility of Braille

display as a mechanical actuator in biomedical analysis. This micromixer setup can be implemented in automated processes for high-throughput biomedical analysis.

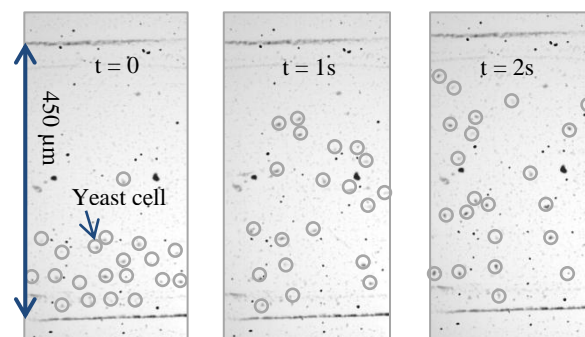


Fig. 10: Snapshots of the yeast cell sample at the downstream of the cross-channel after the onset of Braille actuation. Original flow rate ratio of yeast sample and DI water is 1:10 (total flow rate = 0.4  $\mu\text{L/s}$ ).

## REFERENCES

1. Nguyen, N.-T., *Micromixers, Fundamental, Design and Fabrication*. 2 ed 2012, Waltham, USA: Elsevier.
2. Jeong, G.S., et al., *Applications of micromixing technology*. Analyst, 2010. **135**(3): p. 460-473.
3. Tabeling, P., et al., *Chaotic mixing in cross-channel micromixers*. Philosophical Transactions of the Royal Society of London. Series A: Mathematical, Physical and Engineering Sciences, 2004. **362**(1818): p. 987-1000.
4. Gouillart, E., O. Dauchot, and J.L. Thiffeault, *Measures of mixing quality in open flows with chaotic advection*. Physics of Fluids, 2011. **23**: p. 013604.
5. Tekin, H.C., et al., *Chaotic mixing using source-sink microfluidic flows in a PDMS chip*. Microfluidics and Nanofluidics, 2011. **10**(4): p. 749-759.
6. Duffy, D.C., et al., *Rapid prototyping of microfluidic systems in poly (dimethylsiloxane)*. Analytical chemistry, 1998. **70**(23): p. 4974-4984.
7. Lange, H., P. Taillandier, and J.P. Riba, *Effect of high shear stress on microbial viability*. Journal of Chemical Technology and Biotechnology, 2001. **76**(5): p. 501-505.

Contact

\* Yawar Abbas, eng.yawar@gmail.com

## ENHANCED LIQUID METAL MICRO DROPLET GENERATION BY PNEUMATIC ACTUATION BASED ON THE STARJET METHOD

N.Lass<sup>1</sup>, L.Riegger<sup>1,2</sup>, A. Ernst<sup>1,2</sup>, R. Zengerle<sup>1</sup> and P. Koltay<sup>1,2</sup>

<sup>1</sup>Laboratory for MEMS Applications, IMTEK, University of Freiburg, Germany

<sup>2</sup>BioFluidix GmbH, Georges Köhler Allee 106, 79110 Freiburg Germany

### SUMMARY

We present a **novel pneumatic actuation system for generation of liquid metal droplets** according to the so-called StarJet method. In contrast to our previous work [1, 2], the performance of the device has been significantly improved: The **maximum droplet generation frequency** in continuous-mode has been **increased** to  $f_{max} = 11 \text{ kHz}$  (formerly  $f_{max} = 4 \text{ kHz}$ ). In addition, the **droplet diameter** has been **reduced to 60  $\mu\text{m}$**  by a **new design** of the **star shaped nozzle** made from silicon by MEMS technology. The size of the metal reservoir has been increased to hold up to 22 mL liquid metal and the performance and durability of the **actuator has been improved by using stainless steel and a second pneumatic connection**. Experimental results are presented regarding the characterization of the droplet generation as well as printed metal structures.

### KEYWORDS

StarJet, Molten Metal Droplets, 3D-Printing, Rapid Prototyping, Droplet Generator

### INTRODUCTION

The generation of micro droplets of liquid metals is a challenging area in the field of MEMS technologies. It is applicable in a large field of applications such as the generation of electrical 2D / 3D connections or metal layers in the field of microelectronics or MEMS [3][4], rapid prototyping of electric circuits [5] or 3D prototyping of small metal structures [6,7]. However, the generation of single micro droplets from molten metal at high temperatures is a highly complex task for several reasons: First of all, the dispenser must operate at temperatures above the melting point of the metal. Therefore, all parts of the device must be either fabricated of temperature stable materials or have to be thermally insulated from the hot parts of the system. Especially piezo actuators must be isolated [3] or actively cooled to prevent their destruction. The operation temperature of these materials is limited by the Curie temperature, typically ranging between 150°C and 300°C [8]. Also, the mechanical stress induced by heating up or cooling down the dispensing device requires certain design rules to be considered e.g. material combinations with suitable modulus of

elasticity and appropriate coefficients of thermal expansion. Furthermore, the molten metal inside the device as well as the ejected droplets have to be shielded from oxidation by e.g. the application of protective gas.

The StarJet technology used for the dispensing of liquid metals droplets in the presented work is based on a pneumatic actuation principle. The gas flow which works as actuation mechanism avoids the oxidation of the liquid metal inside the reservoir of the device as well as the dispensed metal droplets in flight. The entire device consists of a pneumatic actuator module made from brass and a star shaped micro nozzle fabricated by silicon micromachining. All connections are sealed by high temperature stable materials e.g. Nova Mica. Thus, the limitation for the maximum operating temperature is the melting point of only the actuator material itself. In consequence, the StarJet technology should be suitable for generating liquid metal droplets of all kinds of metals with high melting points without suffering from the aforementioned problems.

### EXPERIMENTAL SETUP

In contrast to the first StarJet droplet generator [1,2,9], the new actuator is made of stainless steel (Fig. 1) providing enhanced durability and higher working temperatures.



*Figure 1: Enhanced StarJet actuator made from stainless steel.*

The reservoir has been enlarged from 127mm<sup>3</sup> to 22000 mm<sup>3</sup> enabling the printing of extensive structures without refill. Through a drilling hole ( $D = 400 \mu\text{m}$ ) at the bottom of the reservoir, the molten metal is transferred to the nozzle chips. The



alignment of these chips is done by a laser fabricated positioning spring and fittings. In contrast to our previous work, the connection to apply nitrogen for driving the droplet ejection and the connection for rinsing the bypass channels are now separated (see Fig. 2). The pressure pulses can hence be applied faster and with a more precise timing improving the drop-on-demand functionality (DoD) significantly.

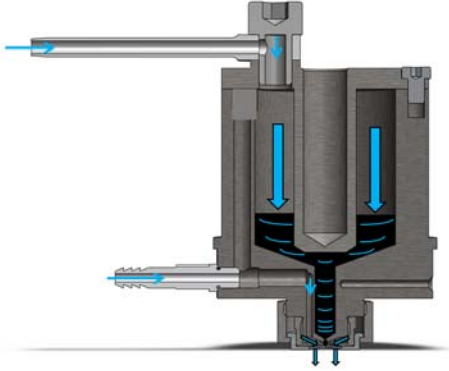


Figure 2: Model cross-section of the StarJet actuator. Blue arrows indicate the pneumatic actuation.

Therefore, an external solenoid valve (Festo GmbH) regulates the gas flow of the inert gas for pneumatic actuation by switching between a low pressure (10 hPa to 30 hPa) to prevent oxidation of the molten metal inside the reservoir and a higher actuation pressure (150 hPa to 1000 hPa) initiating the droplet ejection. The rinse pressure can be adjusted separately to match to the actuation pressure. The reservoir is covered by band heating element (Tueerk-Hillinger GmbH) and in addition a cartridge heater (Hotset GmbH) is placed inside the reservoir. The temperature is monitored by a NiCr-Ni thermopile sensor placed close to the reservoir outlet. The measured temperature is used for a closed-loop temperature regulation. The temperature control as well as the valve control is realised by a self-developed electronic control unit which is connected to a PC via USB port. This unit allows for precise, time defined actuation of the valve in combination with autonomous control of the reservoir temperature.

The fabrication of the StarJet nozzle chips is conducted using the established manufacturing process (see [9]). However, the nozzle size has been reduced by half to 50  $\mu\text{m}$  utilizing a novel chip design via redesigning the photolithography masks. The experimental setup presented in this paper consists of the described StarJet actuator mounted above an x-/y-z-stage. In addition, a spinning axis can be mounted on this stage. Hence in contrast to earlier experiments, the distance between the nozzle and the substrate can be adjusted during the experiments.

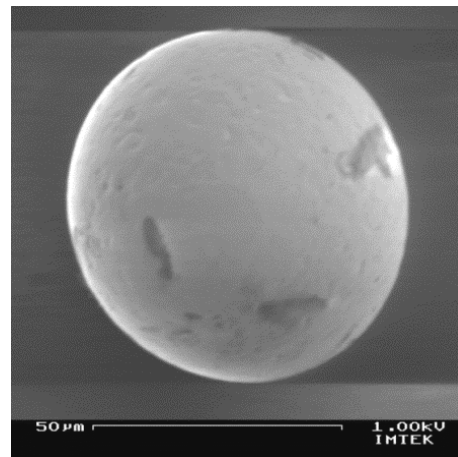
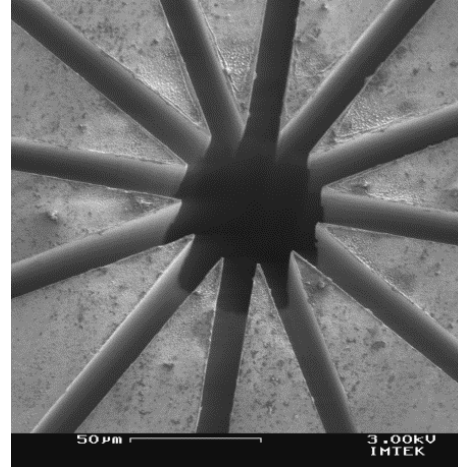


Figure 3a) REM picture of the silicon nozzle chip  
3b) REM picture of a metal droplet generated with a 50  $\mu\text{m}$  nozzle chip.

## EXPERIMENTAL RESULTS

The StarJet technology features two different dispensing modes, the DropOnDemand-mode and the Continuous-mode (for details see [1]). Experiments presented in this paper were performed using both operation modes. In Continuous-mode, droplets are issued from the nozzle continuously at a certain “natural” frequency. This frequency depends on the nozzle geometry, the applied actuation pressure in combination with the rinse pressure and other parameters. Thus, each nozzle chip features an individual frequency range depending on the specific nozzle geometry. Since the new actuator exhibits two pneumatic connections (cf. Fig 2), the rinse pressure can now be adjusted independently of the driving pressure. This enables droplet frequency adjustment at fixed driving pressure (cf. two channel setup blue frames in Fig.4). Thereby, the lowest value is given by  $P_{\text{rinse\_min}}$  which is the minimum rinsing pressure required to prevent a continuous jetting. The upper boundary  $P_{\text{rinse\_max}}$  is the smallest value that inhibits droplet ejection (at fixed driving pressure). In

contrast, the red markers show the frequency/pressure relation of the earlier single channel setup.

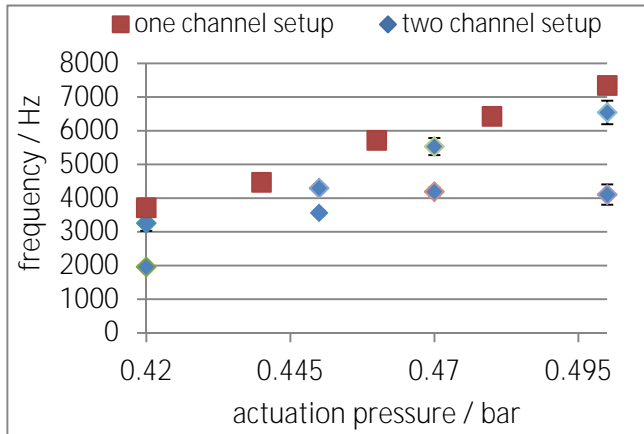


Figure 4: Measurement of droplet generation frequency as function of actuation pressure for 80  $\mu\text{m}$  nozzle-chip.

Actuation pressures beyond  $P_{\text{actuation\_max}}$  led to uncontrolled spraying of metal droplets. In several experiments, frequencies in the range from  $f_{\text{min}} = 200$  Hz to  $f_{\text{max}} = 11$  kHz were evaluated. With the redesigned nozzle (Fig. 3a), a minimum droplet diameter of  $D_{\text{min}} = 60$   $\mu\text{m}$  (Fig. 3b) has been achieved using a 50  $\mu\text{m}$  nozzle chip. We also observed that droplet trajectory and the occurrence of satellites can be optimized by the rinse pressure. The droplet diameter is primarily defined by the nozzle size ( $D = 50$   $\mu\text{m}$  to 360  $\mu\text{m}$  available). By dispensing single droplets at 350°C with a frequency of 5.5 kHz onto a spinning axis, coils can be fabricated using continuous operation. The adaptation of the dispensing frequencies and the rotation velocity of the axis allowed for printing homogeneous structures. Here, the single droplets merge after impact resulting in a solid structure (see Fig. 5). The samples have been created at room temperature without any additional heat conditioning or post treatment.



Figure 5: Coil like structures printed at 350°C metal temperature.

By dispensing multiple layers of single droplets onto a moving substrate, walls can be created. Here, the distance between two droplets has to be set to double the value of the droplet diameter. Thus, the droplets don't merge together resulting in a porous structure (See Fig. 6).

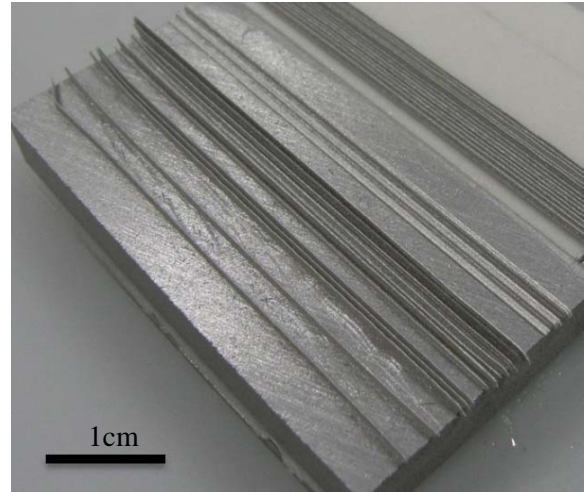


Figure 6: Walls printed at 350°C metal temperature on aluminum substrate.

The close-up view reveals that the droplets lose their spherical shape and solidify in a reformed state while impinging on the solid (See Fig. 7). This leads to a high surface roughness as well as to an enhanced wall thickness of 250  $\mu\text{m}$  compared to the droplet diameter of  $D = 80$   $\mu\text{m}$ . The surface of the printed structure has been measured with a profiler (Tencor, P11) to characterise the roughness of the walls. The structure exhibits an average surface roughness of  $R_t = 94$   $\mu\text{m}$ .

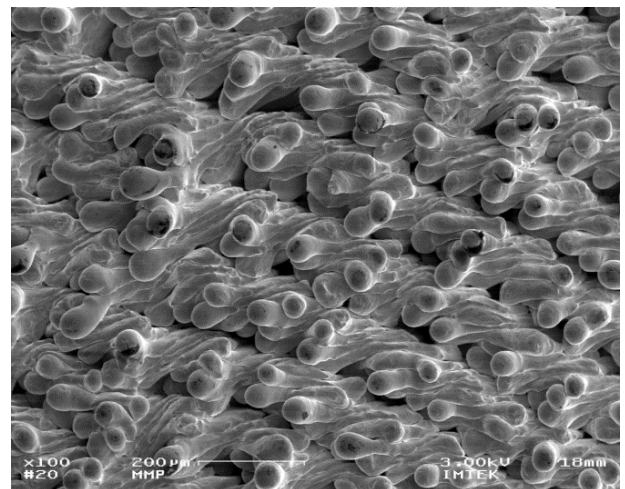


Figure 7: SEM image of a surface of printed solder wall.

Remarkably, only minor oxidation occurs on the surface of the printed structures, which is attributed to

the pneumatic actuation by Nitrogen as described above. This example demonstrates that it is possible to influence the properties of the printed structures (morphology, porosity, wall thickness, roughness etc.) by variation of the process parameters. When operating in Drop on Demand mode, the actuation pressure is applied only in short pulses each leading to the ejection of one single droplet. This is done by opening a solenoid valve periodically for 3-8 ms. The rinse pressure is kept constant all the time to prevent oxidation at the nozzle outlet. A suitable valve opening time in combination with the matching actuation pressure leading to the ejection of single droplets has been experimentally determined for each nozzle chip. However, multiple combinations of valve opening time and actuation pressure are feasible for each chip. The printhead was successfully tested for 5 hours for continuously ejecting droplets in drop-on-demand mode without interruption at frequencies up to 25 Hz. A nozzle chip, generating droplets of  $D_{\text{drop}} = 80 \mu\text{m}$ , was used to print our affiliation logo on an aluminum substrate (see Fig. 8).

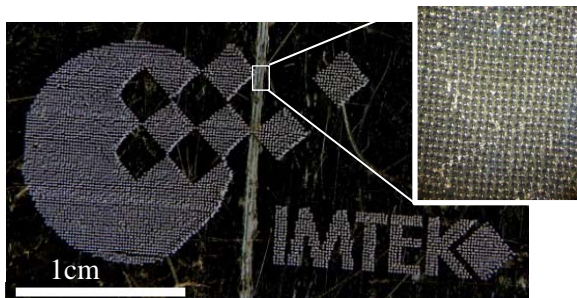


Figure 8: Printed IMTEK Logo, droplet diameter approximately  $80 \mu\text{m}$ .

## CONCLUSION & OUTLOOK

The described improved StarJet metal dispenser was successfully tested experimentally in continuous and DoD-operation mode. The miniaturized nozzle chip in combination with the V2 actuator with two pneumatic connections allows for higher frequencies ( $f_{\text{max}} = 11 \text{ kHz}$ ) and generation of smaller droplets ( $D_{\text{min}} = 60 \mu\text{m}$ ) than before. By adjustment of the rinse pressure, the dispensing frequency can be adjusted. Furthermore, the occurrence of satellites is highly unlikely. The presented results show that the StarJet technology can be successfully applied for the 3D-prototyping of porous and non-porous metal structures. The presented structures demonstrate that depending on droplet temperature as well as other printing parameters, the porosity and wall thickness of the printed structures are controllable. The presented results are of course only a first step towards the controlled prototyping of metal micro-structures by direct printing of liquid metal. More work has to be dedicated to study the solidification and the resulting

morphology of the metal surface as a function of materials and process parameters before more complex shapes can be generated. In the next step, the StarJet method will be applied at even higher temperatures to enable a wider choice of materials to be used for direct metal printing.

## REFERENCES:

- [1] T. Metz, G. Birkle, R. Zengerle, P. Koltay, , *Proc. of IEEE-MEMS 2009*, 2009, pp. 43-46
- [2] A. Tropmann, N. Lass, N. Paust, T. Metz, C. Ziegler, R. Zengerle, P. Koltay, , *Microfluid. Nanofluid.*, vol. 12, pp. 75-84, 2011
- [3] D. Schuhmacher et al. „Erzeugung von Mikrotropfen aus flüssigem Lötzin mittels einer hochparallelen und kontaktlosen Drucktechnik“ *IEEE MEMS 2007*, pp. 357-360
- [4] S. Ho-Young, N. Jae-Woong, P. Kyung-Wook, , *Electronics Packaging Manufacturing, IEEE Transactions on*, , 2005
- [5] M. ESSION, D.M. Keicher, W.D. Miller, „Manufacturing electronic components in a direct-write process using precision spraying and laser irradiation“, Patent, 2000
- [6] Wenbin Cao, Miyamoto, Yoshinari, “Freeform fabrication of aluminum parts by direct deposition of molten aluminum” *Journal of Materials Processing* 173 (2006) 209---212
- [7] Taik-Min Lee: 3D Metal microstructure fabrication using a molten metal DOD Inkjet system; 2007.
- [8] W. Wehl, J.B. Wild, B. Lemmermeyer, A drop-on-demand metal jet printer for wafer bumping” *Proc. IMAPS 2003*
- [9] N. Lass, A. Tropmann, T. Metz, R. Zengerle, P. Koltay: 3D Rapid-Prototyping durch Drucken von flüssigem Metall unter Verwendung der StarJet Technologie; 2011

## ACKNOWLEDGEMENTS

Funding by the Bundesministerium für Bildung und Forschung (FKZ 02PO2872) is gratefully acknowledged.

## CONTACT

Nils Lass, tel: 0049761-20373258;  
nils.lass@imtek.de



## 2. Actuators

**Controllable Active Micro Droplets Merging Device Using Horizontal Pneumatic Valves**Afshan Jamshaid<sup>1</sup>, Masaya Igaki<sup>1</sup>, D.H.Yoon<sup>1</sup>, T.Sekiguchi<sup>2</sup>, S.Shoji<sup>1</sup><sup>1</sup>Major in Nanoscience and Nanoengineering, Waseda University, JAPAN  
Nanotechnology Research Center, Waseda University, JAPAN**ABSTRACT**

This paper describes an active droplet merging device, which can merge various size micro droplets in different ratios by using pneumatically controlled horizontal PDMS microvalves. A merging part consists on main and side channels separated by pillars. Selective droplets merging are successfully achieved by varying the flow resistance of the main and side channel controlled by deformable PDMS horizontal pneumatic microvalves.

**KEYWORDS**

Merging, Pneumatic microvalves, Droplets, Flow resistance

**INTRODUCTION**

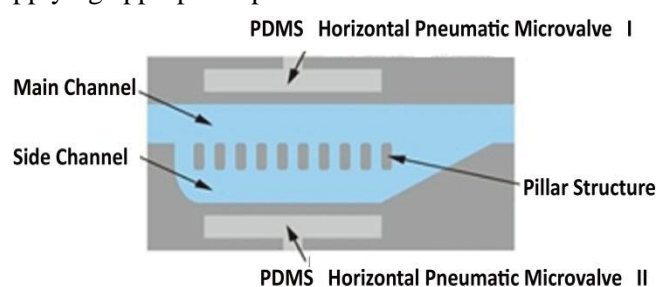
Microfluidic systems that utilize flow instabilities between immiscible fluids to generate suspended droplets have attracted much recent attentions [1]. In such systems, the ability to controllably generate and merge droplets is of high importance when performing complex chemical or biological analysis [2]. Droplet generation is achieved by shearing one fluid phase with another, either at a T junction or by using a flow focusing geometry. However, the process of merging (in effect the reverse of generation) is usually not predictable, due to subtle variations in interfacial tension, surface topography of microchannels, and fluidic properties (such as of droplet size and velocity)[3]. As noted, droplet merging is essential in many applications including sequential reactions [4]; multiple step manipulation of cells or high-throughput bioassays [5]-[6]. Several techniques have been developed to merge droplets. These are either active and involve components such as electric fields [7]-[8] or passive and utilize the surface properties or structure of the fluidic conduit [9]-[10]. To merge micro droplets, with electric field, dielectrophoresis, electrocoalescence and heating have been used [11]-[13]. However, sample destruction and denaturalization were sometimes observed under high electric field, high temperature or high shear stress generated during the operations. On the other hand, a merging system using pneumatic microvalves can prevent these damages efficiently [14].

As we reported an active droplet sorting system

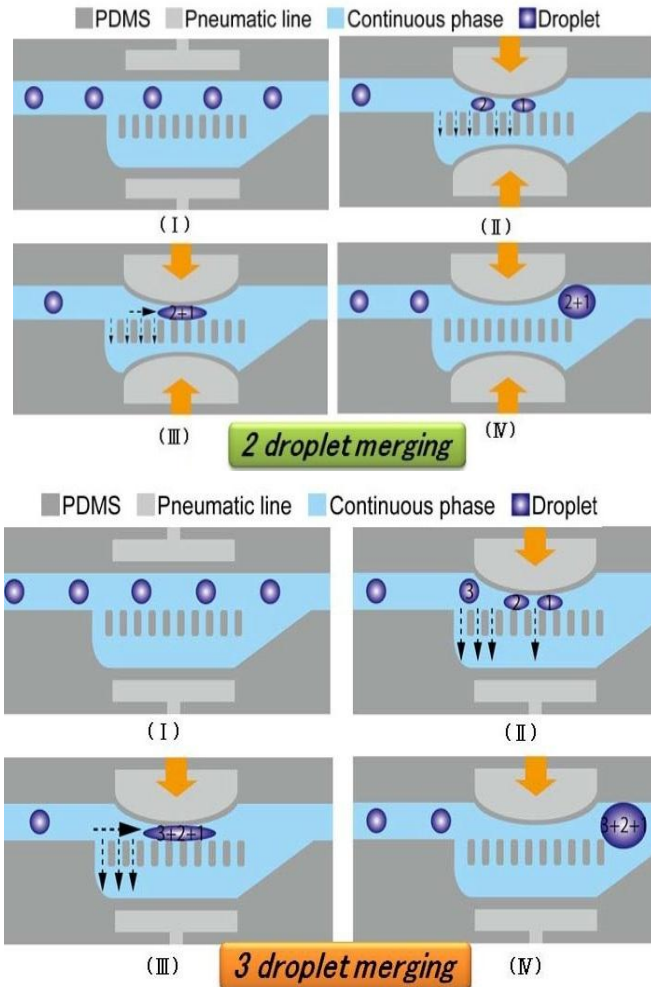
using high aspect ratio PDMS parallel walls and PDMS horizontal pneumatic microvalves [15]. This droplet sorting system can deliver target droplets to five different chambers by pneumatically controlled horizontal PDMS microvalves. Use of the horizontal pneumatic microvalves makes a system very simple with one PDMS layer rather than using vertical pneumatic microvalves which always consist of multi-layer PDMS structures. From this point of view, we chose the pneumatic microvalves control systems for merging the micro droplets. A passive droplets merging device consist of a center channel and two side channels separated by micro pillar arrays was reported [16]. This device achieved continuous and reproducible merging of droplets. However, the size and number of the merged droplets are determined by the micro pillar array structures. In this paper we propose an active droplet merging device using horizontal pneumatic microvalves with a micro pillar array and achieve the merging of different sizes and different number of droplets successfully.

**CONCEPT**

A schematic structure (merging part) as shown in Figure 1(a) and the working principle of micro droplets merging device are shown in Figure 1 (b). Droplets are continuously injected to the reaction part with carrier flow. The Valve I controls flow velocity of the droplets which are widely changed by the droplet sizes. Therefore, the intermediate carrier flows through the pillars by the pressure balance, the space between the droplets can be controlled by combination of Valve I and Valve II. The controlled number of droplets are trapped and then merged by applying appropriate pressure to Valve I and Valve II.



(a) Structure of merging device



(b) Selective two and three droplets merging

Figure 1: Schematics of the structure and principle of droplet merging part

## DESIGN AND FABRICATION

### Design

Figure 2 shows the top view and detailed dimensions of the whole device and merging part, the device consists on a droplet co-flowing generation, merging part, pneumatic microvalves lines and drain channel. In this design, the pillars divide the entire merging element into two channels; one side channel and a main channel (where the width of main channel reduces as a function of distance through the pillar array). These two channels are interconnected via pillars array. The gap between the pillar is designed to be smaller than the representative droplet diameter, to ensure that the droplets will neither go through the side channel thoroughly nor breakup into sister droplets due to drag flow into the side channel. Accordingly, droplets entering the merging chamber will be localized in the main channel, while the continuous phase is able to flow

through all two parallel channels. In a sense, the pillars act as a filter, but also allow for all of the continuous phase to flow back into the main channel at the end of the merging element. Moreover, such a 'single input' and 'single output' merging chamber ensures a constant total fluidic mass between the inlet and outlet, and thus allows the merging element to be installed in any location within the microfluidic network, without inducing asymmetries in mass and pressure distribution. Width of the main channel is  $200\mu\text{m}$ , width of the cross channel of generation part is  $100\mu\text{m}$ . Thickness of the pneumatic valve membrane is  $30\mu\text{m}$  and the gap between the channels and pneumatic microvalves is  $30\mu\text{m}$ . The pillar size is  $50\mu\text{m} \times 100\mu\text{m}$ , and height of all structure is about  $87\mu\text{m}$ .

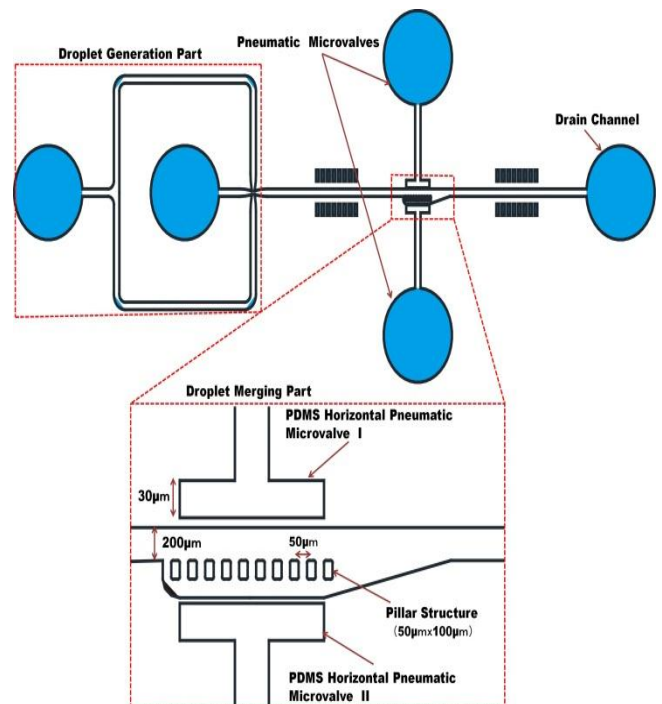


Figure 2: Configuration of whole system and detailed size of merging part

### Fabrication

The fabrication process of the tested device by PDMS using SU-8 3025 mold (fabricated by UV lithography) is shown in Figure 3.  $\text{O}_2$  plasma treatment used for bonding of the PDMS replication with the PDMS plate. In order to realize large deformation, base compound and curing agent were mixed in 15:1 and cured at  $75^\circ\text{C}$  for 45min in an electric oven to control the hardness of the PDMS.

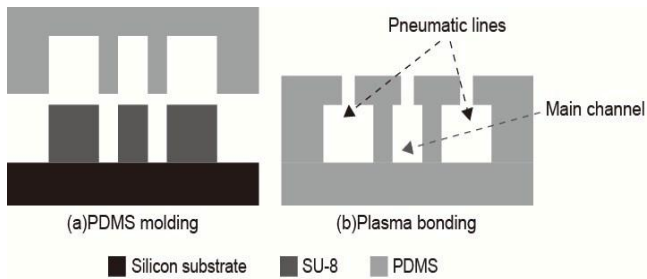


Figure 3: Fabrication process of the droplet merging system

## EXPERIMENTAL SETUP

For fluidic experiments, a syringe (1725CX HAMILTON) and a syringe pump (KDS210, kd Scientific) were used to control volumetric flow rates of oil and water. The air pressure was controlled by pressure regulator (2657 pneumatic pressure standard, YOKOGAWA). In order to evaluate the generation rate and the diameter of micro droplets, the high speed CCD camera (PHOTRON FASTCAM-NEO32KC) was used. This camera system and a data processing computer were utilized for visualization and storage of the droplet behaviours in merging part for different sizes and different ratios.

## RESULTS AND DISCUSSION

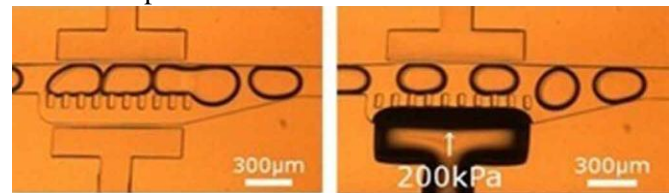
Figure 4(a) shows a large scale of the microfluidic merging device during operation. During initial calibration, 300 $\mu$ m diameter droplets were generated using a co-flowing generation with the flow rate 0.5 $\mu$ l/min of water and carrier (oil). The two droplets merging achieved under pressure of 190kPa (Valve I) and 120kPa (Valve II) as shown in Figure 4 (b) and the three droplets merging achieved under pressure of 150kPa (Valve I) and 50kPa (Valve II) as shown in Figure 4 (c).

We also achieved the different sizes of droplets merging with the three different flow rates of water and carrier (oil), we generated and merged small, medium and large droplets in diameter as shown in Figure 5.

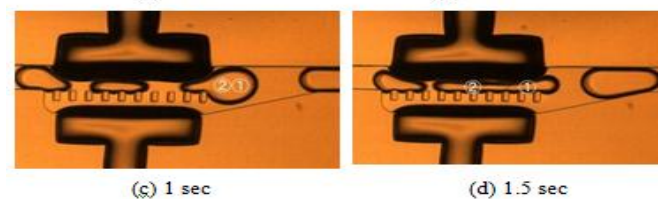
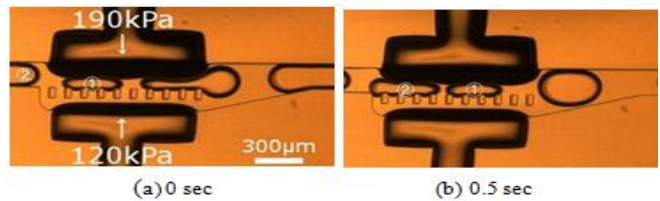
Small droplets generation attained with the flow rates of water 0.1 $\mu$ l/min and carrier (oil) 0.5 $\mu$ l/min. The merging of two small droplets are achieved with the Valve I pressure 170kPa and Valve II pressure 80kPa. The three small droplets merging achieved with the pressure of 160kPa pressure of Valve I as shown in Figure 5(a). Medium droplets were generated with the flow rates of water 0.5 $\mu$ l/min and carrier (oil) 0.5 $\mu$ l/min and two droplets merged with the 190kPa pressure of valve I and 120kPa pressure of Valve II. The three medium droplets merging were also successfully achieved with the 150kPa pressure valve I and 50kPa pressure of valve II as shown in Figure

5(b). The successful merging of large droplets (generated with the flow rate of water 0.8 $\mu$ l/min and carrier (oil) 0.3 $\mu$ l/min) as shown in Figure 5(c) are achieved with the 140kPa pressure of valve I and 125kPa of valve II. The displacement of PDMS wall with pneumatic horizontal microvalves varied the resistance of main and side channel. According to that, the merging of different droplets in numbers and sizes are achieved experimentally as shown in Figure 5, we analyzed with this merging device the efficient mixing of different droplets can be successfully attained in milliseconds.

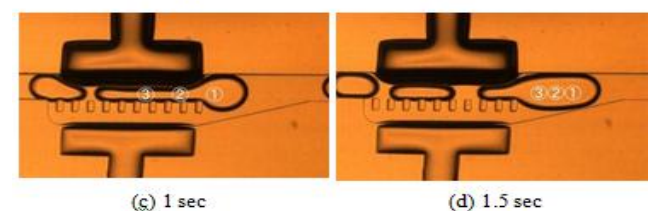
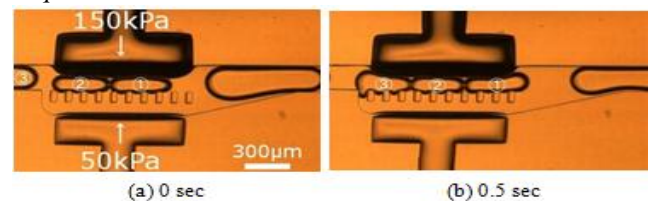
Comparing the results with the previous reported work we achieved the precise controllable merging of different number and sizes of droplets under different pressure conditions.



(a) Initial state (b) 200kPa pressure to valve II  
(a) Captured images of droplet interval changing by pneumatic valves



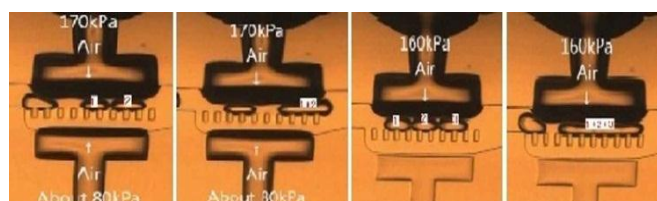
(b) Captured images of two droplets merging with time sequence



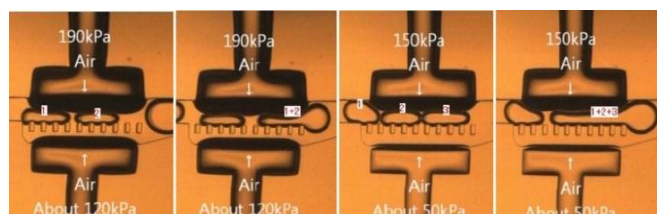
(c) Captured images of three droplets merging with time sequence

Figure 4: Two and three droplets merging under different pressures





(a) Small Size Droplets [(water) = 0.1  $\mu$ l/min, Carrier (oil) = 0.5  $\mu$ l/min]



(b) Medium Size Droplets [(water) = 0.5  $\mu$ l/min, Carrier (oil) = 0.5  $\mu$ l/min]



(c) Large Size Droplets [(water) = 0.8  $\mu$ l/min, Carrier (oil) = 0.3  $\mu$ l/min]

Figure 5: Different sizes and number of droplets merging

## CONCLUSION

Droplet merging using horizontal PDMS pneumatic valves and pillar structure has been successfully demonstrated. The numbers and volumes of merged droplets were controlled precisely by the applied pneumatic pressures. We are currently optimizing the structure of the integrated system or micro total analysis system ( $\mu$ TAS) to realize more precise micro droplet handling for actual chemical and biochemical applications.

## ACKNOWLEDGMENT

This work is partly supported by Japan Ministry of Education, Culture, Sports Science & Technology Grant-in-Aid for Scientific Basic Research (S) No. 23226010 and Nanotechnology Platform of Waseda University for their technical assistances.

## REFERENCES

- [1] H. Song, D. L. Chen and R. F. Ismagilov, Reactions in droplets in microfluidic channels , *Angew. Chem., Int. Ed.*, 45, 7336 (2006).
- [2] Xize Niu and Joshua B. Edel , GEOMETRICALLY MEDIATED DROPLET MERGING IN MICROCHANNELS , Twelfth International Conference on Miniaturized Systems for

Chemistry and Life Sciences October 12 - 16, 2008, San Diego, California, USA

- [3] S. J. Kim, Y.-A. Song, P. L. Skipper and J. Han, *Anal. Chem.*, 2006, **78**, 8011.
- [4] M. Y. He, J. S. Edgar, G. D. M. Jeffries, R. M. Lorenz, J. P. Shelby and D. T. Chiu, *Anal. Chem.*, 2005, **77**, 1539.
- [5] M. Srisa-Art, A. J. deMello and J. B. Edel, *Anal. Chem.*, 2007, 79, 6682.
- [6] C. Priest, S. Herminghaus and R. Seemann, *Appl. Phys. Lett.*, 2006, **89**, 134101
- [7] K. Ahn, J. Agresti, H. Chong, M. M. Marquez and D. A. Weitz, *Appl. Phys. Lett.*, 2006, **88**, 264105.
- [8] L. M. Fidalgo, C. Abell and W. T. S. Huck, *Lab Chip*, 2007, **7**, 984.
- [9] Nguyen N, Wu Z (2005) Micromixers-a review. *J Micromech Microeng*
- [10] Y.-C. Tan, J. S. Fisher, A. I. Lee, V. Cristini and A. P. Lee, *Lab Chip*, 2004, **4**, 292.
- [11] D. R. Link, E. Grasland-Mongrain, A. Duri, F. Sarrazin, Z. Cheng, G. Cristobal, M. Marquez and D. A. Weitz, "Electric control of droplets in microfluidic devices", *Angew. Chem., Int. Ed.*, 2006, 45, pp. 2556–2560.
- [12] L. M. Fidalgo, G. Whyte, D. Bratton, C. F. Kaminski, F. Clemens, C. Abell and W. T. S. Huck, "From microdroplets to microfluidics: selective emulsion separation in microfluidic devices", *Angew. Chem., Int. Ed.*, 2008, 47, pp. 2042–2045.
- [13] Kentaro Kawai, Yoko Shibata and Shuichi Shoji, "100 Picoliter droplet handling using 256 ( $2^8$ ) Microvalve array with 18 multiplexed control lines" The proceeding of Transducers'09, 2009, pp. 802-805
- [14] Yen-Heng Lin, Chun-Hong Lee and Gwo-Bin Lee, "A new droplet formation chip utilizing controllable moving-wall structures for double emulsion applications", The proceeding of MEMS'08, 2008, pp. 22-25.
- [15] D. H. Yoon, D. Wakui, T. Sekiguchi, and S. Shoji, "Selective Droplet Sampling Flow System Using Minimum Number Of Horizontal Pneumatic Valves Formed By Single Step PDMS Molding," *Micro TAS 2010*, pp. 1085-1087, Groningen, NETHERLANDS, 3-7 October, 2010.
- [16] Xize Niu and Joshua B. Edel, "Geometrically Mediated Droplet Merging In Microchannels," *Micro TAS 2008*, pp. 1423-1425, San Diego, USA, 12-16 October, 2008.

## CONTACT

jamshaid@shoji.comm.waseda.ac.jp



## 2. Actuators

# ACTIVE AND PRECISE CONTROL OF MICRODROPLET DIVISION USING HORIZONTAL PNEUMATIC VALVES IN BIFURCATING MICROCHANNEL

*D. H. Yoon<sup>\*1</sup>, J. Ito<sup>1</sup>, T. Sekiguchi<sup>2</sup>, and S. Shoji<sup>1</sup>*

<sup>1</sup> Major in Nanoscience and Nanoengineering, Waseda University, Tokyo, Japan

<sup>2</sup> Nanotechnology Research Center, Waseda University, Tokyo, Japan

## ABSTRACT

This paper presents a microfluidic system for active and precise control of microdroplet division in microchannel. Using two horizontal pneumatic valves formed at the downstream of bifurcating microchannel, outlet flow resistances were variably controlled. Water-in-oil microdroplets were divided into two daughter droplets of different size due to the controlled flow resistance. Volumetric ratio of the daughter microdroplets was quantitatively evaluated. Finally, we discussed flow speed effect for dynamic droplet division, and pressure effect for generation of microdroplet at upstream cross junction. The microfluidic channels and pneumatic valves were fabricated by single-step soft lithography process of PDMS (polydimethylsiloxane) using SU-8 mold.

## KEYWORDS

Microdroplet, Division, Bifurcating microchannel, Horizontal pneumatic valve, PDMS

## INTRODUCTION

Microdroplet technologies are effective methods to control small samples [1]. For example, to use chemical reaction and encapsulation of biological materials, the microdroplet technologies have been developed in recent years [2]. Quantitative volume control, protection, and transportation of the small samples are realized in a miniaturized platform. In the technologies, size and volume control of microdroplet is an important issue in order to maximize their advantages.

Microdroplet generation in cross channel is one of well-known method to control their size [3]. However, the size which is controlled by introduced flow rates and specific structure has limited variation of droplet size. And, limited generation rate of the microdroplets in this structure is also the disadvantage.

To obtain wide size control and high throughput of droplet generation, mechanical division structures have been studied by our group. Using multi-stage divergence microchannel, microdroplet generation of 3800 droplets/sec with about 5  $\mu\text{m}$  in diameter was realized in a single cross channel device [4]. Furthermore, sifted-pillar structure from center of microchannel and asymmetric wall structure with division microchannel made it possible to generate microdroplet of different volume ratio [5]. However,

variation of the droplet size was still limited in the structure. Actively controllable microdroplet division system with high accuracy is required for wide applications.

On the other hand, fluidic devices utilizing pneumatic valves with a flexible material, for example, PDMS (polydimethylsiloxane) are well-defined active flow control system [6]. By deformation of the valves, flow resistance, flow rate, and flow direction in microchannels can be controlled with high accuracy. Furthermore, pneumatic valves of horizontal types realized simple fabrication of high performable fluidic devices.

In this study, we propose a simply and precisely controllable microdroplet division method. By integrating bifurcating microchannel with pneumatic valves, wide size control and high throughput of droplet generation was achieved.

## CONCEPT

Figure 1 shows principle of the division of microdroplets using flow resistance control in the bifurcating channel. When introduced microdroplets are mechanically divided in the microchannel, their volumetric ratio depends on downstream resistance. Thus, if the flow resistances of two downstream channels could be controlled precisely, it is possible to divide microdroplets in any volume ratio at the same time.

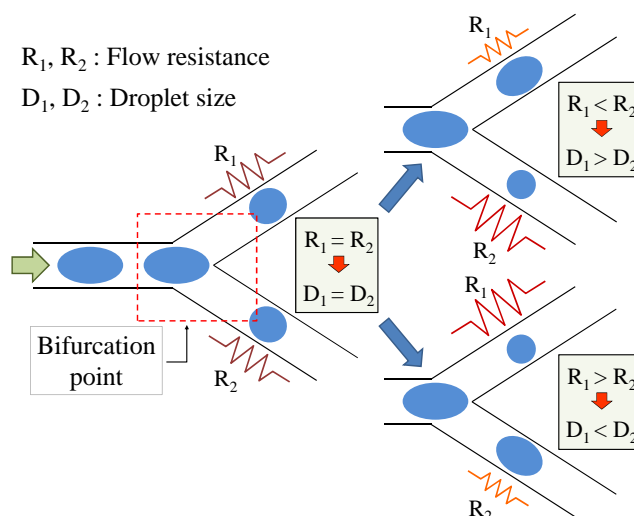


Figure 1: Controllable microdroplet division in bifurcating microchannel using a change in flow resistance of down stream

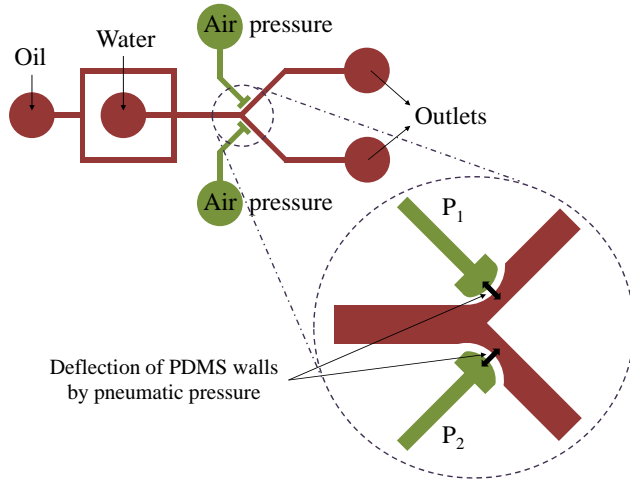


Figure 2: Schematic view of a total device and division part utilizing horizontal pneumatic valves

In order to control the flow resistance of microchannels, two horizontal pneumatic valves are added at downstream of a bifurcation point to droplet division device consist of a cross junction and a bifurcating channel as shown in Figure 2. Each pneumatic line is independently operated and both resistances of the outlet channels are controlled. As the results, original microdroplets generated at cross junction can be divided into two different sizes at the bifurcation point.

## DESIGN AND FABRICATION

Figure 3 shows total design of the microdroplet division device and detailed sizes of each part; droplet generation part, division part, and observation part. Cross channel was designed as 200  $\mu\text{m}$  and this main channel become to a narrow channel of 100  $\mu\text{m}$  width. The nozzle shape makes it possible to locate initial droplets in center of microchannel. As the result, original microdroplets are more stably introduced and divided at bifurcation point.

Thickness of deformable membranes of the valves is designed as 30  $\mu\text{m}$  by considering its flexibility and deformation amount. Finally, for observation of generated droplets, wide area of 300  $\mu\text{m}$  in width was used.

The PDMS device was fabricated by single-step soft lithography as shown in Figure 4 (a). Height of all SU-8 structures is about 100  $\mu\text{m}$ . After PDMS replicating from the SU-8 mold, the structure of PDMS is bonded with PDMS coated glass substrate by  $\text{O}_2$  plasma treatment. To obtain more flexible PDMS structure, resin and curing agent were mixed in 15:1 ratio. SEM (scanning electron measurement) images of each part of fabricated SU-8 mold are shown in Figure 4 (b). Structures for microchannels and pneumatic valves are clearly observed.

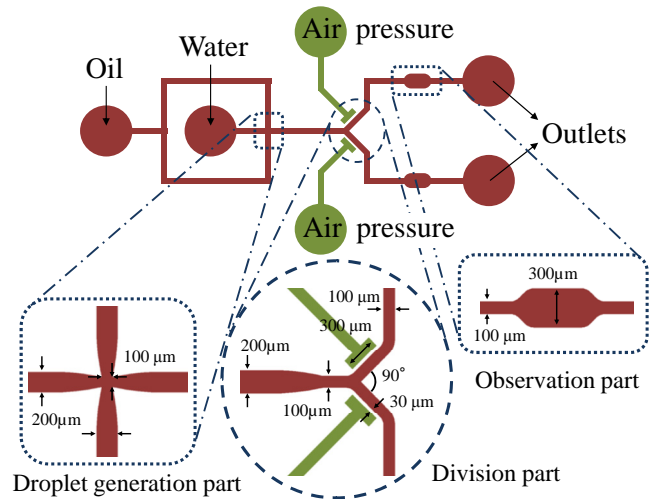


Figure 3: Total design of the droplet division device and detailed sizes of each part

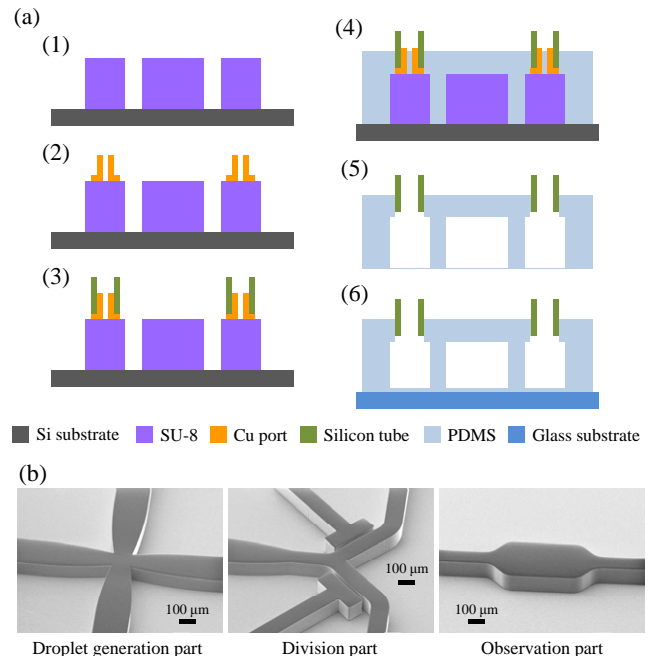


Figure 4: Fabrication process of the droplet division device (a) and SEM images of the SU-8 mold of each part (b)

## EXPERIMENTS

### Experimental set-up

Deionized water and mineral oil (8042-47-5) were used for generation of initial microdroplets, and they were introduced by syringes (1750CX, Hamilton) and syringe pumps (KDS210, kdScientific). Pneumatic pressure was controlled by pressure regulator (2657 pneumatic pressure standard, Yokogawa). Experimental results were captured by high speed camera (FASTCAM-NEO, Photron) and sizes of microdroplets were calculated by pixel counting.

## Experimental results

In Figure 5, microdroplet division results with different pressure are shown. Original microdroplets, about 5 nL in volume, were generated by water and oil of 2  $\mu\text{L}/\text{min}$  volumetric flow rate. When the pneumatic pressure was 0 kPa, introduced water microdroplets was divided almost half and half. With increase in pneumatic pressure of the lower valve, size of microdroplets in lower branch channel decreased.

A change in ratio of droplet size in upper and lower branch channels VS pneumatic pressure is shown in Figure 6. Control of microdroplet division using this system is verified by quantitative result. Microdroplet division of different volumetric ratio from 1 to 1.5,  $V_{\text{upper}}/V_{\text{Lower}}$ , was achieved by pneumatic pressure from 0 kPa to 250 kPa. When the microchannel was almost closed at around 300 kPa, original microdroplets flowed into upper branch channel without division. But, the PDMS valves have mechanical limitation. According to this reason, experimental results between 250 kPa to 300 kPa were not stable.

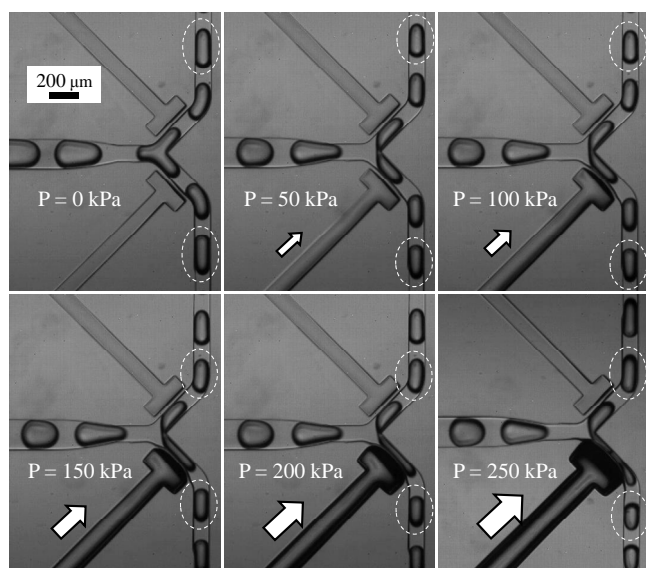


Figure 5: Captured Images of droplet division with operation of pneumatic valves ( $Q_w=Q_o=2\text{ }\mu\text{L}/\text{min}$ )

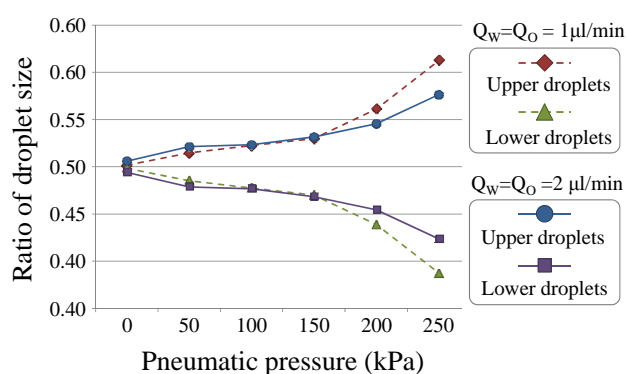


Figure 6: Sizes of divided microdroplets with pressure

## DISCUSSIONS

From experimental results, our investigations are focused on not only controllable division, but also two points as follows; effect of introduction speed to bifurcation point and effect of flow resistance of downstream.

By a change in applied pressure to the valves, sizes of divided droplets also changed. But additionally, when total flow rate was increased, a difference between upper and lower droplet size decreased. It is because time for droplet deformation at the point is not enough by fast introduction speed. This result informs that the introduction speed is an important factor for mechanical division of microdroplets.

Also, generated original microdroplets with different pressure conditions are shown in Fig. 6. When water and oil were introduced as fixed flow rate of 2  $\mu\text{L}/\text{min}$ , the size of generated droplets changed with a change in total downstream flow resistance. The result indicates that the flow resistance of downstream is also the factor for generation of microdroplets, and it is necessary to consider this effect for more precise droplet division control.

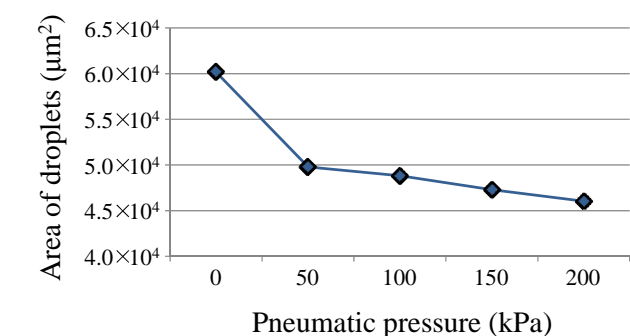
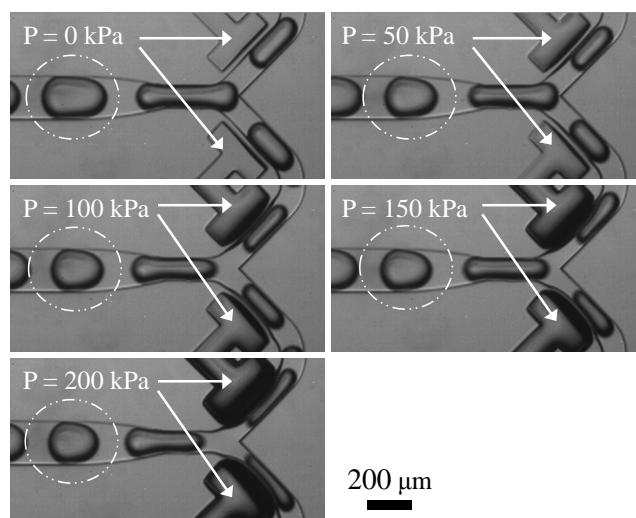


Figure 7: Size change in microdroplets by a change in flow resistance of microchannels with pressure

## CONCLUSIONS

We successfully controlled division of microdroplets in bifurcating microchannel using deformable horizontal pneumatic valves. Also, we discussed flow speed effect for microdroplet division and pressure effect for microdroplet generation. Total integration of droplet merging system and sorting system with proposed division system is under investigation.

## ACKNOWLEDGEMENTS

This work is partly supported by Japan Ministry of Education, Culture, Sports Science and Technology Grant-in-Aid for Scientific Basic Research (S) No. 23226010, and the authors thanks for Nanotechnology Platform of Waseda University for their technical assistances.

## REFERENCES

- [1] S.-Y. Teh, R. Lin, L.-H. Hung, and A. P. Lee, "Droplet microfluidics", *Lab Chip*, Vol. 8, pp.198-220, 2008.
- [2] M. Yamada, S. Doi, H. Maenaka, M. Yasuda, and M. Seki, "Hydrodynamic control of droplet division in bifurcating microchannel and its application to particles synthesis", *Journal of Colloid and Interface Science*, Vol. 321, pp.401-407, 2008.
- [3] L. Shui, J. C. T. Eijkel, and A. V. D. Berg, "Multiphase flow in microfluidic systems - Control and applications of droplets and interfaces", *Advances in Colloid and Interface Science*, Vol. 133, pp.35-49, 2007.
- [4] M. Fujii, K. Kawai, D. H. Yoon, and S. Shoji, "High speed generation of uniform femtoliter volume droplets using cascade multi-stage separation microfluidic device", *MNC2010*, 11C-4-2, 2010
- [5] M. Fujii, K. Kawai, D. H. Yoon, and S. Shoji, "Volume controlled high throughput picoliter droplet generation system using cascade multi-stage separation channel", *MEMS2011*, pp.1201-1204, 2011
- [6] D. H. Yoon, D. Wakui, T. Sekiguchi, and S. Shoji, "Selective droplet sampling flow system using minimum number of horizontal pneumatic valves formed by single step PDMS molding",  *$\mu$ TAS 2010*, pp. 1085-1087, 2010.

## CONTACT

\* yoon@shoji.comm.waseda.ac.jp



## 4. Fluidic control systems

### PRESSURE DRIVEN AND REGULATED DISPENSER FOR THE MICROLITER RANGE

*L. Tanguy<sup>1</sup>, A. Ernst<sup>1,2</sup>, S. Bammesberger<sup>1</sup>, R. Zengerle<sup>1</sup> and P. Koltay<sup>1,2</sup>*

<sup>1</sup> Laboratory for MEMS Applications, IMTEK - Department of Microsystems Engineering, University of Freiburg, Georges-Koehler-Allee 103, 79110 Freiburg, Germany

<sup>2</sup> Biofluidix GmbH, Georges-Koehler-Allee 103, 79110 Freiburg, Germany

#### ABSTRACT

We report a sensor controlled normally closed non-contact fluid dispenser for the microliter range. A commercial disposable syringe is filled with fluid and connected through a T-connector to a pressure sensor separated from the liquid by an enclosed and defined gas volume. The other end of the T-connector is connected to a conventional dispensing valve which is normally closed. By displacement of the syringe plunger a defined pressure inside the enclosed gas volume can be established, controlled by the pressure sensor. The valve is then opened to release a pressure driven liquid jet. It is closed again when a certain pressure difference is detected by the sensor. Dispensed volumes can be easily changed by tuning this pressure difference. Experiments have been performed with water for volumes between 500nl and 25µl with standard deviations below 5%.

#### KEYWORDS

syringe-solenoid dispenser, pressure driven dispenser, liquid jet, micro dispensing

#### INTRODUCTION

The precise non-contact dispensing of volumes between 500nl and 25µl is an important issue for in-vitro-diagnostics (IVD), high-throughput screening (HTS) and industrial applications [1, 2]. Covering such a large range with high precision is a challenging problem, especially when non-contact dispensing of different liquids is required. Currently mainly pipetting tools are used for this purpose, which suffer from following shortcomings: First they are in mechanical contact with the substrates and/or aspirating fluids, thus introducing a high risk of cross-contamination that can be only avoided by intensive and time consuming cleaning protocols. Second there is no indicator or sensors providing a positive confirmation that the quantity of the dispensed liquid matches the requested volume. The development of a normally closed non-contact dispenser for handling a large variety of liquids, capable to determine in real-time (i.e. "online") the volume of the dispensed liquid is thus of high interest for many applications, not only within IVD. In this article we present a normally closed non-contact syringe-driven and sensor controlled dispenser that addresses these limitations.

#### WORKING PRINCIPLE

The presented system in this paper is a non-contact syringe-driven and sensor controlled dispenser. The concept, like depicted in Fig. 1 is similar to the well-known syringe-solenoid dispensers [3]. In contrast to these, the system presented here comprises - in addition to the driving syringe and the dispensing valve - an enclosed gas volume (denoted as  $V_{\text{gas}}$  in the following). The gas volume is in fluidic contact with a pressure sensor attached through a T-connector. The dimensions of the connection channel assure that the gas volume forms a stable meniscus between sensor and liquid, such that liquid never gets in contact with the sensor and the sensor is not contaminated. While the pressure sensor is used to measure the pressure of the enclosed gas volume, the syringe serves as reservoir and pressure source when actuated by the linear drive mechanism.

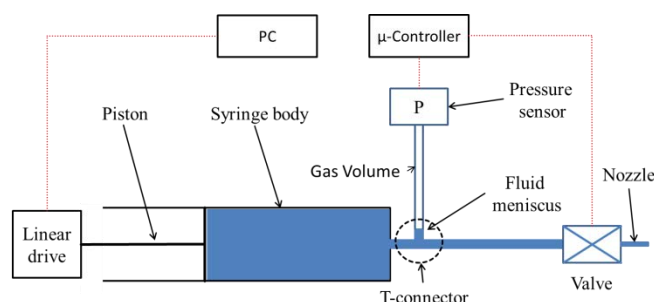


Figure 1: Schematic of the sensor controlled dispenser showing the different parts of the device.

In order to eject liquid out of the system, a positive pressure difference is created between the inside of the syringe and the surrounding environment. A linear drive is therefore used to push the piston which leads to compression of the enclosed gas volume  $V_{\text{gas}}$ . Except of the enclosed gas volume, the process is exactly the same like in conventional syringe-solenoid systems. However, the continuous monitoring of the pressure with the sensor, enabled by the presented setup, allows for a precise control of the movement of the linear stage. The movement can be stopped precisely when a predetermined pressure  $P_I$  is reached inside the gas chamber.

Once the gas is pressurized, the valve can be opened to release the liquid through the nozzle. The liquid is then driven out of the nozzle by the pressure

difference  $P_I$  between the inside of the syringe and the surrounding pressure of the environment. As soon as the fluid moves, the gas pressure begins to drop and the gas volume increases accordingly. An approximate relation between the enclosed gas volume  $V_{gas}$ , the volume of ejected liquid  $V_{liq}$  and the pressure drop measured by the pressure sensor  $\Delta P$  is given by the law of Boyle-Marriottte applied to the enclosed gas volume:

$$V_{liq} = V_{gas} \left( \frac{P_0 + P_I}{P_0 + P_I - \Delta P} - 1 \right) \quad (1)$$

Where  $P_0$  is the environmental pressure in the lab. Though, equation (1) is not considering dynamic effects while the liquid is flowing, it holds for the steady state, i.e. after closing the valve the relation of the quantities in equation (1) is exact. Based on this a simple 0<sup>th</sup>-order control can be established: To control the dispensed volume the user has to choose a defined pressure drop to be established by the device during the dispensing run i.e. after loading the syringe with a pressure  $P_I > \Delta P$ , the valve has to open until the sensor indicates that the set pressure has been reached. Thus, the ejected volume of liquid is approximately given by equation (1) and the bigger the pressure drop the bigger the volume dispensed.

Figure 2 illustrates the working principle with a schematic curve of the pressure inside the gas chamber and shows how a typical dispensing event influences the pressure.

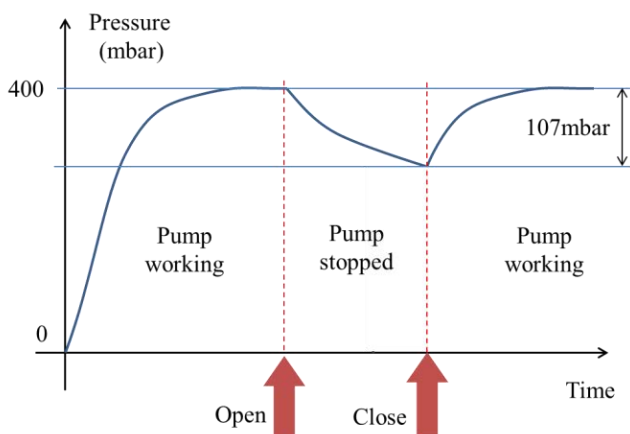


Figure 2: Typical signal during dispense (pressure difference 107 mbar). First the linear drive builds up the pressure by pushing the plunger into the syringe body. When the valve opens (first red arrow), the pressure (blue) drops until a certain pressure difference is reached; the valve is then automatically closed (second red arrow).

One important point that should be mentioned in the context of the description of the working principle is the complete absence of time control on the

dispenser. Since only the physical state variables pressure and volume are related to each other (eq. (1)), moderate changes in fluid properties play no role in the control of the volume. Therefore, the dispensed volume of liquid is in principle independent of changes in viscosity or other fluidic properties.

## MATERIALS AND SET-UP

The experimental setup used to study the described working principle is based on a commercial 20 ml syringe (Plastipak, BD). A T-connector (Festo) is fixed to the end of the syringe. One tube is attached to the pressure sensor RVAQ300GU (Sensortektechnics), designed for measuring 0 to 400 mbar pressures with a sensitivity of 10 mV/mbar (Fig 3-A). The third end of the T-connector is connected to a normally closed piezoelectric valve (Vermes) having a 100  $\mu$ m PEEK nozzle (Fig 3-B). The syringe and the tube connecting the valve are filled with the liquid to be dispensed, whereas the tube connecting to the sensor remains filled with air due to the dead end formed by the sensor. The defined volume  $V_{gas}$  is thus trapped between the liquid and the pressure sensor.

To avoid any capacitive effect inside the system, the individual components are chosen as stiff as possible. Therefore, during the compression only the gas volume inside the tube is changing and no significant expansion of the used plastic parts occurs.

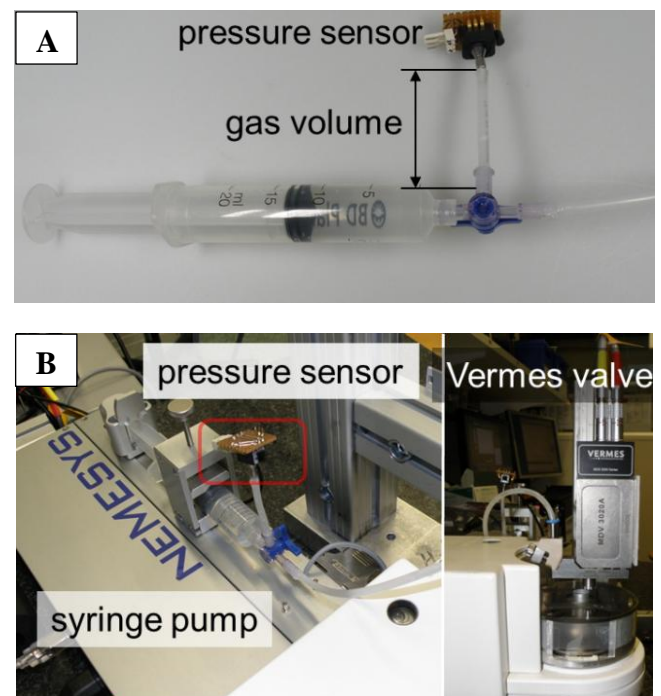


Figure 3: A - View of the syringe with an enclosed gas volume and pressure sensor attached. The other end of the tubing is connected to the valve. B - View of the mounted syringe on the linear drive (neMesys, Cetoni) (left side) and Vermes valve positioned over a microbalance (right side).



A PC-controlled linear drive (neMESYS, Cetoni) is used to move the plunger of the syringe and to build up the pressure inside the gas chamber until a pre-defined value (set-value) is reached. The measurement of the ejected volume of working fluid is done with ultra-microbalance (XP2U, Mettler-Toledo) placed under the nozzle of the valve (fig 3-B). The raw data of the balance is subjected to an evaluation algorithm taking into account effects of evaporation and other environmental factors to calculate the volume [4].

To increase the velocity of the dispensing and to avoid any time consuming communication with the PC, the handling of information coming from the sensor and the valve is realized within a micro-controller. It treats the pressure sensor signal in quasi real-time (approximately 100  $\mu$ s response time) and executes the programmed loop to control the dispensing process.

## EVALUATION OF THE DISPENSER

### Proof-of-principle

This system is characterized with two different liquids, distilled water and Phosphate Buffered Saline (PBS), see Table 1. Both of them are often used in the IVD industry. Water is dispensed to cover the whole operating range (500 nl, 1  $\mu$ l, 5  $\mu$ l and 25  $\mu$ l) whereas PBS is only dispensed at two pressure levels corresponding to 1  $\mu$ l and 25  $\mu$ l. Table 1 presents the physical properties of the two fluids used during these performance tests.

Table 1. Liquids used for experiments and their properties @ 20 °C.

Fluid	Density (kg/m <sup>3</sup> )	Viscosity (mPas)	Surface Tension (mN/m)
Water	998	1.03	71
PBS	1050	1.20	62

The dispenser was set up as shown in Fig. 3. We have chosen to operate the system at the maximum pressure reachable with our pressure sensor ( $P_1 = 400$  mbar) in order to achieve a high Weber number ( $We$ ) and therefore obtain a clean break-up of the jet. It is also important to have a sufficiently large range for  $\Delta P$  available that always leads to jet ejection (i.e.  $We > 8$ ) to cover the complete volume range.

In the experiments the pressure is built up inside the syringe to the desired initial value ( $P_1 = 400$  mbar) by moving the linear drive. Each volume is investigated by one dispensing run composed of 48 individual dispensing events. Figure 4 provides an example of such a run. To obtain an ejected volume of about 470 nl with DI water a pressure drop of 2 mbar

was required. A standard deviation of individual droplet volumes of 3.7 % was determined in this case (see Fig. 4).

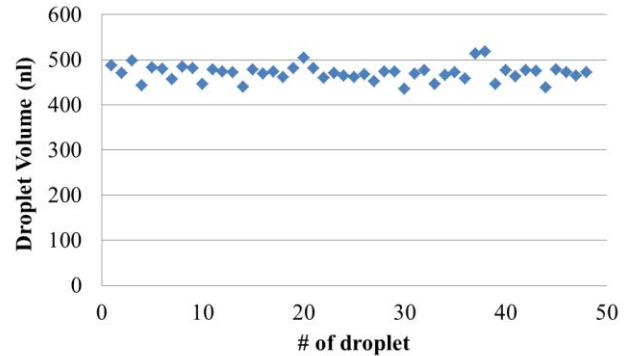


Figure 4: Results of 48 gravimetrically measured droplets of water at a mean volume of 470 nl and a standard deviation of 3.7%.

The total gas volume enclosed inside the dispenser was measured to be approximately 300  $\mu$ l. By using equation (1) it is thus possible to deduce the pressure drop corresponding to the volume dispense. Figure 5 shows the direct correlation between the measured volumes and the theoretical calculations for water based on the enclosed volume of 300  $\mu$ l. Except for small volumes/pressure-drops, the agreement between experiments and theory is very good (see also Table 2). The main reasons for discrepancies are mainly due to two major points:

1 - the signal to noise ratio of the pressure sensor is smaller for small pressure changes. Therefore, the measured results of pressure sensor is less accurate and therefore the dispensed volume, too.

2 - the dynamic increase of the pressure in the first milliseconds is really fast. Therefore, the latency of the micro-controller and/or the valve leads to the effect that the pressure still increases even after the valve was requested by the algorithm to be close.

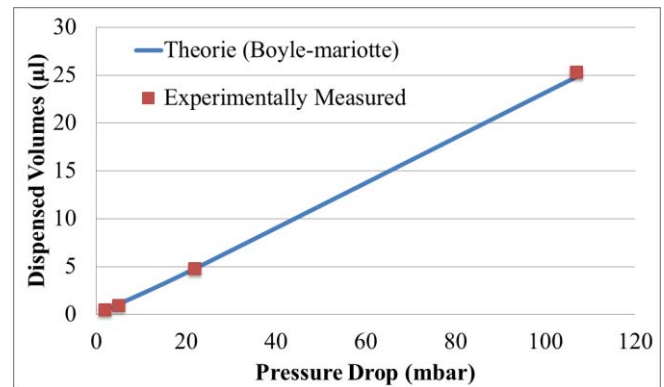


Figure 5: Correlation between equation (1) and ejected fluid volumes. The gas volume is taken as 300  $\mu$ l and the maximum pressure inside the gas chamber is 400 mbar.

## Performances

The performance of the system for the different liquids and volumes investigated is shown in Table 2. The minimum and maximum values used for  $\Delta P$  are 2 mbar to dispense 500 nl and 107 mbar for 25  $\mu$ l. Standard deviations between individual dispenses are between 1 and 5 %. The measured volumes match the expected volumes calculated in previous section.

*Table 2. Summary of the different experiments for the two different liquids and their respective standard deviations. Volumes are calculated using the densities given in table 1. Theoretical volumes are calculated by equation (1).*

Water – 400 mbar			
Pressure difference (mbar)	Theoretical volume (nl)	Mean Volume (nl)	Standard deviation
2	430	467	3,7%
5	1075	952	4,2%
22	4790	4804	2,2%
107	24825	25285	1,5%

PBS – 400 mbar			
Pressure difference (mbar)	Theoretical volume (nl)	Mean Volume (nl)	Standard deviation
5	1075	1077	4,6%
107	24825	24596	0,7%

These results prove the capacity of the proposed sensor controlled system to work with different liquids and a large range of volumes without calibration or any change of the setup. Simply, the measurement of the pressure drop by the applied sensor allows for addressing the whole volume range. The dispense time of course varies along with the volume as well as with the viscosity. In our experiments the dispense time was between 5 ms for 500 nl and 250 ms for the 25  $\mu$ l.

## Optimization potential

One limitation of the presented approach is the large actuation pressure required, in order to obtain clean and precise droplet break-up for all dispensed volumes in the considered range. In contrast to this, the pressure drop needed to address the sub-microliter range is really small. Therefore, a pressure sensor with high burst pressure and large dynamic range is required, if the addressable volume range is to be increased.

The trapped gas volume can also be subject to optimization: A small volume will allow a more precise control in the sub-microliter range, but then will prevent to dispense large quantities in a one-step.

However, within this frame, the presented setup can be easily adapted to different user requirements in terms of volume range by simply selecting an appropriate gas volume and corresponding sensor type. Furthermore, the control algorithm could be further refined to take also dynamic effects neglected in equation (1) into account. Such dynamic flow effects during jet ejection might be the cause for the reduced accuracy of PBS at low volume (cf. Table 2).

Two other environmental limitations of the system exist due to its dependence to the Boyle-Mariotte law. First important changes of laboratory temperature during the use of the system will lead to inaccurate and imprecise dispensing. Second the solubility of air in water is increased by 40% when the pressure is increased by 400mbar. If the system is used over a long period of time, the total gas volume  $V_{\text{gas}}$  and the dispensed volume will both become smaller as expected.

## CONCLUSION AND OUTLOOK

The presented system demonstrates the feasibility and good performances of a non-contact normally closed and pressure regulated smart dispensing system to deliver small aliquots of different liquids without calibration. Future work will be dedicated to the improvement of this system to obtain better accuracy and precision and to cover efficiently an extended range of viscosities and volumes. This may include a better pressure sensor allowing the measurement of larger pressures and also a better precision. Such modifications can help to address the briefly described optimization potential of this dispensing technology.

## ACKNOWLEDGMENT

The authors gratefully acknowledge financial support from the German Federal Ministry for Science and Education (BMBF) through the project “Smart Reagent Dosage” (SPK 16SV5119).

## REFERENCES:

- [1] R. Bosse et al. “Miniaturizing screening: how low can we go today?” *Drug Discovery Today*, 42-47, 2000.
- [2] J. Woelcke and D. Ullmann, “Miniaturized HTS technologies – uHTS2”, *Drug Discovery Today*, 6, 637-646, 2001.
- [3] D. Rose “Microfluidic Technologies and Instrumentation for Printing DNA Microarrays. Microarray Biochip Technology. Eaton Publishing, 2000:35 16
- [4] D. Liang, et al, “Novel gravimetric calibration Method for nano liter liquid handling devices”, *Proc. MFHS Conference*, 2012

**A CALIBRATION-FREE, DISPOSABLE, NON-CONTACT  
REAGENT DOSING CARTRIDGE FOR THE SUB- $\mu$ L RANGE***S. Bammesberger<sup>1</sup>, A. Ernst<sup>1,2</sup>, L. Tanguy<sup>1</sup>, R. Zengerle<sup>1,3</sup> and P. Koltay<sup>1,2</sup>*<sup>1</sup> University of Freiburg, IMTEK - Department of Microsystems Engineering, Freiburg, Germany<sup>2</sup> Biofluidix, GmbH, Georges-Koehler-Allee 103, 79110 Freiburg, Germany<sup>3</sup> HSG-IMIT - Institut für Mikro- und Informationstechnik, Freiburg, Germany**ABSTRACT**

We have developed a prototype instrument for the sub- $\mu$ l range which is calibration-free, i.e. it is able to dispense diverse biochemical reagents without the need for adjustment of dispensing parameters with respect to the different rheological properties (viscosity range: 1.03 to 16.98 mPas, surface tension: 30.49 to 70.83 mN/m). The positive displacement technology is non-contact (i.e. carry-over free per design) and disposable (i.e. no washing procedures are necessary). Aliquots in the sub- $\mu$ l range are dispensed with a high degree of automation, precision ( $CV < 2.0\%$  at 1  $\mu$ l) and accuracy (typical accuracy  $< 4.0\%$ ). A capacitive sensor provides online process control.

**KEYWORDS**

Non-contact dispensing, calibration-free, low-cost, disposable, positive displacement, online process control, capacitive droplet sensor, liquid handling, cartridge

**INTRODUCTION**

Dispensing systems for drug discovery or in-vitro diagnostics applications are facing diverse and challenging requirements [1]: target volumes are decreased down to the sub- $\mu$ l range, a diverse portfolio of reagents exhibits strongly varying rheological properties and potential error sources like cross-contamination must be prevented completely.

To address these challenges, we have developed a non-contact dispensing system which is capable of dispensing liquids with varying rheological properties (viscosity 1.03 to 16.98 mPas and surface tension 30.49 to 70.83 mN/m) without requiring to adjust its dispensing parameters. The dispensing cartridge's design is adapted to common polymer syringes which can be used as disposables rendering elaborate washing procedures obsolete.

**DESIGN**  
**Cartridge**

The cartridge (70 x 30 x 111 mm), shown in Fig. 1, holds up to three commercial low-cost polymer syringes which function as reservoirs for the reagents. Each syringe reservoir is sealed by a polymer piston. A specially developed low-cost tip comprising a

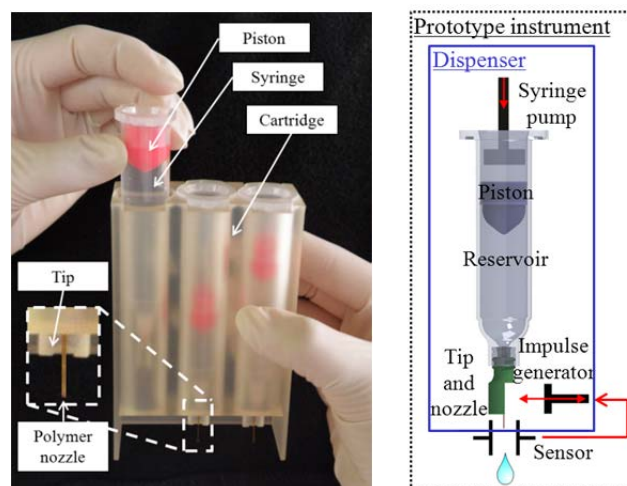


Figure 1: Left: Photograph of the cartridge containing three 10 ml syringes connected to a polymer nozzle each. Right: Sketch depicting the functional elements of one dispensing channel.

polymer nozzle (length 18 mm, diameter 500  $\mu$ m) is connected to the outlet of the syringe by a standard Luer Lock thread. All components feature an injection-moldable design to allow for low-cost mass fabrication. The tip and the cartridge are currently fabricated by 3D printing (material "Visijet EX 200") to realize the prototype instrument.

**Prototype instrument**

The main components of the prototype instrument (239.5 x 282.5 x 442.5 mm) are a syringe pump, a piezoelectric impulse generator and a capacitive sensor (see Fig. 1, right sketch).

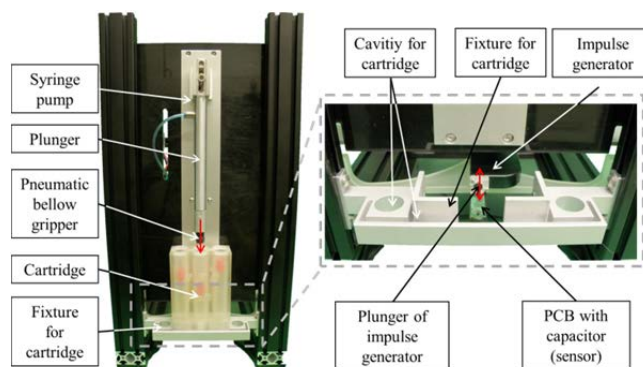


Figure 2: Left: prototype instrument with the inserted cartridge. Right: Close-up of the fixture for the cartridge, the impulse generator and the sensor.



For driving the pistons of the syringes a neMESYS® syringe pump from Cetoni GmbH, Germany is used. The specified positioning accuracy of 70 nm corresponds to a minimum change of volume of e.g. 13  $\mu$ l if 10 ml Optimum® syringes from Nordson EFD, Germany are used as shown in Fig. 1. In this configuration the maximum flow rate of liquid is 1.19 ml/s.

In order to prevent the displaced liquid to remain attached to the nozzle by surface tension, an impulse generator is applied for liquid release. Therefore, a modified PipeJet™ P9 dispenser from BioFluidix GmbH, Germany [2] is used to introduce mechanical impulses into the liquid by hitting the polymer nozzle with a small piston close to the nozzle.

Both actuators together, the syringe pump and the impulse generator, form the dispenser or actuation mechanism of the prototype instrument as depicted in Fig. 1. Prior to the dispensing process, the cartridge is placed manually into the prototype system and connected automatically with the dispenser: The syringe pump grips the piston with a pneumatic bellow gripper and the impulse generator is engaged with the polymer nozzle by the movement of a pneumatic linear stage.

In order to monitor the liquid meniscus at the nozzle, a capacitive sensor, developed by Ernst et al. [3] is applied. It uses a standard PCB through connection (via) with a diameter of 3 mm as a sensing capacitor. The polymer nozzle is positioned concentrically inside this capacitor when the cartridge is placed into the prototype instrument. To prevent the contamination of the sensor by dispensed droplets, the capacitor surrounds the nozzle approximately 2 mm above the nozzle's orifice. The sensor is used to detect the presence of a pending droplet at the nozzle orifice.

## WORKING PRINCIPLE

To perform a dispensing process, the syringe pump positively displaces the target volume by moving the piston into the syringe. Since this cannot be accomplished with high velocity to attain a large Weber number required for liquid break-off, part of the liquid forms a pending droplet at the orifice. After a short idle time (e.g. 0.5 s), waiting for the droplet to fully develop, the impulse generator hits the polymer nozzle close to the orifice to provide sufficient momentum to the pending droplet to detach it.

The capacitive sensor at the nozzle checks whether the droplet tear-off was successful and therefore provides a non-contact, online process control. If the droplet tear-off failed, the parameters of the impulse generator are re-adjusted automatically to provide more energy and re-triggered subsequently.

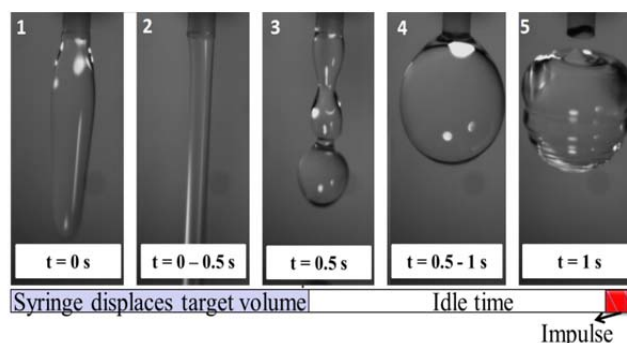


Figure 3. Phases of the dispensing process. The syringe pump positively displaces the target volume (picture 1-3 and blue time beam at the bottom). After a waiting time of 0.5 s (4) a pending droplet forms at the orifice and is knocked off (5) by the impulse generator (red beam).

The total dispensing process, shown in Fig. 3, typically takes 1 to 2 s depending on the target volume and the rheological properties of the liquid. The dispenser and the sensor are not contaminated by the liquid during the dispensing process.

## EXPERIMENTS

In order to evaluate the performance of the dispenser and the capacitive sensor, each sub-system is characterized individually in the following section.

### Dispenser

The basic function of the dispenser has been characterized for a target volume range of 0.5 to 100  $\mu$ l with a simplified early stage set-up (see Fig. 4) not yet featuring the capacitive sensor and the automatic engagement. Standard Combitip Plus® 2.5 ml syringes from Eppendorf, Germany (for target volumes < 5  $\mu$ l) and Plastibrand® 25 ml from Brand, Germany (for target volumes  $\geq$  5  $\mu$ l) were utilized.

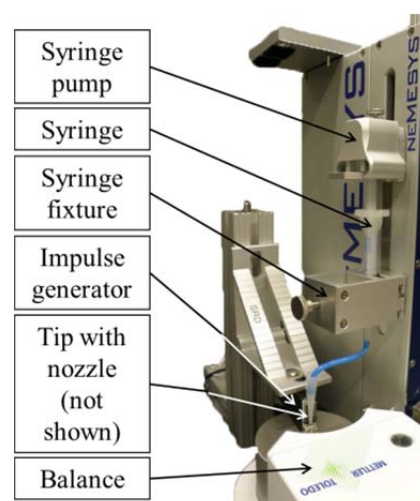


Figure 4. Experimental set-up of the dispenser with the syringe pump and the impulse generator.

The dispensed volume was measured gravimetrically using the measurement method described by Liang et al. [4]. For each volume 24 individual measurements were averaged and the corresponding precision (i.e. coefficient of variation (CV)) and accuracy (i.e. relative deviation from the target volume (Acc)) were evaluated as described in more detail in [5].

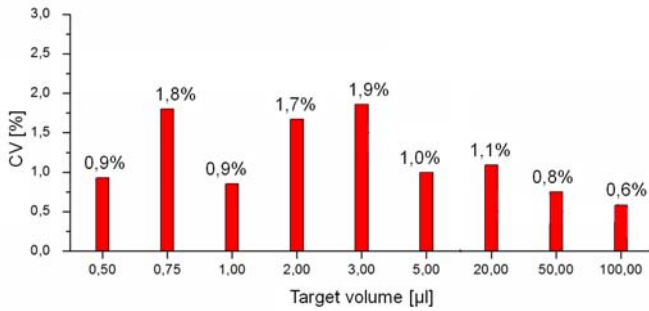


Figure 5. The coefficient of variation (CV) for target volumes of 0.50 µl to 100.00 µl for water.

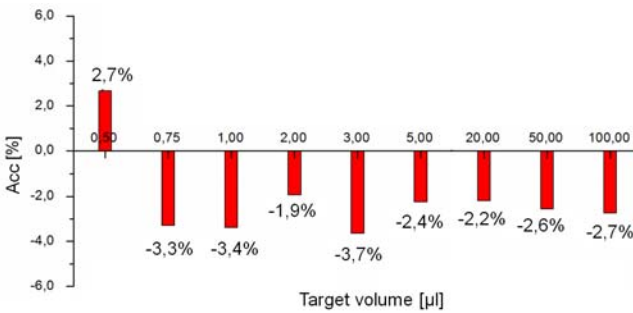


Figure 6. The accuracy (i.e. the relative deviation from the target volume) for target volumes of 0.50 µl to 100.00 µl for water.

Fig. 5 and 6 show the dispensing performance for water in the volume range of 0.5 to 100 µl. The CV ranged between 0.8% at 50 µl to 1.9% at 3 µl. The CV at 0.5 µl was 0.9%. Overall, the dispensing performance with water was very precise. The volumetric accuracy was better than  $\pm 4.0\%$  for the entire volume range, indicating also a very accurate dispensing performance.

To evaluate the dispensing performance for liquids with different viscosities and surface tension than water, exemplary target volumes of 1 and 25 µl were characterized with the test liquids presented in [6] and displayed in Fig. 7. The actuation parameters of syringe and impulse generator were not changed for any liquid, i.e. no calibration was performed. The dispensing performance was as precise for the test liquids as for water, with a CV below 2.0% for all liquids. The accuracy ranged in-between  $+0.6\%$  at 25 µl for liquid B to  $-8.8\%$  at 1 µl for liquid A.

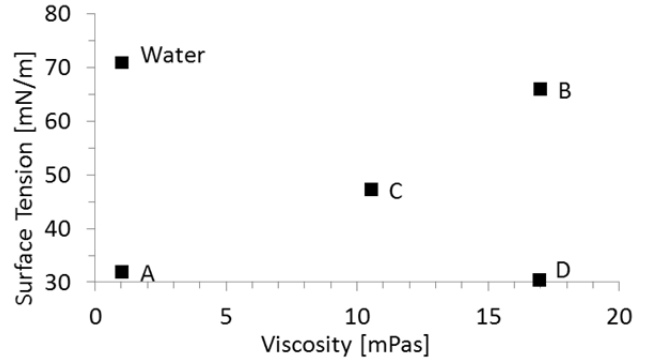


Figure 7. Rheological properties of the tested liquids at 20°C. The test liquids, proposed by Losleben et al. [6], cover the typical range of viscosities (1.03 to 16.98 mPas) and surface tensions (30.49 to 70.83 mN/m) of reagents used in in-vitro diagnostics.

Table 1: The coefficient of variation (CV) and the accuracy (Acc) obtained with the test liquids.

		Water	A	B	C	D
CV	1 µl	0.9%	1.9%	1.8%	1.8%	1.3%
Acc	1 µl	-3.4%	-8.8%	-1.0%	0.3%	-1.3%
CV	25 µl	2.1%	3.7%	0.7%	3.4%	0.7%
Acc	25 µl	+0.5%	-0.9%	+0.6%	-1.2%	-0.3%

### Capacitive sensor

Fig. 8 shows two sensor readouts of five successive dispenses of 1 µl for water and test liquid B. The rising edge (at e.g.  $t_1$ ,  $t_3$ , and  $t_5$ ) depicts the point of time when the syringe pump starts to pump the target volume (corresponding to picture 1 of Fig. 3). The upper level of the sensor signal (e.g. S1 and S3) indicates the pending droplet corresponding to picture 4 in Fig. 3. When the impulse generator is triggered at e.g.  $t_2$ ,  $t_4$ , and  $t_6$  the droplet is detached (see also picture 5 in Fig. 3) and the sensor signal drops suddenly to the lower level. The dispensing time for each dispense was constantly  $\Delta t = 1.4$  s.

The difference between the two sensor signal levels for a 1 µl droplet was  $S1 - S2 \approx 0.29$  V for water or  $S3 - S4 \approx 0.17$  V for fluid B. As expected from theory, the sensor signal is different for liquids with different dielectric constants. This clearly indicates that the droplet tear-off can be detected and verified in real-time by the capacitive sensor for different liquids. The signal peak of 1.9 V at  $t_4$  for water can be explained by the piezoelectric actuation of the impulse generator that can induce spikes into the signal. These are detected only rarely due to the low sampling frequency of 0.1 kHz and the short pulse duration of the impulse generator.



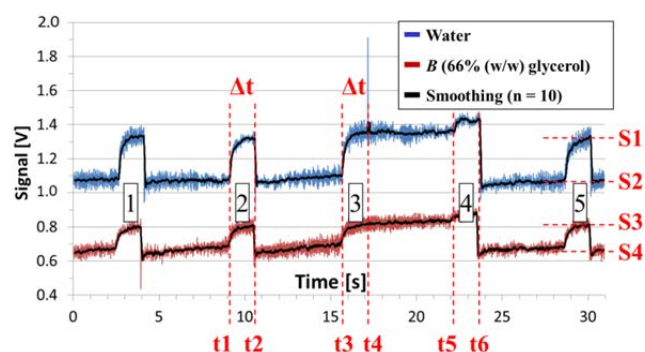


Figure 8. Sensor readout (sample rate 0.1 kHz) of the capacitive sensor of five dispenses of 1  $\mu$ l for water and fluid B. For dispense #3 a failure of the droplet tear-off was detected.

In order to challenge the droplet tear-off detection, the impulse generator's parameters were manipulated to prevent a successful droplet tear-off for dispense #3 at  $t_4$ . The obvious absence of the signal drop at  $t_4$  indicates a still pending droplet. At  $t_5$  a relatively small increase can be seen when the pending droplet's volume was increased from 1 to 2  $\mu$ l by the following actuation of the syringe pump. The subsequent impulse at  $t_5$  successfully removed the droplet finally.

Thus, a feedback loop is easily implemented which automatically increases the impulse generator's stroke and re-issues a trigger if the droplet tear-off was not successful in the first attempt. The effect of such feedback loop on the dispensing performance will be characterized by future experiments.

## CONCLUSION

The presented prototype of a novel positive displacement technology enables calibration-free dispensing of liquid aliquots in the sub- $\mu$ l range. All contaminated parts are made of polymers and are therefore fully disposable rendering elaborate washing procedures obsolete. Due to the non-contact dispensing process the liquid handling is carry-over free per design.

The dispensing performance was very precise (CV < 2.0% at 1  $\mu$ l) and accurate (accuracy -8.8% to +0.3% at 1  $\mu$ l) for test fluids with widely varying rheological properties (viscosity range: 1.03 to 16.98 mPas, surface tension: 30.49 to 70.83 mN/m), corresponding to typical values found for reagents used for in-vitro diagnostic applications. In addition to the good performance, the dispenser is calibration-free, i.e. the only input parameter the system is requiring is the target volume to be delivered independent of the respective liquid to be dispensed.

The capacitive sensor at the nozzle orifice enables an online process control for positive dispensing confirmation and additional safety. A failure of the

droplet tear-off is detectable by the sensor and an adjustment of the impulse generator parameters can be realized by feedback loop to correct for such incidences.

With the ability to hold up to three individual dispensing channels, each hosting a different liquid, the disposable cartridge is capable of performing most assays used within in-vitro diagnostic applications. Thus, the presented technology could be used for safe, low-cost and automated reagent handling in in-vitro diagnostic automation systems or for similar industrial applications.

## REFERENCES

- [1] D. A. Dunn, I. Feygin, Challenges and solutions to ultra-high-throughput screening assay miniaturization: submicroliter fluid handling, *Drug Discovery Today*, vol. 5, pp. 84-91, 2000
- [2] W. Streule, T. Lindemann, G. Birkle, R. Zengerle, P. Koltay, PipeJet: A Simple Disposable Dispenser for the Nano- and Microliter Range, *Journal of the Association for Laboratory Automation*, vol. 9, pp. 300-306, 2004
- [3] A. Ernst, W. Streule, N. Schmitt, R. Zengerle, P. Koltay, A capacitive sensor for non-contact nanoliter droplets, *Sensors and Actuators A: Physical*, vol. 153, pp. 57-63, 2009
- [4] D. Liang, C. Steinert, S. Bammesberger, L. Tanguy, A. Ernst, R. Zengerle, P. Koltay, Novel gravimetric measurement technique for quantitative volume calibration in the sub-microliter range, *Journal of Measurement Science and Technology (submitted)*, 2012
- [5] S. Bammesberger, A. Ernst, N. Losleben, L. Tanguy, R. Zengerle, P. Koltay, Quantitative characterization of non-contact microdispensing technologies for the sub-microliter range, *Drug Discovery Today (submitted)*, 2012
- [6] N. Losleben, P. Koltay, K. Zengerle, Publication is currently under preparation with a title still to be defined (Fluids modelling the range of viscosity, surface tension and density of in-vitro diagnostics reagents of a brand leader in the diagnostic sector), *Journal still to be defined*, 2012

## CONTACT

\* S.Bammesberger, stefan.bammesberger@imtek.de

## ADVANCED CAPILLARY SOFT VALVES FOR FLOW CONTROL IN SELF-DRIVEN MICROFLUIDICS

*M. Hitzbleck and E. Delamarche*

IBM Research GmbH, Rüschlikon, Switzerland

### ABSTRACT

We recently proposed capillary soft valves (CSVs) as a simple to implement, fabricate and actuate solution for stopping and inducing liquid flow inside a microchannel of a capillary-driven microfluidic chip. Here, we present a detailed insight into the working mechanism of CSVs and their applicability for stopping liquids having different surface tensions and wetting properties on surfaces. We furthermore introduce designs for advanced CSVs to minimize creeping of liquids in the corners of a microchannel and show CSVs having more than one inlet channel.

### KEYWORDS

Microfluidics, capillary system, stop valve, liquid control

### INTRODUCTION

Capillary-driven microfluidics allow for autonomous manipulation of micro- to nanoliters of samples and reagents in a precise manner. We earlier emphasized their benefits for point-of-care (POC) diagnostics with “one-step” immunoassays [1] and functional microfluidic elements such as reagent integrators [2]. In some more complex assays, controlled timing for dissolving reagents, heating or chemical reactions is critical. Therefore, many applications use valves for stopping and triggering liquid flow.[3] Devices used in POC applications should be simple to use with minimal actuation. Furthermore, chips with valves should ideally be easy to mass-manufacture. CSVs can stop capillary-driven flow at a precise location in a microfluidic chip and can resume liquid flow upon simple actuation.[4]

### RESULTS

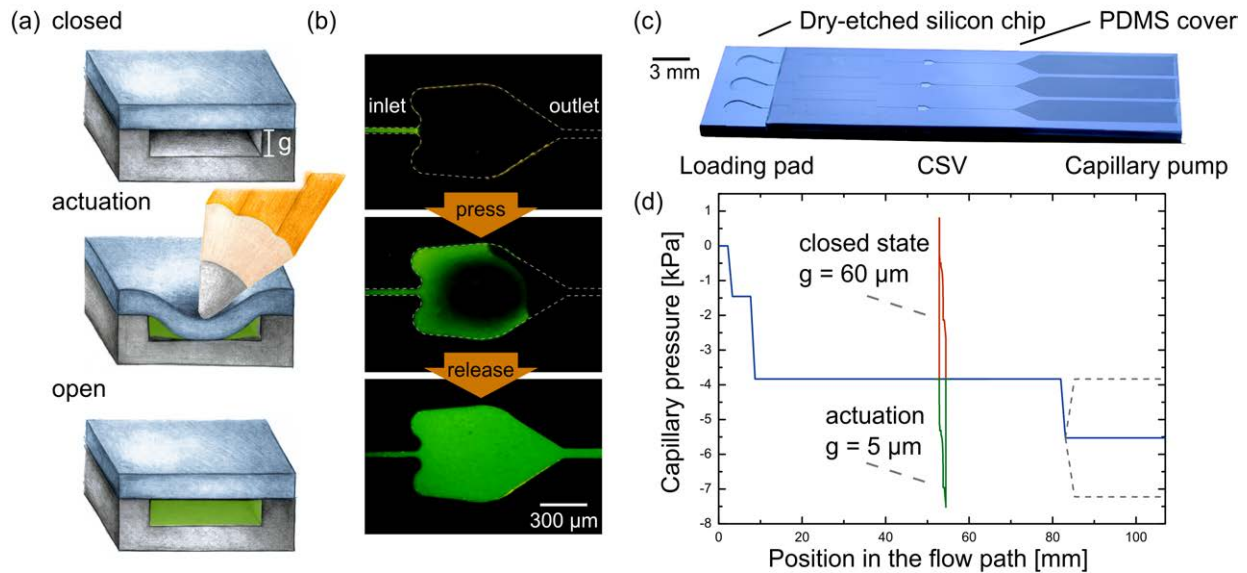
The working principle of a CSV is based on the fact that the wetting properties and dimensions of a microfluidic channel strongly influences its capillary pressure. A CSV consists of an abruptly expanding channel, which induces a barrier of capillary pressure and stops a liquid filling front at the inlet of the CSV. (Fig. 1a,b) Pressing the top of the CSV using, e.g. the tip of a pen, reduces the pressure barrier and the liquid can proceed.

CSVs are small (footprint < 0.6 mm<sup>2</sup>) and can be etched or molded together with other microstructures of the microfluidic chip. The chip is then sealed with a cover, which can be chosen to be slightly deformable such that it provides access for actuation of the CSVs on chip: CSVs are neutral in terms of fabrication complexity. (Fig. 1c)

The distribution of capillary pressure throughout the microfluidic network is key to the performance of a CSV. As demonstrated elsewhere, the capillary pressure can be calculated using the following equation [5]:

$$P_c = -\gamma \cdot \left( \frac{\cos(\theta_b) + \cos(\theta_t)}{d} + \frac{\cos(\theta_l) + \cos(\theta_r)}{w} \right) \quad (1)$$

where  $\gamma$  is the surface tension of the liquid,  $\theta_{b,t,l,r}$  are the advancing contact angles of the liquid on the bottom, top, left and right wall, respectively, and  $d$ ,  $w$  are the width and depths of the microchannel, respectively.



**Figure 1:** CSVs. (a) Working principle of a CSV. (b) Fluorescence micrographs of a solution filling a CSV before, during and after actuation of the CSV. (c) Implementation of CSVs into microfluidic networks, which are dry-etched into a silicon chip and sealed with a PDMS cover. (d) Simulation of the capillary pressure throughout the network showing the pressure barrier formed by the CSV in the closed state and during actuation.

A simulation of the capillary pressure along a microchannel in the silicon chip of figure 1c, is shown in figure 1d. In the closed state the capillary pressure at the inlet of the CSV, increases to positive pressures. This is due to the abruptly expanding microchannel, which induces an increased apparent contact angle as the wall bends away from the meniscus. During actuation the top of the CSV is pressed into the channel and reduces the depth of the channel. The capillary pressure is now dominated by the first term of equation (1). In the simulation presented here we used an average channel height of the CSV to give an estimation of the capillary pressure in the actuated state. A more adequate model for a microchannel would assume two parallel triangular microchannels along the curved outline of the CSV (see Fig. 1b, actuation). However, the actuation of a CSV takes a few seconds and can be released as soon as the meniscus has entered the outlet channel. From there on, the liquid flow can be again adequately described using equation (1). We define the maximum capillary pressure of a CSV in the closed state as barrier height of the CSV. In the following, we will discuss the influence of the barrier height in the performance of a CSV.

The wetting behavior of a liquid on a surface, is expressed by the advancing contact angle  $\theta$ . The contact angle strongly influences the capillary filling of a microchannel, as well as the characteristics of a CSV. Figure 2 shows experimental results of the filling of liquids having different surface tensions in CSVs on microfluidic chips with different surface chemistries. The simulated height of the pressure barrier of the CSV is presented as black line. CSVs having contact angles above  $45^\circ$  ( $\cos(\theta) \leq 0.7$ ) were able to stop a liquid for at least 5 minutes (red rectangles). For intermediate contact angles ( $0.7 \leq \cos(\theta) \leq 0.9$ ) CSVs act as delay valve by slowing down a liquid and letting it pass after less than 5 minutes without actuation of the CSV (gray circles). CSVs with contact angles below  $\sim 25^\circ$  ( $\cos(\theta) > 0.9$ ) mostly fail during filling because liquid creeps along the corners of the CSV and wets the outlet before the entire CSV can be filled (blue triangles).

The simulated capillary pressure supports the classification of stop valves as compared to delay valves. A characteristic of a CSV is the low aspect ratio ( $d/w \ll 1$ ). In this constellation, the capillary pressure is dominated by the first term of equation (1) and can reach positive values when the silicon

chip is not too hydrophilic and a slightly hydrophobic cover is used. Thus, we classify a CSV to be a stop valve when the capillary pressure barrier of the CSV reaches positive values and therefore repels the liquid at the inlet of the CSV.

Furthermore, figure 2 visualizes the fact, that liquids having a higher surface tension than water (6M NaCl,  $\gamma_{\text{NaCl}}=83 \text{ mJ}\cdot\text{m}^{-2}$ ;  $\text{H}_2\text{O}$ ,  $\gamma_{\text{H}_2\text{O}}=72 \text{ mJ}\cdot\text{m}^{-2}$ ) are more easily stopped in a CSV. There are two main reasons for this: a) a liquid of high surface tension tend to have a higher contact angle on a surface and b) its capillary pressure varies stronger for different contact angles as compared to a liquid having a lower surface tension. Therefore, liquids with low surface tension, such as those containing surfactants (e.g. 0.6% PBS Tween20,  $\gamma_{\text{Tween}} = 37 \text{ mJ}\cdot\text{m}^{-2}$ ) require CSVs having a more hydrophobic surface chemistry and are usually more difficult to handle as they tend to creep along the corners of wide microchannels.

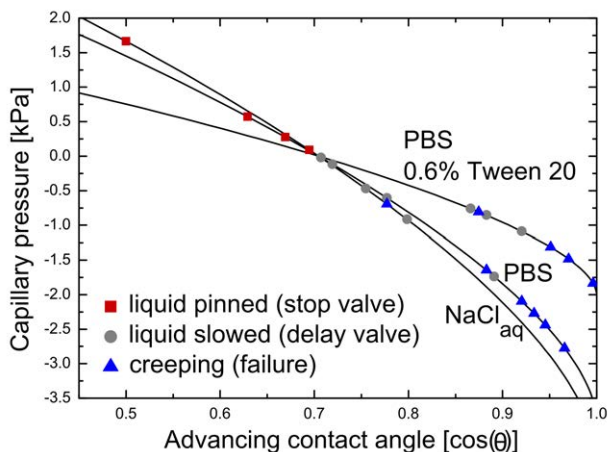


Figure 2. Influence of the advancing contact angle of a liquid filling a microfluidic chip on the performance of the CSV. Several different surface chemistries for the microfluidic chips and liquids having different surface tensions were tested. The capillary pressure barrier of the CSV was simulated and related to the filling behavior of liquids observed experimentally.

We therefore developed advanced CSVs having additional design features to increase the reliability and usability of CSVs for a large variety of liquids. Figure 3a shows CSVs having indentations that delay help to prevent creeping of liquids. Arrays of pillars can hold back the liquid meniscus via a pinning effect (Fig. 3b).[6] Furthermore, the use of half-rounded microchannels, which were molded from reflowed photoresist, reduced creeping significantly. CSVs can have multiple inlets (Fig. 3c,d) which can be useful to synchronize streams of liquid inside microfluidic channels or to define the starting time of their intermixing. Finally, CSVs can be combined in series or parallel in microfluidic networks to allow for more complex flow control.

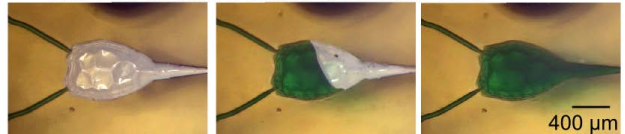
(a) Single-inlet CSV in silicon with indentations



(b) Single-inlet CSV in silicon with pillars



(c) Dual-inlet CSV in epoxy resin with half-rounded channel cross-section



(d) Multi-inlet CSVs in epoxy resin (before unmolding)

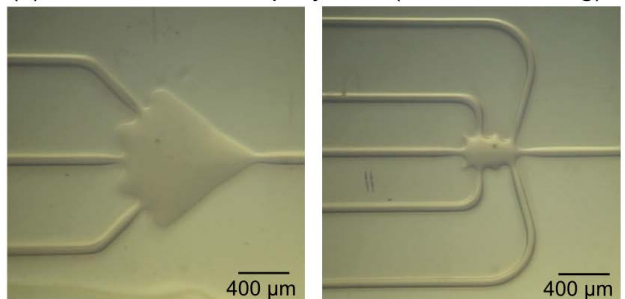


Figure 3. Advanced CSVs and combination thereof. Approaches to prevent creeping of liquids along corners using indentations (a) or pillars (b). Dual- (c) and multi-inlet CSVs (d) in epoxy resin with half-circular channel cross-section.



## EXPERIMENTAL

Microfluidic chips in silicon were produced using optical lithography (photoresist AZ6612, thickness  $\sim 2\ \mu\text{m}$ , exposed with ultraviolet light through a quartz-chrome mask and developed in AZ 400k, diluted 1:4 in  $\text{H}_2\text{O}$ ) and deep reactive ion etching (AMS-200SE, Alcatel Micro Machining Systems). The chips were then cleaned in an oxygen plasma (300 W, 120 s). The surface chemistry was prepared by immersion of the chip for 30 min into solutions of methacryloxysilane, 3-(2-aminoethylamino)propyltrimethoxysilane, glycidyloxypropyltrimethoxysilane, allyltrimethoxysilane, PEG-silane (each 1% v/v in ethanol) or Pluronic<sup>®</sup> (1% w/v in  $\text{H}_2\text{O}$ ) or combinations thereof. Prior to use, chips were covered with a layer of PDMS (Sylgard 184, Dow Corning) which has an advancing contact angle for water of  $110 \pm 5^\circ$ . Plastic chips having half-circular channel cross-sections were molded from reflowed photoresist (AZ40XT, thickness  $\sim 50\ \mu\text{m}$ ), treated with an air-based plasma (100 W, 30 s) and immersed into a solution of Pluronic<sup>®</sup> for 30 min.

## CONCLUSION

CSVs enable precise timing for dissolving and mixing reagents, binding of analytes to receptors, and rinsing, which are all critical for diagnostic tests. CSVs have an intrinsic venting mechanism which is essential for capillary-driven microfluidics wherein a filling liquid needs to displace air. CSVs are single-use valves, which do not require power before and after actuation, and can be triggered within seconds. We believe that advanced CSVs add important control features to self-driven microfluidics and that a profound understanding of the working mechanism of CSVs is crucial for the development of high-performance microfluidic chips.

## ACKNOWLEDGMENTS

We are grateful to Ute Drechsler, Robert Lovchik and Govind Kaigala for discussions and to Michel Despont, Walter Riess and Janos Vörös (ETHZ) for their continuous support.

## REFERENCES

- [1] L. Gervais and E. Delamarche, “Toward one-step point-of-care immunodiagnostics using capillary-driven microfluidics and PDMS substrates”, *Lab Chip*, **9**, pp.3330–3337, 2009.
- [2] M. Hitzbleck, L. Gervais, and E. Delamarche, “Controlled release of reagents in capillary-driven microfluidics using reagent integrators”, *Lab Chip*, **11**, pp.2680-2685, 2011.
- [3] K. W. Oh and C. H. Ahn, “A review of microvalves”, *J. Micromech. Microeng.*, **16**, pp.R13-R35, 2006.
- [4] M. Hitzbleck, L. Avrain, V. Smekens, R. D. Lovchik, P. Mertens and E. Delamarche, “Capillary soft valves for microfluidics”, *Lab Chip*, **12**, pp.1972-1978, 2012.
- [5] M. Zimmermann, H. Schmid, P. Hunziker and E. Delamarche, “Capillary pumps for autonomous capillary systems”, *Lab Chip*, **7**, pp. 119-125, 2011.
- [6] H. Kusumaatmaja, C. M. Pooley, S. Girardo, D. Pisignano and J. M. Yeomans, “Capillary filling in patterned microchannels”, *Phys. Rev. E*, **77**, pp. 067301, 2008.

## CONTACT

E. Delamarche [emd@zurich.ibm.com](mailto:emd@zurich.ibm.com)

## A FULLY INTEGRATED ELECTROCHEMICAL PUMP FOR MICROFLUIDIC CHIP SYSTEMS

P. Meyer<sup>1</sup>, S. Larbi<sup>1</sup>, S. Hakenberg<sup>1</sup>, C. Hermann<sup>1</sup>, G. Dame<sup>1</sup> and G.A. Urban<sup>1</sup>

<sup>1</sup> Laboratory for Sensors, Department for Microsystem Engineering (IMTEK), University of Freiburg, Georges-Köhler-Allee 103, 79110 Freiburg, Germany

Herewith an electrochemical pump is described developed for integration into a dry film-based microfluidic lab-on-a-chip system without additional fabrication steps. A contamination free transport of media between different microcompartments in a lab-on-a-chip system is realized with phaseguide-controlled handling of gas bubbles<sup>1</sup>.

The majority of recently published pressure-driven microsystems are using external pumps for fluid actuation. These systems tend to be “chip-in-a-lab” systems rather than “lab-on-a-chip” systems. Other integrated pump systems use complicated and cumbersome fabrication protocols<sup>2-4</sup>.

So far no system is available that on the one hand can be completely integrated into the chip system and make use of standard processes and on the other hand guarantees the transport of media in a reliably, accurately and contamination-free way.

The described pump is flexible in design and performance thus suitable for integration into Ordyl-based or similar lab-on-a-chip systems<sup>5</sup>. The actuation principle is the electrolytic generation of gas by decomposition of water. A continuous formation of gas bubbles produces pressure in the actuation chamber thus pumping liquid from a sample chamber into a target chamber (see fig. 1). The microfluidic system is driven at low voltage levels (<12 V) via integrated electrodes. To achieve contamination-free pumping, an air bubble separates the actuation fluid and the pumped sample liquid. A reproducible and accurate liquid transport from one chamber to another is demonstrated under constant power consumption. Phaseguides<sup>5</sup> are integrated for a robust and reproducible liquid handling during the pumping process. In this way microfluidic problems related to filling and emptying of the micro-chambers are solved. Furthermore it stabilizes the air bubble used to prevent contamination and mixing of liquids. An actuated chip with the integrated pump can be seen in figure 2.

The fabrication method is a dry film based resist technology with subsequent direct wafer bonding illustrated in figure 4. First Ti/Pt electrodes are vapour deposited onto a Pyrex wafer. The used dry film resist is 30 µm thick Ordyl SY330. The first laminated layer forms the phaseguide-based microfluidic substructure. Three further layers form the channel and chamber walls.

The performance of the pump is characterized in figure 3 at constant supply currents in the range of 0.5 mA – 6 mA which results in flow rates from 1 µl/min up to 50 µl/min. Standard deviation remains below 10%.

Word Count: 382

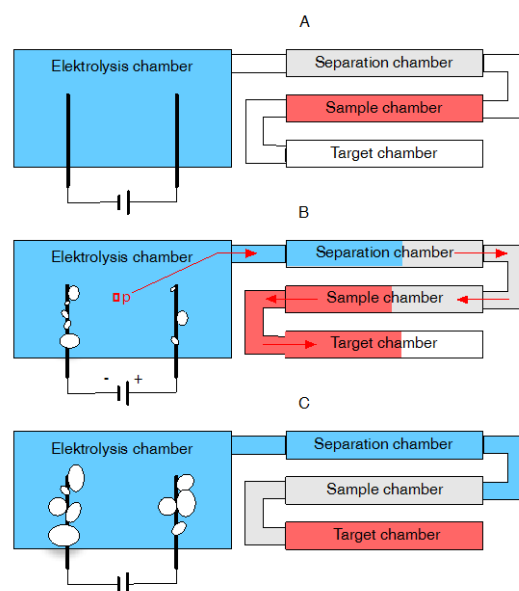


Figure 1: Working principle A) sample chamber is filled fluid while air remains in the separation chamber B) & C) electrolytic pressure moves sample into target chamber

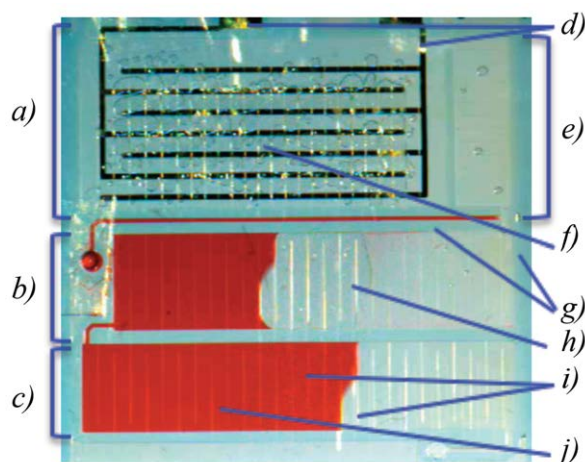


Figure 2. Photo of the actuated pump in a microfluidic chip a) electrolysis chamber b) sample chamber c) target chamber d) platinum electrodes e) separation chamber f) electrolytic gas g) chamber walls h) air bubble to prevent contamination i) phaseguides j) sample fluid

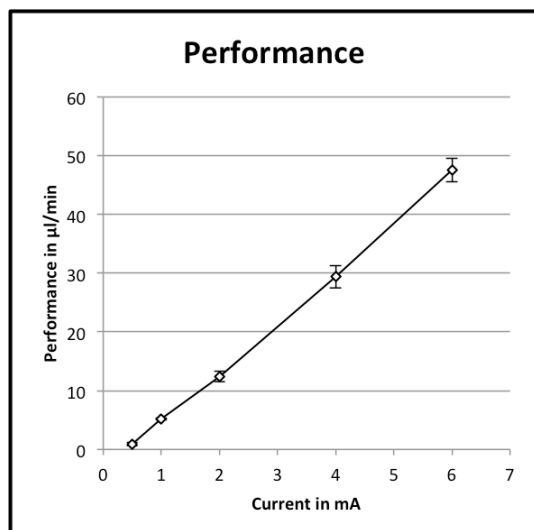


Figure 3. Performance of the pump at several currents in  $\mu\text{l}/\text{min}$

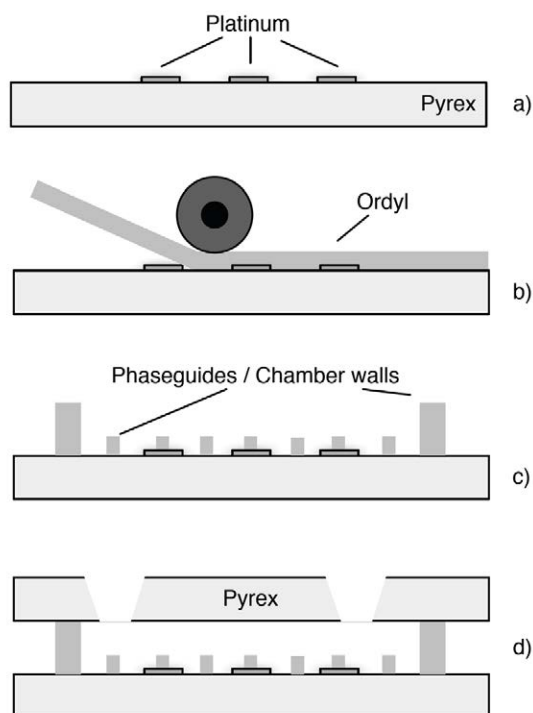


Figure 4. Fabrication steps: a) Lithography process on a Pyrex substrate for depositing platinum electrodes. b) Lamination and exposure of the first dry film resist layer provides the phaseguide structures. The next three layers provide channel and chamber walls. c) Development of the fluidic network d) Direct wafer bonding of a second Pyrex substrate with drilled holes for in- and outlets

## REFERENCES:

1. P. Vulto, S. Podszun, P. Meyer and G. A. Urban, "Phaseguide patterns for advanced liquid handling in Lab-on-a-Chip systems", *Solid-State Sensors, Actuators and Microsystems Conference, 2009. TRANSDUCERS 2009. International, 2009*, 409-412.
2. D. O'Keefe, C. O'Herlihy, Y. Gross and J. G. Kelly, "Patient-controlled analgesia using a miniature electrochemically driven infusion pump", *Br. J. Anaesth.*, 1994, **73**, 843-846.
3. V. I. Furdui, J. K. Kariuki and D. J. Harrison, "Microfabricated electrolysis pump system for isolating rare cells in blood", *J. Micromechanics and Microengineering*, 2003, **13**, 164-170.
4. J. W. Munyan, H. V. Fuentes, M. Draper, R. T. Kelly and A. T. Woolley, "Electrically actuated, pressure-driven microfluidic pumps", *Lab on a Chip*, 2003, **3**, 217-220.
5. P. Vulto, S. Podszun, P. Meyer, C. Hermann, A. Manz and G. A. Urban, "Phaseguides: a paradigm shift in microfluidic priming and emptying", *Lab Chip*, 2010, **11**, 1596-1602.

## 2. Actuators

(please choose category from list)

## Poster or Presentation

(if requesting poster)

### PHASEGUIDES: A PARADIGM SHIFT IN MICROFLUIDIC LIQUID HANDLING

*Paul Vulto<sup>1,2,3</sup>, Sebastiaan J. Trietsch<sup>1,2</sup>, Jos Joore<sup>3</sup> and Thomas Hankemeier<sup>1,2</sup>*

<sup>1</sup> Division of Analytical Biosciences, Leiden/Amsterdam Centre for Drug Research, Leiden University, the Netherlands

<sup>2</sup> Netherlands Metabolomics Centre, the Netherlands

<sup>3</sup> Mimetas BV, the Netherlands

The complexity of conventionally designed microfluidic chips is limited by the ability to properly prime them and eventually recover their content. Particularly non-hydrophilic materials, such as most plastics in their native state, give rise to filling complications, such as air bubble trapping. Complex surface treatments are typically needed to make the surface more hydrophilic and the geometry is compromised to accommodate complete filling.

Recently, we introduced phaseguide technology that gives complete control over filling and emptying of any type of microfluidic structures, independent of the chamber and channel geometry [1]. Phaseguide design adds a new level of engineering complexity to microfluidics that enables to create simplest possible, black box type, microfluidic chips. Geometries are not compromised by handling issues anymore and become fully supportive to the functionality of the chip.

Phaseguides are patterned capillary pressure barriers that induce the liquid-air meniscus to align itself with the boundary before jumping over and aligning with the next phaseguide (see figure 1a and b). Typical phaseguiding behavior is based on the meniscus-pinning effect (see Fig. 1c). For phaseguides patterned in monolithic chips having side wall profiles of 90°, efficient pinning occurs for contact angles that are larger than 45°, which is the case for most plastic chips.

We applied phaseguides for a range of applications including an automated RNA extraction chip [2], cell sorting [3] and enrichment chip [4, 5] and ultimately a massive parallel concept for cell and tissue culturing. Table 1 summarizes operations and applications that have been developed so far.

Phaseguides are currently used to mimic hundreds of micro-organs on a chip, with minuscule channels that serve as blood vessels. These organs-on-a-chip can be used to determine the efficacy and toxic side-effects of new medicines better and faster. They provide a unique, novel bridge between traditional laboratory tests and clinical testing in patients. Showing closer resemblance to humans, they have the potential to revolutionise therapeutic drug development and save many laboratory animals at the same time. Figure 2 shows 48 liver tissues on-a-chip based on a microtiter plate footprint. The 3D cultured HepG2 hepatocytes showed a dose-dependent response to the known hepatotoxin Diclofenac. Currently, MIMETAS develops its products to help pharmaceutical companies make better medicines at lower costs. Ultimately, MIMETAS products will be used to select the best therapy for individual patients, based on direct testing of drugs on diseased cells, so-called personalised medicine.

Phaseguide technology enables complex liquid handling using no more than a standard pipet. This ease of use will enable the transformation of microfluidics as an expert application into a tool for routine use. Applications that have been demonstrated to date are only the very first steps taken in these directions, leaving the true potential of phaseguide design still largely unexplored. Phaseguides will prove a leap forward towards more simple, flexible and reliable microfluidic systems.

**Word Count: 564**



2. Actuators

(please choose category from list)

Poster or Presentation

(if requesting poster)

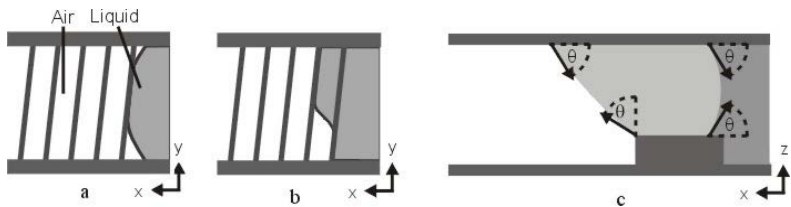

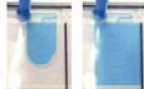
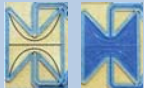




Figure1. Principle of phaseguiding: (a) An advancing liquid aligns itself along a phaseguide before (b) jumping over. (c) Meniscus pinning effect makes the phaseguide act as a pressure barrier. Complete pinning occurs for vertical bumps and contact angles larger than 45°.

Table 1. Overview of phaseguide operations developed so far and their envisioned applications.

Operation		Application
Selective buffer recovery [3]		Particle & cell separation
Gel patterning [4]		Electrophoresis, salt bridges
Complex and square chamber filling & recovery [1]		Microarrays, inkjet printing
Selective phaseguide overflow [1]		Multi-reagent assays
Monolithic chip filling		Mass production of low cost chips

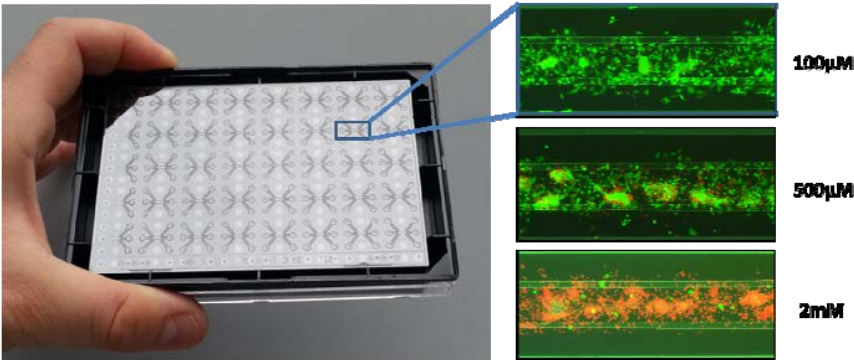


Figure 2. (left) A prototype of the Mimetas three-dimensional culture plate for 35 experiments. Plates of the same size for thousands of experiments are under development. (right) Cells (middle channel) growing inside a Mimetas three-dimensional culture plate after 48 hours exposure to the hepatotoxin Diclofenac.

REFERENCES:

1. "Phaseguides: a paradigm shift in microfluidic priming and emptying," P. Vulto et al. Lab Chip, **11**, 1596-1602 (2011)
2. "Selective sample recovery of DEP-separated cells and particles by phaseguide-controlled laminar flow," P. Vulto et al., J. Micromech. Microeng., **16**, 1847–1853, (2006)
3. "A microfluidic approach for high efficiency extraction of low molecular weight RNA", P. Vulto et al., Lab Chip, **10**, 610-616, (2010)
4. "Enrichment of viable bacteria in a micro-volume by free-flow electrophoresis", S. Podszun et al. Lab Chip **12** (3), 451-457
5. "Microfluidic concentration of bacteria by on-chip electrophoresis", D. Puchberger-Enengl et al., Biomicrofluidics **5** (4), 044111-044111-10

## NEW INSIGHTS GAINED FROM MAKING AND BREAKING EMULSIONS IN MICROFLUIDIC DEVICES

*Karin Schroën<sup>1</sup>, Maartje Steegmans<sup>1</sup>, Koen van Dijke<sup>1</sup>, Thomas Krebs<sup>1,2</sup> and Remko Boom<sup>1</sup>*

<sup>1</sup> Wageningen University, Department of Agrotechnology and Food Sciences, Food Process Engineering group, Bomenweg 2, 6703 HD The Netherlands.

<sup>2</sup> Institute for Sustainable Process Technology, Groen van Prinstererlaan 37, 3818 JN Amersfoort.

Emulsions are relevant in many different fields, including chemistry, paint and coatings, personal care, pharmaceuticals, but also in food. Specifically in food emulsions, the behavior of emulsifiers and stabilizers can be very complex, and a better understanding of droplet formation and coalescence is of paramount importance to design products that are stable and have appreciable shelf-life.

Preparation of emulsions can be carried out in many different ways ranging from the classic high pressure homogenizer to microfluidic systems. Examples of the latter are the T-junctions [e.g. 1], and flow focusing devices [2] that use shear force to form droplets, or microchannels that use spontaneous droplet formation due to changes in Laplace pressure [e.g. 3]. All these devices are known to produce monodisperse droplets, which is known to increase emulsion stability; however, for large scale production it is still a mayor challenge to operate many of these devices in parallel. An interesting new development is the so-called EDGE technology that allows simultaneous droplet formation in one droplet formation unit [4]. But still many questions need to be answered, including surface modification to prevent wettability changes that would disturb droplet formation.

Microfluidic systems have also been used extensively to characterize droplet formation, and scaling relations are available for droplets that are typically in the just below millimeter range. Mostly the shear force and interfacial tension force are used in a balance equation. For food emulsion droplets, typically below 10 micrometer, these scaling relations no longer hold because the interfacial tension can no longer be approached by values measured under equilibrium conditions.

Where others may have been discouraged by this, we have taken this behavior one step further and used it to predict dynamic interfacial tension values at extremely short time scales that are otherwise not accessible. We used a Y-shaped junction [5; Figure 1] and for this device it is known that the droplet formation mechanism can be described with a straight-forward force balance, linking the process conditions such as shear rate, viscosity and interfacial tension to the size of the droplets that are formed, which are always below 10 micron. We first probed systems of which the interfacial tension has a set value, and built a reference curve [Figure 2], and used that to determine the dynamic interfacial tension in systems containing

emulsifiers (e.g. SDS, Tween, but also proteins). In this way we were able to measure at droplet formation rates of up to 10,000 per second.

Besides effects during formation, we also used microfluidic devices to investigate droplet stability (coalescence) under various process conditions. Our microfluidic devices include a collision chamber with which we can precisely form droplets and try to coalesce them under controlled conditions [Figure 3]. We found that the coalescence time varies and a log normal distribution could be used to describe large numbers of coalescence of events taking place under similar conditions [Figure 4]. The collision chamber allows us not only to chart the conditions under which droplet coalesce takes place but also allows us to view coalescence in great detail as depicted in Figure 5.

In conclusion, we would like to mention that microfluidic devices are of great value when trying to investigate very fundamental phenomena such as dynamic interfacial tension behavior of surfactants and coalescence stability of emulsions. They allow systematic variation of process conditions and components, and this leads to the deeper insights that are needed to produce better products, be it in a parallelized microfluidic system or in other devices based on these newly found insights.

**Word Count: 583**

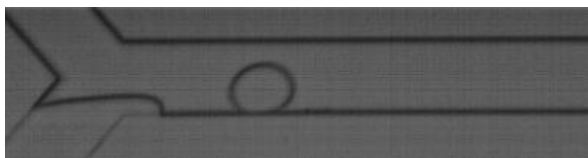


Figure 1: Y-shaped junction used for dynamic interfacial tension measurements [5].

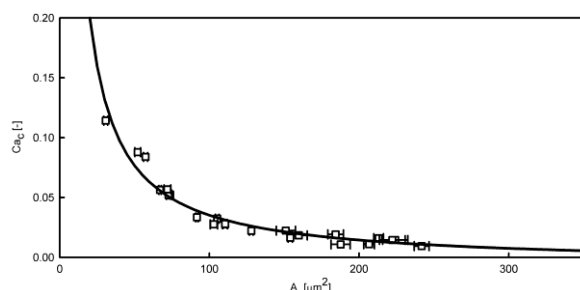


Figure 2. Calibration curve used to link systems with static interfacial tensions to systems with dynamic interfacial tensions [5].

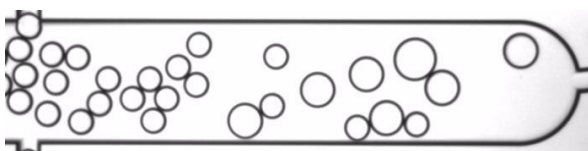


Figure 3. A close up of the collision chamber used in coalescence studies [6].

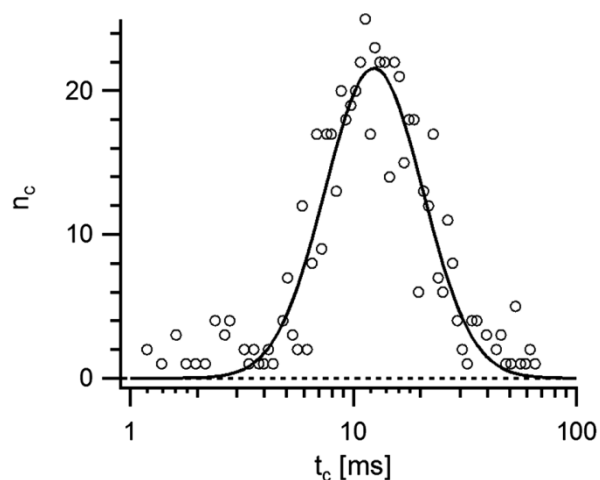


Figure 4. An example of the log normal distributed coalescence times as determined with the collision chamber [6].

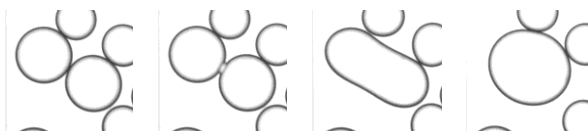


Figure 5. Four consecutive snapshots of coalescing droplets in the collision chamber [6].

## REFERENCES:

- [1] S. van der Graaf, T. Nisisako, C.G.P.H. Schroën, R.G.M. van der Sman, R.M. Boom, "Lattice Boltzmann simulations of droplet formation in a T-shaped microchannel" *Langmuir* 22 (9) - pp. 4144–4152, 2006.
- [2] A.M. Gañán-Calvo Phys. "Generation of Steady Liquid Microthreads and Micron-Sized Monodisperse Sprays in Gas Streams" *Physical Review Letters* 80, 285–288, 1998.
- [3] K.C. van Dijke, C.G.P.H. Schroën, R.M. Boom, "Microchannel Emulsification: From Computational Fluid Dynamics to Predictive Analytical Model". *Langmuir* 24 (18). - pp. 10107 – 10115, 2008.
- [4] K.C. van Dijke, G. Veldhuis, C.G.P.H. Schroën, R.M. Boom, "Simultaneous formation of many droplets in a single microfluidic droplet formation unit" *AIChE Journal* 56 (3), - p. 833-836, 2010.
- [5] M.L.J. Steegmans, A. Warmerdam, C.G.P.H. Schroën, R.M. Boom, "Dynamic Interfacial Tension Measurements with Microfluidic Y-Junctions" *Langmuir* 25 (17). - p. 9751 – 9758, 2009.
- [6] T. Krebs, K. Schroeën, R.M. Boom "A microfluidic method to study demulsification kinetics" *Lab on a Chip* 12(6) Pp. 1060-1070, 2012.

## WATER FLOW CALIBRATION FACILITY IN FRANCE (1 ML/H TO 10 000 ML/H)

*C. David<sup>1</sup>, P. Claudel<sup>1</sup>, J.C. Lötters<sup>2</sup>*

<sup>1</sup> CETIAT (Centre Technique des Industries Aérauliques et Thermiques), Villeurbanne, France

<sup>2</sup> Bronkhorst High-Tech BV, Ruurlo, The Netherlands

### ABSTRACT

Through the world, the tendency to miniaturize all objects is spread widely. Concerning liquid flow metering, several manufacturers are already industrializing instruments specific for small flows. On a metrological point of view, few National Metrological Institutes (NMI) are able to calibrate flowmeters with liquid at flow rate smaller than  $1 \text{ l.h}^{-1}$  ( $2,8 \cdot 10^{-7} \text{ m}^3 \cdot \text{s}^{-1}$ ). During the last five years, LNE-CETIAT (French NMI) was on progress to design and build a new calibration facility to ensure traceability to the international system of units. This paper will present the concepts and the first results obtained during the validation stage of this new standard.

### KEYWORDS

Calibration, water, flow, metrology

### INTRODUCTION

LNE-CETIAT is the French designated institute in the field of water flow calibration. The current facility based on a gravimetric method [1] has the following specifications:

- Type of liquid: water
- Flow range:  $8 \text{ l.h}^{-1}$  to  $36\,000 \text{ l.h}^{-1}$ ,
- Liquid temperature:  $15^\circ\text{C}$  to  $90^\circ\text{C}$ ,
- Pressure of the liquid: 1 bar to 3 bar,
- Uncertainty on volume flow rate:  
 $0.05 \% Q_v < U_{k=2} < 0.16 \% Q_v$ .

As an answer to repeated requests for calibrations at lower flow values than the available range, a study concerning available flowmeters, industrial needs and project feasibility started in 2004 [2]. The aim was to define the best flow range coverage and the potential partners for this project. As a consequence, France decided to develop a new calibration facility to cover lower flow rates in 2006. The objectives in terms of controllable parameters for the project were the following:

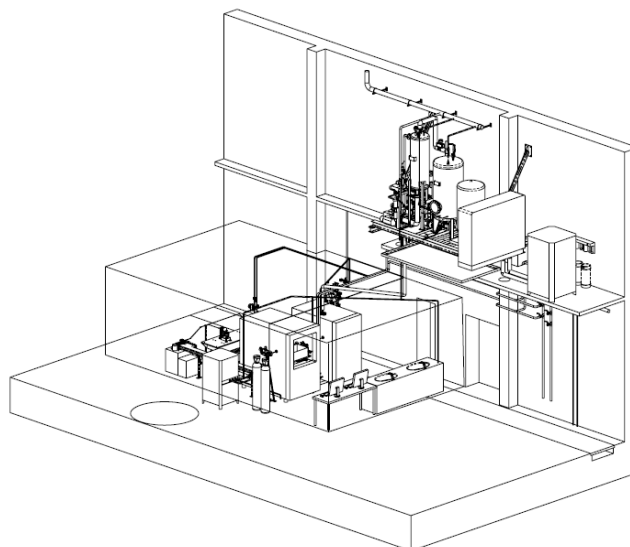
- Type of liquid: water (filtered and degassed),
- Flow range:  $1 \text{ ml.h}^{-1}$  to  $10 \text{ l.h}^{-1}$ ,
- Liquid temperature:  $10^\circ\text{C}$  to  $50^\circ\text{C}$ ,

- Ambient temperature around the flowmeter:  $10^\circ\text{C}$  to  $50^\circ\text{C}$ ,
- Pressure of the liquid: up to 10 bar,
- Uncertainty on volume flow rate:  
 $U_{k=2} \approx 0.1 \% Q_v$ .

### DESCRIPTION OF THE CALIBRATION FACILITY

#### Overview

The global architecture of the bench [3] can be described as follow (see Fig.1). On the first floor, the water is prepared (demineralised, degassed and filtered). At the ground, a clean room with controlled ambient conditions receives the supervision, the flow generation equipments and the measuring instruments.



*Figure 1: 3D view of the calibration facility*

The clean room was tested and its specifications were validated ( $T = 20^\circ\text{C} \pm 2^\circ\text{C}$ ;  $55\% \text{ RH} \pm 5\% \text{ RH}$ ;  $P = P_{\text{atm}} + 20 \text{ Pa}$ ) The temperature around the weighting cell was recorder during 30 minutes (maximum elapsed time for a measurement) and its stability was better than  $0,3^\circ\text{C}$

Flow is generated using a pressurized tank (0,1 to 10 bar) and is controlled tightly by the combination of a constant upstream pressure and the selection of capillaries creating a constant pressure loss.



Measurement of the mass flow rate is ensured by the combination of time and mass measurements.

In order to cover the entire range of flow with the expected uncertainty, the measuring process is implemented on 4 separated lines:

- Line 1: 1 ml.h<sup>-1</sup> to 10 ml.h<sup>-1</sup>
- Line 2: 10 ml.h<sup>-1</sup> to 100 ml.h<sup>-1</sup>
- Line 3: 100 ml.h<sup>-1</sup> to 1 000 ml.h<sup>-1</sup>
- Line 4: 1 000 ml.h<sup>-1</sup> to 10 000 ml.h<sup>-1</sup>

### Water preparation equipment (Fig. 2)

Water was chosen as the best fluid to be used for this new standard [2]. The main reasons are its availability, the absence of toxicity, the absence of hazards and finally the compatibility with most of the applications and technologies for flow measurement.

A complete absence of particles with a size larger than 10 µm is necessary to avoid any clogging of the pipes. The inner diameter of some of the capillaries involved in the measuring process can reach 100 µm as a minimum. To cope with this aspect, several filters are positioned along the circuit. The first one is situated near the entry of the water preparation equipment and filters most of the existing particles. A second filter is situated just before the flow generator and stop particles created by moving part or specifics equipments (pump, heater,...).

Bacteria and algae are a second type of particles that could be encountered. To avoid their development, water is saturated with bubbling nitrogen in a first tank and a small amount of fungicide is incorporated. The influence of this modification of the water composition on its viscosity and density is small. Specifics measurements have shown that these specificities had no influence on the final uncertainty budget.

The presence of bubbles in the circuit could affect the measuring process. The “dead zone” in the circuit could allow bubbles to agglomerate and clog the small capillaries. Due to changes of the local pressure in the pipes, the presence of bubble could induce variation of the flow by compressibility phenomenon. To avoid these specifics issues, water is degassed and most of the dissolved gasses are removed. The degassing process is done in a second tank using a shower that blow the water in a medium at negative relative pressure.

Calibration can be done between 10°C and 50°C. The water preparation equipment is used to maintain the temperature of the fluid before its introduction in

the flow generator. All equipments are compatible with such temperatures and are isolated to avoid heat exchanges. Temperature is regulated in the second tank with a continuous circulation of the fluid through a heat exchanger.



Figure 2: Water dispense stage

### Flow generation

The amount of water flowing through the instrument under calibration is maintained and controlled by the combined use of two specific equipments.

The first equipment is a tank with a capacity of 10 liters where the pressure is tightly regulated in a bellow. Compressed nitrogen allow the control of the pressure in with a stability better than 0,05% of the expected value. This stability is obtained by the selection of an orifice plate (3 available diameters) and the suitable pressure gauges (6 sensors are used to cover the complete range). To maintain the water temperature, the tank with its bellow is situated in a thermostatic chamber with a set up value corresponding to the set point (in the range of 10°C to 50°C). The temperature regulation was tested in the thermostatic chamber. The homogeneity was better than 0,6°C and the stability was comprised between 0,05°C and 0,1°C.

The second equipment used to control the flow is composed of eight capillaries (see Fig.3) located after the flowmeter under calibration. Thanks to the selection of one of the capillaries, a constant pressure drop is imposed in the circuit. It allows the control of the flow and the pressure in the flowmeter. The choice of the inner diameter (from 100 µm to 500 µm) and the length (from 1 to 3 m) of a capillary induce its coefficient of discharge.

Using this set of capillaries, the generation of any

flow rate in the complete range is possible for three different upstream pressures. To ensure the stability of the pressure drop, all capillaries have been designed to be used at laminar flow. For that regime, the stability of the flow is highly influenced by the viscosity of the fluid which is dependent of the temperature. To avoid variation of the viscosity, capillaries are immersed in a thermostatic bath with temperature stability better than  $0.01^{\circ}\text{C}$ .

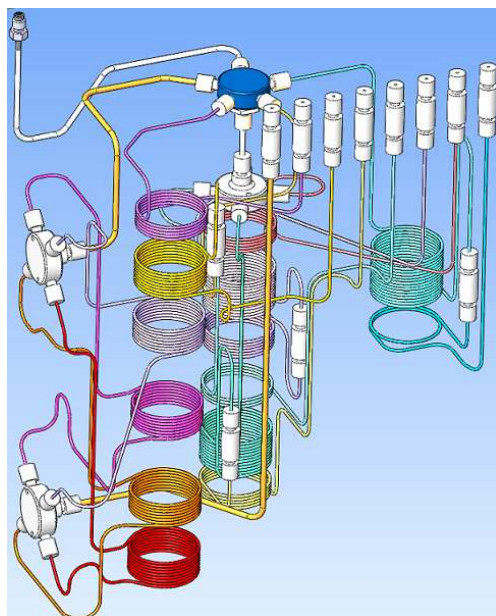


Figure 3: View of the set of 10 capillaries

### Flow measurement

The measuring part of the system is separated in four individual lines (see Fig. 4) covering each a decade of the total flow range. The gravimetric method is used to measure the flow (tractability to S.I. units via mass and time measurements). The volume flow rate is deduced from the mass flow rate with the use of water density. The concept of the four lines is identical; the main difference is the maximum load capacity of the weighting cells and the size of the circuits. For each line, water is received in a reservoir covered by a moisture saturator (see Fig.5) in order to avoid evaporating phenomenon.

The four weighting cells are positioned on a marble to reduce vibrations. For each line, the weighted mass of water is independent of the measured flow rate ( $0.5\text{ g}$  for the line n°1 (range:  $1\text{ ml.h}^{-1}$  to  $10\text{ ml.h}^{-1}$ );  $5\text{ g}$  for the line n°2 (range:  $10\text{ ml.h}^{-1}$  to  $100\text{ ml.h}^{-1}$ ) etc... The measure of the filling elapsed time is used to calculate the mass flow rate.



Figure 4: Weighting cells covering the calibration range

The volume of one drop is not enough small in comparison to the quantity of water that is measured. To avoid possible “drop effects”, the reservoir always contain water and the fluid is introduced under the free surface. Jet impact in the reservoir is also reduced by the use of a sprinkler.



Figure 5: Weighting cell, reservoir and moisture saturator for the line n°2 ( $10\text{ ml.h}^{-1}$  to  $100\text{ ml.h}^{-1}$ ).

Several other technical aspects were taken into account to ensure the stability of the flow. Dead zones and internal volumes were lowered by the use of special fittings and sealing. Variation of density is reduced by the use of a co-current loop with a  $0.1^{\circ}\text{C}$  temperature stability.

### Conclusion

This paper presents the new water flow calibration facility in France. The official inauguration of this bench was held in Lyon (FRANCE) on January the 21<sup>th</sup> of 2012. The concept of this calibration facility is

presented in the article. This standard enable calibration for low flow of liquid ( $1 \text{ ml.h}^{-1}$  to  $10\,000 \text{ ml.h}^{-1}$ ). The liquid flowing through the device under test is purified water (filtered and degassed) with controlled temperature  $10^{\circ}\text{C}$  to  $50^{\circ}\text{C}$ . The four lines of the laboratory ( $1 \text{ ml.h}^{-1}$  to  $10\,000 \text{ ml.h}^{-1}$ ) are already used for customers calibrations at  $20^{\circ}\text{C}$ . Ongoing validations will allow us to perform calibration with water temperature going from 10 to  $50^{\circ}\text{C}$ .

### **Acknowledgment**

The authors are grateful to the LNE (French National Metrological Institute), Rhône Alpes region, CETIM (French technical center for mechanical industries) and BRONKHORST HIGH TECH (NL) for their financial support.

### **REFERENCES**

- [1] ISO, "Measurement of liquid flow in closed conduits – Weighing method", ISO 4185
- [2] N. Bediat, "La métrologie des débits de liquide inférieurs à 1 litre par heure", in Proceedings of the 12<sup>th</sup> International congress of metrology, 2005.
- [3] P. Claudel, C. David, "Towards a new standard for the low flows of liquid", in Proceedings of the 14<sup>th</sup> International congress of metrology, 2009.

### **CONTACT**

\* C. David, [christopher.david@cetiat.fr](mailto:christopher.david@cetiat.fr)

## ENHANCED ENERGY CONVERSION FROM THE STREAMING POTENTIAL BY POLYMER ADDITION

*T. Nguyen, Y. Xie, L. J. de Vreede, A. van den Berg, J.C.T. Eijkel*

University of Twente, MESA+ Institution of Nanotechnology, BIOS lab on chip group, Enschede, The Netherlands

### ABSTRACT

In this contribution, we present the experimental results of energy conversion from the streaming potential when a polymer, polyacrylic acid (PAA) with concentration from 200 ppm to 4000 ppm in background electrolyte KCl solution was used as the working fluid. The results show that when PAA was added in KCl 0.01 mM solution, the energy conversion efficiency of the system was enhanced a factor of 447 as compared to the case without polymer. An enhancement factor of 257 was also observed when PAA was in the higher ionic strength background solution, KCl 1 mM. These are the first experimental demonstrations of this effect.

### KEYWORDS

Energy conversion, efficiency, streaming potential, polymer.

### INTRODUCTION

Energy harvesting from the streaming potential is based on the electrokinetic phenomena which are associated with interfacial charges. In general, every surface obtains a surface electrical charge when brought into contact with a polar medium. These interfacial charges, in turn, influence the ion distribution in the polar medium and lead to the formation of the electrical double layer (EDL). The streaming potential is generated by pressure-driven transport of the net charged liquid in the EDL. The main goal of researchers in the field is to increase the energy conversion efficiency (Eff) of the systems.

The Eff equals the ratio of (electrical) output power ( $P_{out}$ ) and (hydrodynamic) input power ( $P_{in}$ ):

$$Eff = \frac{P_{out}(\text{electrical})}{P_{in}(\text{hydrodynamic})} \quad (1)$$

Recently, Berli et al. [1] predicted theoretically that addition of polymer to the working fluid in a microfluidic channel can enhance the Eff. However, this prediction has not yet been investigated experimentally.

When non-adsorption polymers are introduced into a microchannel, depletion layers near the channel walls are formed due to the repulsive force between polymer chains and the walls, which is of entropic origin (Fig. 1a). The thickness of these layers ( $\delta$ ) will

be approximately equal to the radius of gyration of the polymers ( $R_g$ ). This results in two different viscosity zones in the channel, one of low viscosity ( $\eta_s$ ) within and the other of high viscosity ( $\eta_p$ ) outside the polymer depletion layers.[2] Figure 1b shows the approximate predicted velocity profile of the fluid flow for polymer solutions (solid curve) and for normal viscosity electrolyte solutions (dash curve). The decrease of the bulk velocity on polymer addition will decrease the hydrodynamic input power  $P_{in}$ . Because the thickness of the depletion layers can be varied from a few tens to hundreds of nanometers depending on the polymers of choice, it can be made larger than the thickness of the EDL, so that the transport of charge and hence  $P_{out}$  remain unaffected. Thus, one can gain Eff by reducing the volumetric flow rate in the bulk liquid without affecting the electrokinetic phenomenon which happens only inside the EDL (Fig. 1b)

In this paper, we present for the first time the results from experiments of energy conversion from streaming potential when polymer solutions were used as working fluids, and show that the energy conversion efficiency can be strongly enhanced.

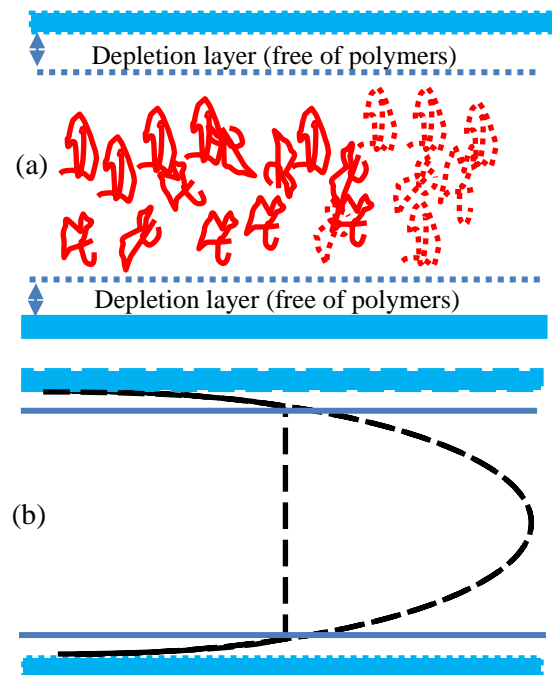


Figure 1: (a) a scheme of depletion layers when polymer is added to the working fluid. (b) predicted velocity profile of the fluid flow for polymer solutions, (solid curve) and for normal electrolyte solutions, (dash curve).



## EXPERIMENT

In this work we focus on the effect of polymers on Eff in a long, straight and smooth microchannel. Microfluidic devices were fabricated in the clean room of MESA+. The Pyrex glass chip has a microchannel with dimensions of width (w) 40  $\mu\text{m}$ , height (h) 10  $\mu\text{m}$  and length (L) 3.8 mm. The scheme of the experimental set up is shown in Fig. 2. A 99% purity nitrogen gas source was employed to drive the liquid flow from the reservoir via fused silica capillary tubing through the microfluidic chip to the downstream collector by a high accuracy gas pressure pump (Fluigent MFCS). A flow meter from Fluigent Maesflo was used to measure the liquid flow rate  $Q$ . Two Ag/AgCl electrodes were placed into the reservoirs for electrical measurements. Voltages were applied by a Keithley 2410 voltage source, and current measurement was performed by a Keithley 6485 pico-ammeter.

Polyacrylic acid (PAA, Mw 1250000 g/mol, gyration radius shown in table 1) was obtained from Sigma-Aldrich (USA). In order to have a full insight into the effect, the experiments were conducted in two different batches. In the first batch, potassium chloride KCl 1 mM (approximate EDL thickness 9.5 nm), pH 9.5 was used as the background electrolyte solution. This background solution was then employed as solvent for preparation of PAA solutions with varying concentrations of 200 ppm, 500 ppm, 1000 ppm, 2000 ppm, 4000 ppm. In the second batch of experiments, KCl 0.01 mM (approximate EDL thickness 100 nm) pH 9.5 was used to prepare PAA solutions with the same set of concentrations as the batch number one. All the PAA solutions were adjusted to pH 9.5.

Table 1: gyration radius of PAA in different ionic strength background solutions

KCl concentration	$R_g = 1.57 \times n^v$ (nm); n is the number of monomer in polymer chains [3, 4]	
1 mM	$v = 0.5$	$R_g = 207$
0.01 mM	$v = 0.6$	$R_g = 549$

Prior to the introduction of the different solutions into the apparatus, the microchannel and the entire tubing system were bidirectionally rinsed with KOH 100 mM for 15 mins. Following that, a second 15-min rinsing cycle was initiated using MiliQ water and the third cycle was 15 mins of the desired solution before performing measurement. The transparent nature of the microchannel surfaces allowed visual inspection of the channel (via a microscope) to ensure that all bubbles had been removed. The working solution was allowed to flow into the system until the equilibrium

was reached which was manifested by the stability of the flow rate and the streaming current. Once the equilibrium was established, the measurement was conducted. All the measurements were repeated in triplicate and carried out at ambient temperature.

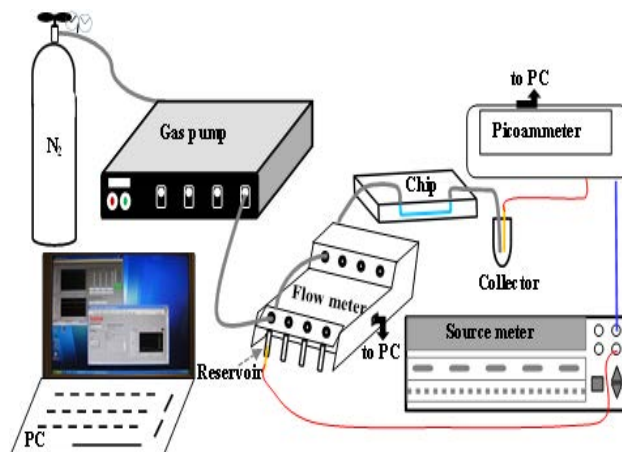


Figure 2: Scheme of experimental set up

## RESULTS AND DISCUSSION

### Input power

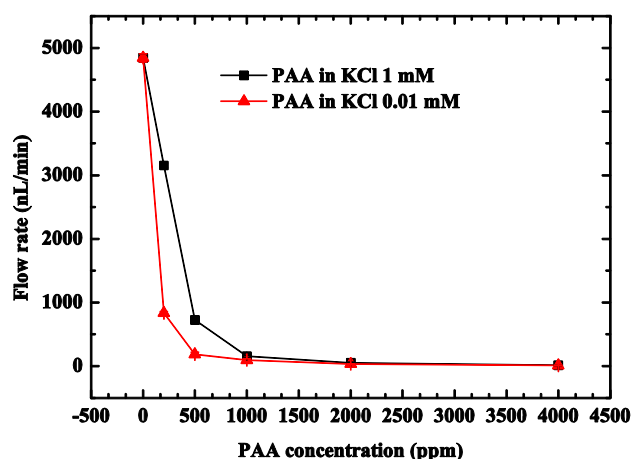


Figure 3. Reduction of flow rate when PAA is added into working fluid.

Fig. 3 compares the reduction of volumetric flow rate in both experimental batches. It is clear that the volumetric flow rate was reduced when the polymer concentration increased. This is reasonable since the polyelectrolyte viscosity is proportional to the square root of its concentration.[5] Moreover, the reduction of the flow rate in case of KCl 0.01 mM at small added PAA is larger than in KCl 1 mM. This can be explained by the changes of polymer conformation according to the ionic strength of the solvents (background electrolyte solution). In the case of high ionic strength solution, counter ions, in our case  $\text{K}^+$  will strongly screen the negative charges on polymer chains. This results in polymers having random coil

conformation. If one now reduces the ionic strength of the solvent, the polymer conformation will be changed from random coil to expanded stage due to lesser screening and hence repulsive force of negative charges along the polymer chains. At expanded stage, the random coils take more space; increasing the viscosity of the solution (fig. 4).[6] This explains why the volumetric flow rate was reduced more rapidly by PAA addition to the low ionic strength background solution.

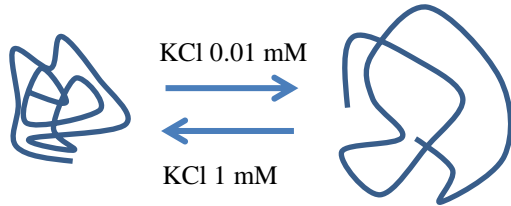


Figure 4: scheme of the changes on polymer conformation according to ionic strength in the solvent

### Output power

In order to find the maximum output power of the whole system, an I-V characterization was performed by applying different voltages against the streaming potential between the electrodes, a procedure equivalent to introducing larger load resistances. Our previous work [7] can be referred to for further information on this procedure.

The I-V characterization of the system is shown in figs. 6a and 6b. In both experimental batches, the streaming current increased and the streaming potential decreased with increasing polymer concentration. The reduction of streaming potential can be explained by the increase of bulk conduction when acidic polyanion PAA was added to the working solutions. The underlying mechanism for the increase of streaming current is under discussion. The streaming current for a rectangular microchannel in Cartesian coordinates (fig. 5) is defined by [8]

$$I_s = 2 \int_0^{h/2} v_y \cdot \rho(z) w dz \quad (2)$$

Where  $v_y$  is the velocity profile of the fluid and  $\rho(z)$  is the volume density of the net charge across the channel.

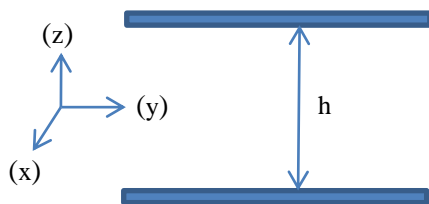


Figure 5. Scheme of geometrical dimensions and the coordinate system.

According to equation (2), the streaming current is a function of the velocity and the charge density across the channel. Hence, the increase of streaming current must be caused by the increase of net charge density and/or the increase of the velocity of the unbalanced ions in the diffused layer of the EDL. On this account, it is reasonable to hypothesize the following: (i) possibly there was a faster speed of solution inside the depletion layer since the streaming current is proportional to the velocity in the electrical double layer inside the depletion layer or (ii) possibly a movement of the solution occurred in between the polymer network with respect to the polymer. Figs. 6a and 6b also show that there was a sharp increase of the streaming current when PAA was used with low ionic strength background solution (KCl 0.01 mM) as compared to the higher ionic strength one (KCl 1 mM).

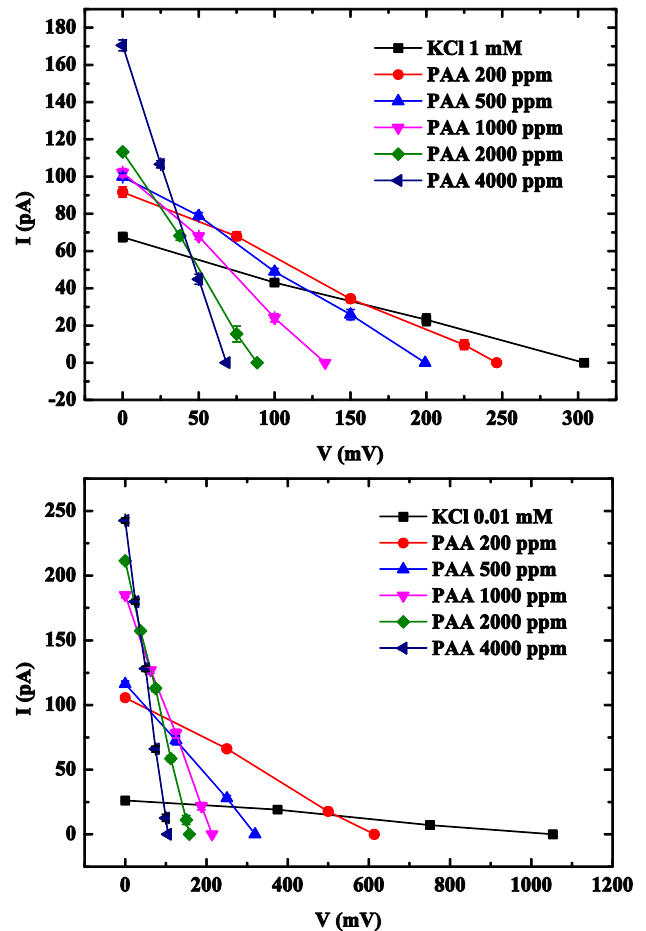


Figure 6 (a) and (b): I-V characterization of the system.

### Conversion efficiency

Due to the strong reduction of volumetric flow rate and the significant increase of streaming current, the Eff of the entire system was increased enormously (according to equation 1). In particular, compared to the Eff of the normal viscosity electrolyte solution, the

enhancement of the Eff for PAA added into KCl 0.01 mM solution was a factor of 447 and for the case of PAA in KCl 1 mM it was a factor of 257, as shown in fig. 7. The maximal energy conversion efficiency we obtained for the entire system is 0.038 % and it was 0.34% for the chip. It is worth stressing that the result from this work is for single microchannel and yet, in case of without polymer, this result can only be attained in nanochannels of diameters of 100 nm to 200 nm [9, 10].

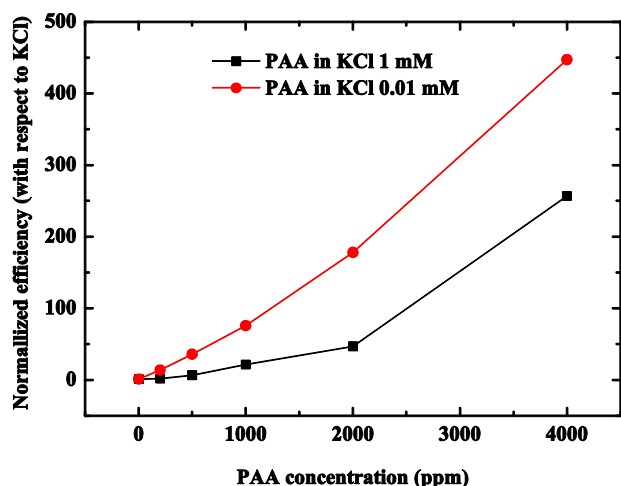


Figure 7: Normalized energy conversion efficiency of PAA containing solutions with respect to normal viscosity KCl 0.01 mM and 1 mM solutions

## CONCLUSIONS

The energy conversion efficiency from the streaming potential in microchannel with polyacrylic acid (PAA) added to background electrolyte KCl solution was investigated experimentally. The results showed that the presence of this charged polymer caused a reduction of input power, an increase of streaming current and a decrease of streaming potential simultaneously. Furthermore, PAA in low ionic strength solution (KCl 0.01 mM) caused a large reduction of input power and increase of streaming current than at the higher ionic strength (KCl 1 mM). These combined factors resulted in an enhancement of the energy conversion efficiency of the system with a factor of 447 in case of PAA in KCl 0.01 mM and a factor of 257 for PAA in KCl 1 mM. The maximal energy conversion efficiency we obtained for the entire system is 0.038 % and it was 0.34% for the chip.

## REFERENCES

- [1] C. L. A. Berli, "Electrokinetic energy conversion in microchannels using polymer solutions," *Journal of Colloid and Interface Science*, vol. 349, pp. 446-448, 2010.
- [2] C. L. A. Berli and M. L. Olivares,

"Electrokinetic flow of non-Newtonian fluids in microchannels," *Journal of Colloid and Interface Science*, vol. 320, pp. 582-589, 2008.

[3] G. D'Adamo, A. Pelissetto, and C. Pierleoni, "Coarse-graining strategies in polymer solutions," *Soft Matter*, vol. 8, pp. 5151-5167, 2012.

[4] G. Miquelard-Garnier, C. Creton, and D. Hourdet, "Strain induced clustering in polyelectrolyte hydrogels," *Soft Matter*, vol. 4, pp. 1011-1023, 2008.

[5] A. V. Dobrynin and M. Rubinstein, "Theory of polyelectrolytes in solutions and at surfaces," *Progress in polymer science*, vol. 30, pp. 1049-1118, 2005.

[6] H. J. Butt, K. Graf, M. Kappl, and J. Wiley, *Physics and chemistry of interfaces vol. 1*: Wiley Online Library, 2003.

[7] Y. Xie, J. D. Sherwood, L. Shui, A. van den Berg, and J. C. T. Eijkel, "Strong enhancement of streaming current power by application of two phase flow," *Lab on a Chip*, vol. 11, pp. 4006-4011, 2011.

[8] J. H. Masliyah and S. Bhattacharjee, *Electrokinetic and colloid transport phenomena*. Hoboken, N.J.: Wiley-Interscience, 2006.

[9] F. A. Morrison and J. F. Osterle, *Electrokinetic Energy Conversion in Ultrafine Capillaries* vol. 43: AIP, 1965.

[10] M. C. Lu, S. Satyanarayana, R. Karnik, A. Majumdar, and C. C. Wang, "A mechanical-electrokinetic battery using a nano-porous membrane," *Journal of Micromechanics and Microengineering*, vol. 16, pp. 667-675, Apr 2006.

## CONTACT

Trieu Nguyen, t.nguyen@utwente.nl

# POLYMER MICRO FLUIDIC SYSTEMS FABRICATED BY ULTRASOUND

*J. Sackmann<sup>1</sup>, K. Burlage<sup>1</sup>, C. Gerhardy<sup>1</sup>, D. Loibl<sup>2</sup>, L. Cui<sup>1,3</sup>, W.K. Schomburg<sup>1</sup>*

<sup>1</sup> RWTH Aachen University, KEmikro, Aachen, Germany

<sup>2</sup> Herrmann Ultraschalltechnik GmbH & Co. KG, Karlsbad, Germany

<sup>3</sup> Tianjin University, Tianjin, P.R. China

## ABSTRACT

Fabrication processes of micro fluidic systems from polymer have been developed which are performed within a few seconds. These processes are enabled by employing ultrasonic welding machines. This way, only little investment and production costs are necessary which are affordable even for small enterprises and are economic also in small scale production.

Micro channels are produced by ultrasonic hot embossing of grooves into polymer foils and welding a lid on top. Fluidic contacts are fabricated by welding tubes into the channels or connection pieces on top of them. Electrical contacts are achieved by metal wires or foils. This way, also sensors and electrical circuits are fabricated.

## KEYWORDS

Polymers, Ultrasonic hot embossing, Micro fluidic systems, Electronics in polymer foils

## FABRICATION PROCESS

Molding of thermoplastic polymers is known as a class of low-cost fabrication processes of micro devices, especially for micro fluidic applications [1]. The polymer is softened by heating and adapted to the shape of a tool. Now it has been discovered that both cycle times and the costs of investment and fabrication are even more reduced when the polymer is heated by ultrasound.

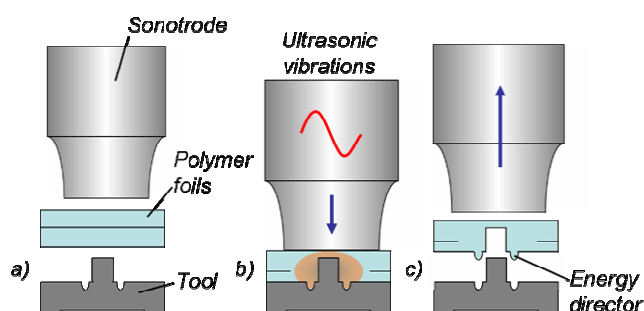


Figure 1: Ultrasonic hot embossing.

Micro cavities are produced by the combination of ultrasonic hot embossing and welding [2]. For ultrasonic hot embossing a stack of polymer foils is placed on top of a tool with protruding micro structures (cf. Fig. 1a). When ultrasound is applied via a sonotrode, friction between the protruding micro structures

on the tool and the foils and between the foils generates heat melting the foils (Fig. 1b). The molten foils adapt to the shape of the tool and solidify when ultrasound is switched off again. This entire process is performed in a few seconds. Typical micro channels generated this way are shown in Fig. 2.

So called energy directors are generated by ultrasonic hot embossing around the channels (cf. Fig. 1c). The energy directors are molten when another polymer foil is welded on the channel as a lid.



Figure 2: Micro channels, 270  $\mu\text{m}$  in width and 150  $\mu\text{m}$  in depth, generated by ultrasonic hot embossing.

The tools required for ultrasonic hot embossing have been fabricated by milling from aluminum plates, 4 mm in thickness. Therefore, the smallest micro structures which can be fabricated are limited by the size of the available milling heads (as small as 50  $\mu\text{m}$  in diameter). Smaller structures such as grooves as narrow as 7  $\mu\text{m}$  could be ultrasonically hot embossed with nickel tools fabricated by x-ray lithography and electroplating.

The overall size of a micro fluidic system fabricated by a one-step ultrasonic hot embossing process is limited by the dimensions of the sonotrode and the energy and force provided by the ultrasonic machine. The largest machine employed so far at KEmikro works at 20 kHz and has a sonotrode with a width and length of 40 mm and 60 mm, respectively. Maximum force and ultrasonic power are 3128 N and 2200 W, respectively.

Not all combinations can be welded with each other. This is taken advantage of when micro structures are punched out of a foil with ultrasound (cf. Fig. 3). Therefore a tool with cutting edges is



produced, with the shape of the corresponding embossed structure. A buffer-foil is employed preventing damages of Sonotrode and punching tool. Heat is generated at the tips of the cutting edges, by the ultrasound and the embossed structure is trimmed out of its surrounding foil.

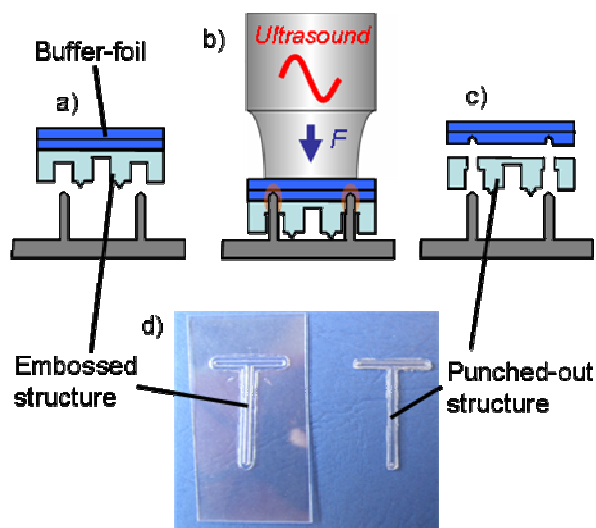


Figure 3: Punching process by means of ultrasound and photograph of a micro mixer channel punched-out of a PVC-foil.

## MATERIALS

In principle all thermoplastic polymers can be micro patterned or welded with ultrasound. The polymer of choice is situational. Polyvinyl chloride (PVC) is a comparatively cheap plastic with excellent welding and embossing performance. Drawbacks of the material are the relatively low decomposition temperature and the formation of acidic decomposition products.

Polyvinylidene fluoride (PVDF) is a material with an excellent resistance against a wide range of chemicals and also shows good results in ultrasonic hot embossing and welding.

Polyethylene (PE) and polypropylene (PP) are two examples for low price plastics with attractive handling properties. These two materials are mostly used in cases where high formability with low energy input is needed (e.g. thermoforming).

Some polymers like PS require a heated tool reducing the needed ultrasonic power. Table 1 shows a list of the thermoplastic polymers which have been micro patterned so far by ultrasonic hot embossing.

Table 1: Thermoplastic polymers employed for ultrasonic hot embossing so far.	
PVC	Polyvinyl chloride
PVDF	Polyvinylidene fluoride
PP	Polypropylene
PE	Polyethylene
PA	Polyamide
MABS	Methylmethacrylate acrylonitrile butadiene styrene copolymer
PC	Polycarbonate
PEEK	Polyetheretherketone
PS	Polystyrene
SAN	Styrene-acrylonitrile copolymer
PMMA	Polymethylmethacrylate

## MICROFLUIDIC DEVICES

Several options for connecting micro channels to the macroscopic world have been realized. One possibility is gluing fluidic connectors to inlets and outlets. An alternative is a plate serving as a connection piece welded onto the channels. Such a plate provides a stable substrate for delicate micro structures. When threaded through holes are installed from the backside of the plate, standard fittings can be employed (cf. Fig. 4).



Figure 4: Standard fittings providing access to a micro channel on the opposite side of a connection plate from PVDF.

Good welding results are obtained when connection plate and micro system are made of the same polymer.

Another approach suitable for channels with comparatively larger diameters is welding tubes directly into the channels (Fig. 5). The PTFE (polytetrafluoroethylene) tubes, 300  $\mu\text{m}$  and 760  $\mu\text{m}$  in inner and outer diameter, respectively, were forced into the channels from PVDF, and welded in when a cover layer from PVDF was ultrasonically welded onto the channels.

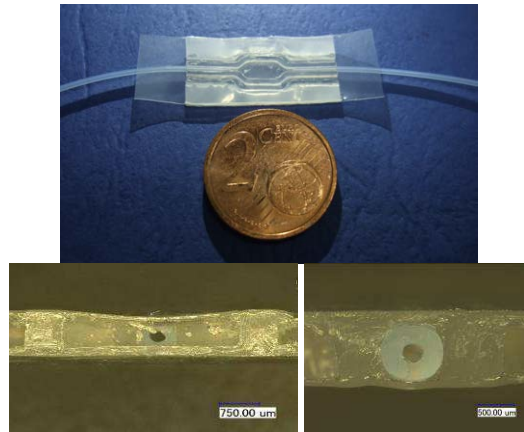


Figure 5: Photograph of tubing welded directly into micro channels (top) and cuts through the channel and the welded in tube (bottom left / bottom right).

The tubing material doesn't need to be the same as the channels but acts as a surface inside of the channel generating heat by friction and facilitating welding in the tube.

Sensors have been integrated into micro channels also by ultrasound. When a thin wire is placed perpendicular over a micro channel before welding a cover layer, the wire is tightly welded into the polymer and provides access for sensors inside of the channel. Employing the wire as a heater an anemometric flow sensor was realized (Fig. 6 and 7).

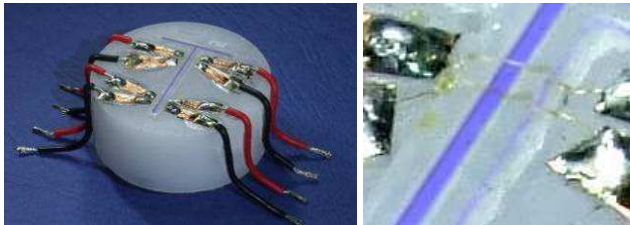


Figure 6: Micro mixer with anemometric flow sensors (left). Parallel gold wires, 50 μm in thickness, placed perpendicular over the micro mixer channel (right).

With the gold wire blockages or leakages of micro channels can be detected. The flow carries away heat from the wire and lowers its temperature this way (cf. Fig. 7b). The electrical resistance of the wire is a function of temperature. Therefore, the voltage drop over the wire is a measure of the flow when a constant current is generated through the wire (Fig. 7a). Figure 7c shows the measured voltage when the flow through a channel was switched on and off.

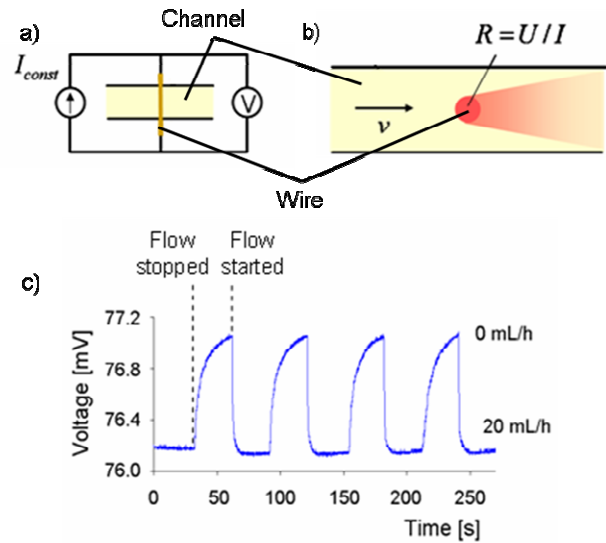


Figure 7: Detection of a flow change by hot-wire anemometry [3].

With two parallel gold wires the lengths of slugs in a Taylor-flow of a liquid-liquid dispersion was measured [3]. For this measurement an alternating voltage was applied to the gold wires and the electric current between the wires is detected. As soon as a phase with high electric conductivity touched both wires an increased signal was recorded. A deflection of the signal was not observed if the droplet did not touch both wires at the same time, thus the length of the probed slug needs to exceed the distance between the wires.

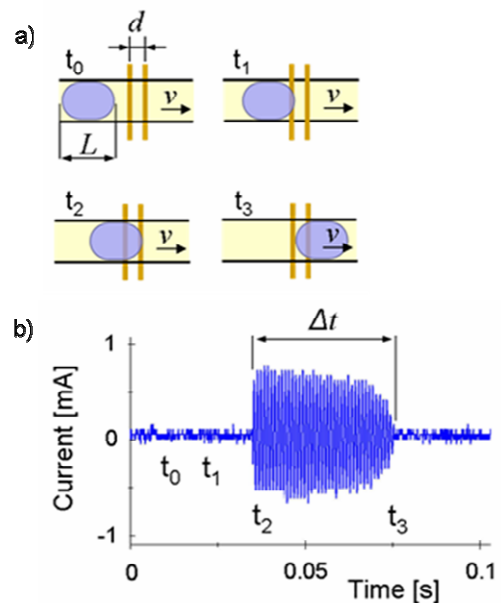


Figure 8: Slug length monitoring by measuring the electrical current between two parallel gold wires in a channel [3].

## ELECTRONIC BOARDS

Electronic elements such as resistors, transistors, capacitors, and LEDs were also ultrasonically welded into polymer foils from styrene-acrylonitrile (SAN). Figure 9 and 10 show the electronic elements and conductor paths, 500  $\mu\text{m}$  in width, of a multivibrator circuit welded into and onto SAN foils.

The multivibrator consists of two parts, the fixing frame for the SMD-components and a carrier which contains the conductor paths, 500  $\mu\text{m}$  in width, of a multivibrator circuit welded into and onto SAN foils.

First thermoplastic polymer dispersion was spin-coated on top of a metal foil (e.g. aluminum or copper). It served as an adhesive layer between the metal and the polymer foils. Afterwards the coated metal foil and a stack of polymer foils were placed on top of a tool with protruding cutting edges (cf. Fig. 9a). When ultrasound was applied the metal foil was cut and welded onto the SAN-foils. Areas of the metal not welded, were removed with an adhesive tape (cf. Fig. 9b). The remaining parts provided the conductor paths (cf. Fig. 9c).

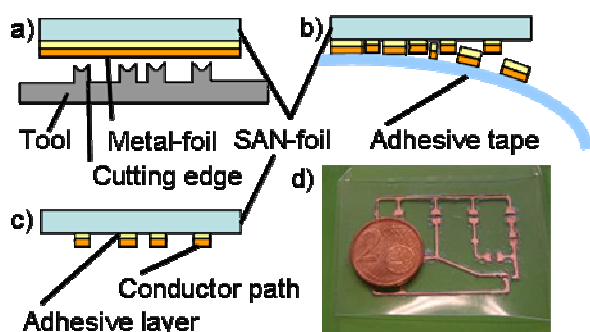


Figure 9: Fabrication process of the conductor paths on top of a stack of SAN-foils.

For the fixing frame of the electronic components, gaps with various depths were embossed into a stack of SAN-foils (cf. Fig. 10a). Thereby the size and position of the gaps had been adapted to each component to achieve in the following fabrication step a common level height over the foil for the upper sides of the components. The SMD-components were force fitted into the cavities (cf. Fig. 10b). For a better connection of the electronic elements to the conductor paths an ACF-layer (anisotropic conductive film) was placed between the parts shown in Figure 10. In the last fabrication step these two parts were ultrasonically welded to form the desired device (cf. Fig. 10d).

This shows that in the near future even the electronics for sensors in micro fluidic devices may be integrated into polymer foils by ultrasound.

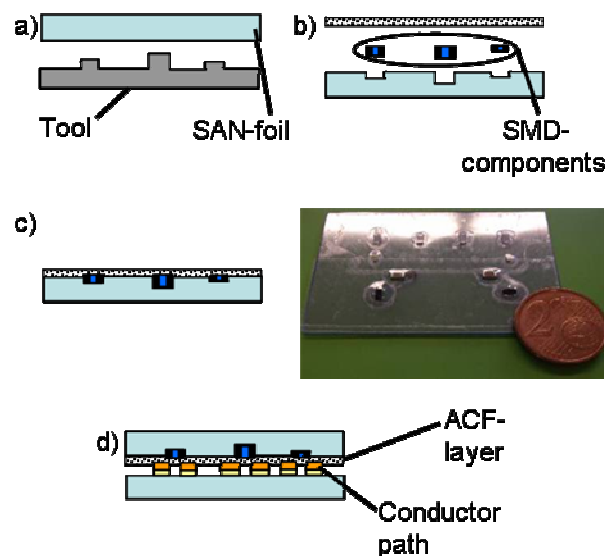


Figure 10: Fabrication process of the carrier for the electronic components.

## CONCLUSIONS

Ultrasonic hot embossing and welding are techniques suitable for the fabrication of micro devices and systems. Fabrication by ultrasound is much cheaper and quicker than even injection molding and hot embossing. Cycle times are just a few seconds and equipment costs are limited to some 10,000 €. The process is very flexible and even small-scale production can be economic. A variety of thermoplastic polymers can be processed and chosen appropriate to the respective application. Electric and fluidic ports are easily provided. Even electronic components can be integrated into polymer foils by ultrasonic hot embossing and welding.

## REFERENCES

- [1] M. Hecke, W.K. Schomburg, "Review on Micro Molding of Thermoplastic Polymers", J. Micro-mech. Microeng. Vol. 14, pp. R1 - R14, 2004. doi: 10.1088/0960-1317/14/3/R01.
- [2] W.K. Schomburg, K. Burlage, C. Gerhardy, "Ultrasonic hot embossing", Micromachines 2, 157-166, 2011. ISSN: 2072-666X, doi: 10.3390/mi2020157.
- [3] K. Burlage, C. Gerhardy, H. Praefke, M.A. Liauw, W.K. Schomburg, "Slug Length Monitoring in liquid-liquid Taylor-Flow integrated in a novel PVDF Micro Channel", Chemical Engineering Journal, doi: 10.1016/j.cej.2012.08.070.

## CONTACT

\* J.Sackmann, sackmann@kemikro.rwth-aachen.de

## Microbeads for Sampling and Mixing in a Complex Sample

Drew Owen<sup>1,2</sup>, Wenbin Mao<sup>2</sup>, Alex Alexeev<sup>2</sup>, Jenifer Cannon<sup>3</sup>, Peter J. Hesketh<sup>1,2</sup>

<sup>1</sup>Institute for Bioengineering and Bioscience, Georgia Institute of Technology, Atlanta, GA, USA

<sup>2</sup>School of Mechanical Engineering, Georgia Institute of Technology, Atlanta, GA, USA

<sup>3</sup>Center for Food Safety, Dept. Food Science & Technology, University of Georgia, Griffin, GA, USA

### ABSTRACT

This paper presents work on the development of a microfluidic device using super-paramagnetic beads for sampling and mixing. The beads are manipulated via an external rotating permanent magnet in a microfluidic channel. Efficient mixing is achieved in a short distance with this method. Modeling shows the variables which influence the mixing are flow rate, bead rotation speed and the number of beads. Displacement of the bead relative the rotating magnetic field sets an upper limit on the bead rotation speed due to viscous drag. Future work will examine optimization of this system for capture of pathogens from a complex mixture.

### KEYWORDS

Microfluidics, convective mixing, magnetic microbeads, complex sample

### INTRODUCTION

#### Background

Detection of low concentrations of bacteria, viral particles and parasites in food samples is a challenging process [1]. The separation of the target from the food matrix is a key step that needs to be carried out with highly specific capture of the target onto a mobile phase. This can subsequently be separated and concentrated for detection with fluorescent, electrochemical or quantum dot labeling. The capture of the target can be more effectively carried out with efficient mixing.

Microfluidics provides exciting possibilities for miniaturized biosensors allowing for highly parallel and high throughput tests to be performed in miniaturized “lab-on-a-chip” packaging with a great deal of control utilizing the low Reynolds number flows. However, laminar flow makes mixing of fluid difficult. Passive mixers stretch and fold fluids, shortening diffusion lengths or use herring-bone features in a channel to achieve mixing [2]. These mixers require either complicated 3-D fabrication, relatively long mixing lengths or both. Active mixers exert time-dependent disturbances.

Microfabricated magnetic devices have been made for a variety of manipulation of paramagnetic beads based on the principle of magnetophoresis

(MAP). For example, microscale core/coil design [3], current-carrying wires [4], wire matrix [5], and micropatterned conductors [6] have been used for trapping, transport, and catch-and-release of magnetic beads. However, micro-electromagnetic systems are limited to manipulation of small numbers of beads and with low magnetic forces due to Joule heating and complexity concerns.

### Device Principles and Design

We present a simple magnetophoresis system capable of controlled transport of rotating paramagnetic beads among soft magnetic patterns. Low aspect ratio super-paramagnetic NiFe discs (150 nm tall, diameter 3  $\mu\text{m}$ ) are patterned onto a silicon wafer. A PDMS channel is bonded onto the wafer to create the microfluidic channel. An external permanent magnet attached to a motor provides a magnetic field, which can be rotated at different speeds while magnetizing the NiFe discs in the channel. Paramagnetic microbeads (Dynabeads MyOne® & M-280, Invitrogen) introduced into the channel with a syringe pump are trapped at the poles of the now magnetized soft magnetic discs. Rotation of the external permanent magnet will also rotate the induced magnetic poles in the soft magnetic discs which will in turn rotate the trapped microbeads (Figure 1).

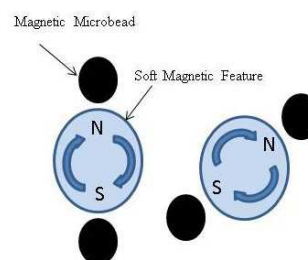


Figure 1: Magnetic attraction between paramagnetic beads and induced magnetic poles. As the external permanent magnet rotates, the induced poles within the soft magnetic features also rotate, pulling the magnetic microbead.

### RESULTS

#### Computational Modeling

Computer modeling is being done to investigate the dynamics of the system. We employ a hybrid computational method [7, 8] to model the dynamic



## 5. Applications

## Presentation

interactions between paramagnetic beads, soft NiFe disks and viscous fluid in the channel. Our approach integrates the lattice Boltzmann model for the dynamics of fluid and the lattice spring model for the motion of magnetic beads and static disks. Figure 2 shows the location of the beads relative to the magnetic features in a slice through the channel. The model will facilitate study of important design parameters, including bead diameter, fluid viscosity, flow rate, sample volume and their effect on capture efficiency [6].

Soft materials are characterized by a high permeability and a low coercivity, which makes them easy to magnetized and demagnetize. Therefore, NiFe disks are saturated easily under the external magnetic field and follow the rotation of external field. The magnetization of paramagnetic beads is much smaller than NiFe disks, so the influence of beads on the magnetic field is negligible. The magnetic field of single cylindrical soft magnet (NiFe disks) can be calculated theoretically [9]. Due to the linearity of magnetic field, we can obtain the total magnetic field in the channel using superposition [10]. The magnetic bead can be treated as a magnetic dipole. When beads is placed in a non-uniform magnetic field  $\mathbf{B}$ , the magnetic force on beads is given by  $\mathbf{F}_M = (\mathbf{m} \cdot \nabla) \mathbf{B}$ , where

$$\mathbf{m} = V \frac{3\chi}{3 + \chi} \frac{\mathbf{B}}{\mu_0} \quad (1)$$

is the magnetic dipole moment with  $V$  being the bead volume and  $\chi$  being the apparent magnetic susceptibility of the bead [11].

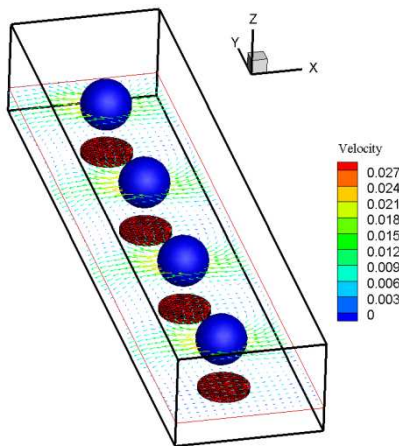


Figure 2: Computational model describes magnetic beads rotating around the NiFe disks at the bottom of the substrate.

Our computational setup is shown in Fig. 4 with periodic boundary in x direction. The box dimensions

are  $H = 2a$ ,  $W = 13a$ , where  $a$  is the diameter of bead. We choose disk diameter  $D_d = a$ , disk height  $h = 0.05a$ , and the spacing  $s$  between disks varies from  $2a$  to  $1.5a$ . All these dimensions match experimental measurement.

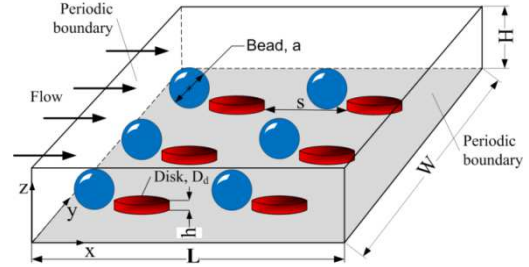
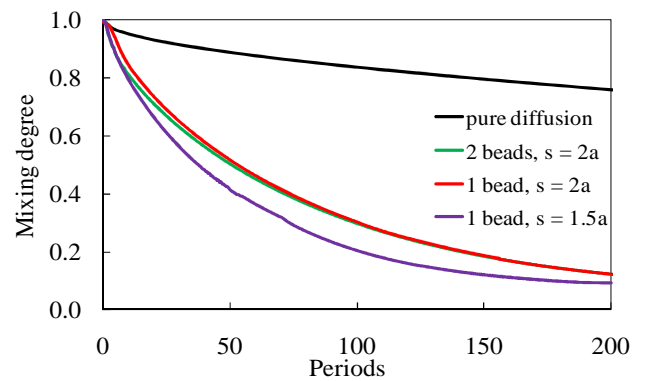


Figure 4: Computational setup of magnetic mixer.

We first examine the mixing performance without fluid flow. We define a dimensionless parameter mixing degree

$$\sigma = \sqrt{\frac{1}{N} \sum_{i=1}^N (\phi_i - \bar{\phi})^2} \quad (2)$$

to characterize the efficiency of mixing, where  $\phi$  is the concentration of fluid. When  $\sigma$  equals 1, it means two fluids are fully separated. When it equals 0, it means fully mixed. In Figure 5a, we compare the mixing performance of pure diffusion and the magnetic mixer. It is obvious that mixing is much faster using magnetic beads. Different configurations of mixer are also compared, and we find the mixing is enhanced as the spacing between disks decreases. Figure 5b shows the snapshots of concentration profile for different configurations. In the figure, the black circle denotes the disk and the green circle denotes the magnetic bead. We find that the rotation of beads could stretch the interface between two fluids, thus enhancing mixing significantly.



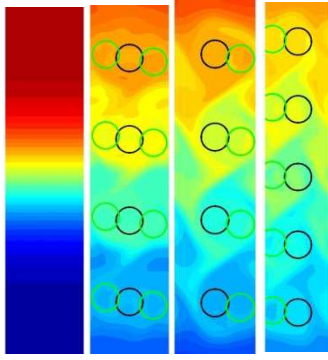


Figure 5: (a) Comparison of mixing efficiency between pure diffusion and magnetic mixer without channel flow. (b) Concentration field when the period equals 80 in the channel with different configurations: leftmost, pure diffusion; left, 2 beads rotation per disk with  $2a$  spacing; middle, 1 bead per disk with  $2a$  spacing; right, 1 bead per disk with  $1.5a$  spacing.

Next, we examine the effect of flow rate on mixing. We keep the same rotation speed of beads and the same configuration (1 bead rotation per disk with  $1.5a$  spacing). In Figure 6, we find as channel flow rate increases, the mixing performance decreases. From our simulation, we find that the channel flow tends to flatten the interface, thus suppressing the mixing. So in order to obtain better mixing performance, we need increase rotation speed of beads.

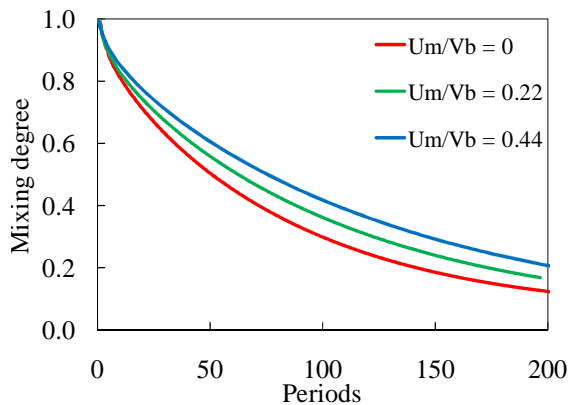


Figure 6: Mixing degree versus time for different flow rates ( $U_m$  is the maximum velocity of channel flow,  $V_b$  denotes the rotation velocity of beads).

### Current Device Characterization

The individually controlled bead transport with synchronized circulating motion provide strong interact between the particles and the fluid flow, which is good for sampling in microchannels. The effective transport of the beads also facilitates the uniform distribution of beads among the soft magnetic patterns, which is important to many biological total-analyses on a chip (see Figure 7).

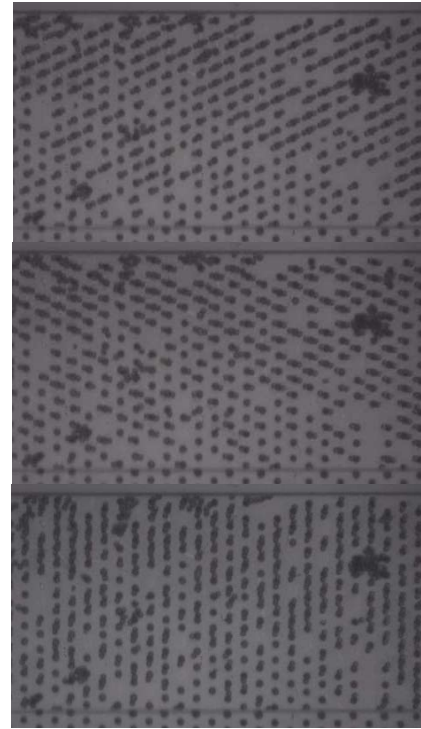


Figure 7: M-280 (2.8 micron diameter) magnetic microbeads are trapped at magnetized NiFe discs (3 micron in diameter, 150 nm tall) in a microfluidic channel. The rotation of the M-280 beads is caused by the rotation of the external permanent magnet.

Based upon our modeling work (data not shown), it is expected that if the magnetic field is rotated to high enough speeds, paramagnetic beads will no longer rotate in phase with the magnet. This will begin to express as a phase angle lag between of the magnetic field lines and the beads. The lag will progress until the beads no longer maintain the same frequency as the magnetic field lines. This drag is due to fluid drag resistance as the bead spins around the disk. To better understand the operating conditions of the device, the phase angle lag was measured using high speed Phantom cameras (v210 and v9.0, Vision Research).

Experiments were carried out at two different magnetic field strength values, 1800 and 880 Gauss, showed a noticeable increase in phase angle lag under similar rotational speeds, 2400 and 2990 rpm, respectively. Figure 8 shows an images from the experiment. The average measured phase angle under the weaker field condition was  $19.9^\circ$  ( $n=18$ , low  $15.9^\circ$ , high  $27.4^\circ$ )



Figure 8: Phase angle lag of rotating M-280 Dynabeads in the presence of a rotating magnetic field; left, magnetic field is rotating at 2400 rpm with a field strength of 1800 Gauss; right, magnetic field is rotating at 2990 rpm with a field strength of 880 Gauss

In order to quantify the amount of material capture on the beads, we injected fluorescent nanospheres (Fluosphere, 40nm diameter, from Invitrogen) labeled with biotin which bind to streptavidin coated M-280 beads (2.8 micron diameter). The nanospheres, suspended in a 0.5% solution by volume in PBS + 0.1% Tween-20, were introduced into the channel at a linear velocity of 0.19 mm/s for 5 minutes. Figure 9 shows that capture has taken place at the surface of the beads.

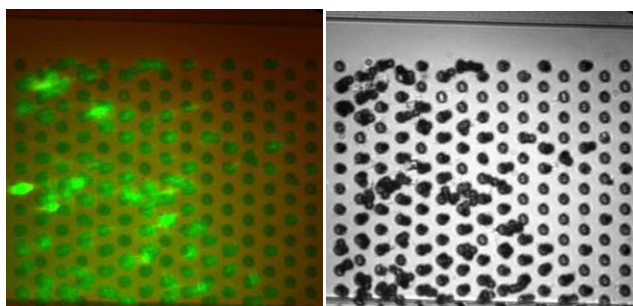


Figure 9: Streptavidin coated M-280 microbeads (Invitrogen). The fluorescence in the image is the presence of biotin-labeled Fluospheres (Invitrogen) bound to the M-280 microbeads. The image on the right is the brightfield image showing the positions of the M-280 microbeads

### DISCUSSION AND FUTURE WORK

Efficient mixing is achieved in a short distance with the paramagnetic beads. Modeling shows the variables which influence the mixing are flow rate, bead rotation speed and the number of beads in the channel. Displacement of the bead relative the rotating magnetic field sets an upper limit on the bead rotation speed. Finally we have demonstrated the capture of fluorescent nanospheres on the beads. Future work will investigate the effects of device geometry by optimizing the flow rate and bead rotation speed in order to capture particles of different sizes efficiently forms a complex mixture. The long term objective of this work is to develop a practical compact portable pre-concentration and pathogen purification system for complex mixtures important

for food and environmental safety that can be applied to a wide range of assays.

### ACKNOWLEDGEMENTS

Many thanks to Zhengchun Peng and Elena Cox for fabrication of the NiFe features on the silicon chips used in these experiments. Thanks to the staff at the Nanotechnology Research Center at Georgia Tech for their technical support, and to Prof.'s D. Hu and T. Sulchek, for loan of the high speed cameras. Financial support from the NSF CBET grant is also acknowledged.

### REFERENCES

- [1] H. P. Dwivedi, L. A. Jaykus, Critical Reviews in Microbiology, Vol. 37, No. 1, pp 40-63 (2011).
- [2] Stroock, A.D., et al., Chaotic mixer for microchannels. Science, Vol. 295, No. 5555, pp. 647-651 (2002).
- [2] Q. Ramadan, V. Samper, D. Poenar, and C. Yu, Biomed. Microdevices, vol.8, p. 151 (2006)
- [3] T. Deng, G. M. Whitesides, M. Radhakrishnan, G. Zabow, and M. Prentiss, Appl. Phys. Lett. Vol. 78, p. 1775 (2001)
- [4] H. Lee, A. M. Purdon, V. Chu, and R. M. Westervelt, Nano Lett., vol. 4, p. 995 (2004),
- [5] R. Wirix-Speetjens and J. de Boeck, IEEE Trans. Magn. Vol. 40, p. 1944 (2004).
- [6] W. Mao, Z. Peng, P. J. Hesketh, A. Alexeev, Microfluidic mixing using an array of superparamagnetic beads," APS Meeting, Dallas, Texas, March 21 - 25, (2011).
- [7] Alexeev, A., R. Verberg, and A.C. Balazs, Modeling the motion of microcapsules on compliant polymeric surfaces. Macromolecules, vol. 38(24): p. 10244 (2005).
- [8] Mao, W. and A. Alexeev, Hydrodynamic sorting of microparticles by size in ridged microchannels, Physics of Fluids, vol.23(5) p. 051704 (2011).
- [9] Furlani, E. P. Permanent magnet and electromechanical devices materials, analysis, and applications. 2001. Available from: <http://www.engineeringvillage.com/controller/servlet/OpenURL?genre=book&isbn=9780122699511>.
- [10] Furlani, E.P., Analysis of particle transport in a magnetophoretic microsystem. Journal of Applied Physics, vol.99(2) p. 2492 (2006).
- [11] Rosensweig, R.E., Ferrohydrodynamics. 1997, Mineola, N.Y.: Dover Publications.

### CONTACT

DL Owen, [gtg983r@mail.gatech.edu](mailto:gtg983r@mail.gatech.edu)



## 5. Application:energy

(please choose category from list)

## Presentation

### HIGH EFFICIENCY ENERGY CONVERSION FROM LIQUID JET FLOW

*Yanbo Xie, Lennart de Vreede, Trieu Nguyen, Hans L. de Boer, Ad Sprenkels, Albert van den Berg, Jan C.T. Eijkel*

BIOS lab on chip group, MESA+ Institution of Nanotechnology, University of Twente

#### ABSTRACT

We investigate the performance of a microfluidic energy conversion system using jetting flow. Preliminary results indicate that a voltage can be generated of several kilo-Volts and energy efficiencies can reach 15%. Such values are by far the highest obtained for electrokinetic conversion systems and open new perspectives for energy conversion.

#### KEYWORDS

liquid jet, energy conversion; streaming potential

#### INTRODUCTION

The energy crisis is one of the most pressing topics due to the rapid increase of electrical power consumption and projected decreasing availability of traditional sources of energy such as fossil and fuels. Novel sources of electrical energy, such as fuel cells and solar cells are therefore developed to replace the traditional sources of energy. Such new energy sources should preferably cause less harm to our environment than traditional ones, for example by not producing carbon dioxide or toxic chemicals. A relative little known method of energy conversion is electrokinetic conversion of fluidic mechanical energy to electrical energy.[1]

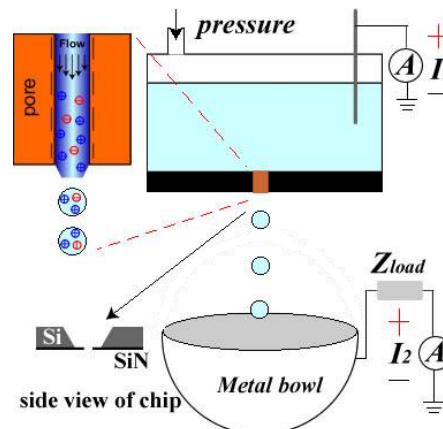
Electrokinetic energy conversion relies on the transport of the layer with net charges that is present close to most solid/liquid interfaces. When this charged layer is transported in a channel, an ionic current is generated (streaming current) as well as a potential difference between the channel ends (streaming potential).[2] In the past ten years, many investigators have tried to enhance electrokinetic energy conversion efficiency using micro- or nanochannels. The highest experimental efficiencies reached were about 5%[3-5] when nanopores were used in which double layers of opposing walls partially overlapped. Theoretical predictions using numerous assumptions predicted maximal efficiencies in such systems of 40%. [6]

Recently, Duffin and Saykally reported on the use of a microjet for energy conversion. [7] Under high pressure water was forced through a membrane orifice, forming a jet which broke up into droplets. The droplets were charged due to the electrokinetic

phenomenon described above, and the charged droplets were collected by a downstream electrode. These authors found an energy conversion efficiency of around 10% in this two phase system.

In their analysis, Duffin and Saykally attribute the enhancement of efficiency in their two-phase system with respect to the values in traditional single phase systems to the occurrence of low resistance fluidic entrance flow in the pore due to its short length and high pressure applied, as well as to electrical isolation offered by the air which prevented back flow of current. In this paper, we however show that the energy conversion mechanism of this jetting flow is radically different from the traditional electrokinetic energy conversion mechanism. We show it relies on a direct conversion of the kinetic droplet energy conversion potential energy. This knowledge of the conversion mechanism allowed us to minimize the loss factors and obtain a conversion efficiency of 15%.

Setup



*Figure 1: A liquid jet produced by pressure applied across a  $\text{Si}_3\text{N}_4$  membrane pore breaks into (charged) droplets which are collected in a stainless steel bowl. Streaming current  $I_1$  flows through the pore and current  $I_2$  flows through large electrical resistors. Both are measured by a pico-ammeter.*

Figure 1 shows the scheme of our experimental setup. A silicon nitride membrane was machined with a thickness of 650nm containing a single pore with a diameter of 10  $\mu\text{m}$ . The chip was mounted with a pressurized reservoir and liquid was expelled through the pore using a gas source (99%  $\text{N}_2$ ) controlled with a high accuracy gas pressure pump (Fluigent MFCS).



The liquid jet produced from the pore broke into droplets, which were received by a stainless steel bowl. Droplets were charged due to the streaming current generated in the pore. Two pico-ammeters were used to measure the generated upstream streaming current ( $I_1$ ) as well as the current ( $I_2$ ) flowing from the bowl to ground. Series connected resistors ( $4 \times 500\text{G}\Omega$ ;  $4 \times 400\text{G}\Omega$  and  $2 \times 100\text{G}\Omega$  resistors with voltage ratings 1kV) were used to generate the electrical output power, which was calculated by multiplying  $I_2$  with the generated voltage  $V = I_2 \times R_{\text{load}}$ .

### Loss factors

Several factors can be identified in this process, which can be split in two stages. Firstly during the pore passage the input energy is incompletely converted to kinetic energy due to the friction with the pore wall. We can define the efficiency for this conversion as a power ratio:

$$\text{eff}_1 = P_{\text{kin}} / P_{\text{in}} = (P_{\text{in}} - P_{\text{pore fric}}) / P_{\text{in}} \quad (1)$$

where  $P_{\text{kin}}$  and  $P_{\text{in}}$  (J/s) are droplet kinetic power and hydrodynamic input power, respectively. Here and  $p_{\text{pore fric}}$  is the power dissipation by pore friction. Subsequently, during the passage of the droplets through the air, the kinetic energy is in completely converted to electrical energy due to air friction and by charge evaporating from droplets. We can define efficiency for this second conversion as:

$$\text{eff}_2 = P_{\text{el}} / P_{\text{kin}} = (P_{\text{kin}} - P_{\text{air fric}} - P_{\text{evap}}) / P_{\text{kin}} \quad (2)$$

where  $P_{\text{el}}$  is electrical output power;  $p_{\text{air}}$  is the power dissipation by friction with air and  $P_{\text{evap}}$  is the power loss due to charge evaporating from the droplet. The final energy conversion efficiency then can be calculated from multiplying the efficiencies of both separate processes:  $\text{eff} = \text{eff}_1 \cdot \text{eff}_2$ .

### Experimental results

Charged droplets were collected by the bowl. They generated electrical current from the downstream reservoir through the large resistors to ground, creating a voltage, which produced an electrical field. Since the polarity of voltage and droplets are the same, droplets needed to overcome this electrical field to reach the bowl, while being subject to other energy dissipation processes, such as air friction and evaporation.

The dissipation by air friction will decrease the velocity of droplets. Hence, to reach the bowl the kinetic energy of droplets has to be larger than the sum of electrical energy and air friction energy dissipation. The latter can be estimated from drag force:  $FD = 0.5 \cdot \rho u^2 CDA$ , where  $\rho$  is mass density of

fluid,  $CD$  is drag coefficient;  $A$  and  $u$  are reference area and velocity of droplet. Since  $P_{\text{air fric}} = \int FD dx$ , the droplets trajectory length ( $h$ ), is directly related to the air friction power dissipation, making it quite more important.

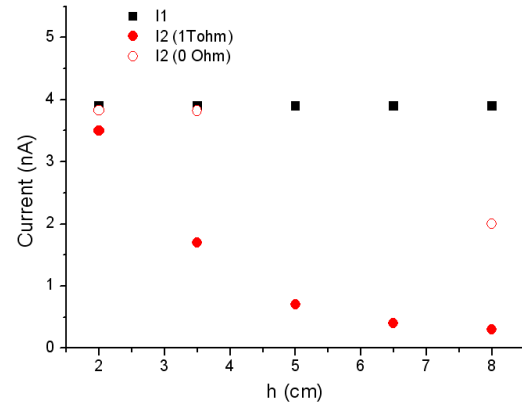


Figure 2. Current  $I_1$ (black) and  $I_2$ (red) as function of droplets trajectory distance  $h$ .  $I_2$  decreases quickly as  $h$  increases, when a 1 TOhm resistance is connected. This decrease is much smaller without a resistance connected.

Figure 2 shows an experiment where we obtained the current (1.9bar applied pressure) as a function of distance  $h$ . Current  $I_1$  is generated at the top reservoir and independent of the distance  $h$ , but  $I_2$  (both with and without a 1TOhm resistance connected) decreases with increasing distance  $h$ .  $I_2$  however decreases much faster when 1 TOhm resistance was connected. This is probably due to the increase in the droplets trajectory time spent in the electrical field generated in the bottom circuit: the voltage generated on the bowl will decelerate the droplets, causing the charge and droplets to evaporate more.

To prevent the charge loss in air, in another experiment we kept the trajectory length  $h$  around 3cm and studied the influence of the resistance. Upstream ( $I_1$ ) and downstream ( $I_2$ ) current are shown in figure 3 as a function of load resistance ( $R_{\text{load}}$ ). Both  $I_1$  and  $I_2$  decreased slightly with increasing load resistance. The upstream current was always larger than the downstream current, which can be explained by droplet loss in the air.

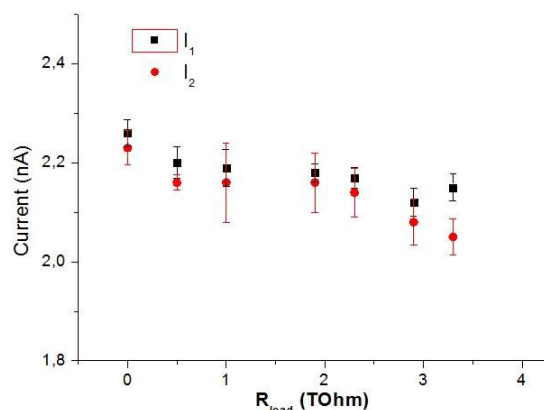


Figure 3: Upstream ( $I_1$ ) and downstream ( $I_2$ ) current decreased only slightly with increasing load resistance.

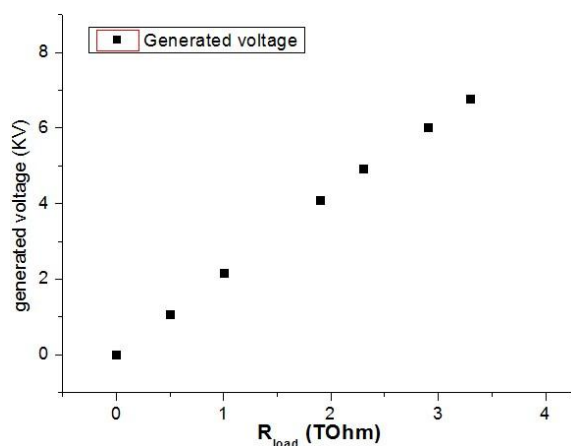


Figure 4: The generated voltage calculated by multiplying  $I_2$  and load resistance, could reach 6.77KV.

The generated voltage between bowl and membrane can be calculated by  $I_2 R_{load}$ , and is shown in figure 4. It increases almost linearly with resistance (maximum 6.77KV). The output power can now be estimated as  $P_{out} = I_2 \cdot V$ .

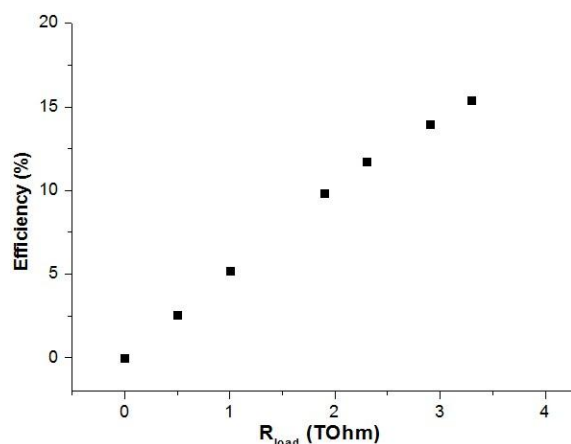


Figure 5: Energy conversion efficiency increased with load resistance, reaching 15% at a resistor value of 3.3 T.

The input power was estimated by multiplying the constant input pressure ( $\Delta P_{in}: 1.1 \text{ bar}$ ) with the flow rate ( $Q: 0.90 \mu\text{L/s}$ ):  $P_{in} = \Delta P \times Q$ . Finally, the efficiency obtained ( $eff = P_{out}/P_{in}$ ) is shown in Figure 5. The efficiency increased with load resistance, reaching a maximum of 15%. At present experiments are performed to confirm and improve these preliminary results. The value of 15% represents the highest value obtained at present in electrokinetic energy conversion experiments.

## REFERENCES:

- [1] Pennathur S., Eijkel J. C. T., Albert van den Berg, Lab Chip, 7, 1234-1237 (2007)
- [2] Osterle, J.F., J. Appl. Mech. 31, 161 (1964).
- [3] Yang, J., F.Z. Lu, L.W. Kostiuk, and D.Y. Kwok, J. Micromech. Microeng. 13 (6), 963-970 (2003).
- [4] van der Heyden, F.H.J., D.J. Bonthuis, D. Stein, C. Meyer, and C. Dekker, Nano Letters 7 (4), 1022-1025 (2007).
- [5] Xie, Y.B., X.W. Wang, J.M. Xue, K. Jin, L. Chen, and Y.G. Wang, Appl. Phys.Lett. 93 (16), 163116 (2008).
- [6] Y.Ren., D. Stein., Nanotechnology. 19, 195707 (2008).
- [7] Duffin, A.M. and R.J. Saykally, J. Phys. Chem. C 112 (43), 17018-17022 (2008).

## CONTACT

Yanbo Xie [y.xie@utwente.nl](mailto:y.xie@utwente.nl)

Jan Eijkel [J.C.T.Eijkel@utwente.nl](mailto:J.C.T.Eijkel@utwente.nl)

## 5. Applications

## REALIZATION OF A MINIATURIZED MASS SPECTROMETER BASED ON A MICROFLUIDIC DEVICE

*W.J. Kuipers<sup>1</sup>, M. Deilmann<sup>1</sup>, M. Gerding<sup>1</sup>, T. Neumann<sup>1</sup>, M. Vogt<sup>1</sup>,  
G. Quiring<sup>2</sup>, R.M. Ramírez Wong<sup>2</sup>, M. Reinhardt-Szyba<sup>2</sup>, H. Wehrs<sup>2</sup> and J. Müller<sup>2</sup>*

<sup>1</sup> KROHNE Messtechnik GmbH, Duisburg, Germany

<sup>2</sup> Hamburg University of Technology, Hamburg, Germany

### ABSTRACT

Miniaturization is generally considered to enable widespread field application of mass spectrometry. The miniaturized mass spectrometer presented here is based on a microfluidic device, which integrates all components in a single self-aligned layer. The electrical and fluidic periphery of the microfluidic device has been moved first-time from a scientific measurement setup to an industrial mass spectrometer demonstrator.

### KEYWORDS

Miniaturized Mass Spectrometer, Microfluidic Device, MEMS, Process Analysis

### INTRODUCTION

Mass spectrometry is a powerful tool for the analysis of gases and vaporized liquids. Because of its high resolution in mass and concentration it is well-established in chemical, biological, and medical laboratories. The current trend in mass spectrometry goes towards robust and fast field applications, which can be found in healthcare, environmental analysis, homeland security, or process industry. However, field application is still rather limited due to the demand of current mass spectrometers on volume, power, infrastructure, specialist knowledge, handling, vacuum ( $10^{-8}$  –  $10^{-3}$  Pa), and financial resources.

Miniaturization is generally considered to enable widespread field application of mass spectrometry. Accordingly, several approaches have been undertaken to realize mass spectrometers by means of MEMS technology. However, this research mostly concerns the miniaturization of a specific mass spectrometer subsystem, such as e.g. the mass analyzer.

The portable mass spectrometer presented here is based on a microfluidic device that integrates all essential mass spectrometer functions (i.e. electron impact ionization, mass separation, and signal detection) on a single chip [1-5]. It allows for operation under relaxed vacuum conditions ( $< 1$  Pa), small volume and low weight, robustness against shock and vibrations, low power consumption as well as low cost and reproducible mass production.

The first part of this paper is concerned with the fully integrated mass spectrometer chip. The second part describes the corresponding electrical and fluidic

periphery of this microfluidic device, which has been moved first-time from a scientific measurement setup to an industrial miniaturized mass spectrometer (MS) demonstrator [3].

### MICROFLUIDIC DEVICE

Essential to successful realization of a fully integrated MS chip is the definition of all MS components by a single masking layer. It not only offers self-alignment of said components, but also enables straightforward fabrication. Although microfabrication is limited in sizing range and commonly restricted to  $2\frac{1}{2}$  D only, conventional MS components are not. Therefore, subsystems need a complete redesign or even alternative physical principles have to be applied using entirely new structures.

### Design

The functional plane of the MS chip is shown in Figure 1 and needs to be sandwiched in between additional top and bottom substrates. Not only to support various electrodes, but also to form capillary guiding structures and to realize different pressure stages while operating at a single base pressure.

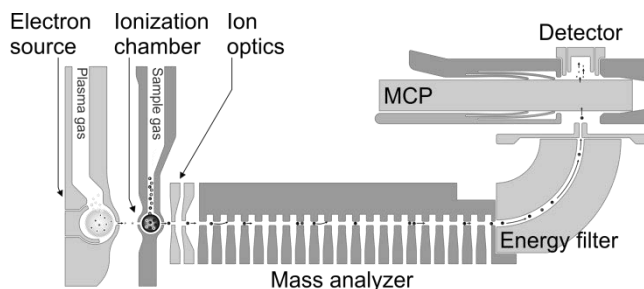


Figure 1: Layout of the MS chip

The working principle is best explained referring to Figure 1, starting at its left hand side, where electrons are extracted from a 2.45 GHz microwave plasma and accelerated into the ionization chamber. Ions are generated by electron impact ionization and then focused into the mass analyzer. At constant energy each mass-to-charge-ratio corresponds to a single final ion velocity. If it equals the velocity of a moving field-free zone in the mass analyzer, the ions are able to pass and reach the next stage. The 90° energy filter removes ions, which unintentionally passed the mass analyzer. An optional micro channel plate (MCP) in front of the detector provides on-chip current amplification.

### Electron source

The electron yield does not only depend on the rate of electron generation, but also on the efficiency of electron extraction and subsequent focusing. Electrons are efficiently focused into the ionization chamber, due to the contour of the outer walls of both the electron source and the ion source. It assures highest electrical field strength in between the orifices. Optimum field strength is obtained with a potential difference of 100 V, which closely resembles the optimum energy for electron impact ionization (70 eV).

The electron source is governed by both fluidic and electrical requirements. Aperture design, for example, is a compromise between minimum gas flow to maintain chamber pressure and extraction efficiency. The latter depends on the intrusion depth of the extracting field. Because secondary electrons are not created in the direct vicinity of the electrodes (dark space) and field intrusion is relatively weak, RF electrode design aims to minimize the dark space at the aperture electrode (ground). Furthermore, electrodes are designed to minimize reflected power at operating pressure (100 pA) as well as during spark ignition at increased pressure (900 pA).

With the aid of electron trajectory simulations optimum dimensions are found to be 600  $\mu\text{m}$  chamber diameter and 40  $\mu\text{m}$  aperture width. Stable argon plasmas can be operated down to 500 mW microwave power and 30 Pa chamber pressure.

### Ionization chamber

Similar to the electron yield, the ion yield depends on fluidic (i.e. gas pressure) and electrical parameters. Aperture width (40  $\mu\text{m}$ ) is a compromise between gas consumption and field intrusion at the ion outlet or electron current at the inlet. Although the ionization rate increases with the diameter of the ionization chamber, ion extraction only takes place near the aperture. Maximum ion yield is therefore obtained with a relatively small chamber diameter of 320  $\mu\text{m}$  at 15 Pa chamber pressure.

### Ion optics

The potential difference between the ion source at electron extraction potential (100 V) and the mass analyzer at ground potential accelerates ions up to an energy of 100 eV. It implies that each mass enters the mass analyzer with a unique velocity.

In between ion source and analyzer, two pairs of electrodes are responsible for the formation of a concentrated parallel ion beam. Therefore, ions are accelerated by the first and then decelerated by the second pair of electrodes. Arrangement and shape of the electrodes as well as the optimum potentials (-25 and 67 V) are determined using trajectory simulations.

### Mass analyzer

The micro MS is based on a new mass analyzer

concept. It is called synchronous ion shield (SIS) and can be considered as a velocity filter [1].

As can be seen from Figure 1 the mass analyzer consists of a comb structure and opposing finger electrodes. Whereas the comb structure is connected to ground, the finger electrodes are connected to a rectangular wave, alternating between 0 and 5 V, both in terms of time and space. As a result, there is a field-free region traveling through the mass analyzer and only ions traveling at analyzer speed are able to pass. Consequently, a complete spectrum is obtained by a frequency sweep, as each mass-to-charge ratio  $m/z$  corresponds to a single frequency  $f$  according to [1]:

$$m/z = kU(fx)^{-2}$$

where  $U$  represents the accelerating potential (100 V),  $x$  the spatial period consisting of two finger electrodes (400  $\mu\text{m}$ ), and  $k$  is a constant ( $1.93 \cdot 10^8 \text{ C/kg}$ ).

Based on the analyzer geometry only and assuming a large number of finger electrodes, the resolving power  $m/\Delta m$  can be approximated as [4]:

$$\frac{m}{\Delta m} = \frac{L}{4d}$$

where  $L$  stands for the overall analyzer length (4 mm) and  $d$  represents the distance between the finger electrodes (100  $\mu\text{m}$ ). Accordingly, the resolving power of the analyzer shown in Figure 1 is approximately 10.

### Energy filter

Thermal scattering in the ionization chamber and fringing fields in between the finger electrodes lead to energy and consequently mass distribution among the ions leaving the analyzer. Therefore, additional energy filtering is implemented after mass separation. The filter consists of a semicircular path, across which a constant electrical field is applied. Ions can only pass, when the centripetal force exerted by the electrical field equals the centrifugal force corresponding with the radius of the circular path (1.2 mm) and the set kinetic energy (100 eV).

### Detector

After optional on-chip amplification using a removable micro channel plate (MCP), ion detection is realized with a Faraday cup.

### Microfabrication

The MS chip is fabricated using standard wafer-based silicon-glass microtechnology. Electrodes of high spatial resolution and aspect ratio are made in highly-doped silicon with deep reactive ion etching (DRIE). Borosilicate glass is a suitable electrically isolating substrate material, which can be hermetically bonded to silicon by anodic bonding. Thin film conductors on the bottom glass substrate alloy with silicon electrodes at one end and allow for wire bonding at the other. The microfabrication sequence is schematically



shown in Figure 2. First, the silicon substrate of 300  $\mu\text{m}$  thickness is prepared for anodic bonding and the bottom glass substrate (500  $\mu\text{m}$ ) is provided with metal thin film conductors using sputter deposition and wet chemical etching (Figure 2a). Nickel serves as the conducting material, whereas gold patches alloy with silicon during anodic bonding (b). After bonding, all functional structures are fabricated simultaneously by DRIE trench etching (c) to prevent inhomogeneous etching due to aspect ratio dependent etching (ARDE). Subsequently, released silicon structures are removed (d), followed by anodic bonding of the top glass substrate (500  $\mu\text{m}$ ) (e). Finally, chips are singularized (f) and the top glass is partly removed to enable wire bonding (g). Chip dimensions are 7 mm x 10 mm x 1.3 mm.

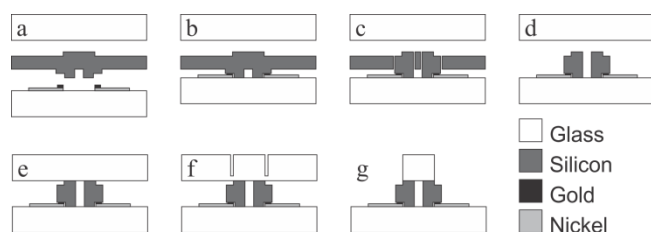


Figure 2: Microfabrication sequence

## Results

In order to obtain  $m/z < 1$  at  $f = 270$  MHz,  $x$  was artificially doubled (800  $\mu\text{m}$ ) by corresponding wiring of the finger electrodes. The result is shown in Figure 3 depicting a mass spectrum of methane, in which hydrogen is clearly visible at  $m/z = 1$  [4].

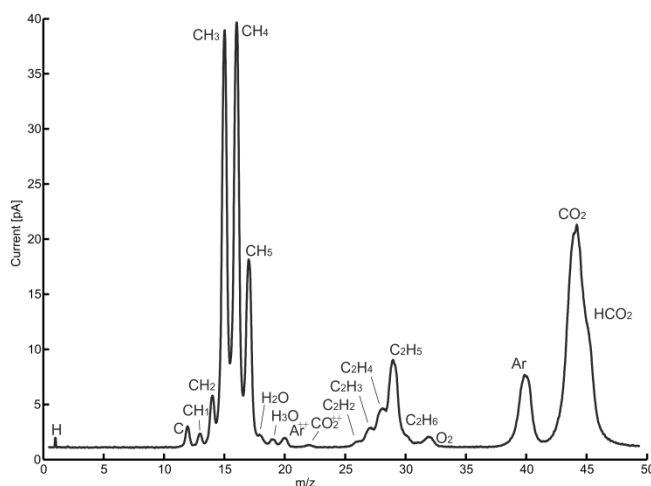


Figure 3: Methane spectrum [4]

The resolving power at the base is approximately 8.5, which is smaller than expected by theory (10). Other measurements [5] yield a resolving power at full width half maximum (FWHM) of 43 and a concentration detection limit below 100 ppm.

## MINIATURIZED MASS SPECTROMETER

Figure 4 shows a schematic representation of the complete MS demonstrator. The microfluidic device is the heart of the system, which otherwise consists of

fluidic (dark grey, ---) and electronic (grey, —) periphery. The fluidics can be subdivided in the vacuum system and the gas supply system.

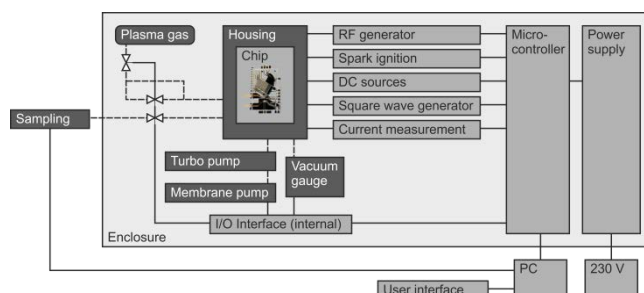


Figure 4: Schematic representation of the MS demonstrator

Figure 5 shows a photograph of the MS demonstrator. All components are arranged within a standard 19" table top enclosure (19" x 19") of 4 rack units (RU) height (7").



Figure 5: Photo of the MS demonstrator

Electronic plug-in units (3 RU height) consisting of printed circuit boards (PCBs) are inserted at the front and are all interconnected via two backplanes. The first backplane connects 4 off-the-shelf 230 V mains adapters (24 V (2x), 15 V, 5 V) with up to 6 functional modules at the second backplane.

The first functional plug-in unit accommodates an input/output interface for control of all fluidic components. It contains a number of relays for actuating gas valves and switching between preset rotational speeds of membrane pump and turbo pump. It also controls fan speed by pulse width modulation. Finally, integrated A/D conversion allows for digital read-out of pressure and turbo pump rotational speed.

The DC signals for electron and ion optics are generated using two separate plug-in units, housing either 4 unipolar or 2 bipolar sources each. For flexibility during chip development and tuning purposes DC signals are adjustable up to + or  $\pm$  150 V. Therefore, a non-inverting amplification circuit with feedback loop is supplied with + or  $\pm$  150 V from a Royer converter. 16 bit D/A conversion of the input voltage results in output

quantization below 5 mV.

The microwave generator occupies another plug-in unit. It generates up to 2 W microwave power at 2.45 GHz. Frequency stabilization is realized with a phase locked loop (PLL). Read-out of power, reflected power, and bias voltage allows for plasma monitoring and control.

The final plug-in unit directly connects to the horizontally arranged carrier PCB (Figure 6), carrying the microfluidic device. This so-called main unit also accommodates the microcontroller, which controls all other functional modules by SPI and communicates with an external PC by USB. Furthermore, spark ignition, analyzer signal generation, and processing of the amplified current signal is implemented here.

The high-voltage for spark ignition is generated by sudden interruption of a current carrying circuit comprising the primary coil of a transformer. Accordingly, a high-voltage is induced over the secondary coil, which is connected to on-chip spark electrodes.

A traveling wave with variable velocity is realized by means of two inverse square waves with variable frequency. A direct digital synthesizer (DDS) generates a sine wave, which is then transferred into two 180° phase shifted square waves oscillating between ground and 5 V using logic converters.

Whereas transimpedance current amplification is realized on the carrier PCB, close to the MS chip, 16 bit A/D conversion and averaging of up to  $2^{12}$  values using a field programmable gate array (FPGA) is implemented in the main unit.

Figure 6 shows the carrier PCB, which receives signals from the main unit via a multi-pin connector and transfers them via an inner layer into the vacuum chamber, where wire bonds are used to electrically connect the MS chip. The RF signal is received directly from the microwave generator via coaxial cable and SMA connectors. The carrier PCB also includes shielded ion current amplification and waveform improvement circuitry.

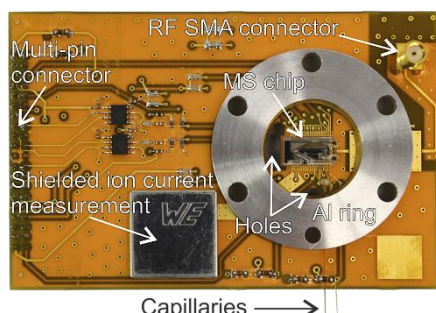


Figure 6: Photo of the carrier PCB

Large area holes in the carrier PCB fluidically connect the microfluidic device at its top to the vacuum system at its bottom side. Sample and plasma gas supply capillaries are glued into the microfluidic

device. Capillary vacuum feed through is realized by an aluminum ring with channels for both capillaries, which is glued to the PCB's top side. The vacuum chamber is covered with a PMMA lid (Figure 5).

The vacuum system is positioned behind the electronics (Figure 5) and comprises a membrane pump, a turbo molecular pump, and a vacuum gauge. A custom made vacuum adapter allows for compact assembly leaving space for a 1 l plasma gas cartridge with a pressure reducing regulator. The cartridge is fixed to the hinged back panel, which allows for easy replacement.

The ½ RU below the central 3 RU accommodates sample and plasma gas supply systems, consisting of a capillary system and an electrically controlled inlet valve. Capillary flow resistances are consistent with the operating pressures of the electron source (100 Pa) and the ion source (15 Pa) at the outlets, and plasma gas supply pressure of 0.5 bar (g) and sampling from atmospheric pressure at the inlets. Increased pressure for plasma ignition (900 Pa) is obtained by adding a second plasma gas flow path in parallel by opening an additional valve (Figure 4). Two radial cooling fans positioned in the upper ½ RU ensure stable electronic operation.

## CONCLUSIONS

The fully integrated microfluidic MS chip is characterized with 43 FWHM resolving power, a mass detection limit below  $m/z = 1$ , and a concentration detection limit below 100 ppm. The electrical and fluidic periphery has been successfully moved from a scientific measurement setup to an industrial miniaturized MS demonstrator.

## ACKNOWLEDGEMENT

This work was funded by the German Federal Ministry of Education and Research (BMBF) within the framework concept "Research for Tomorrow's Production" (02PC2100). Bayer Technology Services GmbH and Ehrfeld Mikrotechnik BTS GmbH are acknowledged.

## REFERENCES

- [1] Hauschild, J.-P., Wapelhorst, E., and Müller, J., Int. J. Mass Spectrom. 264-1, pp. 53-60, 2007
- [2] Reinhardt, M. et al., Int. J. Mass Spectrom. 295, pp. 145-148, 2010
- [3] Deilmann, M. et al., Automation 2012, Baden-Baden, Germany, June 13-14, 2012
- [4] Quiring, G., Reinhardt-Szyba, M., and Müller, J., MST Kongress 2011, Darmstadt, Germany, October 10-12, 2011
- [5] Quiring, G. et al., HEMS 2011, St. Pete Beach, FL, USA, September 19-22, 2011

## CONTACT

W.J. Kuipers: w.kuipers@krohne.com

# DETERMINATION OF THERMAL GAS PROPERTIES AND FLOW SPEED USING THERMAL FLOW SENSORS

C.J. Hepp<sup>1</sup>, F.T. Krogmann<sup>1</sup> and G.A. Urban<sup>2</sup>

<sup>1</sup>Innovative Sensor Technology IST AG, Wattwil, Switzerland

<sup>2</sup>Laboratory for Sensors, Department of Microsystems Engineering, University of Freiburg, Freiburg, Germany

## ABSTRACT

Time modulated heating of a thermal flow sensor was used in order to extract gas type at a certain flow rate. Experimental results of the sensor's response signals showed a correlation between gas type and flow velocity. It could be shown that thermal conductivity is the dominant physical parameter in a non flowing fluid. Moreover, it was possible to extract gas type and flow speed from amplitude and phase shift, if thermal conductivity of the gas varies.

## KEYWORDS

Thermal flow sensor, thermal gas properties, flow speed, AC-excitation

## INTRODUCTION

Different types of thermal flow sensors are developed since many decades from several research groups [1-3]. Many commercial applications require thermal flow sensors as well [4]. The sensors are characterized by a high sensitivity in low flow speed range, low power consumption and a simple implementation in the application [5]. One drawback of these sensors is the calibration to the specific gas, where they are applied in. A variation of the gas composition over time results in a change of thermal gas properties and therefore an inaccurate flow speed measurement. Due to this fact a recalibration of the system is necessary or further sensors have to be implemented for compensation in order to enable exact flow speed measurements. These issues increase the costs of maintaining the system and are furthermore complicated for the user [6].

Conductivity sensors based on the thermal principle are well known to analyze the gas composition and are established on the market [7-8]. In addition there are several publications, which show that calorimetric flow sensors can be used as well to distinguish thermal gas properties. In this case an alternating excitation is chosen in contrast to the state-of-the art DC-excitation. A prior condition is that the flow rate is already established or the sensors operate under no flow conditions [9-11]. Hence, the gas independent flow measurement is still a challenge, because the extraction of the thermal gas properties of an inconstantly flowing fluid is complex.

Table 1 summarizes the main thermal properties as thermal conductivity  $\lambda$ , specific heat capacity  $c_p$ , density  $\rho$  and thermal diffusivity  $a$  of several gases. The table expresses that there is a wide range in the thermal gas properties.

Table 1: Thermal gas properties of several gases at a temperature of 25°C and a pressure of 1bar [12].

Gas	Thermal conductivity $\lambda$ [W/(mK)]	Specific heat capacity $c_p$ [J/(gK)]	Density $\rho$ [10 <sup>-3</sup> g/cm <sup>3</sup> ]	Thermal diffusivity $a$ [10 <sup>-6</sup> mm <sup>2</sup> /s]
Air	0.026	1.006	1.169	22.11
CO <sub>2</sub>	0.0169	0.851	1.785	11.17
Ar	0.0178	0.522	1.612	22.33
He	0.1548	5.147	0.162	184.3

In this context, we used oscillating heat generation of an unsymmetrical resistor array on a thin membrane. Time depending heating offers more readout possibilities like amplitude and phase shift between heater and temperature sensors. Within this work we succeeded to extract a thermal gas property from the amplitude at different flow speeds. If phase shift is considered besides amplitude, it is possible to specify flow rate and gas species or composition in a certain flow range.

## SENSOR CHIP DESCRIPTION

The chip with a size of 10.8 mm x 4.8 mm x 0.51 mm is equipped with three platinum resistors. One centered resistor is used as joule heating element and is surrounded by an up- and downstream, high ohmic temperature sensor to detect changes in the gas temperature. The distance between temperature sensors and heater is different in order to maximize the temperature distribution on the chip.

All three resistors are located on a thermal isolating membrane (2 mm x 1 mm) to minimize the heat transfer from the heater to the temperature sensors through the membrane.

A detailed view of the sensor is presented in Fig. 1. The established fabrication process of the sensor is precisely described in a previous work [13].



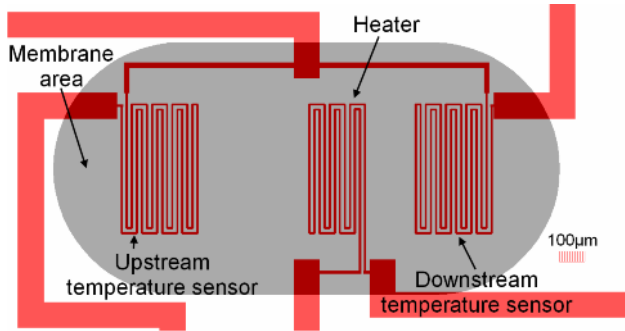


Figure 1: Detailed view of sensor structure.

## MEASUREMENT PRINCIPLE

### Electronic description

Heated platinum resistors vary the resistance value depending on the force of the convection and the gas where they are implemented. A constant applied voltage on the heater leads to a change of heating power. A controller, implemented in a LabView program, was developed in order to establish a constant heat generation of the sensor despite the gas and whether the flow velocity is changing or not.

The power generated by the heater is  $P = 5 \cdot (1 + \sin(2 \cdot \pi \cdot f \cdot t))^2$  [mW], where  $f$  is the oscillating frequency. The amplitude of the heat generation is 20 mW (peak-to-peak). The average temperature difference between heater and surrounding air is calculated to a temperature of  $T = 120$  K but varies for other types of gases. The excitation frequency is 1 Hz.

The oscillating voltages of each resistor are detected with a DAQ-card (NI USB-6225). A Fast Fourier Transformation (FFT) analyzes these voltages. Three periods are acquired. Afterwards the FFT is carried out for every resistor whose amplitude (half of peak-to-peak) and phase shift are obtained. The values at a frequency of  $f = 1$  Hz are further investigated.

A change in flow velocity and gas concentration results in an amplitude difference of the temperature sensors and a variation in phase shift between heater and temperature sensors.

### Description of measurement conditions

At first, the chip is characterized in a gas chamber without forced flow, in order to check the behavior of amplitude and phase shift for different gases. In a second step, the variance of these parameters is investigated by a change in flow velocity.

For investigations in no flow condition the sensor was inserted in a gas chamber (volume approximately two liters). Temperature and pressure in the chamber was controlled during the measurements and held under constant conditions (Temperature  $T = 25^\circ\text{C}$ , pressure  $p = 940$  mbar). The gases carbon dioxide, air, argon, helium and binary mixtures of argon and helium in different concentrations (20%/80%,

40%/60%, 50%/50%, 60%/40%, 80%/20%) are analyzed.

A rectangular flow channel (height = 1 mm; width = 2 mm) was designed and fabricated in order to evaluate the sensor signals in flow condition. The channel length was 100 mm in order to guarantee a fully developed flow profile. The sensor was placed in the middle of this channel.

The sensor was embedded in a cavity at the channel bottom. The sensor's topside is flush with the channel's bottom.

The fluid, which is analyzed, is in the flow channel above the membrane area. In any case the cavity below the membrane is filled with air (non flowing). The volume flow in the channel was adjusted with a mass flow controller between 10 sccm and 150 or 200 sccm (for evaluation the volume flow is converted into m/s). The variation of amplitude and phase shift in a flowing fluid was investigated for carbon dioxide, argon and air.

A laminar, parabolic flow profile in the channel can be assumed for all tested gases, since the Reynolds number of the used gases is between 155 and 270. These values are far below the Reynolds number of 2300, which is mentioned in the literature and describes the value until only laminar flow in a pipe occurs [14].

## CHARACTERISATION

### No Flow Condition

The theoretical values of thermal diffusivity and conductivity of the analyzed gases are obtained by commercial software [12]. Thermal conductivity and diffusivity in different concentrations of the binary gas mixture (argon and helium) are presented in Table 2. Further values of the thermal gas properties are taken from Table 1.

Table 2: Thermal gas properties of a binary gas mixture of argon and helium at a temperature of  $25^\circ\text{C}$  and a pressure of 1 bar [12].

Gas concentration	Thermal conductivity $\lambda$ [W/(mK)]	Thermal diffusivity $\alpha$ [ $10^{-6}$ mm <sup>2</sup> /s]
Ar 20%; He 80%	0.0317	37.75
Ar 40%; He 60%	0.0496	59.08
Ar 50%; He 50%	0.0605	72.15
Ar 40%; He 60%	0.0733	87.35
Ar 20%; He 80%	0.1546	126.57

Amplitude versus thermal diffusivity and conductivity is shown in Fig. 3 and Fig. 4. An empirical correlation was found out by comparing the



figures. As can be seen, amplitude corresponds to thermal conductivity and not to thermal diffusivity. By that, it is possible to correlate the response of the element to the thermal conductivity of the gas. The amplitude values of carbon dioxide and argon show a deviation of 1%, the amplitude values of air and argon differ about 23%. The thermal conductivity of argon and carbon dioxide has a difference of 5%, air and argon of 32%.

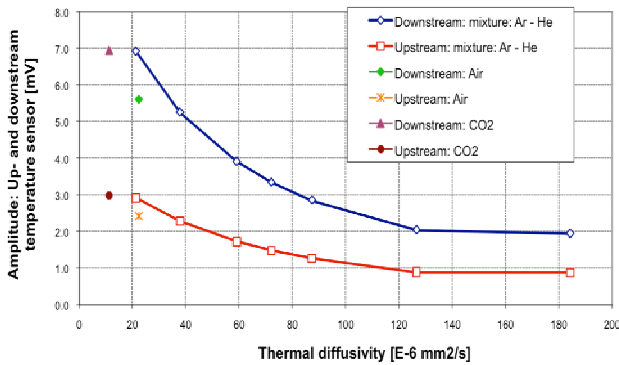


Figure 3: Amplitude versus thermal diffusivity.

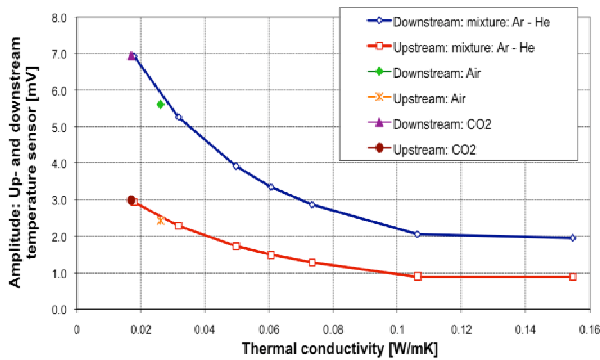


Figure 4: Amplitude versus thermal conductivity.

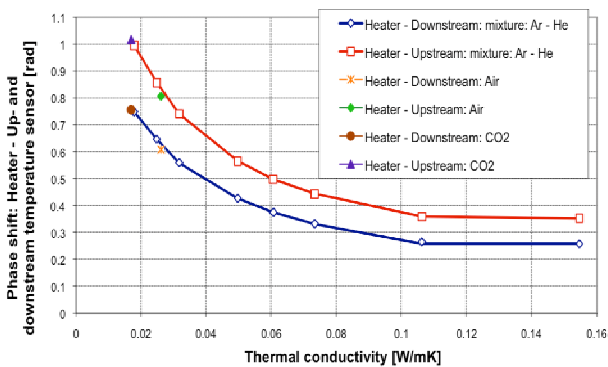


Figure 5: Phase shift between heating element and up- and downstream temperature sensors as function of thermal conductivity.

Almost the same resolution regarding the thermal conductivity is shown in Fig. 5. This figure presents phase shift as function of thermal conductivity. The difference in phase shift between argon and carbon dioxide is 2%. The sensitivity drops if the thermal conductivity increases. No correlation was found

between phase shift and thermal diffusivity.

As the figures 3-5 show, a detection of gas composition in a non-flowing fluid can be handled.

### Change in flow velocity for certain gases

Figure 6 shows that flow speed has a significant influence on amplitude. For all tested gases, the amplitude of the downstream resistor increases and is almost stable between 0.4 m/s and 1.25 m/s.

The amplitude values of the downstream resistor show no significant difference between carbon dioxide and argon. These two gases have almost the same thermal conductivity (5% deviation). These results correlate to the no flow experiments. The amplitudes of air and argon show a high difference (35%). Thermal conductivity of these two gases is not the same either, as Table 1 shows.

Within this flow range it can be assumed to distinguish between the gases air and argon or carbon dioxide. A gas type distinction is possible, if the thermal conductivity of the gas is different.

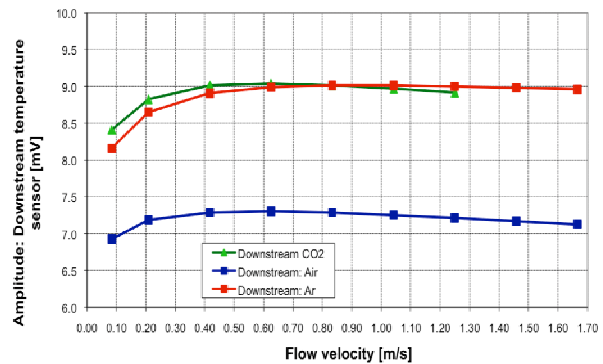


Figure 6: Amplitude variation of downstream temperature sensor as function of flow velocity.

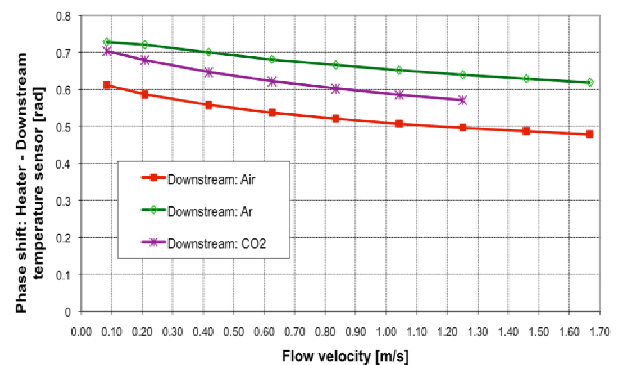


Figure 7: Phase shift between heating element and downstream temperature sensor as function of flow speed.

Phase shift is also strongly affected from flow speed (Fig. 7). An increase in flow speed decreases phase shift between heating element and downstream resistor. No curves show the same progression by a variation in flow speed, although an almost equal shape is suggested from the sections above.

Taken both approaches - phase shift and amplitude - into account, it is possible to detect gas and flow speed simultaneously. Hence, an accurate flow measurement can be carried. Firstly gas species is extracted from amplitude. In a second step flow speed is assessed by phase shift.

### Discussion

The carried out measurements suggest that the generated heat is much better and faster conducted in the fluid with an increase in thermal conductivity, due to decreased temperatures at the resistors and phase shift.

Flow shifts the primarily symmetrical distributed heat downstream; this leads to an increase of the amplitude. Furthermore, the heating element is cooled with a rising flow speed. Both issues together can be an explanation of the curve flatness in a certain flow range. A decreasing phase shift with increasing flow velocity can be caused by a lower mean heat flux path through the fluid, which results from a decreasing boundary layer. Based on the carried out measurements, no reason of the phase shift behavior for gases with same thermal conductivity can be found during a variation in flow velocity. Since the propagation speed of the generated heat waves is more affected by the thermal diffusivity and/or the volumetric heat capacity, a closer look into the relationship between phase shift and these parameters is necessary for the future work.

### CONCLUSIONS

In this paper new experimental results were presented, which show that it is possible to extract the gas type by the use of thermal flow sensors under certain conditions. No flow and flow measurements for different gases are performed in order to get an experimental correlation between the amplitude of a thermal flow sensor and the type of gas. It could be shown that the main physical parameter for this relationship is thermal conductivity. By using an AC-excitation and analyzing the response signal in phase and amplitude of a distanced platinum resistor, both, gas type and flow speed, can be derived as long as the thermal conductivity differs between the gases.

### REFERENCES

[1] B. van Oudheusden, A. van Herwaarden, "High-sensitivity 2-D Flow Sensor with an Etched Thermal Isolation Structure", *Sensors and Actuators A: Physical*, Vol. 22, No. 1-3, pp. 425-430, 1989.

[2] M. Elwenspoek, "Thermal flow micro sensors", *Proc. Semiconductor Conference, 1999. CAS '99 Proc. 1999 International*, Oct. 5-9, Sinaia, Romania, 1999, pp. 423-435, Vol. 422.

[3] F. Kohl, A. Jachimowicz, J. Steurer, R. Glatz, J. Kuttner, D. Biacovsky, F. Olcaytug, G. Urban, "A micromachined flow sensor for liquid and gaseous fluids", *Sensors and Actuators A: Physical*, Vol. 41, No. 1-3, pp. 293-299, 1994.

[4] Innovative Sensor Technology IST AG, "Datasheet, Flow Sens FS5/FS5A, Thermal Mass Flow Sensor for all-purpose use in Gases", accessed August 25<sup>th</sup>, 2012, [http://www.ist-ag.com/eh/ist-ag/resource.nsf/imgref/Download\\_DFFS5\\_E1.0.pdf/\\$FILE/DFFS5\\_E1.0.pdf](http://www.ist-ag.com/eh/ist-ag/resource.nsf/imgref/Download_DFFS5_E1.0.pdf/$FILE/DFFS5_E1.0.pdf)

[5] A. Cubukcu, E. Zernickel, U. Buerklin, G. Urban, "A 2D Thermal Flow Sensor with sub-mW power consumption", *Sensors and Actuators A: Physical*, Vol. 163, pp. 449-456, 2010.

[6] T. Lammerink, F. Dijkstra, Z. Houkes, J. van Kuijk, "Intelligent gas-mixture flow sensor", *Sensors and Actuators A: Physical*, Vol. 47, No. 1, pp. 380-384, 1995.

[7] I. Simon, M. Arndt, "Thermal and gas-sensing properties of a micromachined thermal conductivity sensor for the detection of hydrogen in automotive applications", *Sensors and Actuators A: Physical*, Vol. 97-98, pp. 104-108, 2002.

[8] P. Tardy, J.-R. Coulon, C. Lucat, F. Menil, "Dynamic Thermal Conductivity Sensor for gas detection", *Sensors and Actuators B: Chemical*, Vol. 98, No. 1, pp. 63-68, 2004.

[9] A.S. Cubukcu, G. Urban, "Sensitivity maximizing and error-reducing design of a flow and thermal property sensor", *Proc. of the EuroSimE Conference, Freiburg, Germany*, April 21-23, 2008, pp. 1-6.

[10] H. Ernst, A. Jachimowicz, G. Urban, "Dynamic thermal sensor-principles in MEMS for fluid characterization", *IEEE Sensors Journal*, Vol. 1, No. 4, pp. 361-367, 2001.

[11] A.S. Cubukcu, G. Urban, "Simulation and fabrication of a 2D-flow sensor for simultaneous fluid characterization", *Proc. of the Eurosensors XXIII Conference, Procedia Chemistry, Lausanne, Switzerland*, Sept. 6-9, 2009, pp 887-890.

[12] NEL PPDS – Physical Properties of Fluids

[13] C. Hepp, F. Krogmann, J. Polak, M. Lehmann, G. Urban, "AC Characterisation of Thermal Flow sensors with Fluid Characterisation Feature", *Proc. of the 16<sup>th</sup> Int. Conference on Solid-State Sensors, Actuators and Microsystems – Transducers, Beijing, China*, June 5-9, 2011, pp 1084-1087.

[14] F. Incropera, D. DeWitt, T. Bergman, A. Lavine, "Fundamental of Heat and Mass Transfer", 6<sup>th</sup> edition, John Wiley, 2007.

### CONTACT

Christoph J. Hepp, christoph.hepp@ist-ag.com

## 1. Sensors

### ONLINE LIQUID CALIBRATION TECHNOLOGIES

*D. Liang<sup>1</sup>, T. G. Muniyogeshbabu<sup>2</sup>, L. Tanguy<sup>2</sup>, A. Ernst<sup>2,3</sup>, R. Zengerle<sup>1,2,4</sup>, P. Koltay<sup>2,3</sup>*

<sup>1</sup> HSG-IMIT - Institut für Mikro- und Informationstechnik, Georges-Koehler-Allee 103, 79110 Freiburg, Germany

<sup>2</sup> Laboratory for MEMS Applications, IMTEK - Department of Microsystems Engineering, University of Freiburg, Georges-Koehler-Allee 103, 79110 Freiburg, Germany

<sup>3</sup> BioFluidix GmbH, Georges-Koehler-Allee 103, 79110 Freiburg, Germany

<sup>4</sup> BIOSS - Centre for Biological Signaling Studies, University of Freiburg, Germany

#### ABSTRACT

Three online liquid volume calibration methods – image processing, flow sensing and capacitive droplet detection – are simultaneously used to measure the volume of single nanoliter sized droplets. Good precision (imaging method  $CV < 2.7\%$ , flow sensing method  $CV < 3.2\%$ , capacitive droplet sensing method  $CV < 4.1\%$ ) and reasonable accuracy in comparison to a gravimetric reference method have been observed in 192 dispensing experiments. Besides the quantitative performance comparison, the three methods are qualitatively benchmarked. The benchmark shows all of these methods to be consistent and to enable equally non-contact measurement of liquid volumes with CV better than 5% in the volume range 12 to 54 nl.

#### KEYWORDS

Online volume calibration, droplet detection, capacitive sensor, flow sensor

#### MOTIVATION

The miniaturization of liquid-handling devices is requiring new calibration technologies for volumes in the nanoliter range. In comparison to standard offline calibration technologies like gravimetric [1] or photometric [2] methods, where the liquid used for calibration is wasted, non-contact online methods have big advantages such as the continuous monitoring, the possibility

to apply closed loop control mechanisms and a smaller volume detection limit. Based on previous studies [3-5] a multi-principle calibration system has been built. With this system single liquid droplets in the range from 2 nl to 70 nl can be characterized simultaneously with three online methods – the imaging, the flow sensing and the capacitive sensing method. A comprehensive study and benchmark of the three online calibration methods is presented.

#### EXPERIMENTAL SETUP

In order to compare the performance of the three online liquid calibration methods with the same nanoliter droplet, the experimental setup shown in Figure 1 has been used. A PipeJet P9 dispenser (Biofluidix GmbH, Germany) is employed to generate the droplets. The dispenser was selected because of its high reproducibility and the open reservoir that does not require a pressure source to generate the droplet. Thus, the reservoir inlet could be connected to a flow sensor (HSG-IMIT, Germany), which measures the air flow into the reservoir during dispensing. From the air flow the liquid volume can be determined by integration of the flow signal over time [3]. In addition a capacitive droplet sensor is directly mounted below the nozzle of the dispenser. This sensor detects the change in capacitance when a droplet passes through the electrodes like described in previous work [4].

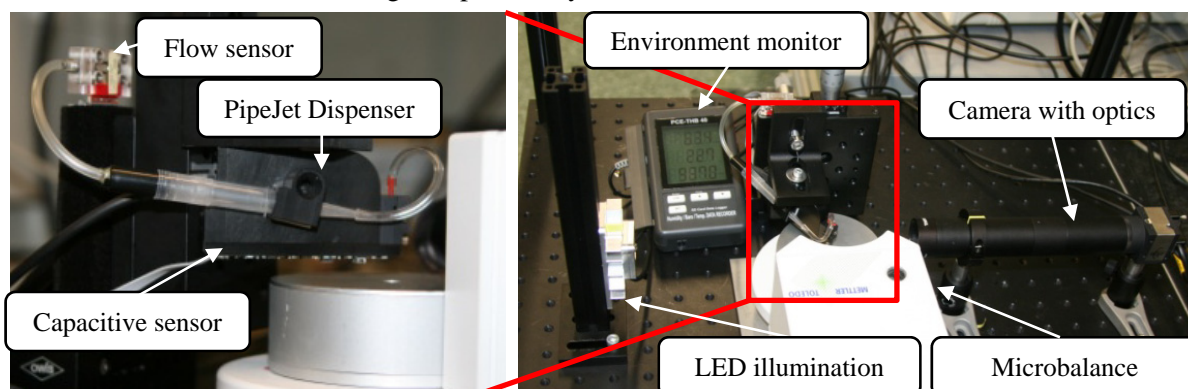


Figure 1: Experimental setup of the multi-principle liquid volume calibration station



Below the nozzle of the dispenser a microbalance XP2U (Mettler-Toledo, Switzerland) is placed in 5 mm distance for gravimetric reference measurements according to the GRM-R method [1]. This distance allows a stroboscopic camera to record the droplet in flight. With the imaging processing as described below the volume of the captured droplet can be precisely detected. The experimental setup includes environmental monitoring of humidity, temperature and pressure. Whenever necessary corrections with respect to the environmental factors have been made to achieve comparable results referring to  $T = 20\text{ }^{\circ}\text{C}$ .

### FLOW SENSING METHOD

The investigated flow sensing method [3] is realized by mounting a flow sensor at the opening of the dispenser reservoir and detecting the air reflow into the reservoir during droplet ejection (Figure 2(a)). The flow sensor involved in the presented method is an OEM air flow sensor from HSG-IMIT based on calorimetric measuring principle. In contrast to direct measuring the liquid flow signal the presented strategy with indirect measuring the air reflow can detect the volume independently of the fluid properties like density, viscosity and specific heat. A specific calibration for each fluid is therefore not required.

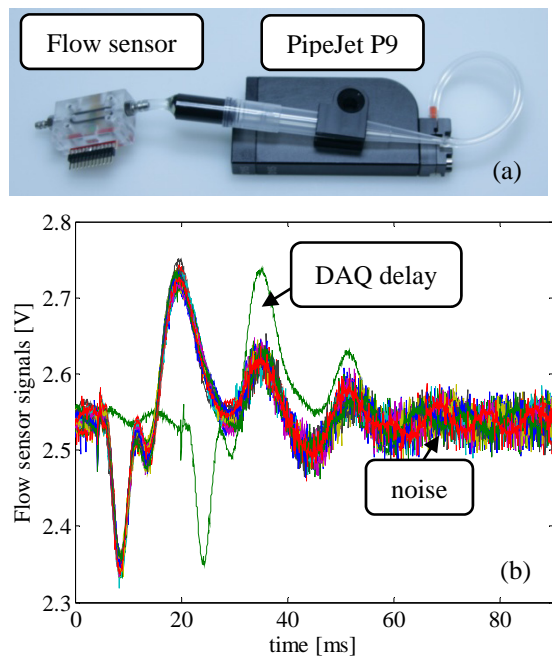


Figure 2: (a) Mounting of the flow sensor at the opening of the dispenser reservoir. (b) Typical flow sensor signals (24 measurements with 36 nl droplets).

The typical flow sensor signals gathered during dispensing are shown in Figure 3. Due to the working principle of the PipeJet dispenser, which creates a short backflow into the reservoir before droplet ejection, a negative peak can always be observed at the beginning of the data acquisition (DAQ) of the flow sensor signals. The volume is calculated from the flow by equation:

$$V_{flow} = F_1 \cdot \int U_{flow} dt + F_2 \quad (1)$$

Where  $V_{flow}$  is the measured volume of the flow sensing method.  $U_{flow}$  is the flow sensor signal.  $F_1$  and  $F_2$  are calibration constants that have been experimentally determined. In this work  $F_1$  and  $F_2$  were calibrated by two experiments with 29 and 36 nl droplets.

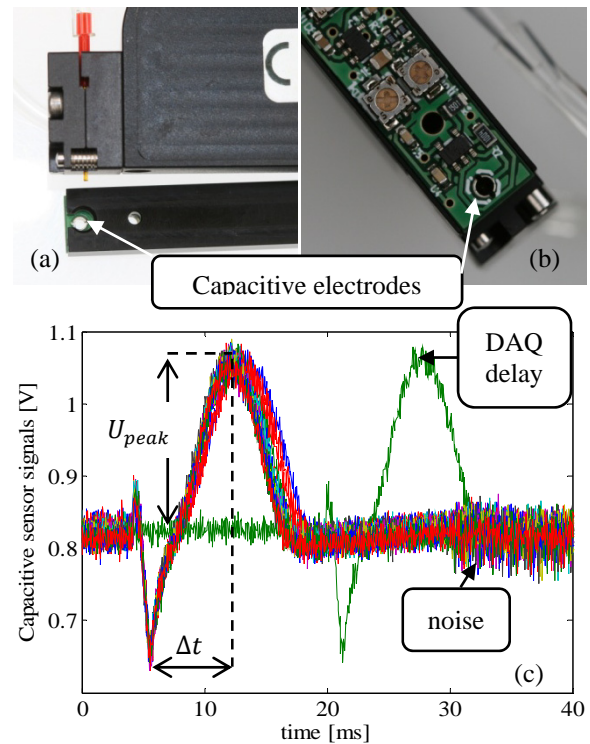


Figure 3: (a) Zoom view of PipeJet nozzle and capacitive sensor (b) Inside view of capacitive sensor (c) Typical capacitive sensor signals (24 measurements with 36 nl droplet).

### CAPACITIVE SESENSING METHOD

The presented capacitive sensing method is realized through a capacitive sensor prototype from BioFluidix (Figure 3(a), (b)) described in [4]. The typical signal when a droplet passes through the capacitive electrodes is shown in



Figure 3(c). The signal begins with an obvious negative peak that is caused by capacitive coupling effect when the ejected droplet is still coupling with the grounded nozzle. The droplet volume  $V_{cap}$  has a linear relation to the positive peak value  $U_{peak}$  and the droplet velocity, which is proportional to  $\frac{1}{\Delta t}$  described the equation [4]:

$$V_{cap} = C_1 \cdot U_{peak} + C_2 \cdot \frac{1}{\Delta t} + C_3 \quad (2)$$

Where  $U_{peak}$  is the positive voltage peak value of capacitive sensor signal.  $\Delta t$  is the time between the negative peak and positive peak.  $C_1$ ,  $C_2$ , and  $C_3$  are calculation constants that needs to be calibrated. In this work  $C_1$ ,  $C_2$ , and  $C_3$  were calibrated by three experiments with 26 nl, 36 nl and 54 nl droplets.

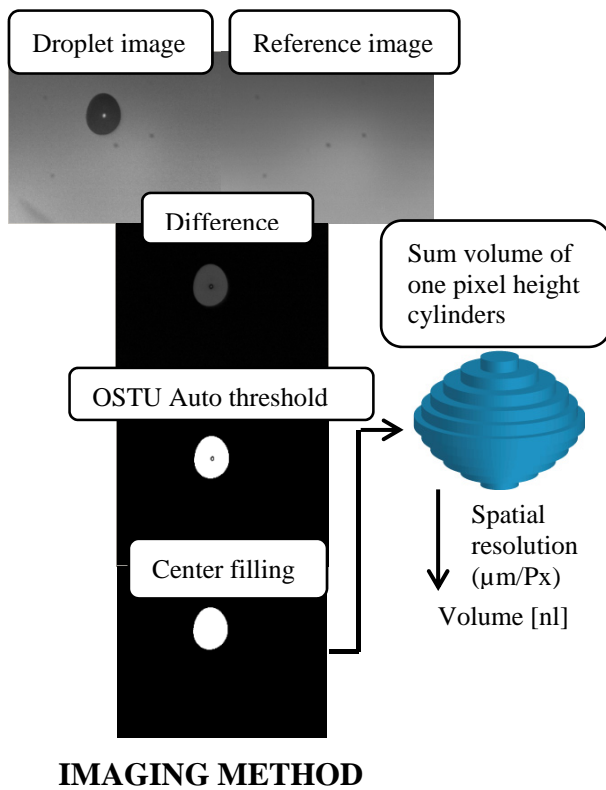


Figure 4: Working principle of the imaging method for volume reconstruction from droplet image

In stroboscopic imaging the droplet is photographed during flight with short shutter time (9µs). The captured droplet image is then firstly compared in greyscale value pixel by pixel with a reference image without droplet. With the Otsu auto-threshold algorithm [6] and a simple corresponding center filling algorithm the droplet is separated very clearly from the background

(Figure 4). The volume calculation from the droplet contour is described in [5]. The droplet is regarded as the stack of many cylinders, which have the height of one pixel each (Figure 4). The droplet volume is then the sum of the volume of all these small cylinders.

In order to get accurate volumes in nl the magnification of the used camera and optics had to be calibrated to yield a spatial conversion parameter. This calibration was experimentally carried out with a positive 1951 USAF test target which has traceability to NIST. The spatial conversion parameter was 1.986 µm/pixel.

## EXPERIMENTS AND RESULTS

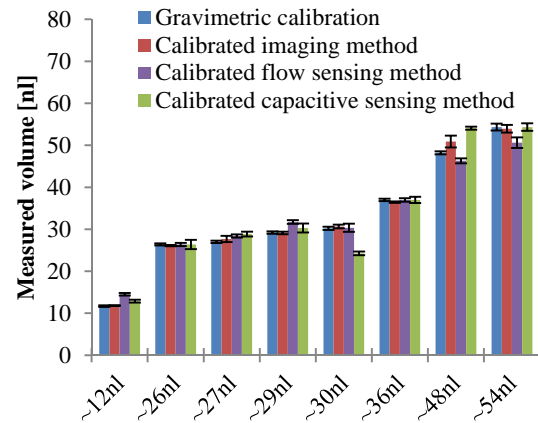


Figure 5: Benchmark results for all three methods

The results of 192 benchmark experiments for 8 different droplet volumes (24 dispenses for each volume) are presented in Figure 5. For all experiments double distilled water was used. The imaging method always provides the best repeatability in terms of the coefficient of variation (CV). It remains consistent with the gravimetric reference, except at 48 nl, where non-spherical shaped droplets have been observed as possible reason for this. The negative bias of the flow sensor results compared to the gravimetric reference at 48 nl and 54 nl may be caused by insufficient data acquisition time (90ms in experiments). Except experiments at 30 nl (electronic error) and at 48 nl (dispenser disturbed) the capacitive sensor has shown high consistency with the gravimetric reference.

## DISCUSSION

Besides the quantitative proofs of the performance, the three methods have been compared in a qualitative manner concerning Signal-to-Noise-Ratio (SNR), user-friendliness,

working range, integration size and liquid suitability (Figure 6). Due to the best SNR and simple calibration (better user-friendliness) the imaging method may have less risk to achieve reliable results than the other two methods. However, the imaging method as used here cannot deliver reliable results for liquid jets instead of droplets, which limits its application range to small volumes. High precision imaging can detect droplets down to picoliters but always needs special camera and optics, which increases the costs and the equipment size.

In contrast, the flow sensing method can be applied for liquid jet measurement as well, which extends its upper working range. In case of allowing modification of the reservoir as presented above, the size and the integration of the flow sensor can have advantages over the imaging method. In the presented experimental conditions the flow sensing method has lower SNR than the imaging method, which limits its application at very small volumes. The calibration of the flow sensor is also more complicated than for the optics and camera.

The most innovative method – the capacitive sensing – has unfortunately similar calibration difficulties and lower SNR, but it provides the smallest integration size as well as lowest costs. With some modifications the capacitive sensor might also be used for jet measurement under specific conditions. In our experiments the capacitive sensing method had almost the same lower limits of working range as the flow sensing method. All the three methods have in principle no limitation regarding the testing liquid.

## CONCLUSION

Three online liquid calibration technologies - the flow sensing, the capacitive sensing and the imaging method - have been benchmarked in both quantitative and qualitative manner. The quantitative evaluation of the three methods was carried out by measuring the same droplet with a special designed multi-principle liquid calibration station. The results show all of these methods to be consistent and to enable measurement of liquid volumes with CV better than 5% in the considered volume range (12-54 nL). The qualitative benchmark consists of the comparison of the three calibration methods in SNR, user-friendliness, working range, integration size and liquid suitability. Such a comprehensive experimental study of three different liquid calibration methods executed on the same droplet

has never been reported so far. All the three methods have been found to have good potential in further development of calibration standards or for smart integration of online sensing in micro fluid liquid handling devices.

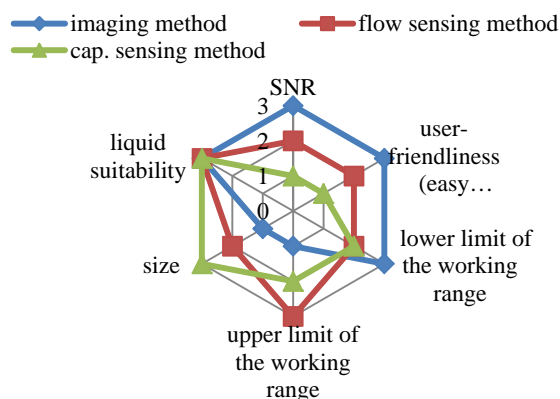


Figure 6. Qualitative comparison in terms of SNR, user-friendliness, working range, size and liquid suitability. Higher numbers show relative advantage.

## ACKNOWLEDGEMENT

The authors gratefully acknowledge financial support from the German Federal Ministry for Science and Education (BMBF) through the project “Smart Reagent Dosage” (SFK 16SV5119).

## REFERENCES:

- [1] D. Liang, et al, “Novel gravimetric calibration Method for nano liter liquid handling devices”, Proc. MFHS Conference, 2012
- [2] J. Bradshaw, et al, “Multichannel Verification System (MVS): a Dual-Dye Ratiometric Photometry system for performance verification ...”, JALA, 2005.
- [3] W. Streule, et al, “Kontaktfreie und medienunabhängige Volumenbestimmung in Nanoliter Dispensern”, Proc. MST-Kongress 10.-12. October 2005, Freiburg, Germany, 2005
- [4] A. Ernst, et al, “Numerical investigations on electric field characteristics with respect to capacitive detection of free-flying droplets”. Sensors 2012, 12(8), 10550-10565
- [5] K.Thurow, et al, “An optical approach for the determination of droplet volumes in nanodispensing.” J. of automated methods & management in chemistry, 2009
- [6] N. Otsu. "A threshold selection method from gray-level histograms". IEEE Trans. Sys., Man., Cyber. 9 (1): 62–66, 1979.

## A MICRO-THERMAL FLOW SENSOR FOR SHUNT BLOCKAGE DETECTION IN PATIENTS WITH HYDROCEPHALUS

*F.W. Hamlin, C. Reay and A.J. Gallant*

Durham University, School of Engineering and Computing Sciences, Durham, UK

### ABSTRACT

This paper details the design and testing of a micro thermal flow sensor, ultimately destined for long term implantation in the human body, for telemetric measurement of shunt patency in patients with hydrocephalus. The results show that the measurement technique is able to produce resolution and accuracy sufficient for this task at the flow rates present in a functioning shunt. This is accomplished whilst maintaining biocompatibility and ruggedness of the membrane, and only consuming approximately 600 mJ of energy for the measurement, both key factors for an implanted device.

### KEYWORDS

Thermopile, Hot-Film, Polyimide, Flow Sensor, Hydrocephalus

### INTRODUCTION

Hydrocephalus is a condition where an individual is subject to abnormally high intracranial pressure (ICP) due to a build-up of cerebrospinal fluid (CSF). Left untreated this can cause severe disability or potentially death. Treatment usually comprises of a surgically implanted shunt system, which regulates ICP by draining excess fluid into the peritoneal cavity in the abdomen. Shunt implantation rate is around 160000 per annum [1]. Unfortunately the failure rate is high, with around 30% failing in the first year and 5% annually after that, as a result 80% of shunts will fail at some point during their lifetime [1]. The main failure mode in shunt systems is through blockage of the silicone tube annulus. Shunt blockage is difficult to detect clinically, and shunt systems are often deemed to have failed and are then removed and replaced on suspicion of being blocked, without confirming the diagnosis. Unfortunately, many of these procedures are unnecessary with the removed shunt being in perfect working order, and other causes identified for the blockage like symptoms [2-3].

### DESIGN AND MANUFACTURE

#### Device Topology

To solve this problem, an implantable micro-flow sensor is being developed. The fabricated device consists of an isolated membrane suspended within the fluid flow. A resistive heater provides a consistent power input to the membrane. A thermopile consisting of 48 nickel - nichrome junction pairs in series then measures the temperature rise of the membrane required to dissipate this heat into the fluid flow. As the thermal resistance of the film to fluid interface is dependent on the boundary layer thickness and thus the flow velocity, as the flow velocity changes so does the temperature difference between film and fluid required to drive the applied thermal flux across the resistance into the fluid. Fig. 1 shows a schematic of the different metallisation layers within the device construction, the location of the heater element and coincident thermopile hot junctions (labelled A), and the reference cold junctions located out of the fluid flow within the sensor housing (labelled B) are also shown.

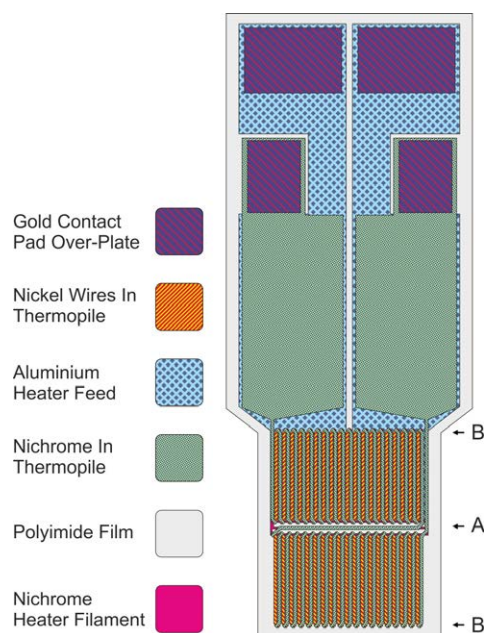


Figure 1. Sensor structure showing the location of the heater / hot junctions (A) and thermopile cold junctions (B)

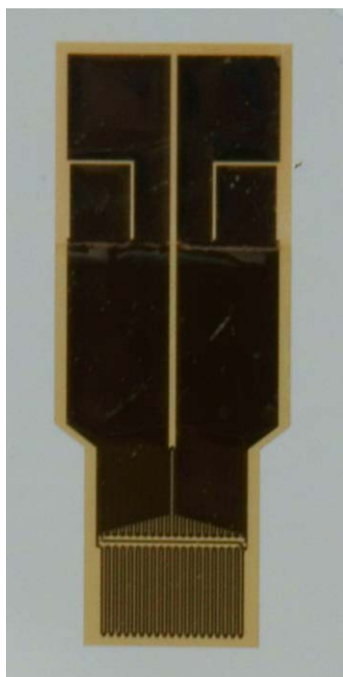


Figure 2. Photograph of released sensor, held between microscope slides and backlit to show thermopile detail.

The micro-fabricated membrane is fitted inside a two-part housing. This housing is produced using additive layer manufacturing from a UV cured acrylic in a multi-jet rapid prototype machine (ProJet HD 3000), which allows for a compact design with a precision bore, as well as locating features to ease assembly and hose barbs to be integrated into the housing design with minimal effort. During assembly the membrane is placed across the diameter of the bore of the housing to maximise thermal isolation and is glued in place. A low viscosity epoxy is used to control the glue film thickness and spread during the manual assembly procedure. The design and assembly of the housing is shown rendered in Fig. 3.

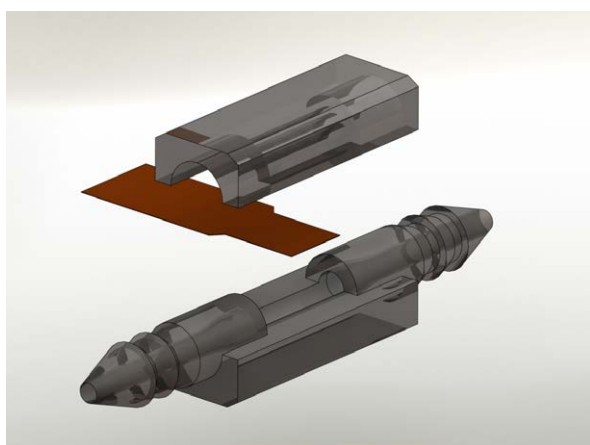


Figure 3 Exploded Render of Housing Assembly

For the purposes of testing, the film and housing were mounted to microscope slides to allow for easy manipulation of the device using a vacuum chuck and stage as well as allowing electrical contacts to be made using tungsten probes onto the exposed pads. This is shown in Fig. 4.

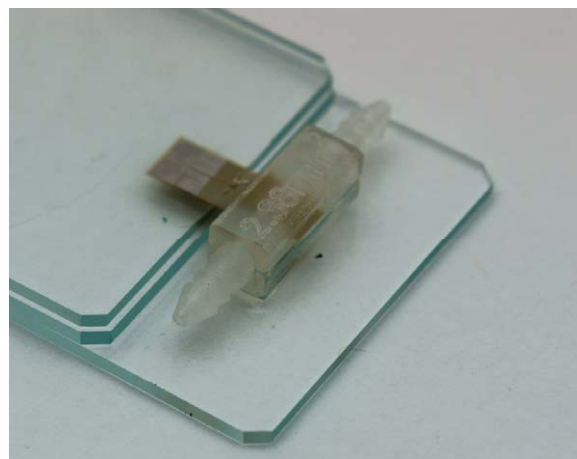


Figure 4. View of sensor within a rapid prototyped housing mounted to a glass microscope slide for testing

### Process Flow

The device is fabricated using standard lithographic micromachining techniques (see Fig. 5). A base layer, consisting of 3 layers of polyimide (HD Microsystems PI 2610) is spun, baked and then cured on a silicon substrate. Then the nichrome heater structure is sputtered and patterned using a bi-layer lift-off technique. An aluminium layer is subsequently laid down using an e-beam evaporator and patterned, again using bi-layer lift off, to lie on top of the previously deposited leads, this is done to minimise parasitic heating which, if ignored, can affect the temperature of the ‘cold’ reference junctions, thus reducing the accuracy of the sensor. These two metallisations are then encapsulated in a further single layer of polyimide, which allows for the thermopile elements to be stacked coincident with the heater structure. Additional sputtering and lift-off processes define the nickel and nichrome tracks for the thermopile. A final layer of polyimide encapsulates the whole device to ensure it is biocompatible. An aluminium hardmask, itself patterned by lift-off, is used to allow the dry etching of the polyimide using an  $O_2 / CF_4$  plasma to define the individual sensors from the polyimide sheet. A stainless steel shadow mask with the same dry etching technique is used to define the contact pad holes,



which are etched back through the PI layers until the required metallization layer is reached. Finally, without removing the shadow mask a thin cap of gold is evaporated to improve contact pad reliability.

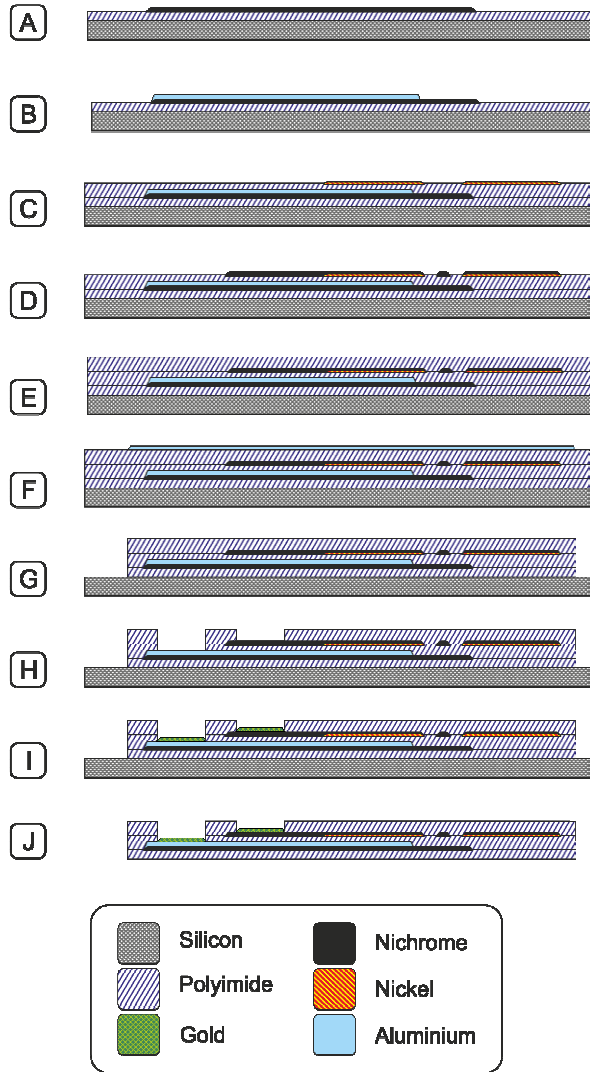


Figure 5. Process flow - (A) Spin Pi, pattern and deposit NiCr Heater. (B) Pattern and deposit Al over leads. (C) Encapsulate with Pi, pattern and deposit Ni thermopile elements. (D) Pattern and deposit NiCr thermopile elements. (E) Encapsulate with Pi. (F) Pattern and deposit Al hard-mask (G) Dry etch Pi, wet etch to remove hard-mask. (H) Dry etch Pi using shadow mask to expose contact pads. (I) Evaporate gold onto contact pads. (J) Peel From substrate.

## EXPERIMENTAL METHOD

Results were obtained using automated logging software controlling a syringe pump (WPI Aladdin), a constant current power supply (Keithley 6221) and a nanovoltmeter (Keithley

2182a). Flow rates were randomly generated to remove bias and the sensor was purged between readings to remove any pre-heated fluid remaining from the previous reading. The test procedure involved running the syringe pump at the desired flow rate and then waiting for continuously collected base line readings to stabilise to within 0.01 mV of each other, over a 5 second rolling window. The average over this period was taken as the heater-off control, the constant current power supply was then turned on, and set to deliver 15 mA or approximately 50 mW into the heater. A six second pause allowed the device to stabilise, then 10 readings of the thermopile output voltage were taken, each reading taken by the nanovoltmeter was set to integrate over 25 mains frequency cycles so as to best reject this source of noise from the system. A simple arithmetic mean of these readings was then performed to provide the output voltage data point for that flow rate. The data collection cycle was repeated until, when queried, the syringe pump reported < 0.5ml of fluid remaining in the system.

## RESULTS

Fig. 6 shows a typical set of results, the plotted points represent the difference between the output voltages obtained during the baseline and heater-on portion of the reading cycle, also shown is the accompanying power law calibration curve. For an isothermal flat plate experiencing heat loss through lamina forced convection, re-arrangement and expansion of the non-dimensional groups in Newton's law (Equation 1) implies that for a fixed input power  $P$ , device geometry and ambient fluid temperature, a relationship between flow and wall temperature can be described by equation 2.

$$P = \frac{k}{L} Nu_l A (\Delta T) \quad (1)$$

where  $k$  is thermal conductivity,  $L$  is length,  $A$  is area,  $Nu_l$  is the Nusselt Number and  $\Delta T$  is the temperature difference between wall and fluid

$$T_{wall} \propto (U_{\infty})^{-0.5} \quad (2)$$

where  $T_{wall}$  is the temperature of the plate wall and  $U_{\infty}$  is the freestream velocity.

The actual measured calibration relationship is given in equation 3. The reason for the difference is likely to be attributed to the boundary layer effects caused by the tube wall

and conduction across the substrate into the housing, we are currently modelling this behaviour to better understand these influences.

$$V \propto Q^{-0.38} + C \quad (3)$$

where  $V$  is the output voltage from the thermopile which is nominally proportional to the wall temperature, volumetric flow rate  $Q$  is proportional to  $U_{\infty}$ , and  $C$  is a constant.

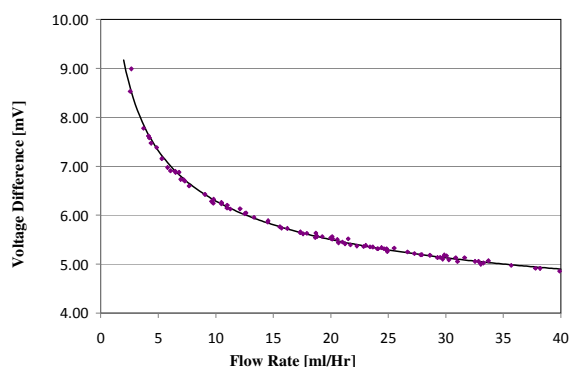


Figure 6 Graph showing the difference in thermopile output voltage between the heater-off state and the heater-on state at varying flow rates. The solid black line indicates the derived calibration curve.

Fig. 7 shows the analysis of the error obtained by comparing the actual flow rate to that inferred from the voltage and calibration curves. As can be seen the error is low, certainly sufficient to be able to distinguish between poorly functioning shunts (<6ml/Hr) and properly functioning shunts (>10ml/Hr) with the achieved error being around  $\pm 10\%$  of the indicated flow over this range.

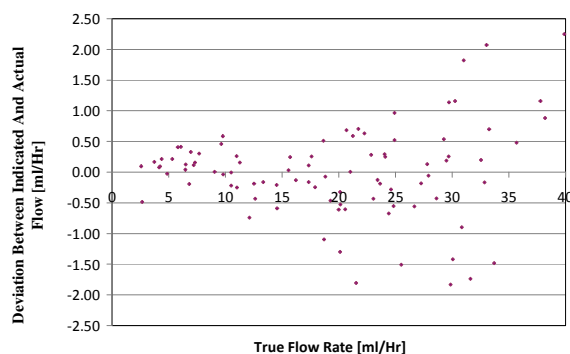


Figure 7. Graph showing observed error from the comparison of the true flow rate to that inferred from the measured voltage and the previously obtained calibration curve (Figure 3).

## REFERENCES

- [1] S. Sgouros, "Spina Bifida Hydrocephalus and Shunts," Medscape, 8 11 2011. [Online]. Available: <http://emedicine.medscape.com/article/937979-overview>. [Accessed 12 07 2012].
- [2] J. R. Madsen, G. S. Abazi, L. Fleming, M. Proctor, R. Grondin, S. Magge, P. Casey, T. Anor, "Evaluation of the ShuntCheck Noninvasive Thermal Technique for Shunt Flow Detection in Hydrocephalic Patients," Neurosurgery, vol. 68, no. 1, pp. 198–205, Jan 2011.
- [3] M. Hidaka, M. Matsumae, K. Ito, R. Tsugane, Y. Suzuki, "Dynamic measurement of the flow rate in cerebrospinal fluid shunts in hydrocephalic patients," Eur. J. Nucl. Med., vol. 28, no. 7, pp. 888–893, Jul 2001.

## CONTACT

\*Fred Hamlin, F.W.Hamlin@durham.ac.uk

# STANDARDS FOR LOW TO ULTRA-LOW FLOW RATES FOR DRUG DELIVERY APPLICATIONS<sup>1</sup>

*P. Lucas<sup>2</sup>, I.J. Nielsen<sup>3</sup> and C. Melvad<sup>3</sup>*

<sup>2</sup>Dutch Metrology Institute (VSL), Delft, Netherlands

<sup>3</sup>Danish Technology Institute, Aarhus, Denmark

## ABSTRACT

Primary standards for ultra-low flow rates are currently limited to flow rates down to 10 µl/min, whereas they have not been validated for flow rates lower than 100 nl/min. An extension of the metrological infrastructure is required in order to meet the demands of, amongst others, calibration of special drug delivery devices, HPLC and lab-on-a-chip applications. This research, therefore, focuses at upgrading the metrological infrastructure to enable traceable and accurate flow rate calibrations down to 10 nl/min. The resulting infrastructure will be used to characterize commercial flow meters as well as drug delivery devices.

## KEYWORDS

Primary standards, micro and nanoflow, drug delivery, intercomparison

## INTRODUCTION

For most drug delivery applications, the total delivered volume or mass is the parameter of interest. However, there are a significant percentage of drugs for which also the actual and temporal flow rate is important for a sound patient treatment. This is for example the case for drugs that have a very short half-life and a narrow therapeutic band width, or for drugs that require a very small blood concentration because of their toxicity.

With the existing metrological infrastructure, however, it is currently rather complicated, if not impossible, to properly set, measure and calibrate flow meters/ generators for flow rates lower than 10 µl/min. Such low flow rates are important for neonatology, critical drug delivery and multi pump infusion. Applications beyond drug delivery are, amongst others, HPLC and lab-on-a-chip applications. Therefore, in June 2012, an EU funded project [1]

started which aims at upgrading the metrological infrastructure such that devices working in this flow regime can be properly calibrated. Upon realization of the upgraded metrological infrastructure, this project will investigate and determined the characteristics of commercial flow meters and drug delivery devices. In this project the following institutes are cooperating: VSL (Netherlands, lead institute), CETIAT (France), CMI (Czech republic), DTI (Denmark), EJPD (Swiss), IPQ (Portugal) and Tubitak (Turkey).

The extension of the metrological infrastructure will be for flow rates down to 10 nl/min and will be realized with the combination of gravimetric standards and a relatively new concept based on volume expansion. The latter one will be used for flow rate calibrations from 10 nl/min to 1000 nl/min, whereas the gravimetric standards will cover flow rate calibrations down to at least 100 nl/min (the current state of the art is roughly 10 µl/min), thus allowing for a comparison. Gravimetric standards based on different principles will be developed, where the difference comes from how to avoid evaporation. These principles are either based on an oil-based cover, or on realizing an almost 100% relative humidity level. In the next sections these facilities will be discussed in more detail.

## STANDARD BASED ON VOLUME EXPANSION

For realization of the metrological infrastructure of the flow rates down to 10 nl/min, the concept of volumetric expansion will be used. In earlier work [2], it has been shown that this principle can be used to generate a constant flow rate. This concept can be compared with an open ‘thermometer’ where the expansion of some liquid, due to an increasing temperature, results in a volumetric flow rate.

The volumetric expansion can be correlated to a flow rate as follows. First, consider the definition of density, i.e.:

$$V = \frac{m}{\rho}$$

<sup>1</sup> This project is carried out with funding by the European Union under the EMRP. The EMRP is jointly funded by the EMRP participating countries within EURAMET and the European Union.

where  $V$  is the volume,  $m$  is the mass of the expanding water and  $\rho$  is the density. With relative simple analyses, one can show that the volumetric flow rate is given by:

$$Q = -\frac{1}{2} \frac{mk}{\rho^2} \left( \frac{\partial \rho}{\partial T} \right)_p$$

where  $Q$  is the volumetric flow rate,  $k$  the temperature gradient in time (thus the increase of temperature per unit time) and  $\left( \frac{\partial \rho}{\partial T} \right)_p$  the derivative of the density with respect to temperature at constant pressure.

From Eq. (2), it follows that this standard can be directly traceable to SI units. Therefore, one needs to determine the mass of the expanding water, the temperature gradient and the fluid properties. The latter can be traceable determined for any liquid, however, for pure water are detailed by Wagner and Pruß [3]. Next, the set up and calibration procedure will be discussed.

In Fig. 1 a sketch of the set up is shown, whereas in Figs. 2 and 3 the design is shown. The calibration procedure will be as follows. Connect the meter under test to the nano-flow generator. Prime the MUT (and the remainder of the facility) for at least 15 minutes by opening the valves and turning on the pump. By priming and using a degasser, bubble formation should be avoided. In case priming is not sufficient to remove the air, one could consider techniques as discussed in [4]. After priming the upstream valve is closed. Then, a temperature gradient is set with the temperature controlled water bath. This temperature gradient defines  $k$  in Eq. (2) and thus the flow rate.

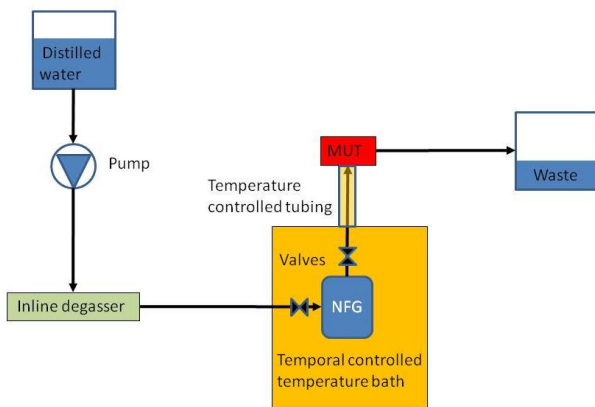


Figure 1: Sketch calibration set up.

With  $k$  known from the temperature measurement inside the reservoir, and the fluid properties known

from the Wagner and Pruß [3] equations, mass is the final parameter that needs to be traceable determined. For this the following procedure has been determined. First, the empty weight of the nanoflow generator is determined (this consists of roughly the black parts in Fig. 3). Then, the NFG is connected and the set up is primed with pure water. After a significant priming time, both valves are closed. Finally, the weight of the filled NFG is determined. The mass follows from the difference between the two mass determinations.

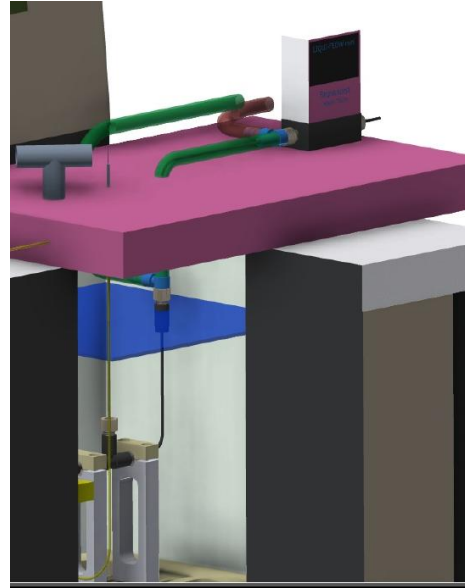


Figure 2: Current design. The reservoir holding the expanding liquid is inside a temperature controlled water bath. Above the water bath there is the required infrastructure to place and connect a meter under test.

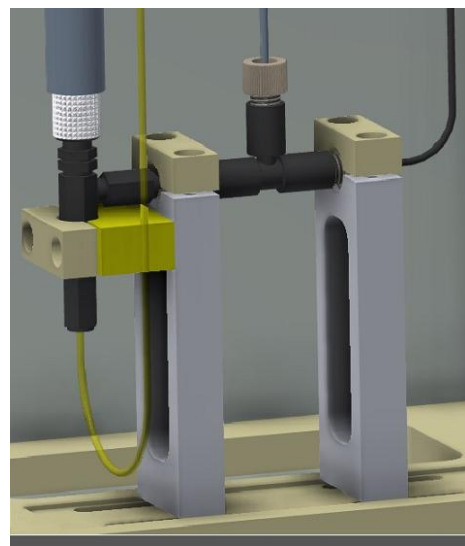


Figure 3: Close up design including reservoir. Yellow tube comes from inline degasser (Figure 2), black tube goes to meter under test. Gray tube (middle tube) contains the electrical wires of the thermistor (no liquid).



Currently, the design is under development. Upon completion, the set up itself will be realized. Thereafter, the set up will be validated by means of comparing the results with other primary standards. For the relatively 'large' flow rates a comparison will be made with the gravimetric standards. For lower flow rates a comparison is anticipated with a calibration set up by FH Lübeck [6].

## GRAVIMETRIC STANDARDS

The second type of standards used and developed in this project is of the well-known gravimetric principle. A gravimetric setup requires a scale, a measuring beaker, a flow-generator, a water reservoir and connections between them. In the project three different variations of the gravimetric principle will be realized. The difference comes from how the standards avoid evaporation. In the primary standard of DTI an oil-based coverage is used to avoid evaporation. The primary standards of CETIAT, EJPD and IPQ use water-saturated air around the measurement beaker to avoid evaporation, however based on different principles. Next, the gravimetric principle is discussed in more detail, where DTI's standard [5] is used as an example.

To get a stable reading of the balance, it is placed upon a vibration-free base. The measuring beaker is completely clean and acclimatized to the balance. On top of the water an oil-based cover is laid to minimize evaporation. Demineralized water is filled into a reservoir and then led through an inline vacuum degasser system consisting of an air permeable, but not water permeable membrane. If the Device under test (DUT) is a flow-meter then the demineralized, and now degassed, water runs through a pulsation free pressure driven pump and into the DUT (see Fig. 4). If the DUT is a syringe-pump the water is led directly to the syringe (see Fig. 5). Different types of pumps (syringe-pump or infusion-pump) are used depending on the DUT. The water exits the DUT and is led to the balance via non-water absorbing tubing, e.g. made of stainless steel. The tip of the tube is traversed through the oil-based cover and into the water in the measuring cup wherein the water is pumped.

In order to minimize the impact of environmental conditions, the balance is placed in a custom built, isolated chamber. The goal is to keep both temperature and pressure constant inside the chamber and thus to minimize draft and convection effects. The chamber is made of aluminum and has a window front to get access to the chamber and to get a clear view during operation. In order to facilitate a continuous

read out, the balance is read out by a computer with a frequency of 20Hz. Traceability for time is achieved with a dedicated timing card. By having continuous readout it is possible to detect the actual flow over time opposed to static weighing where the delivered mass is measured and divided by elapsed time.

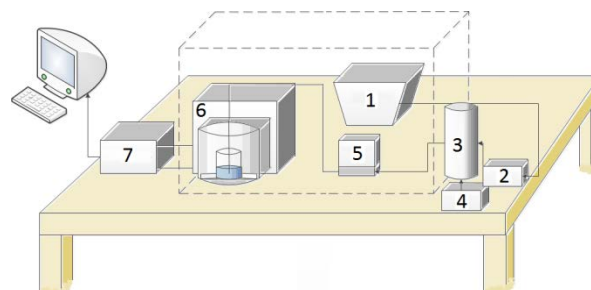


Figure 4 - Setup where DUT is a flow meter. Water is led from the reservoir (1) through the degasser (2) and into a pressure driven pump (3) which is connected to a compressor (4). From the pump water is led through the flow meter (5) to the balance (6) via non-water absorbing tubing. The tip of the tube is traversed through the oil-based layer and into the water in the beaker. The balance is connected to balance electronics (7) and to a PC.

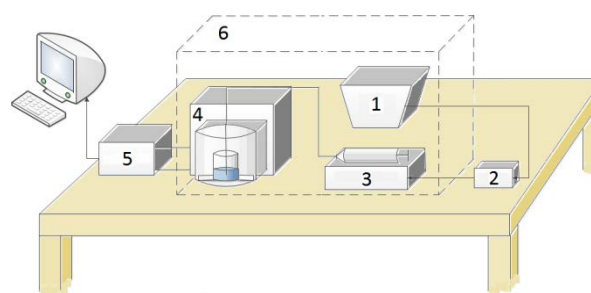


Figure 5 - Setup where DUT is a syringe pump. Water is led from the reservoir (1) through the degasser (2) and into the syringe pump (3). From the syringe pump water is led to the balance (4) via non-water absorbing tubing. The tip of the tube is traversed through the oil-based layer and into the water in the beaker. The balance is connected to balance electronics (5) and to a PC. The setup is enclosed in a chamber (6).

## INTERCOMPARISON

For studies in nano- and microflow, typically discrepancies between various studies are reported. This is often due to small differences in test methods combined with too optimistic uncertainty estimates. Due to the scaling laws of size, surface forces are dominant compared to volume related forces. Several new uncertainty components have been identified doing the thorough analysis of liquid microflow calibration.

Therefore, in order to verify the correct working of the various standards, an intercomparison will be carried out. Here the various principles will prove valuable, because various principles cannot lead to the same systematic errors. The intercomparison will be carried out in two steps. The first one is for flow rates in the range 10 ml/min down to 10  $\mu$ l/min and the second one is for flow rates from 50  $\mu$ l/min down to 1 nl/min. The intercomparison aims at validating the primary standards, hence upon serious discrepancies, the primary standards need to be upgraded.

## CHARACTERIZATION

After validation of the primary standards, they will be used to characterize commercial existing flow meter. Here, characterization implies the performance (uncertainty and deviation) as function of certain process parameters such as temperature. Finally, the primary and secondary standards will be used to characterize drug delivery devices.

## REFERENCES

- [1] Lucas, P., "Metrology for drug delivery", 2012 - 2015, partners VSL, Cetiat, CMI, DTI, EJPD, IPQ, Tubitak project summary at [http://www.euramet.org/index.php?id=emrp\\_c\\_all\\_2011](http://www.euramet.org/index.php?id=emrp_c_all_2011)
- [2] Beek, M.P. van der, Lucas, P., "Realizing primary reference values in the nanoflow regime, a proof of principle" *Measurement Science and Technology* 2010, 21, number 7.
- [3] Wagner, W. and Pruss, A. The IAPWS formulation 1995 for the thermodynamic properties of ordinary water substance for general and scientific use. *J. Phys. Chem. Ref. Data* **31**, 387–535. <http://dx.doi.org/10.1063/1.1461829>
- [4] Goldschmidtboeing, F., Rabold, M. and Woias, P. "Strategies for void-free filling of micro cavities", *J. Micromech. Microeng*, 16, pp 1321-1330, 2006
- [5] Melvad, C et al, "Design considerations and initial validation of a liquid micro flow calibration setup using parallel operated syringe pumps", *Meas. Sci. Technol.*, 21, 2010
- [6] Damiani, C., Klein, S., Wuttig, D. and Nestler, B., "Measurement and Control of Ultra-low Liquid Flowrates for drug delivery Application". *Proc. 14th North Baltic Conf. on Biomedical Engineering and Medical Physics NBC 2008*, Riga, Latvia, June 2008

## MICRO CORIOLIS MASS FLOW SENSOR FOR CHEMICAL MICROPROPULSION SYSTEMS

*R.J. Wiegerink<sup>1</sup>, T.S.J. Lammerink<sup>1</sup>, J. Groenesteijn<sup>1</sup>, M. Dijkstra<sup>1</sup> and J.C. Lötters<sup>1,2</sup>*

<sup>1</sup> University of Twente, Transducers Science and Technology, Enschede, The Netherlands

<sup>2</sup> Bronkhorst High-Tech BV, Ruurlo, The Netherlands

### ABSTRACT

We have designed a micromachined micro Coriolis flow sensor for the measurement of hydrazine ( $\text{N}_2\text{H}_4$ , High Purity Grade) propellant flow in micro chemical propulsion systems [1]. The sensor measures mass flow up to 6 mg/s for a single thruster or up to 24 mg/s for four thrusters. The sensor will first be used for measurement and characterization of the micro thruster system in a simulated space vacuum environment. Integration of the sensor chip within the micro thruster flight hardware will be considered at a later stage. The new chip has an increased flow range because of an integrated on-chip bypass channel.

### KEYWORDS

Micro Coriolis mass flow sensor, hydrazine flow sensing

### INTRODUCTION

The EU FP7 project PRECISE focuses on the research and development of a MEMS-based monopropellant micro Chemical Propulsion System ( $\mu\text{CPS}$ ) for highly accurate attitude control of satellites [1]. The availability of  $\mu\text{CPS}$  forms the basis for defining new mission concepts such as formation flying, advanced robotic missions and rendezvous maneuvers. These concepts require propulsion systems for precise attitude and orbit control maneuverability. Within PRECISE, research is performed towards a micro Coriolis mass flow sensor for measurement of the hydrazine propellant flow. The sensor will first be used for measurement and characterization of the micro thruster system in a simulated space vacuum environment. Integration of the sensor chip within the micro thruster flight hardware will be considered at a later stage. The required flow range is up to 6 mg/s for one thruster and up to 24 mg/s for four thrusters together.

Coriolis flow meters [2-4] are mostly used for measuring large flow rates, since the relatively weak Coriolis forces are correspondingly harder to detect for small flows. In general, the signal to noise ratio is very sensitive to fabrication and construction errors, as well as external influences of temperature and mechanical nature. In [5] we proposed to fabricate a micro Coriolis mass flow sensor using silicon nitride as the tube material. This resulted in a very thin

(1.2  $\mu\text{m}$ ) tube wall, so that the mass of the tube is small compared to the mass of the moving fluid. This was a significant improvement over [6] and [7], which use silicon as the tube material, leading to a relatively heavy and stiff tube. We demonstrated that a silicon nitride sensor could reach a resolution in the order of 3  $\mu\text{g/s}$  [5], however at that time no readout structures were integrated and a laser vibrometer was needed to optically measure the out-of-plane Coriolis motion of the tube. In [8, 9], we added an integrated capacitive readout and we demonstrated liquid flow measurement with a full scale range of 0.3 mg/s and a measurement accuracy of 1% of full scale.

In this paper, we present a new design with an integrated by-pass channel in order to extend the flow range from 0.3 mg/s to 6 mg/s as needed for the propellant flow measurement in the PRECISE project.

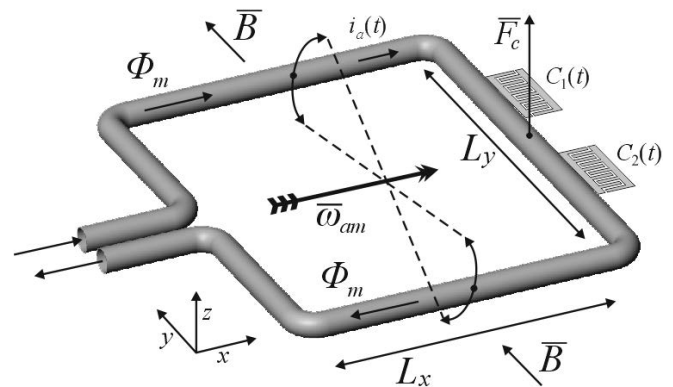


Figure 1: Operating principle.

### OPERATING PRINCIPLE

A Coriolis type flow sensor consists of a vibrating tube. An important advantage of Coriolis sensors is that they are only sensitive to the true mass flow, independent of flow profile, pressure, temperature and properties of the fluid (density, viscosity, etc.). Figure 1 shows a schematic drawing of the Coriolis sensor based on Lorentz force actuation and capacitive sensing. The tube is actuated in torsion mode, indicated by  $\omega_{am}$ . A mass flow  $\Phi_m$  inside the tube induces Coriolis forces that excite the other vibration mode, resulting in a vibration amplitude proportional to the mass flow. Both the actuation and the Coriolis movements are detected using two capacitors ( $C_1$  and

$C_2$  in Figure 1) at the outside of the loop. The mass flow can be extracted from the two output signals by detecting the phase difference, which is exactly proportional to the amplitude ratio of the Coriolis and actuation movements. By applying a bypass ratio of approximately 1:20 respectively 1:80 the measurable flow range can be extended from 0.3 mg/s up to 6 respectively 24 mg/s.

## FABRICATION

Here we give a brief summary of the fabrication process. A more detailed description can be found in [9].

Starting with a highly doped <100> p++ wafer, a 500 nm thick low stress LPCVD silicon-rich silicon nitride ( $\text{Si}_x\text{N}_y$ ) layer is deposited. Then the fluidic inlet/outlet holes are etched from the backside of the wafer using the  $\text{Si}_x\text{N}_y$  layer at the top side as etch stop (Fig. 2a). Next, a 1  $\mu\text{m}$  thick TEOS (tetraethyl orthosilicate) oxide layer is deposited and removed from the front side of the wafer. Then a 50 nm layer of chromium is sputtered on the front side of the substrate. This chromium layer is patterned using a mask containing arrays of  $5 \times 2 \mu\text{m}$  holes, spaced 3  $\mu\text{m}$  apart. This pattern forms the centerline of the final channel. The pattern is then transferred into the nitride layer by reactive ion etching and subsequently the channels are etched in the silicon using isotropic plasma etching (Fig. 2b). The TEOS layer and chromium mask are then removed and another  $\text{Si}_x\text{N}_y$  layer is grown with a thickness of 1.8  $\mu\text{m}$  to form the channel walls and seals the etch holes in the first nitride layer (Fig. 2c). A 10/200 nm layer of chromium and gold is sputtered (chromium serving as the adhesion layer for gold) and patterned to create the metal electrodes for actuation and readout (Fig. 2d). Next, the release windows are opened by reactive ion etching of the  $\text{Si}_x\text{N}_y$  layer (Fig. 2e) and the structure is released by isotropic silicon plasma etching (Fig. 2f)).

Figure 3 shows a photograph of a fabricated sensor chip. The sensor tube with dimensions  $L_x=2.5\text{mm}$  and  $L_y=4\text{mm}$  is clearly visible in the center of the chip. The tube diameter is approximately  $40\mu\text{m}$ . The entire chip measures  $7.5\text{mm} \times 15\text{mm}$ .

## INTERFACING ELECTRONICS

### Actuation

As mentioned earlier, actuation of the sensor is achieved by Lorentz forces using a constant external magnetic field in combination with an alternating current. The permanent magnetic field is created by two NdFeB rare earth magnets [10], placed on either side of the chip. The structure is actuated at the resonance frequency  $\omega_{am}$  and thanks to the quality factor of approximately 40 (in air) an actuation current

amplitude of 2 mA, corresponding to approximately 1 mW power dissipation, is sufficient to obtain vibration amplitudes in the order of 10  $\mu\text{m}$  at the outer corners of the sensor structure.

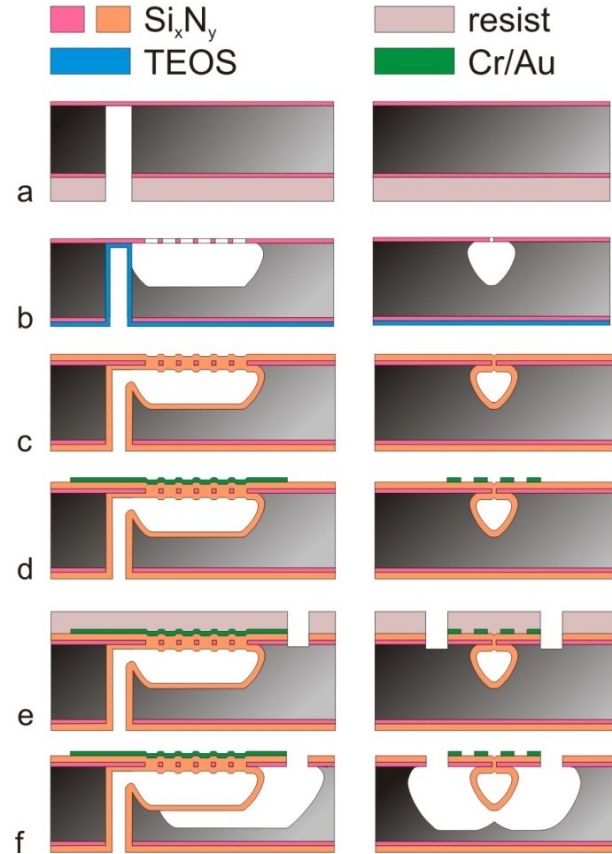


Figure 2: Outline of the fabrication process. Left column: cross-section along the length of the tube. Right column: cross-section perpendicular to the sensor tube.

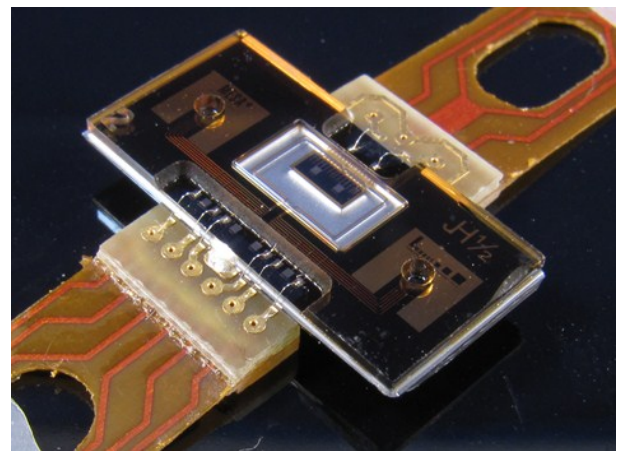


Figure 3: Photograph of the sensor chip, which measures  $7.5\text{mm} \times 15\text{mm}$ . Bond-pads for electrical connections are at the front side of the chip. Fluidic connections are located at the back side.



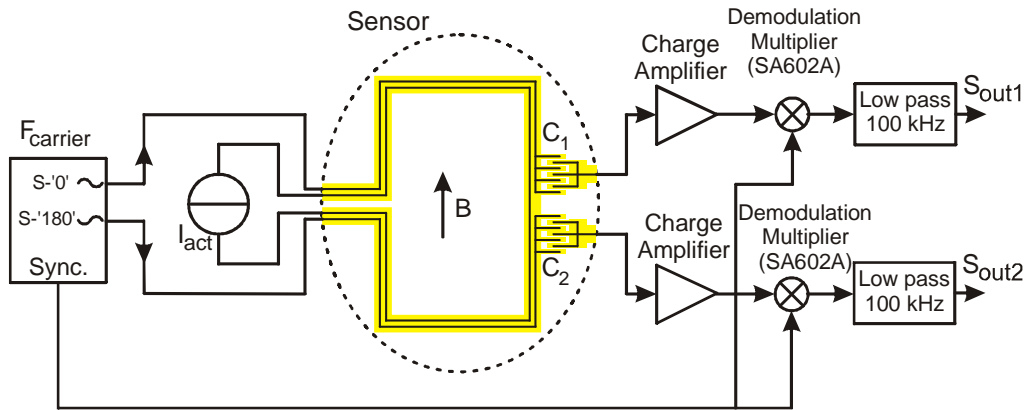


Figure 4: Schematic diagram of the actuation and readout electronics.

### Detection

A mass flow inside the tube induces Coriolis forces as indicated by  $F_c$  in Figure 1, resulting in an out-of-plane vibration of the tube. At maximum flow, the amplitude of the out-of-plane vibration is the order of 100 nm. To be able to detect these deflections, a capacitive on-chip read-out structure is used consisting of comb-like structures which function as a parallel plate capacitor when the two combs are separated out-of-plane. Using comb structures has two important advantages: 1) it greatly simplifies the fabrication process because only a single metal layer is needed, and 2) it avoids squeezed film damping which would occur in a traditional parallel plate capacitive readout. A disadvantage is that the operation of the structure relies on a static deflection of the tube due to the stress caused by deposition of the metal layer, which may vary in time, between different chips and as a function of temperature. Fortunately, the signal of interest is in fact the ratio between the Coriolis induced displacement and the actuation displacement, which are both equally affected by a change in comb distance.

### Complete sensor system

Figure 4 shows a schematic diagram of the complete sensor system with actuation and readout electronics. The comb-shaped readout capacitors are indicated by  $C_1$  and  $C_2$ . The combs that are attached to the moving sensor tube are connected to a signal source with frequency  $F_{carrier}$  equal to about 1 MHz. Two counter-phase signals are used so that substrate currents due to parasitic capacitance are largely eliminated. The fixed combs are connected to charge amplifiers and the resulting amplitude modulated signals are demodulated by multiplication with an in-phase reference signal using SA602 analog multipliers. Low pass filters with relatively high cut-

off frequency of 100 kHz are used to prevent phase shift at frequencies below 3 kHz, i.e. the vibration frequency of the tube.

The sum of the two output signals ( $S_{out1} + S_{out2}$ ) is a measure for the difference in capacitance ( $C_1 - C_2$ ), i.e. the actuation amplitude. The difference between the two output signals ( $S_{out1} - S_{out2}$ ) is a measure for the common variation in the capacitors due to the Coriolis effect. The measured mass flow can be extracted from the signals in two ways: 1) by measuring the sum and difference amplitudes separately using lock-in amplifiers at the vibration frequency of the tube and calculating the ratio between the amplitudes, and 2) by measuring the phase difference between  $S_{out1}$  and  $S_{out2}$ , which is in fact proportional to the amplitude ratio. Both ways result in similar measurement accuracy.

## INTEGRATED BY-PASS TUBE

In order to increase the full scale flow range a new design was made with an integrated fluidic by-pass. Figure 5 shows the new mask designs. An analytical model based on Bernoulli's equation and Poiseuille's law for tube flow shows that, at the required flow range and assuming all channels are the same, the bypass-ratio is mainly dependent on the difference in channel length and the amount of channels

A new batch of chips has been fabricated which are currently being characterized. Initial results will be presented at the conference.

## CONCLUSIONS

A design for a micromachined micro Coriolis flow sensor with on-chip by-pass channels has been presented. The new sensor will be used for the measurement of hydrazine ( $N_2H_4$ , High Purity Grade) propellant flow in micro chemical propulsion systems. The integrated by-pass channels reduce the flow

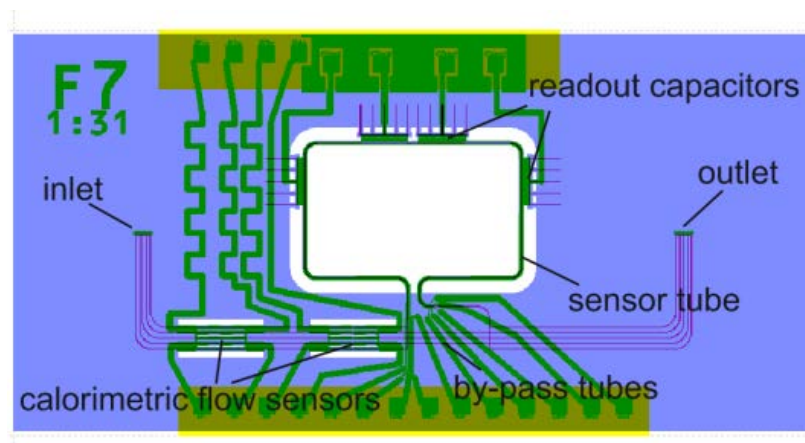


Figure 5: Mask layout.

through the sensor tube significantly, allowing the sensor to be used for mass flow up to 6 mg/s for a single thruster or up to 24 mg/s for four thrusters.

### ACKNOWLEDGEMENT

This research is part of the PRECISE project, which is funded from the European Community's Seventh Framework Programme ([FP7/2007-2013]) under grant agreement n° 282948.

Further information on PRECISE can be found on [www.mcps-precise.com](http://www.mcps-precise.com).

### REFERENCES

- [1] M. Gauer, D. Telitschkin, U. Gotzig, Y. Batonneau, H. Johansson, M. Ivanov, P. Palmer, R.J. Wiegerink, *48th AIAA/ASME/SAE/ASEE Joint Propulsion Conference & Exhibit 2012*.
- [2] R.C. Baker, *Flow. Meas. Instrum.*, 5, 1994, pp. 229-246.
- [3] M. Anklin, A. Drahm Wand Rieder, *Flow. Meas. Instrum.*, 17, 2006, pp. 317-323.
- [4] A. Mehendale and P.P.L. Regtien, *3rd Int. Symp. Sens. Sci. (Jülich, Germany, Jul. 18-21)*, 2005
- [5] J. Haneveld, T.S.J. Lammerink, M. Dijkstra, H. Droogendijk, M.J. de Boer and R.J. Wiegerink, *Proc. MEMS 2008*, pp. 920-923.
- [6] P. Enoksson, G. Stemme and E. Stemme, *J. MEMS* 6 (1997), pp. 119-125.
- [7] D. Sparks, R. Smith, J. Cripe, R. Schneider, N. Najafi, *Proc. IEEE Sensors Conference 2003*, pp. 90-92.
- [8] J. Haneveld, T.S.J. Lammerink, M.J. de Boer and R.J. Wiegerink, *Proc. MEMS 2009*, pp. 463-466.
- [9] J. Haneveld, T.S.J. Lammerink, M.J. de Boer, R.G.P. Sanders, A. Mehendale, J.C. Lotters, M. Dijkstra and R.J. Wiegerink, *J. Micromech. Microeng.*, 20, 2010, 125001, doi:10.1088/0960-1317/20/12/125001
- [10] <http://www.supermagnete.de>

### CONTACT

\* R.J.Wiegerink, [r.j.wiegerink@utwente.nl](mailto:r.j.wiegerink@utwente.nl)

# CMOS MEMS BASED MICROFLUIDIC SYSTEM FOR CYTOMETRY AT 5 GHz

*S. Guha<sup>1,2</sup> K. Schmalz<sup>1</sup> C. Meliani<sup>1</sup> Ch. Wenger<sup>1</sup> and W. Krautschneider<sup>2</sup>*

<sup>1</sup> IHP Microelectronics GmbH, Frankfurt (Oder), Germany

<sup>2</sup> Hamburg University of Technology (TUHH), Hamburg, Germany

## ABSTRACT

In this paper we investigate a co-integration approach of CMOS MEMS electrochemical sensor for a cytometric application to detect the concentration of cells in a suspension using label free dielectric spectroscopy at 5 GHz. The change in effective dielectric permittivity of a cell suspension with the concentration of cells was investigated based on dielectric dispersion. Interdigitated comb capacitor structure has been proposed to detect the change in permittivity of cell suspension, based on fringing electric field sensing. An LC tank circuit with a cross-coupled VCO topology is shown as the read out circuit. The interdigitated capacitor structure is the variable capacitor of the LC tank circuit.

## KEYWORDS:

Co-integration, CMOS MEMS, cytometry, interdigitated capacitor, VCO

## INTRODUCTION

The compatibility of MEMS and CMOS processes aided the development of label free electrochemical sensors relying solely on electrical measurements for read out, thus ushering a new era of biosensors. Typical biosensors, especially based on optical principles are affinity based and require selective target analyte combination for functioning [1]. These sensors are faced with the challenge of a complex read out mechanism usually based on fluorescence detection [2]. The advantage of simple read out circuits coupled with the ease of fabrication of CMOS MEMS devices have therefore made electrical biosensors very lucrative.

Common electrical bio sensors or electrochemical sensors are based on the impedance measurement technique [3-7]. Such a sensor configuration requires a microfluidic system in order to carry the fluid suspension and CMOS or BiCMOS circuit for the measurement of the impedance. Often the microfluidic system is fabricated from a polymer like PDMS, and a carrier chip containing the readout circuit is integrated with the microfluidic system [5]. This hybrid integration is needed because the microfluidic system has a greater real estate compared to the CMOS circuitry. The readout mechanisms although simpler than the optical sensors, often involve complex circuit designing like coherent detection technique [4]. The impedance measurement can also be performed over a frequency range and is called impedance spectroscopy [4].

In this work we propose a novel way of co-integrating the microfluidic system with the CMOS sensor circuit based on backside etching of silicon wafer thus eliminating the need of a separate microfluidic system on a polymer as required for hybrid integration. The interdigitated capacitor fabricated on top of the microfluidic channel senses the change in dielectric permittivity of the cell suspension, by the change in its capacitance. As a read out circuit a cross coupled VCO topology [7] is proposed.

## DIELECTRIC DISPERSION

Dielectric dispersion has been a proven non-invasive technique over decades for analyzing cell suspensions [8]. Biological cell suspensions show three noted dielectric dispersions over the frequency range of 1 Hz to 100 GHz, namely  $\alpha$  dispersion,  $\beta$  dispersion and  $\gamma$  dispersion respectively [8]. The  $\alpha$  and  $\beta$  dispersions are principally low frequency phenomena up to few hundred megahertz. In this work we focus on the  $\gamma$  dispersion of the cell suspension as the operating frequency of the sensor is centered around 5 GHz. The  $\gamma$  dispersion is caused by the polarization of the water molecules within the cell and has a characteristic frequency of 14 GHz [9]. The effective dielectric constant of the cell suspension is given by the Debye equation,

$$\epsilon' = \epsilon_a + \frac{\Delta\epsilon}{1 + (f/f_c)^2} \quad (1)$$

where  $\epsilon'$  is the effective dielectric permittivity of the solution,  $\epsilon_a$  is the high frequency permittivity of the suspending medium,  $\Delta\epsilon$  is the dielectric dispersion of the cell suspension dependent on the concentration of the cell as shown later,  $f_c$  is the characteristic frequency of the dispersion process and  $f$  is the measuring frequency.

A standard yeast cell can be modeled based on Asami's single shell model [8] as shown in fig. 1. The membrane capacitance  $C_m$  per unit area given by  $C_m = \epsilon_m \epsilon_0 / d$  and is around 0.5  $\mu\text{F}/\text{cm}^2$  to 1  $\mu\text{F}/\text{cm}^2$  and is considered to be a constant. The membrane thickness is given by  $d$  and the permittivity  $\epsilon_m$ . The dielectric dispersion  $\Delta\epsilon$  is given by,

$$\Delta\epsilon = \frac{9PrC_m}{4\epsilon_0} = \frac{3\pi r^4 C_m}{\epsilon_0} N \quad (2)$$

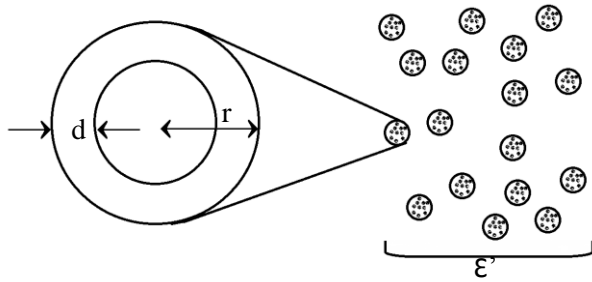


Figure 1: Single shell model of yeast cells

The cell concentration, given by  $N$  is the number of cell per unit volume.  $P$ , the volume fraction of the cell given by  $P = \frac{4\pi r^3 N}{3}$ , gives the total number of cells in the suspension. It is obvious that  $\Delta\epsilon$  has a linear relationship with the concentration of the cells. However the effect of  $\gamma$  dispersion is noted at the operating frequency of 5 GHz. The influence of frequency on effective dielectric permittivity for a concentration of 50 cells within the fluidic channel around the characteristic frequency of 14 GHz is shown in fig. 2. Thus the effective permittivity of the cell suspension is also dependent on the frequency of operation along with the cell concentration.

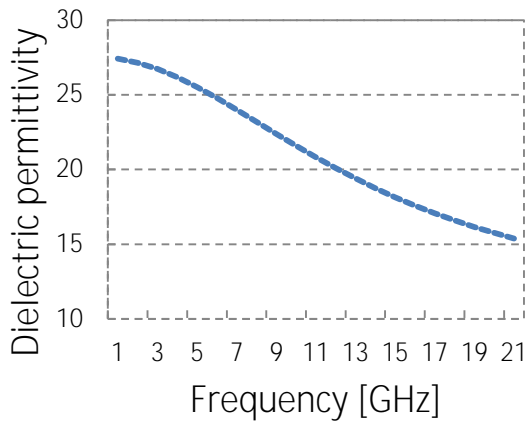


Figure 2: Variation of effective dielectric permittivity with measurement frequency of cell suspension of 50 cells in the microfluidic channel

### Interdigitated Capacitor design

The change in dielectric permittivity of the cell suspension is sensed by interdigitated electrode structure placed on top of the microfluidic channel. The change in dielectric permittivity of the cell suspension varies the capacitance of the interdigitated structure which is integrated as the variable capacitor of an LC tank. Thus the change in capacitance varies the tank resonance frequency. The interdigitated capacitor is fabricated by the standard metallization process of IHP pilot line, shown in fig. 3, with the fingers being stacked with metal 1 to top metal 2.

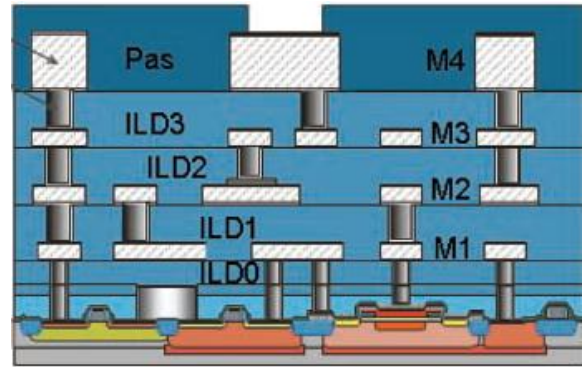


Figure 3: Back end of line (BEOL) process of IHP

Fig. 4 shows the microfluidic channel with the interdigitated electrode structure placed on top of it. The fringing electric fields between the fingers of the interdigitated structure penetrate into the fluid flowing in the microfluidic channel. Thus with the change in the permittivity of the fluid, these fields are affected thus attributing to the change of capacitance of the structure.

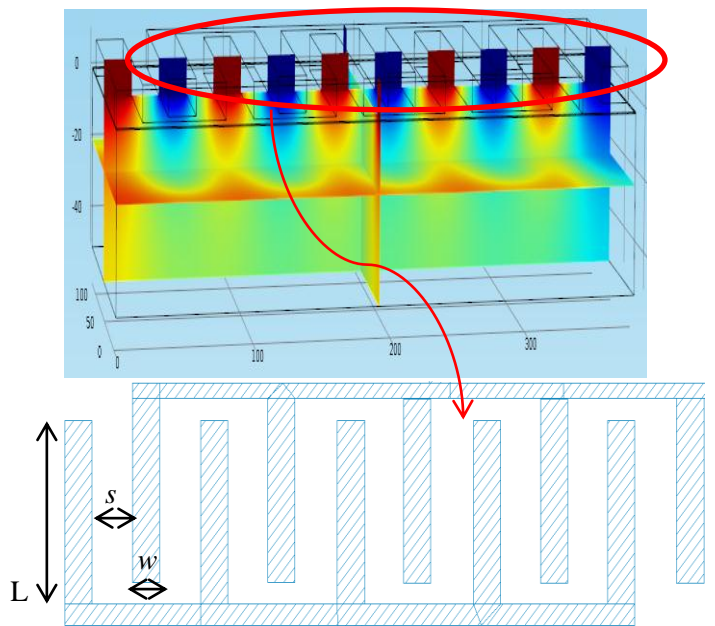


Figure 4: Microfluidic channel with interdigitated capacitor on top, perpendicular to the flow of fluid. EM-simulation of the fringing electric field in the structure penetrating into the fluid is observed. The design parameters of the interdigitated capacitor are shown.

The length  $L$  and width  $w$  of the fingers along with their separation  $s$  between each other are the principle parameters of design for the interdigitated structure. In our design the width of the finger is 30  $\mu\text{m}$ , the length of the finger is 100  $\mu\text{m}$  and their separation 20  $\mu\text{m}$ .



Width of the finger is approximately made equal or of the order of the space between the fingers, to have a symmetrical design. The length of the finger is made much greater than the thickness of the finger for fringing field sensing mechanism. As mentioned above, the metallization of the fingers is obtained by stacking with metal 1 to top metal 2 of IHP pilot line, thus reducing resistive losses. The proposed fabrication technique of the microfluidic channel below the sensor circuit is by the backside etching of the silicon wafer on which the sensing circuit has been designed.

### MICROFLUIDIC CHANNEL

The silicon wafer was patterned based on the dimensions of the microfluidic channel. The width of the channel is 100  $\mu\text{m}$ , which is equal to the overlap dimension of the interdigitated electrodes and the length of the channel is 500  $\mu\text{m}$ . Deep reactive ion etching (DRIE) has been used to etch the microfluidic channel. The etching process is followed by a polishing step. This is because a standard 8" silicon wafer has a thickness of 750  $\mu\text{m}$ , therefore a complete backside etching of the wafer would produce a channel depth of 750  $\mu\text{m}$ . Hence the wafer is polished down to 250  $\mu\text{m}$ . The complex techniques needed for handling thin wafers are avoided by performing polishing after the process of deep reactive ion etching. The channel is closed by an anodic bonding step and the inlets and the outlets are drilled using a drilling mechanism. The fabrication steps are shown in fig. 5

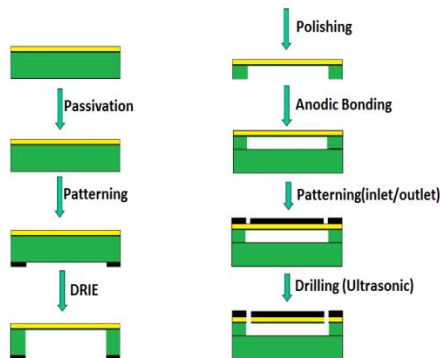


Figure 5: Fabrication process steps for the microfluidic channel

Test microfluidic channel has been fabricated to check if the wafer sustains the process of polishing after the deep reactive ion etching step. Fig. 6 shows the SEM image of the test microfluidic channel structure, confirming the sustainability of the etching step followed by the polishing step.

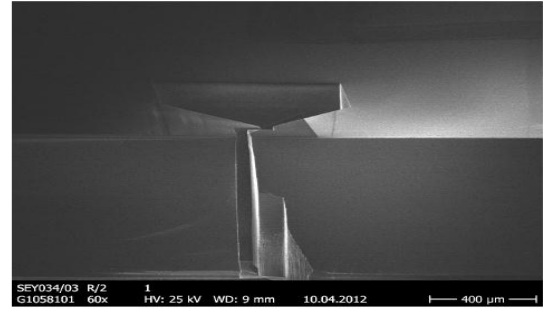


Figure 6: SEM image of the test Microfluidic channel

### CIRCUIT DESIGN

The interdigitated capacitor structure is integrated as the variable capacitor of an LC tank, whose resonance frequency varies with the variation of the capacitance. Thus a change in the effective dielectric constant of the cell suspension changes the resonance frequency of the LC tank.

The LC tank is used in a cross-coupled VCO (Voltage Controlled Oscillator) topology. The VCO is designed for a current of 30 mA operating with a power supply  $V_{dd}$  of 3.3 V. The core VCO circuit is shown in fig. 7

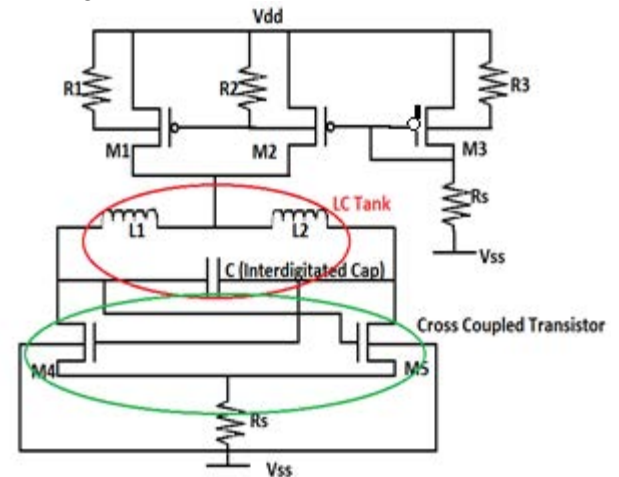


Figure 7: VCO circuit with the interdigitated capacitor for tuning the oscillating frequency

The transistors M1, M2 and M3 form the current mirror supplying the desired current to the VCO. The transistors M4 and M5 are used as the cross coupled transistor for the VCO. A differential buffer is also designed to isolate of the VCO. The output is obtained from the differential buffer.

In order to investigate the effect of  $\text{SiO}_2$  of the BEOL on the proposed structure and to confirm that the microfluidic channel is the main contributor to the change of the resonance frequency, we performed simulations for interdigitated capacitance with and without  $\text{SiO}_2$ . Fig. 8 shows the variation of the capacitance over permittivity for both structures.

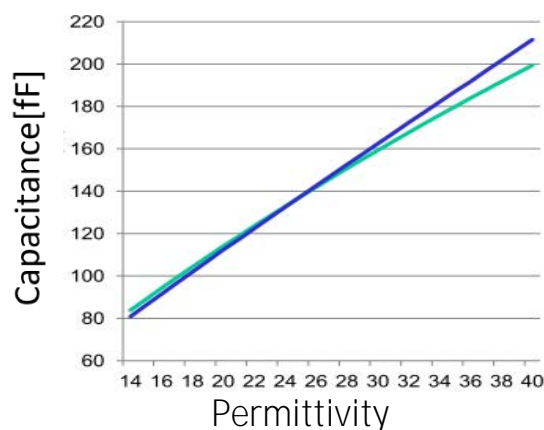


Figure 8: Variation of capacitance with dielectric permittivity of cell suspension. The green line shows the variation with  $\text{SiO}_2$  layer and the blue line without  $\text{SiO}_2$ .

The effective capacitance obtained from Momentum simulation on ADS over frequency is shown in fig.9. The structure is mainly capacitive over the frequency range of our interest and is relatively constant.

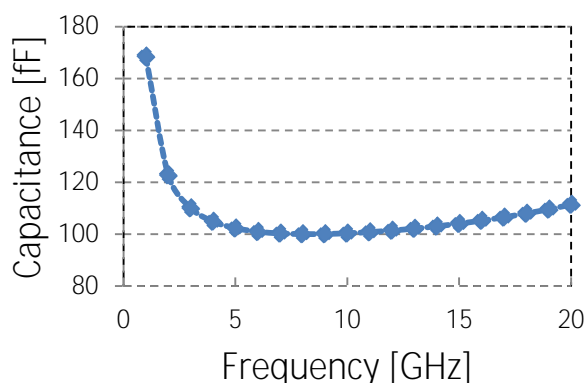


Figure 9: Capacitance of the interdigitated structure over frequency. When fabricated over silicon without the microfluidic channel, it is found to be 100 fF over 5 GHz to 20 GHz.

## CONCLUSION

CMOS MEMS co-integrated electrochemical sensors can nullify the use of polymer structure for the microfluidic system used for hybrid integration.

In this work we investigated a fringing field sensor based on an interdigitated capacitor. The sensitivity of the system could be increased by the use of phase frequency detecting circuit along with the proposed VCO at 5 GHz. Furthermore, the sensor can also be optimized by varying the geometry of the interdigitated capacitor structure.

The dimension of the sensor is a trade-off between the penetration depth of the field in the microfluidic

channel, the capacitance value, and the resistive losses due to the dimension of the interdigitated structure.

The proposed concept is a realistic and interesting solution to realize a sensor with simple read-out circuits. The use of a monolithic micro-fluidic system allows high operation frequencies, which increases sensitivity.

## REFERENCES

- [1] J.Daniels and N.Pourmand , “ Label Free Impedance Biosensors:Opportunities and Challenges”, *Electroanalysis*, Vol 19, No. 12, pp 1239-1257, 2006.
- [2] K. Tainaka, R.Sakaguchi, H.Hayashi, S.Nakano, F.Liew and T.Morii, “Design Strategies of Fluorescent Biosensors Based on Biological Macromolecular Receptors”, *Sensors*, Vol.10 pp 1355-1376, 2010
- [3] E. Krommenhoek , J.Gardeniers,J.Bomer, A.Van der Berg, X.Li,L.van der Wielen, G.van Dedem, M.Van Leeuwen,W. Van Gulik and J.Heijnen, “ Monitoring of Yeast cell concentration using a micromachined impedance sensor”, *Sensors and Actuators B* 115 pp 384-389, 2005
- [4] A.Manickam, A.Chevalier, M.Mcdermott A.Ellington and A.Hassibi, “ A CMOS Electrochemical Impedance Spectroscopy (EIS) Biosensor Array”, *IEEE Transactions on Biomedical Circuits and Systems*, Vol. 4, No. 6, pp 379-390, December 2010.
- [5] L.Jeng, C.Wu and C.Liu, “Fabrication of microfluidic devices for packaging CMOS MEMS impedance sensors”, *Microfluid Nanofluid* Vol. 7, pp 869-875, 2009
- [6] Y.Huang and A.Mason, “ Lab-on-CMOS: Integrating Microfluidics and Electrochemical Sensor on CMOS”, *Proceedings of 2011 6<sup>th</sup> IEEE International Conference on Nano/Micro Engineered Molecular Systems*, pp 690-693
- [7] F.Tasdemir, S.Zehir, E.Ozeren, J.Niazi, A.Quersh, S.Kallempudi, M.Kaynak, R.Scholz and Y.Gurbuz, “A New Lab-on-Chip Transmitter for Detection of Proteins using RNA Aptamers”, *Proceedings of 40<sup>th</sup> European Microwave Conference*, pp 489-492, September 2010, France.
- [8] K.Asami, “Characterization of biological cells by dielectric spectroscopy”, *Journal of Non-Crystalline solids* 305, pp- 268-277, 2002
- [9] C.Harris and D.Kell, “The Radio Frequency Dielectric Properties of Yeast Cells Measured with a Rapid, Automated, Frequency –domain Dielectric Spectrometer”, *Bioelectrochemistry and bioenergetics*, Vol.11, pp-15-28, 1983

Contact:

- S.Guha, guha@ihp-microelectronics.com

## COMPARISON OF TWO TYPES OF HYBRID MICROFLUIDIC VALVES FOR COMPLEX MICROFLUIDIC FLOWPATH CONFIGURATIONS

A. Prak<sup>1</sup>, T.T. Veenstra<sup>1</sup>, F. Schreuder<sup>1</sup>, F. Falke<sup>1</sup>, G. Borst<sup>2</sup>

<sup>1</sup> LioniX BV, Enschede, The Netherlands

<sup>2</sup> Dutch Space, Leiden, The Netherlands

### ABSTRACT

In this paper, two types of microfluidic valves for realizing complex microfluidic flowpath configurations are compared. The first approach is based on the combination of multiple switching valves, whereas the second approach is based on the functional principle of a rotary valve. Both valves have on-chip integrated fluidic elements, while their actuation has deliberately chosen to be implemented off-chip for reasons of power requirements.

### KEYWORDS

Microfluidics, Rotary Valve, Switching valve

### INTRODUCTION

In recent years the demand for on-chip configurable fluidic networks has grown as there is a need to integrate multiple functions like sample preprocessing and sample analysis functions. These functions require on-chip switching of various liquid streams from different sources and to different destinations. In many occasions it is not a realistic option to use off-chip valves as the number of fluidic connectors and associated internal volumes would increase rapidly. On the other hand, the many attempts undertaken to fabricate fully integrated microvalves have shown that the integration of reliable microactuators providing the valve with enough power is still one of the major challenges to be solved. Therefore, we have chosen to use integrated fluidic elements which give the valve essential advantages such as an extremely small internal volume and low/zero swept volume, while we use external actuators to give the valve robust characteristics with regard to leakage rate.

Our first approach is a membrane valve actuated by a solenoid and a lever. Our second approach is a rotary valve operated by a stepper motor. Both valves can be used to design complex on-chip fluidic networks.

### VALVES

#### Array of Switching Valves

Figure 1 and figure 2 explain the construction and functioning of a single binary valve. This binary valve

has been employed to create a fluidic system with possibilities to redirect the flow within the system.

A ridge is situated around the inlet of a fluidic channel. Over this valve-seat a flexible membrane – either Viton or PDMS – is placed, which can freely move out-of-plane from the valve-seat. The membrane is pressed tightly on the chip-surface, ensuring a leaktight seal. The membrane can be forced down exactly over the valve-seat, which causes blockage of the flow-path.

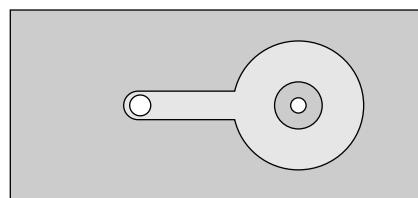


Figure 1: Top view of the binary valve.



Figure 2: Open- and closed- configuration of the binary valves.

Actuation of the valve is done by pushing down a guided pin on the membrane at the exact location of the valve-seat. See also figure 3. This actuation is performed by a solenoid actuator, which pushes up a rotating beam. The other end of the beam pushes down on the guided pin, which closes the valve. Actuation in this manner enables a tight packing of valves since the size of the actuator is not limiting the minimum pitch between the valves.

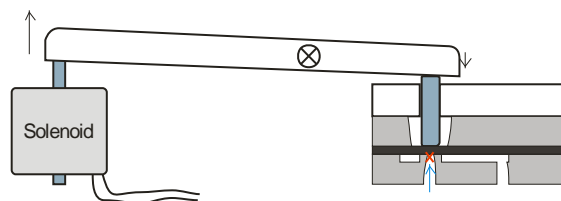


Figure 3: Valve-actuation mechanism

The volume of the channel around the valveseat represents the dead volume of the valve. This volume is well below 0.1  $\mu\text{l}$ .

The volume displaced when pushing down the membrane is estimated to be in the order 0.2  $\mu\text{l}$ . These numbers make this valve comparable to high-end commercial valves.

The performance of the binary valve has been tested. A syringe pump loaded with water was connected to the inlet of the valve, taking care to include an airbubble within the syringe. This airbubble ensures a slow and even build-up of pressure on the valve. The pressure in front of the valve was monitored during the period the syringe pump was dispensing fluid at 100 microliters/minute. Figure 4 shows the development of the pressure over time.

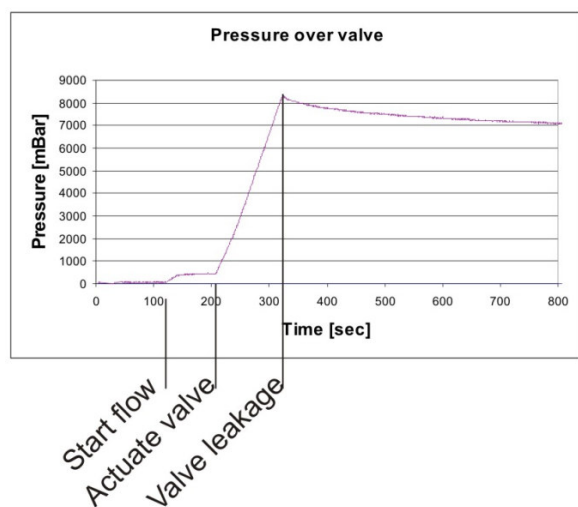


Figure 4: measurement on holding pressure of the binary valve.

The moments in time at which the flow was started and at which the valve-actuation was started are indicated. It is seen that the valve can withstand about 8 bars before it starts to leak. Though this has not been tested, it seems straightforward that a stronger solenoid would result in a higher break-through pressure.

A number of these valves can be combined into a fluidic network to create extended functionality. This is shown in Figure 5 and Figure 6, which show a small fluidic system in which each of three inlets can be

directed either over sensing electrodes or directly to a waste channel.

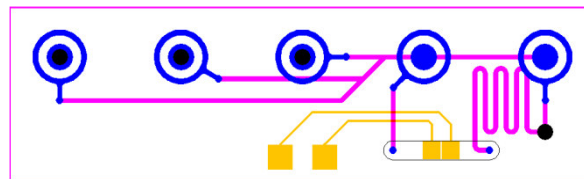


Figure 5: Top view of the combination of multiple binary valves to construct a more complex fluidic network.

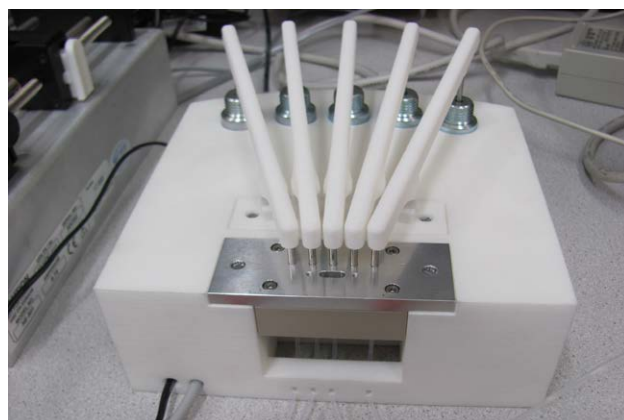


Figure 6. Photograph showing a fluidic system based on an array of switching valves.

The shown geometry has been developed for performing capacitive measurements in a sample solution. With the three inlets reference, sample and washing buffers could be applied to the measuring electrodes.

### The Rotary Valve

The presented example of the rotary valve is part of the so called Life Marker Chip (LMC) instrument which performs a key role in the sample analysis of a Martian soil sample in the search for past or present life on Mars. The analysis is based on immuno assay techniques. Details of analysis subsystem of the Life Marker Chip are given elsewhere [1].

The rotary valve comprises a stator and a rotor which are kept aligned and compressed by a bolt through a central axis. The stator is integrated in a micromachined glass manifold, which is fabricated by etching, powder blasting and fusion bonding of two fused silica wafers to form a network of channels, chambers and sensors (Figure 7). The rotor (Figure 8) is made of a plastic material which is pressed against the stator to form a leaktight seal. The rotor has a number of milled grooves which make various connections by rotating the rotor to different index positions. The rotor is driven by a miniature stepper motor. The presented rotary valve show one on/off



valve (valve 1) and two 3-way selection valves (valves 2 and 3), see Figure 10 and Table 1. It will be clear that other, very complex configurable stream diagrams can be realized by design. However, once the design is fixed, and the parts are fabricated the configurability is not flexible anymore.

Preliminary tests in a comparable device with a much larger contact surface show a leak tightness up to above 1 Bar. In the presented configuration the leak tightness has not been tested, however we expect it to be larger than 1 Bar because of its smaller contact surface between the stator and the rotor.

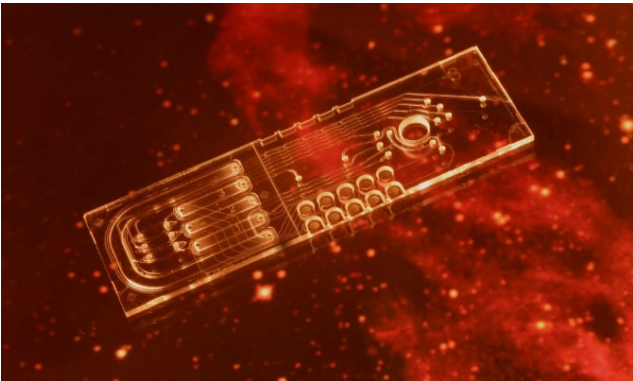


Figure 7. Glass chip performing sample preparation and analysis of a Martian soil sample including the stator of a rotary switching valve.



Figure 8: Photograph of the milled channels in the rotor (left) and the assembled valve rotor (right)

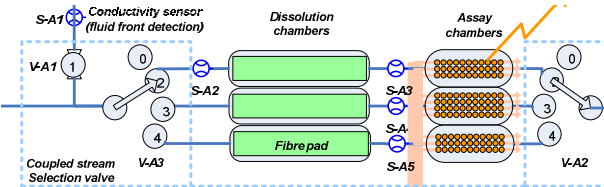


Figure 9. Schematic diagram of the glass manifold comprising several channels, chambers, valves and sensors.

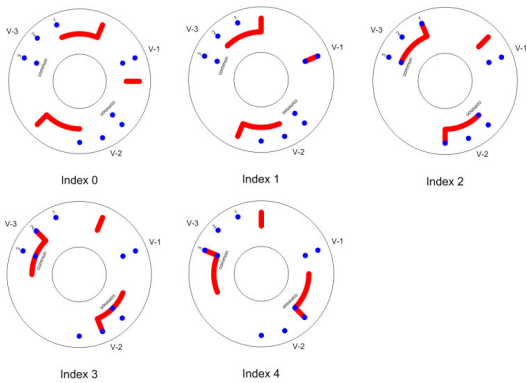


Figure 10: This figure shows which connections are made between the inlets of the fluidic chip (blue dots) and the grooves in the rotor (red stripes) for the five different index positions of the rotary valve.

Table 1. Switching logics of the rotary valve

Index	Valve 1	Valve 2	Valve 3
0	Closed	Closed	Closed
1	1	Closed	Closed
2	Closed	1	1
3	Closed	2	2
4	Closed	3	3

Other advantages of the rotary valve are:

- Extremely low internal volume
- Zero volume displacement upon switching, i.e. no pressure pulse
- Zero power consumption at rest
- Low costs per extra port

Major disadvantages of the rotary principle are:

- Slow switching time

### COMPARISON OF BOTH VALVES

Both approaches have a number of common characteristics, for example both valves have a hybrid composition comprising a glass microfluidic manifold which is completely configurable by design and an off the shelf actuator (a solenoid coil and a stepper motor respectively).

Upon actuation, the rotary valve does not introduce a volume displacement, whereas the switching valve will push away a small volume upon actuation. This possibly leads to an uncertainty in the liquid control in the system.

*Table 2; comparison chart between the valves.+ advantage; - disadvantage;*

	<b>Array of Switching Valves</b>	<b>Rotary valve</b>
Configurability by design	+	+
Configurability during use	+	-
Speed of switching	+	-
Internal volume	-	+
Dead volume [ $\mu$ l]	0,1	0,1
Displaced volume [ $\mu$ l]	0,2	0
Power consumption	-	+
Wetted materials	Glass, silicon, Viton/PDMS	Fused silica, rotor material
Costs per extra switch	-	+
Leakage pressure [Bar]	8	>1

## CONCLUSION

A comparison between two complex fluid switching solutions is presented. The rotary valve based solution excels in power usage and overall size, whereas the switching valve performs better in situations where fast switching is required or where the exact switching protocol needs to be reconfigurable.

## REFERENCES

[1] Integration of Optical Waveguides and Microfluidics in a Miniaturized Antibody Micro-Array System for Life Detection in the NASA/ESA ExoMars Mission, A. Prak , H. Leeuwis, R.G. Heideman, A. Leinse, and G. Borst, Proc. Of SPIE Vol. 7928

## 2. Actuators

# STRUCTURE CONTROLLED POLYMERIC MICROLENS FABRICATION USING MULTIPHASE DROPLET ASSEMBLY

K. Hasegawa<sup>1</sup>, D. H. Yoon<sup>1</sup>, A. Nakahara<sup>1</sup>, T. Sekiguchi<sup>2</sup>, S. Shoji<sup>1</sup>

<sup>1</sup> Major in Nanoscience and Nanoengineering, Waseda University, Tokyo, Japan

<sup>2</sup> Nanotechnology Research Center, Waseda University, Tokyo, Japan

## ABSTRACT

This paper describes a simple assembly method of controllable polymeric microlens at an appropriate position using a microdimple structure. A microlens is formed from the multiphase microdroplet including air core. The size of the lens is controlled by diameters of the microdimple structure. Controllable sizes from 79  $\mu\text{m}$  to 171  $\mu\text{m}$  in diameters and radiuses of curvature from 47  $\mu\text{m}$  to 120  $\mu\text{m}$  are achieved. The proposed method is applicable for in line microlens assembly for optical detection area.

## KEYWORDS

Microlens, Multiphase droplet, Droplet assembly, Buoyancy, Air

## INTRODUCTION

Microlens assembly is interesting issue because it has been widely used for optical devices. Conventionally, a variety of fabrication, for example imprint technique and reflow method, has been reported [1], [2]. However, on demand change of the lens diameter and radius of curvature is difficult in these techniques once the mold is fabricated. Also, some specific method using fluidic system realized high controllability, but complicated structure and precisely integrated optical device is required [3].

On the other hand, generation methods of microdroplets using microfluidic devices are well known as good size controllability using simple microchannel structures [4].

In our previous works, the fabrication method of size controllable microlens [5] applied for generation of gas-organic-water multiphase droplet [6] and the assembly method of polymeric microlens at required position using microdimple structure of a PDMS were reported [7]. In this paper, we propose a simple control method of microlens structures using multiphase droplet assembly by changing sizes of microdimples.

## PRINCIPLE

The proposed method of controllable microlens fabrication utilizes droplet based microfluidics. Figure 1 (a) shows that the multiphase droplets are generated using three phase fluids. In this case, air is used as a core of the organic droplet. The droplets are

introduced into the trapping microchannel on which microdimples are fabricated on the top side wall. As shown in Figure 1 (b), the droplets are trapped easily at the circular microdimples due to buoyancy of droplets including air core. Then, the air core moves up by buoyancy while the surrounding organic solution flows down because the density of organic solution and that of air are extremely different. Lastly, the air core is disappeared, only polymer dissolved organic solvent cures at the microdimple. The unbalanced density between each fluid makes a specific shape like a microlens. In the case of the same size droplet, the larger diameter and radius of curvature of the microlens is formed at the larger microdimple, while the smaller diameter and radius of curvature of the microlens is formed at smaller microdimple as shown in Figure 1 (c).

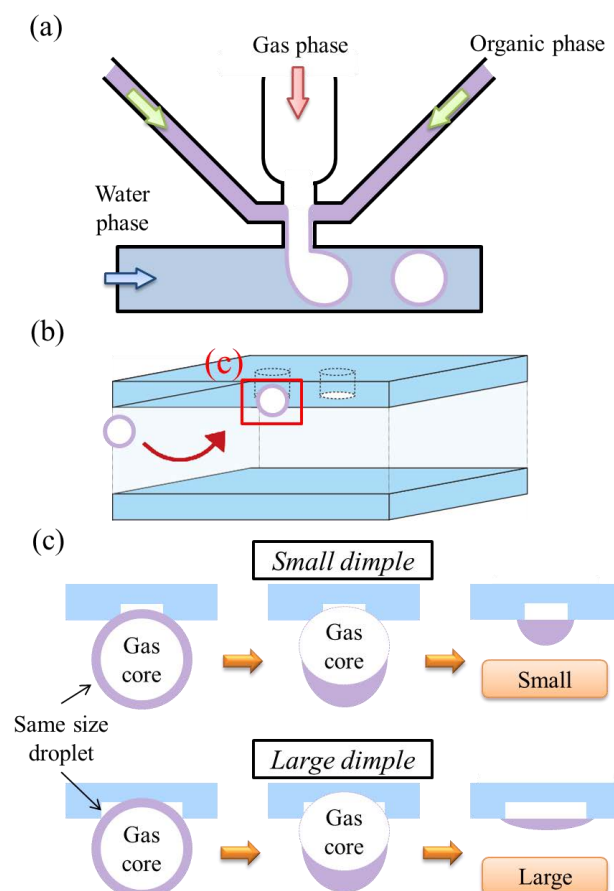


Fig. 1: The principle of the microlens fabrication method; (a) generation of three phase droplet (b) droplet trapped at the circular microdimple by buoyancy (c) organic solution segregation and lens structure formation.

## DESIGN AND FABRICATION

### Design

The system for microlens fabrication divides into two parts, droplet generation part and microlens formation part. Figure 2 (a) shows an overall view of the droplet generation part and the magnified structure of its fluidic junction. This part has three inlets and one outlet. One of the inlets is for gas phase as a core of the droplets, and another is for organic phase and the other is for water phase as carrier flow. The multiphase droplets are observed at the observation area. Width of the designed junction and main flow microchannel are 50  $\mu\text{m}$ , and 100  $\mu\text{m}$  respectively. The structure of microlens formation part is shown in Figure 2 (b). This part has circular microdimple array on the top side wall. Three types of dimple size design are fabricated as shown in Table 1.

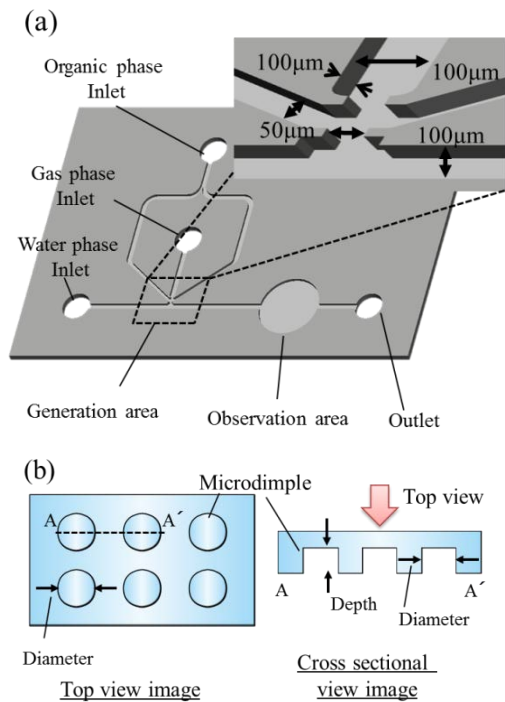


Fig. 2: The system design for microlens fabrication; (a) droplet generation part, (b) microlens formation part.

Table 1: Fabricated microdimple design

Dimple size type number	Diameter [ $\mu\text{m}$ ]	Depth [ $\mu\text{m}$ ]
I	50	50
II	100	50
III	150	50

### Fabrication

Figure 3 shows the fabrication process of the system. For droplet generation part, microchannel is fabricated by two step photolithography and dry etching processes from both top side and bottom side of a 200  $\mu\text{m}$  thickness silicon wafer. Fabricated

microchannel on the silicon wafer is anodically bonding with a glass substrate for visualization and sealing. Finally, copper inlets and outlet ports are bonded and tubes are connected on the bottom side of the silicon wafer. The microlens formation part is fabricated by PDMS molding with SU-8 mold. The SU-8 mold is made by photolithography process. SU-8 is spin coated on the silicon substrate and exposed as microdimple array structure. Figure 4 (a) show SEM images of the overall view and magnified structure of droplet generation part, and the fabricated SU-8 mold and PDMS structure are shown in Figure 4 (b).

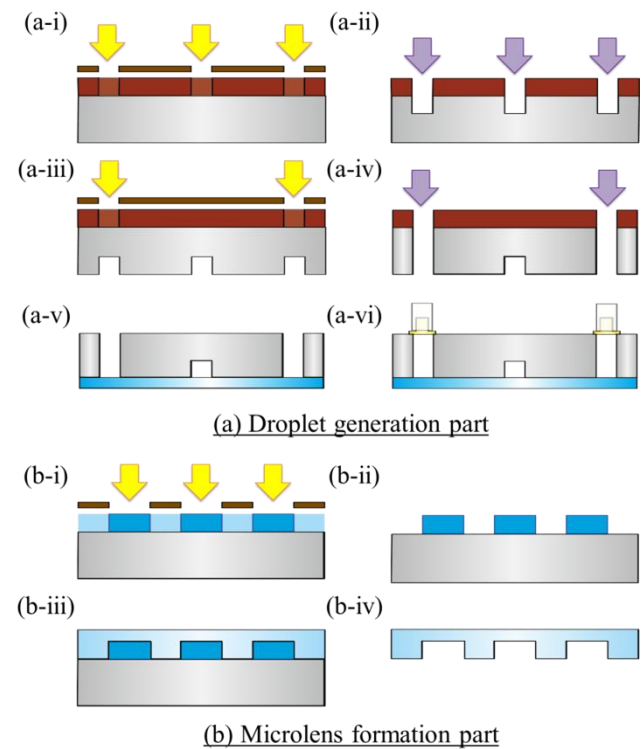
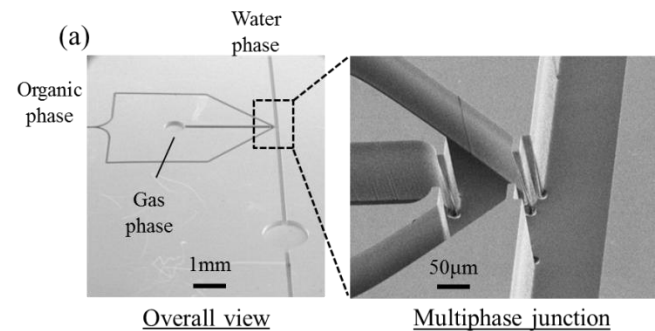


Fig. 3: Fabrication process. (a) Droplet generation part; (i, iii) exposure, (ii, iv) dry etching, (v) anodic bonding, (vi) copper ports bonding and tubes connecting. (b) microlens formation part; (i) exposure, (ii) development, (iii) PDMS molding, (iv) release.





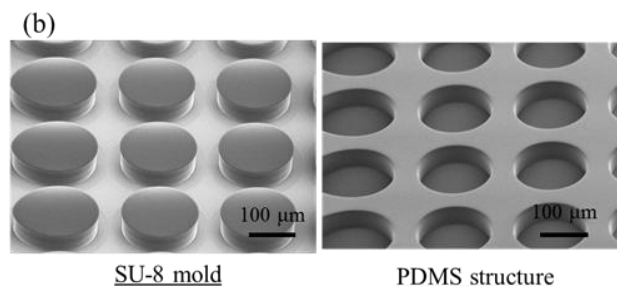


Fig. 4: SEM images of (a) droplet generation part and (b) microlens formation part of type number III.

## EXPERIMENTAL SET UP

Droplet generation part is set in a petri dish. Three phase fluids of air as gas phase, dichloromethane dissolving 5 wt% polystyrene as organic phase, and 3 wt% polyvinyl alcohol (PVA) aqueous as water phase are used. The liquid phase fluids are introduced into the microchannel of the droplet generation part by using syringes (1750CX, HAMILTON) and syringe pumps (KDS210, kdScientific). The air pressure is controlled by pressure regulator (2657 pneumatic pressure standard, YOKOGAWA). Also, a high speed CCD camera (FASTCAM-NEO 32K, Photron) and data processing computer are utilized for visualization and storage of the droplet generation processes. 1.5 wt% PVA aqueous is filled in the petri dish, and microlens formation part is floated on the PVA aqueous. Droplets generated from the outlet are trapped to the microlens formation part. Trapped droplets are monitored from the top side through the microlens formation part by an epi-illumination microscope (BX51, OLYMPUS). The side view is observed by a digital microscope (Advanced KH-3000, HIROX). The structure of the cured polystyrene formation is evaluated by a SEM (VE-7800, KEYENCE).

## RESULTS AND DISCUSSION

### Multiphase Droplet Generation

Figure 5 shows generation of three phase multiphase droplets including air core and organic membrane at the junction area and the observation area in droplet generation part. Their sizes are defined by the combination of flow rate of each phase.

### Droplet Assembly

Some droplets are trapped to microdimples in microlens formation part as shown in Figure 6 (a). If the pitch size of microdimples is optimized, droplets are expected to be trapped to all microdimples. Figure 6 (b) shows that the droplet is maintained its structure after trapping. It indicates that a lens is formed by the proposed simple method.

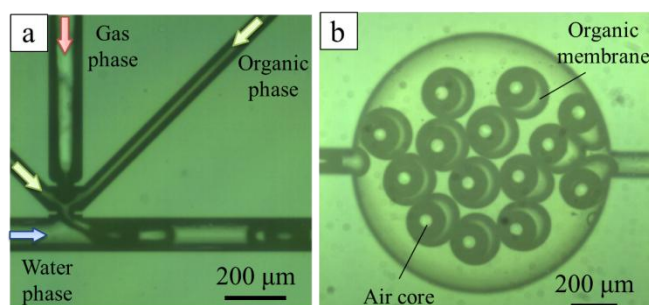


Figure 5: Captured images of generated multiphase droplets at (a) the junction area and (b) the observation area.

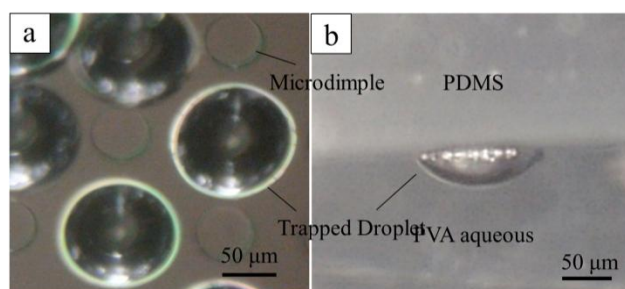


Figure 6: Microscope images of trapped droplets at the microdimples (a) top view, (b) side view.

### Fabricated Microlens

The SEM images of fabricated polymeric microlens observed at the microdimple are shown in Figure 7. At the observation area in the droplet generation part, size of droplets is 192  $\mu\text{m}$  in diameter uniformly. Three different radius of curvature of 71  $\mu\text{m}$ , 88  $\mu\text{m}$ , and 94  $\mu\text{m}$  are obtained in the cases of dimple sizes of 50  $\mu\text{m}\phi$  (type: I), 100  $\mu\text{m}\phi$  (type: II) and 150  $\mu\text{m}\phi$  (type: III). Figure 8 shows results of lens diameter VS dimple diameter and radius of curvature VS dimple diameter. The diameters of fabricated microlens are from 79  $\mu\text{m}\phi$  to 171  $\mu\text{m}\phi$ . Also, radiuses of curvature are ranged from 45  $\mu\text{m}$  to 120  $\mu\text{m}$ . The results indicate that the use of combination between droplet size and dimple size can control the microlens structures. Also, combination between droplet diameter control and microdimple structure control is able to obtain a high controllability of microlens structures.

### Optical Characteristic

Figure 9 shows the optical set-up to characterize the fabricated microlens. The character of "JPN" is located underneath of the microlens formed PDMS substrate. The measured position of inverted real image difference between type II and type III is about 50  $\mu\text{m}$  while the calculated value is about 27  $\mu\text{m}$ .

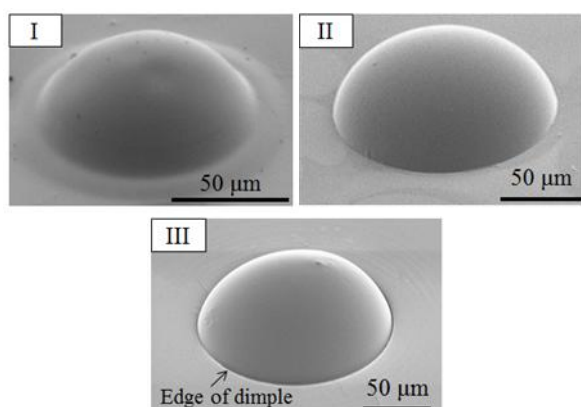


Figure 7: SEM images of microlens on different microdimples. Microdimple of 50  $\mu\text{m}\phi$  (type I), 100  $\mu\text{m}\phi$  (type II), and 150  $\mu\text{m}\phi$  (type III).

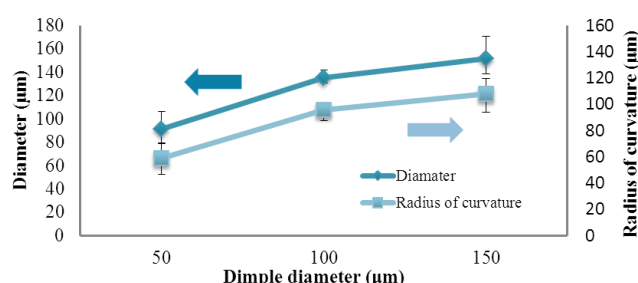


Figure 8: Diameter and radius of curvature of fabricated microlens on different microdimples.

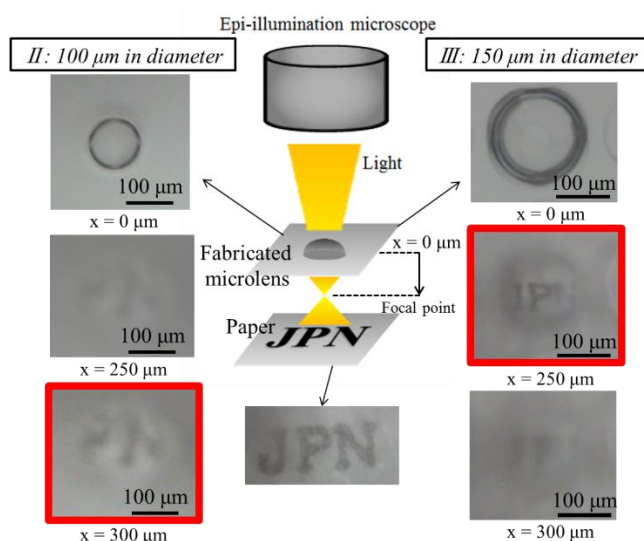


Figure 9: Optical characteristic measurement set-up of microlens. Left; images of the microlens (type II). Right; images of the microlens (type III).

## CONCLUSION

We propose the structure controlled on demand microlens fabrication and assembly method. The diameters and radii of curvature of microlens are successfully controlled by the use of combination between droplet size and dimple size. Also, their basic performances are optically evaluated. In addition, this principle can be applied for position and size control

of in line microlens.

## ACKNOWLEDGEMENTS

This work is partly supported by Japan Ministry of Education, Culture, Sports Science and Technology Grant-in-Aid for Scientific Basic Research (S) No. 23226010, and the authors thank for Nanotechnology Platform of Waseda University for their technical assistances.

## REFERENCES

- [1] X. H. Zhang, Wenxiu Que, C. Y. Jia, J. X. Hu, W. G. Liu, "Fabrication of micro-lens arrays built in photosensitive hybrid films by UV-cured imprinting technique", *Jornal of Sol-Gel Science Technology*, 2011, 60, pp.71-80.
- [2] Li Feng, Chen Sihai, Luo Huan, Zhou Yifan, Lai Jianjun, Gao Yiqing, "Fabrication and characterization of polydimethylsiloxane concave microlens array", *Optics and Laser*, 44, 2012, pp. 1054-1059.
- [3] S. K. Y. Tang, C. A. Stan, and G. M. Whitesides, "Dynamically reconfigurable liquid-core liquid-cladding lens in a microfluidic channel", *Lab Chip*, 8, 2008, pp. 395-401.
- [4] L. Yobas, S. Martens, W.L. Ong, N. Ranganathan, "High-performance flow-focusing geometry for spontaneous generation of monodispersed droplets", *Lab Chip*, 6, 2006, pp. 1073-1079.
- [5] D. H. Yoon, T. Arakawa, J. S. Go, S. Shoji, "Size controllable polymeric microlens fabrication by using a multiphase droplet including air core",  $\mu\text{TAS}2010$ , Groningen, The Netheland, October 3-7, 2010, pp.1118-1120.
- [6] D. H. Yoon, T. Arakawa, J. S. Go, S. Shoji, "Generation of polystyrene microcapsules as nanoliter volume gas encapsulants by using gas-organic-water multiphase junction",  $\mu\text{TAS}2009$ , Jeju, Korea, November 1-5, 2009, pp.1422-1424.
- [7] K. Hasegawa, D. H. Yoon, A. Nakahara, T. Sekiguchi, S. Shoji, "A study on simple assembly method of polymeric microlens using buoyancy of droplets", *ISMM2012*, Hsinchu, Taiwan, June 10-13, 2012, pp.55-56.

## CONTACT

\* Kenta Hasegawa,  
hasegawa@shoji.comm.waseda.ac.jp

## PASSIVE VALVE BASED MICROFLUIDIC STRUCTURE FOR METERING AND ON-CHIP REAGENT STORAGE

*Michael Suppan<sup>1</sup>, Sylvia R. Scheicher<sup>1</sup>, Heinz Pichler<sup>1</sup>, Markus Rumpler<sup>2</sup>,  
Valentin Satzinger<sup>1</sup>, Martin Hajnsek<sup>2</sup>, and Stefan Köstler<sup>1\*</sup>*

<sup>1</sup> JOANNEUM RESEARCH, MATERIALS – Institute of Surface Technologies and Photonics, Graz, Austria.

<sup>2</sup> JOANNEUM RESEARCH, HEALTH – Institute of Biomedicine and Health Sciences, Graz, Austria.

### ABSTRACT

“Passive valve based microfluidic structure for metering and on-chip reagent storage.” We describe the development of a microfluidic chip for metering a certain sample volume and simultaneously incubating it with on-chip stored reagents (proteins). The chip comprises a system of micro channels, cavities and passive hydrophobic valves for fluid actuation. Fluoropolymer coating of the microfluidic channels was used for fabricating the passive valve structures. Porous membrane pads were incorporated for reagent storage. The basic working principle for metering and the successful reconstitution of fluorescently labelled proteins could be demonstrated.

### KEYWORDS

Lab-on-a-chip, metering, reagent storage, passive valve, polymer microfluidic device, bioassay, inkjet, surface modification, hot embossing, COP

### INTRODUCTION

Metering of sample volumes and subsequent incubation with reagents are essential unit operations in almost every bioanalytical method or assay. In laboratory based bioanalysis, these tasks are usually performed either during sample drawing or as a separate task prior to the actual assay or measurement. Nowadays, there is a steadily growing demand for miniaturized bioanalytical and diagnostic devices allowing for on-site or point-of-care applications. These, so called labs-on-a-chip or micro-total analysis systems ( $\mu$ -TAS) should ideally enable convenient sample-in – result-out type operation. Therefore, the entire sample preparation (including tasks like metering, separation, extraction, reagent incubation, etc.) should be performed on-chip.

Different microfluidic solutions have been developed for the unit operation of metering fluids, e.g. based on pressure driven flow, centrifugal forces or electrokinetics [1]. A convenient way of fluid manipulation in such metering structures is the use of so called passive valves. Passive valves retain the liquid meniscus in a microchannel by carefully balancing capillary forces [2]. The capillary pressure acting on a liquid can be controlled by the dimensions

and wettability of microfluidic channels. Therefore, such passive valves have often been used in metering structures through channel restrictions and/or hydrophobic surface coatings [3-5]. Furthermore several different techniques have been developed for on-chip storage of reagents for lab-on-a-chip bioassays [6-9]. A very convenient technique uses porous membranes incorporated into the chip as supports for the reagents [7].

In this contribution, we describe a cyclic olefin polymer (COP) based microfluidic chip, combining sample metering and dissolution/incubation with reagents stored on-chip. The metered sample volume and desired incubation/dissolution times can be defined by the channel layout. The system works under constant externally applied pressure using only passive valving for actuation.

### MATERIALS AND METHODS

Injection molded Zeonor 1060R slides in 75x25x1 mm format were used as substrates for the COP based microfluidic chips. The microfluidic channels were fabricated by mechanical micromilling or a combination of hot embossing and mechanical micromilling of through and access holes. The whole channel system has been designed using COMSOL Multiphysics® for computational flow modelling.

Hydrophobic valves were produced by fluoropolymer coating of the COP channel surface using Hyflon® AD dissolved in octafluorotoluene. The fluoropolymer coatings were deposited into the microfluidic channels using piezoelectric drop-on-demand inkjet printing (Dimatix DMP 2800 materials printer) or manual dispensing. The channel structures were sealed using pressure sensitive adhesive (PSA) foil (Greiner BioOne). A small, circular piece of a hydrophobic PTFE membrane (pore size 0.2  $\mu$ m) was used as air venting membrane and mounted at the outlet of the overflow compartment using PSA.

Two different membrane types, a cellulose fiber sample pad (CFSP203000, Millipore) and a glass fiber conjugate pad (GFCP103000, Millipore) were used for investigating on-chip reagent storage. These membranes were punched into circular pieces with a diameter of 2 mm, subsequently treated with 10



mg/mL bovine serum albumin (BSA) solution in Tris buffer (10 mM, pH 7.5) for 30 min and rinsed with water. Then they were inserted into the reagent incubation chamber on the chip and loaded with 2  $\mu$ L of either 6.5  $\mu$ M fluorescein isothiocyanate labelled BSA (BSA-FITC) or 5.2  $\mu$ M Cy3 labelled streptavidin (Strept-Cy3) solution in Tris buffer containing 10 wt.% threalose.

All proteins and other reagents were obtained from Sigma-Aldrich and used as received. Fluorescence micrographs were taken using a Olympus BX51 microscope and the respective filter sets. Fluorescence spectra during reagent release were taken by a fiber-optic spectrometer (Ocean Optics HR4000) integrated into the fluorescence microscope. Contact Angles of water were determined by analysis of the profile of sessile drops using a dataphysics System OCA15+ (Dataphysics, Germany).

## RESULTS AND DISCUSSION

### Metering Structure

The described metering structure in the COP chips consists of a system of channels, cavities and passive valves (see Figure 1).

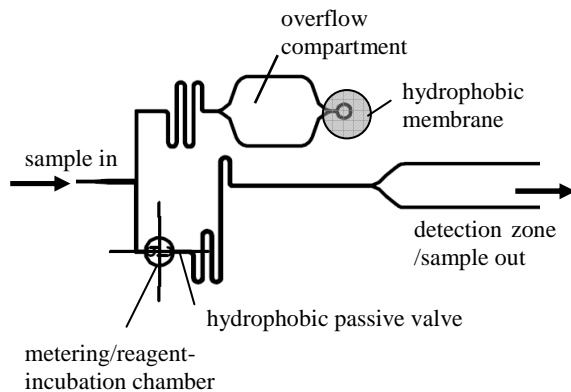


Figure 1: Scheme of the channel structure used for metering sample volumes on-chip.

The key features are a T-junction for splitting the liquid flow right after the sample inlet, a passive hydrophobic valve positioned at the outlet of the metering/reagent-incubation chamber, and a hydrophobic membrane for air venting and stopping the liquid flow in the overflow channel. The whole channel system has been designed using COMSOL Multiphysics® for computational flow modelling. Examples of modelling the splitting of the sample liquid flow in the asymmetric T-junction, guiding the main flow toward the metering chamber (left channel) and a minor part of the liquid towards the overflow compartment (right channel) is shown in Figure 2A. The metering chamber itself is designed as a through-chip via structure connecting the channel systems on the front- and backside of the COP chip. The design

and liquid flow pattern in the metering chamber is depicted in Figure 2B.

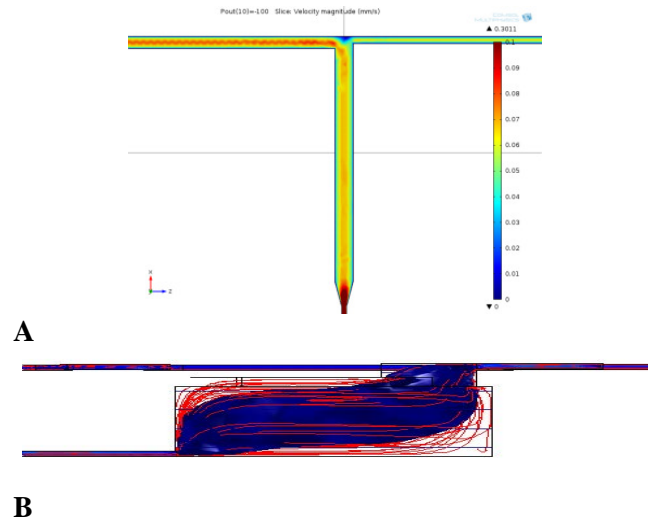


Figure 2: Simulations of liquid flow in (A) the asymmetric T-junction and (B) through the metering chamber (cross section of the chip) by COMSOL Multiphysics®

The hydrophobic valve at the outlet of the metering chamber was fabricated by coating of the COP channel surface with a fluoropolymer coating by inkjet printing or manual dispensing. The water contact angle on the fluoropolymer coated surface areas increased to values around 120° compared to approx. 90° for pristine COP surfaces. This hydrophobization leads to a marked increase in the capillary pressure and thus prevents the liquid meniscus from flowing across the hydrophobic area (see Equation 1 and Figure 3).

$$P_c = \cos \theta_{\text{wall}} \frac{2h+w}{hw} + \cos \theta_{\text{cover}} \frac{w}{hw} \quad (1)$$

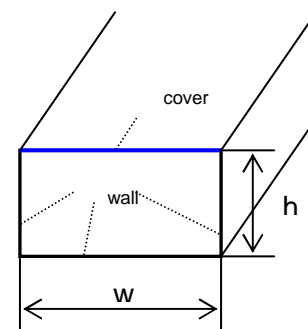


Figure 3: Schematic view of microfluidic channel and parameters used in Equation 1

Differences in capillary pressure around 1,5 kPa can be obtained between the pristine channels and hydrophobic patches, for 250  $\mu$ m wide and 30  $\mu$ m high channels (contact angle of the silicone based PSA around 110 °). Figure 4 shows micrographs of such fluoropolymer coatings in a microchannel.



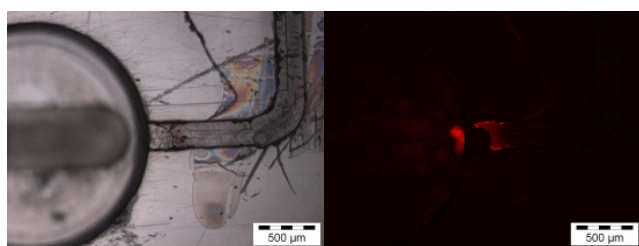


Figure 4: Micrograph and fluorescence micrograph of fluoropolymer coating (stained with fluorescent dye) in COP microchannel used as passive valve structure.

The working principle of the whole microfluidic structure is illustrated in Figure 5. After a liquid sample is introduced into the chip, the first structure is an asymmetric T-junction for splitting the liquid flow (5A). The branch having the larger channel guides the major part of the sample into a larger cavity used for metering and reagent storage. The channel leaving this chamber on the opposite side is equipped with a hydrophobic coating acting as passive valve in order to retain the sample within the chamber (5B). In the second channel branch, a comparatively small liquid flow is guided to an overflow compartment. After the whole sample volume has entered the chip, air enters the overflow channel and separates the two liquid plugs at the T-junction (5C). The outlet of the overflow compartment is sealed with a hydrophobic fluoropolymer membrane. This membrane also acts as passive valve, as it allows air-venting of the channel and overflow compartment but does not allow passage of liquid. As soon as the liquid reaches the membrane covered outlet, this branch of the channel system is blocked. Therefore, automatically the whole pressure applied at the sample inlet port acts on the hydrophobic valve sealing the metering/incubation chamber (5D). Thus the liquid front can overcome the capillary forces, pass the valve and leave the metering/incubation chamber. The metered volume and also the time span for dissolution/incubation of prestored reagents, before the metered sample will break the passive valve, can be exactly determined by the dimensions of channels and cavities.

### On-chip reagent storage

We combined the above described metering structure with a versatile strategy for on-chip reagent storage, by incorporating porous membranes into the metering/incubation chamber. Reconstitution of two different fluorescently labelled proteins (BSA-FITC, Strept-Cy3) loaded onto two different membrane pad materials (cellulose, glass fibre) were investigated using fluorescence microscopy and spectroscopy (Figures 6-8).

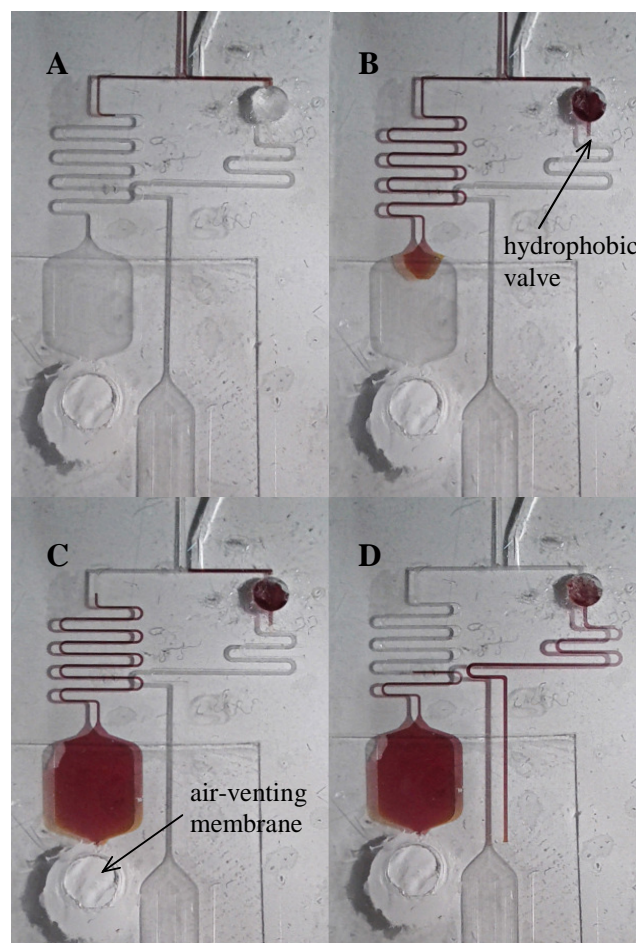


Figure 5: Demonstration of the basic working principle of the metering structure using dyed water: A) splitting of the liquid flow B) stopping of liquid flow at the hydrophobic valve after filling of the metering chamber, start of filling overflow chamber C) total liquid volume introduced into the chip, air entering the inlet and separating the liquid plugs in the two channel branches D) overflow compartment completely filled, air pressure acting on the right hand branch leads to bursting of the hydrophobic valve and emptying of the metering chamber.

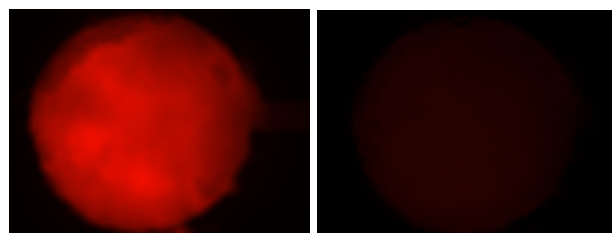


Figure 6: Fluorescence micrographs of a cellulose membrane pad loaded with Strept-Cy3, after filling (left) and subsequent rinsing (right) with buffer solution.

Fluorescence spectra recorded before and after rinsing the chamber containing the cellulose membrane with fresh buffer solution, show that the fluorescence intensity (peak area) decreases to about 20 % of the initial value (Figure 7A). Using glass fiber membranes even lower residual fluorescence intensities of about 10 % can be obtained (Figure 7B).

Using suitable membranes, the storage and almost complete reconstitution of fluorescently labelled proteins could be demonstrated (see e.g. another example for BSA-FITC in Figure 8).

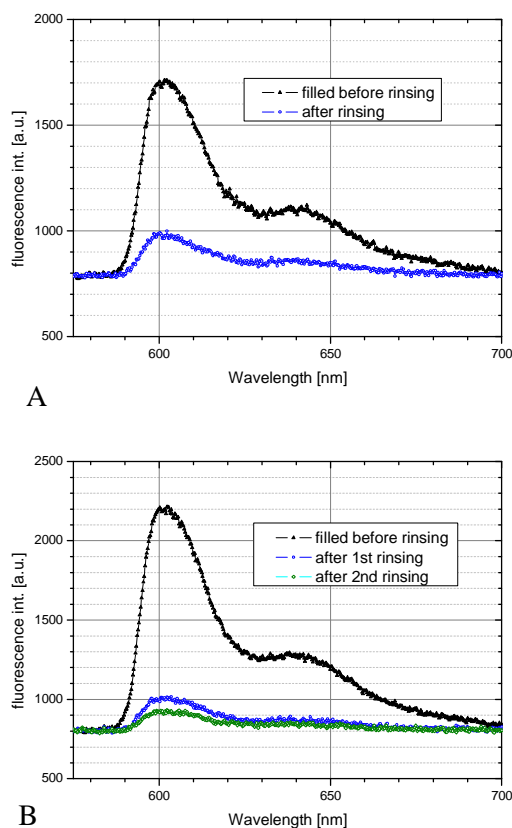


Figure 7: Fluorescence spectra of the reconstitution of Strept-Cy3, dried onto a cellulose (A) and glass fiber (B) membrane in the reagent chamber.

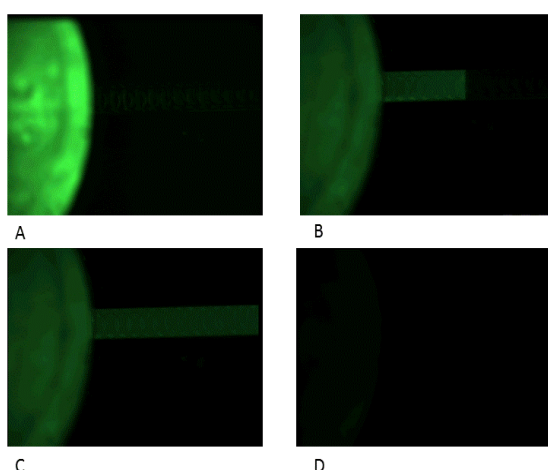


Figure 8: Fluorescence micrographs of the dissolution/reconstitution of FITC labeled BSA, dried onto a glass fiber membrane in the reagent chamber.

## REFERENCES:

- [1] S. Haeberle, R. Zengerle, "Microfluidic platforms for lab-on-a-chip applications", *Lab Chip*, Vol. 8, pp.1094-1110, 2007.
- [2] H. Andersson, W. van der Wijngaart, P. Griss, F. Niklaus, G. Stemme, "Hydrophobic valves of plasma deposited octafluorocyclobutane in DRIE channels", *Sens. Actuators B: Chem.*, Vol. 75, pp.136-141, 2001.
- [3] L. Furuberg, M. Mielnik, A. Gulliksen, L. Solli, I.-R. Johansen, J. Voitel, T. Baier, L. Riegger, F. Karlsen, "RNA amplification chip with parallel microchannels and droplet positioning using capillary valves", *Microsyst. Technol.*, Vol. 14, pp.673-681, 2008.
- [4] D. Mark, T. Metz, S. Haeberle, S. Lutz, J. Ducr e, R. Zengerle, F. von Stetten, "Centrifugo-pneumatic valve for metering of highly wetting liquids on centrifugal microfluidic platforms", *Lab Chip*, Vol. 9, pp.3599-3603, 2009.
- [5] L. Riegger, M.M. Mielnik, D. Mark, W. Streule, M. Clad, R. Zengerle, P. Koltay, "Teflon-carbon black as new material for the hydrophobic patterning of polymer labs-on-a-chip", *Digest Tech. Papers, Transducers 2009 Conference, Denver, CO, USA*, June 21-25, 2009, pp.2026-2029.
- [6] E. Garcia, J.R. Kirkham, A.V. Hatch, K.R. Hawkins, P. Yager, "Controlled Microfluidic Reconstitution of Functional Protein From an Anhydrous Storage Depot", *Lab Chip*, Vol. 4, pp. 78-82, 2004.
- [7] D.Y. Stevens, C.R. Petri, J.L. Osborn, P. Spicar-Mihalic, K.G. McKenzie, P. Yager, "Enabling a microfluidic immunoassay for the developing world by integration of on-card dry reagent storage". *Lab Chip*, Vol. 8, pp.2038-2045, 2008.
- [8] M. Hitzbleck, L. Gervais, E. Delamarche, "Controlled release of reagents in capillary-driven microfluidics using reagent integrators" *Lab Chip*, Vol. 11, pp. 2680-2685, 2011.
- [9] J.L. Garc a-Cordero, "Low-Cost Microfluidic Single-Use Valves And On-Board Reagent Storage Using Laser-Printer Technology", *Digest Tech. Papers MEMS '09 Conference, Sorrento, January 25 - 29, 2009*, pp. 439 - 442.

## CONTACT

\* S. K stler, stefan.koestler@joanneum.at

## 2. Actuators

# SIMPLIFIED MICROFLUIDIC-BASED SYSTEM TO GENERATE DOUBLE EMULSION MICRO DROPLETS FOR BIOMEDICAL APPLICATIONS

*R. Sekine<sup>1</sup>, H. Okada<sup>2</sup>, T. Sakurai<sup>2</sup>, D. H. Yoon<sup>1</sup>, R. Iizuka<sup>2</sup>, T. Sekiguchi<sup>3</sup>, T. Funatsu<sup>2</sup> and S. Shoji<sup>1</sup>*

<sup>1</sup> Major in Nanoscience and Nanoengineering, Waseda University, Tokyo, Japan

<sup>2</sup> Graduate School of Pharmaceutical Sciences, The University of Tokyo, Tokyo, Japan

<sup>3</sup> Nanotechnology Research Center, Waseda University, Tokyo, Japan

## ABSTRACT

We present two simple microfluidic systems of one-chip and two-chip for generating water-in-oil-in-water (W/O/W) droplets (double emulsion). A microfluidics device generates include two or more internal aqueous droplets with two cross-junctions was fabricated on one-chip. The two-chip system consists of two separated one cross-junction devices, which enables efficient W/O/W droplet formation with thin oil shell layer. We have also prepared W/O/W droplet containing newly-synthesized protein using the two-chip system.

## KEYWORDS

Microfluidics, Double emulsion, Uniform droplets, Protein synthesis.

## INTRODUCTION

Microfluidic droplet is an important technique to be applied to various applications in foods, cosmetics, drug delivery and cell culture. We are now developing droplet-based microfluidic screening platform for protein engineering and directed evolution. Double emulsions can provide advantages over simple water-in-oil (W/O) droplets for screening and sorting single droplets according to their fluorescence, because the carrier environment can be maintained at aqueous condition. Various techniques have been demonstrated so far for the production of double emulsions [1-3]. These microfluidic devices require multilayer structure, or unique surface treatment for changing wettability. In this paper, we present microfluidics-based systems of formation of double emulsion using simple structures.

## MATERIALS AND METHODS

### Microfluidic device design and fabrication

Fig. 1 shows device designs used in this study. One-chip system consists of one microfluidics device with two cross-junctions (Fig. 1 (a)). This system generates W/O/W droplets using shear stress obtained by the buoyance of the oil (Fig. 1 (b)). Two-chip system consists of two same microfluidics devices with one cross-junction (Fig. 1 (c)). This system employed two-step generation. After creating W/O droplets with first chip, the droplets are transported to

the second device to produce W/O/W droplets.

The devices were fabricated by polydimethylsiloxane (PDMS) casting using a SU-8 mold. In the one-chip system, the mold is formed by two step SU-8 photolithography. In the two-chip system, the mold is formed by one step SU-8 photolithography.

### Surface treatment

Generation of O/W droplets or W/O/W droplets by PDMS microfluidic chip is difficult, because of PDMS hydrophobicity. To convert the characteristic of PDMS channel into hydrophilic, the surface of channel was treated with deionized water containing 1% (v/v) Pluronic F-127, which is an amphiphilic block copolymer, before use.

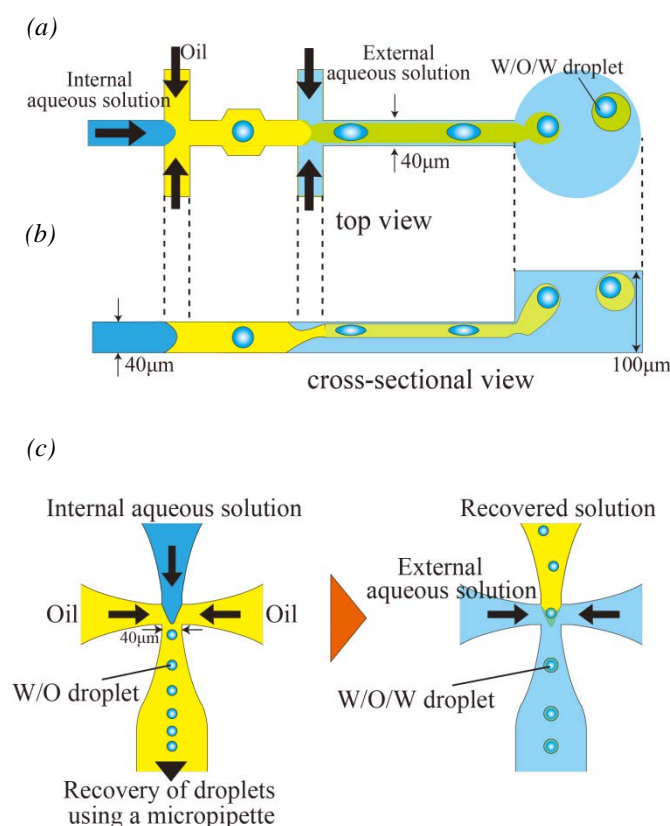


Figure 1: Schematic view of the microfluidic device for generating W/O/W droplets.; (a) Top view of one-chip system (b) Cross-sectional view of one-chip system (c) Two-chip system



## Materials

The internal aqueous solution was deionized water or rhodamine B solution. The intermediate oil consisted of mineral oil with 3% (v/v) Abil EM90, and 0.5% (v/v) Span 80. The outer aqueous solution was deionized water containing 0.25% (v/v) Pluronic F-127.

## RESULTS AND DISCUSSION

### W/O/W droplet formation in the one-chip system

Fig. 2 shows formation of W/O/W droplets in one-chip system. Internal droplets (approximately 47  $\mu\text{m}$  in diameter) were formed within the stream of the oil phase at the first cross-junction (Fig. 2 (a)). Each internal droplet was then encased within an oil phase at the second cross-junction. Finally, W/O dispersion was sheared by the buoyance of the oil, and then W/O/W droplets (approximately 96  $\mu\text{m}$  in diameter) were generated (Fig. 2 (b)).

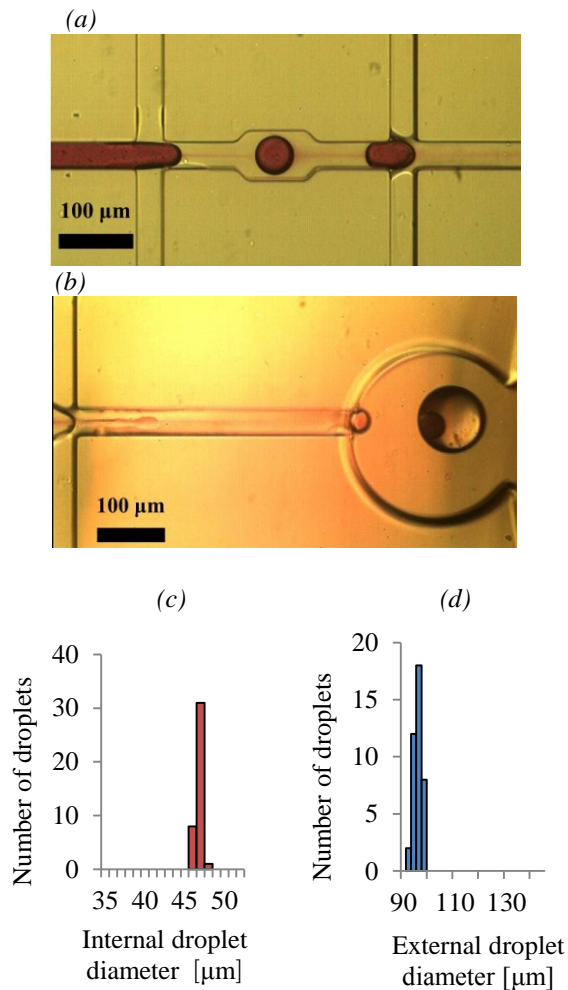


Figure 2: (a) Top view of W/O droplets formation in one-chip system. (b) Image of W/O/W droplets encapsulated one internal droplet. (c) Size distribution of internal droplets. (d) Size distribution of external droplets.

The numbers of internal droplets, two to eight were able to control by changing flow rate of the external aqueous solution (Fig. 3, Table 1). We were able to create W/O/W droplets encapsulated up to twelve internal droplets stably and continuously. Fig. 4 shows size distribution of the internal droplet and external droplet in each condition. In any case, droplet size shows a narrow distribution. However, the number of the internal droplets to be encapsulated is increased, the diameter of the internal droplets was slightly decreased, and diameter of the external droplet was increased. This is because the shearing force and the relative flow rate of oil increased, by reducing the flow rate of external solution in order to increase the number of internal droplet.

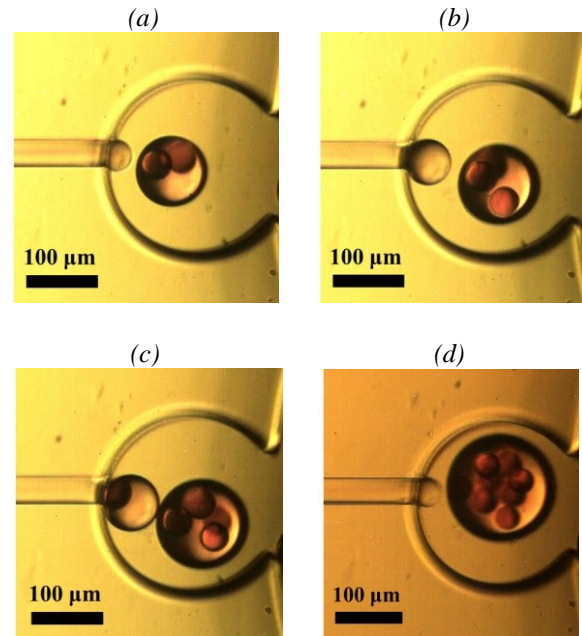


Figure 3: Formation of W/O/W droplet with a controlled number of internal droplets.; (a) Image of W/O/W droplet encapsulated two internal droplets. (b) Image of W/O/W droplet encapsulated three internal droplets. (c) Image of W/O/W droplet encapsulated four internal droplets. (d) Image of W/O/W droplets encapsulated eight internal droplets.

Table 1: Flow conditions in one-chip system.

Flow rate [ $\mu\text{L}/\text{min}$ ]			Number of enclosed droplets
$W_{in}$	O	$W_{ex}$	
0.01	0.05	0.8	1
0.01	0.05	0.6	2
0.01	0.05	0.4	3
0.01	0.05	0.3	4
0.01	0.05	0.05	8
0.01	0.1	0.05	12

$W_{in}$ : internal aqueous solution B, O: oil solution,  $W_{ex}$ : external aqueous solution.



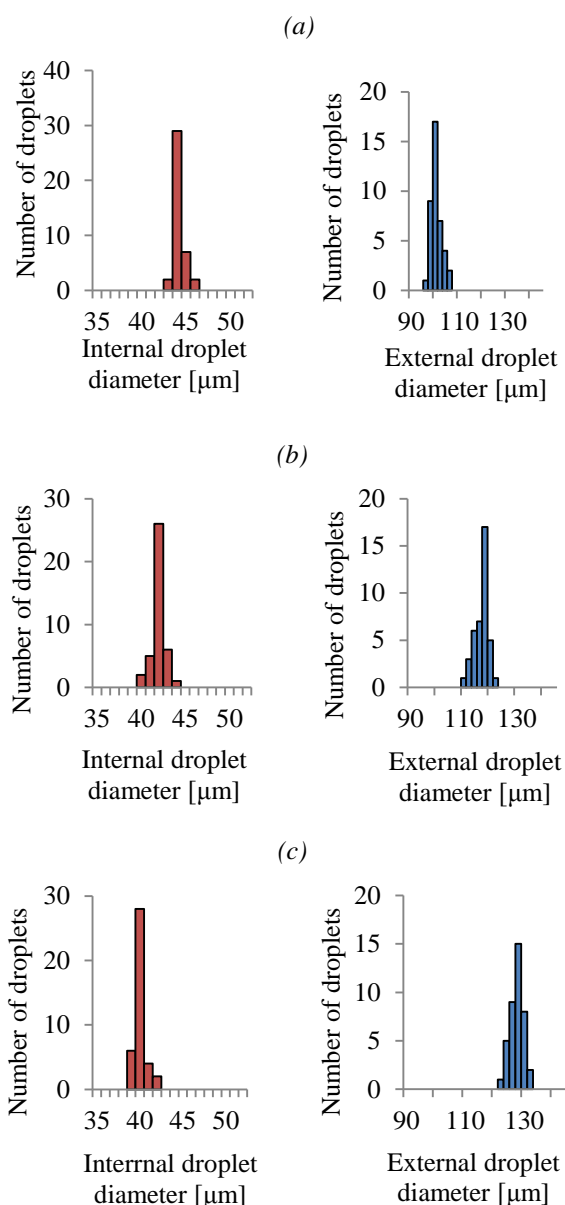


Figure 4: Size distribution of W/O/W droplets generated in the one-chip system.; (a) W/O/W droplets containing two internal droplets. (b) W/O/W droplets containing three internal droplets. (c) W/O/W droplets containing four internal droplets.

### W/O/W droplet formation in the two-chip system

Fig. 5 shows formation of W/O/W droplets in two-chip system. To stain oil shell layer, a lipophilic fluorophore Bodipy FL (excitation maximum wavelength: 503 nm, fluorescence maximum wavelength: 512 nm) was added to oil solution. Meanwhile, the internal aqueous droplet was visualized by green fluorescent protein (GFP) (Fig. 6). The resultant W/O/W droplets contained a single internal aqueous droplet and showed proper structural integrity. The mean internal and external diameters

were approximately 15 and 17  $\mu\text{m}$ , respectively (Fig. 7 (a) and (b)). The thickness of oil layer was estimated to be approximately 1.4  $\mu\text{m}$  (Fig. 7 (c)). The thickness of oil shell layer was much smaller than that of droplets generated in one-chip system.

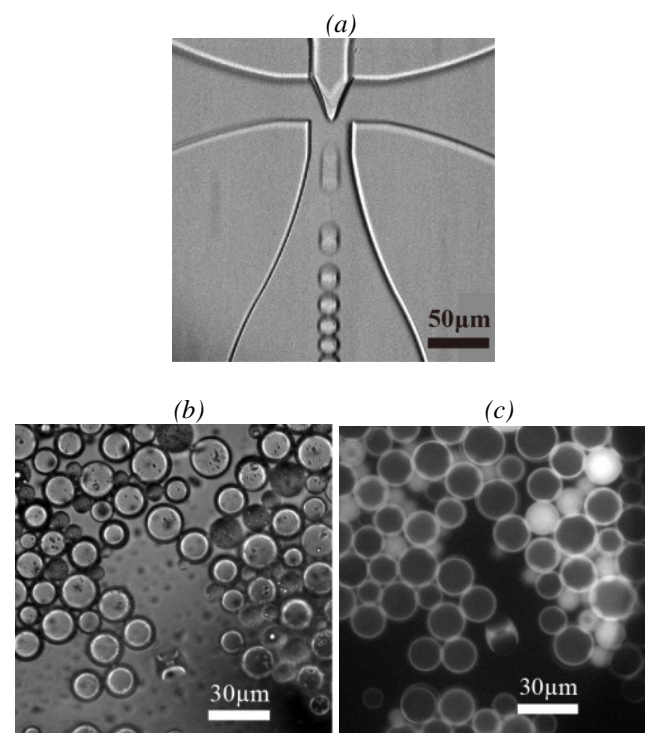


Figure 5: (a) Top view of W/O droplets formation in two-chip system. (b) Bright-field images of W/O/W droplets generated in two-chip. (c) Fluorescence images of W/O/W droplets generated in two-chip system. Oil layer was stained by a lipophilic fluorophore Bodipy FL.

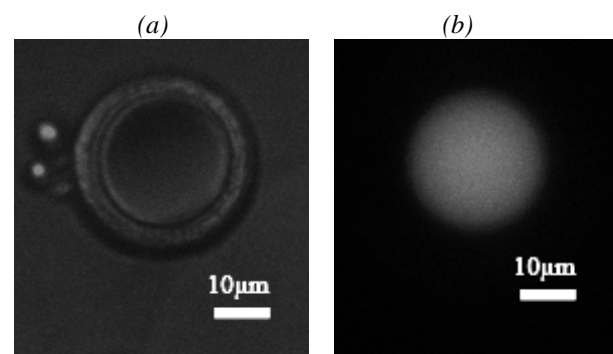


Figure 6: (a) Bright-field images of W/O/W droplets containing GFP. (b) Fluorescence images of W/O/W droplets containing GFP. The fluorescent image shows GFP fluorescence encapsulated in droplets.

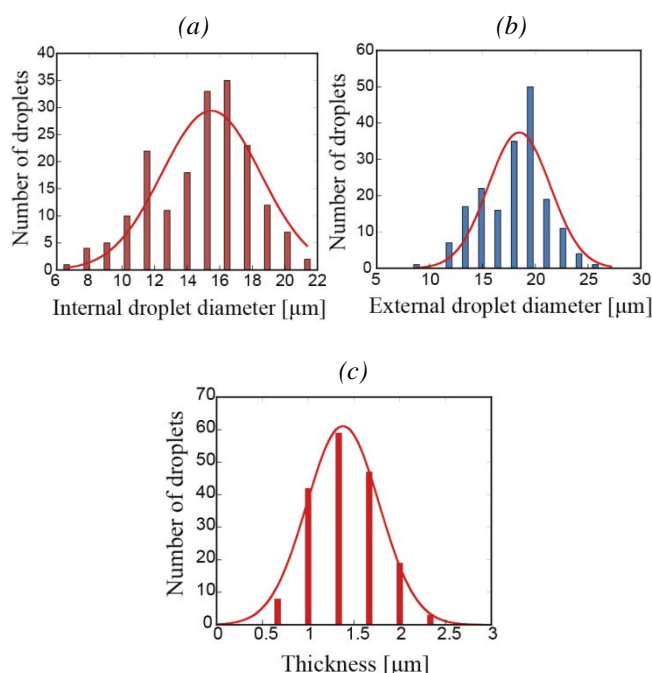


Figure 7: Size distribution of W/O/W droplets in the two-chip system.; (a) Internal diameter. Mean diameter was 15 μm. (b) External droplets. Mean diameter was 18 μm. (c) Thickness of oil layer. Mean thickness was 1.4 μm.

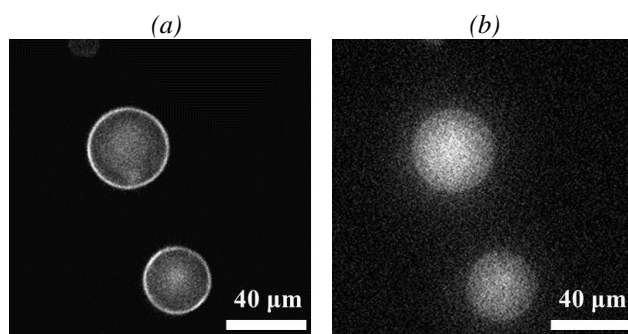


Figure 8: Fluorescence images of W/O/W droplets containing newly-synthesized protein.; (a) Oil layer was visualized by Bodipy FL (excitation wavelength: 490 nm). (b) Internal aqueous droplet was visualized by mCherry (excitation wavelength: 520 nm).

Using two-chip system, we also prepared W/O/W droplets containing newly-synthesized red fluorescent protein mCherry (excitation maximum wavelength: 587 nm, fluorescence maximum wavelength: 610nm). After the W/O droplets containing template DNA encoding mCherry and a reconstituted cell-free coupled transcription–translation system were incubated at 37°C for 1 hour, W/O/W droplets were generated. Fig. 8 shows fluorescence images of the resultant W/O/W droplets. Oil shell layer was stained by Bodipy FL (Fig. 8 (a)). mCherry was successful enclosed in the droplets (Fig. 8 (b)). The result shows

our method allows for the safe encapsulation and manipulation of an assortment of biological entities, including proteins, and nucleic acids.

## CONCLUSIONS AND OUTLOOK

We have developed simple one-chip and two-chip W/O/W droplet generation systems. In one-chip system, W/O/W droplets containing multiple internal aqueous droplets were obtained. The number of enclosed droplets was controlled by the flow rate of the external aqueous solution. On the other hand, two-chip system rendered W/O/W droplets with a single aqueous droplet and a thin oil shell layer were generated. These two different features are expected to be used for a wide range of applications. We will employ these systems as screening platforms for protein engineering and directed evolution.

## ACKNOWLEDGEMENTS

This work is partly supported by Japan Ministry of Education, Culture, Sports Science & Technology Grant-in-Aid for Scientific Basic Research (S) No. 23226010 and Young Scientists (B) No. 24710247. The authors thank for Nanotechnology Platform of Waseda University for their technical assistances.

## REFERENCES

- [1] A. S. Utada, E. Lorenceau, D. R. Link, P. D. Kaplan, H. A. Stone, D. A. Weitz, “Monodisperse Double Emulsions Generated from a Microcapillary Device”, *Science*, 308, 537-541, 2005.
- [2] Adam R. Abate, Julian Thiele, Marie Weinhart and David A. Weitz “Patterning microfluidic device wettability using flow confinement”, *Lab on a Chip*, 10, 1774–1776, 2010.
- [3] Ryan T Davies, Donghwan Kim and Jaesung Park, “Formation of liposomes using a 3D flow focusing microfluidic device with spatially patterned wettability by corona discharge, *J. Micromech. Microeng*, 22, 055003, 2012.

## CONTACT

\* Rui Sekine, sekine@shoji.comm.waseda.ac.jp

## 3. Interfaces

# A MICROFLUIDIC INTERPOSER BASED ON THREE DIMENSIONAL MOLDED SUBSTRATE TECHNOLOGY

*T. Leneke, M. P. Schmidt, S. Hirsch and B. Schmidt*

Institute of Micro and Sensor Systems, Otto-von-Guericke-University, Magdeburg, Germany

## ABSTRACT

Three dimensional molded interconnect devices (MID) with fluidic features offer new possibilities for the packaging of microfluidic components. This paper reports about an MID based fluidic interposer to bridge the micro-macro gap of fluid delivery in microfluidic systems. The interposer is fabricated by standard MID fabrication technology and includes a metallization for electrical signals and channel structures for fluidic functions. A microfluidic test chip is assembled to the interposer by a flip-chip process. The proposed interposer is suitable for pressure and capillary driven flows. Results from pressurization testing with liquids and gases are given.

## KEYWORDS

fluidic interposer, microfluidic packaging, molded interconnect device, flip-chip

## INTRODUCTION

Microfluidic devices are popular in medical, chemical and biological applications. There, various processes take advantage of the miniaturization capabilities of such systems. Microfluidic chips include e.g. channels, valves, pumps or mixers with micrometer dimensions. Mostly silicon, glass or polymer materials are used and processed with standard MEMS or micro-fabrication techniques.

However, the packaging of such microfluidic chips is difficult. The supply of fluids to the microfluidic chip requires a transformation from the macro scale (environment side) to the micro scale (microfluidic chip side) [1]. Furthermore mechanical fixation and leak tightness of the fluidic interconnections needs to be guaranteed by the package. Gluing of miniaturized fluid ports or tubes directly on the microfluidic chip is a possible solution. Also overmolding or the use of wells has been reported. But most common solutions require manual assembly steps and are thus prone to errors, not compatible to automatic assembly processes and expensive.

We propose an MID based fluidic interposer for the packaging of microfluidic chips. Electrical interposers are common in chip packaging to reroute, distribute, sort and scale electrical signals. A fluidic interposer can scale, distribute and route fluidic media. The chosen MID fabrication technology allows the parallel implementation of fluidic and electrical

features [2]. A concept of an MID based fluidic interposer is given in Figure 1. The microfluidic chips are assembled by a flip-chip process. Multiple fluid in- and outlets can be realized e.g. by solder connections between a microfluidic chip and the fluidic interposer. The production and assembly processes are compatible to automated manufacturing equipment.

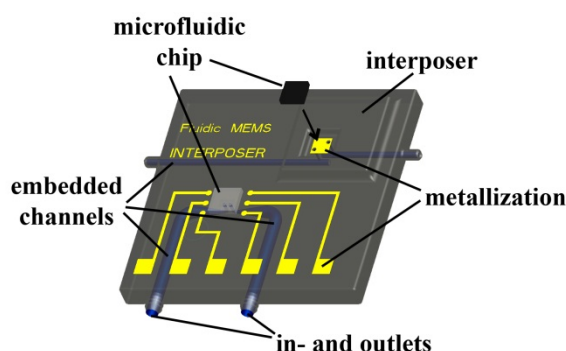


Figure 1: Concept of an MID (molded interconnect device) based fluidic interposer for the packaging of microfluidic chips.

## FABRICATION AND DESIGN

### MID Fabrication Process

A standard MID manufacturing process is used to fabricate the fluidic interposer. The LDS-process (laser direct structuring) [3] consists of the steps injection molding, laser activation and metallization. A suitable thermoplastic polymer is processed by injection molding. The liquid crystal polymer material (LCP Vectra E820i LDS from Ticona) contains organometallic compounds for subsequent laser activation and is compatible to process temperatures up to 270 °C. Furthermore this liquid crystal polymer is resistant to most solvents and acids and appropriate for microfluidic applications [4]. After injection molding the substrate surface is locally activated by means of laser radiation (Nd:YAG laser; 1064 nm). The organometallic compounds that are exposed to the laser radiation become catalytic nuclei for the following electroless metallization. The metallization process includes three deposition steps – 5 µm copper, 5 µm nickel and 0.1 µm gold. This Cu/Ni/Au metallization is suitable for standard packaging processes, e.g. lead free soldering or wire bonding [5]. Figure 2 shows an overview of the LDS fabrication process that is used for the fluidic interposer.



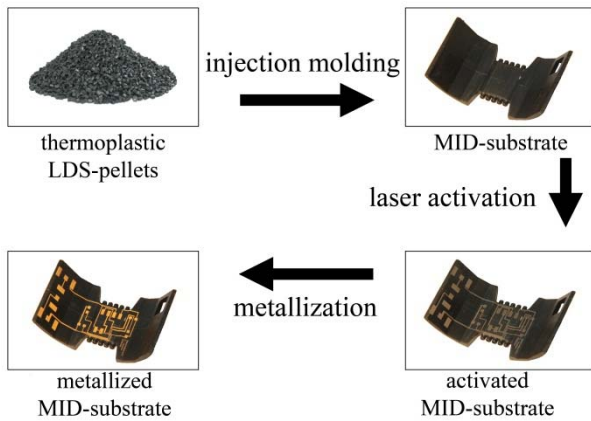


Figure 2: LDS (laser direct structuring) fabrication process used to fabricate the fluidic interposer.

### Fluidic Interposer Demonstrator Design

The injection molded fluidic interposer demonstrator is a semicircular shaped substrate with a flat mounting area for the assembly of microfluidic chips. Five embedded channels with a diameter of  $1500\text{ }\mu\text{m}$  run under the mounting area. Channels with a diameter of  $650\text{ }\mu\text{m}$  are created by laser drilling to connect the embedded channels with the mounting area surface. The fluidic interposer in- and outlet ports are designed to fit to tubes that can be attached manually. For the fluidic interconnections between microfluidic chip and fluidic interposer a ring shaped metallization is formed around the channel openings on the mounting area by the LDS process. Since the microfluidic chips will be placed by flip-chip it is necessary to prevent the channel openings on the mounting area and on the microfluidic chip from accidental clogging during assembly processes. Clogging might occur from the solder or glue that is squeezed between microfluidic chip and fluidic interposer. To control the assembly of the respective microfluidic chips, spacer features with a height of  $250\text{ }\mu\text{m}$  are created during injection molding. These spacers allow an exact definition of the gap between the fluidic interposer and the microfluidic chip and can prevent the clogging of the respective fluidic channels during flip-chip assembly. The injection molded fluidic interposer is shown in Figure 3.

### Microfluidic Test Chip Fabrication

To characterize the fluidic interposer different microfluidic test chips have been fabricated. These test chips are made of silicon and glass. Microchannels with  $100\text{ }\mu\text{m}$  depth and  $275\text{ }\mu\text{m}$  width are formed in the silicon using dry etching. The silicon wafer with the microfluidic channels is sealed

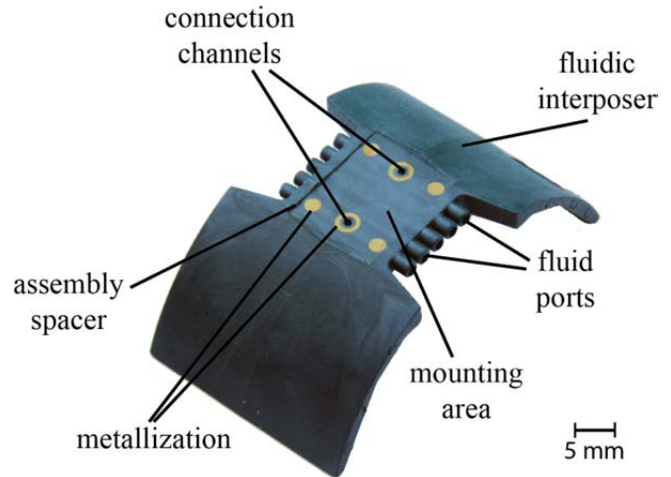


Figure 3: Fabricated fluidic interposer demonstrator.

with a glass wafer by an anodic bonding process. Laser drilling is used to establish a contact between the microfluidic channels and the environment. The front side of a microfluidic test chip is given in Figure 4 (a). The chip metallization is deposited by an aluminum PVD (physical vapor deposition) process. To receive a solderable metallization the aluminum metallization is treated with an electroless zinc-nickel-gold under-bump-metallization (Zn/Ni/Au UBM) process [6]. In Figure 4 (b) the back side of a microfluidic test chip is shown.

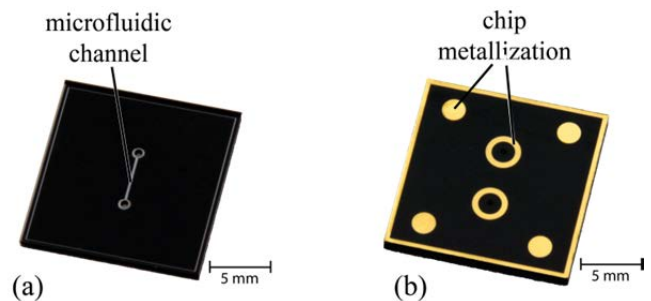


Figure 4: Example of a microfluidic test chip used for characterization of the fluidic interposer. Part (a) shows the front side with a glass covered microfluidic channel. Part (b) shows the back side with a Al/Zn/Ni/Au metallization.

### ASSEMBLY PROCESS

To connect the fluidic interposer to a microfluidic chip a flip-chip assembly process is chosen. The fluidic interconnection can be created by soldering or gluing, depending on the restrictions of the used materials and desired applications. We used soldering to create the fluidic interconnections. Lead free solder paste (SAC305) is dispensed with a semi-automatic dispenser to the respective metal surfaces on the fluidic interposer. Then, the microfluidic chip is flip-chip mounted to the fluidic interposer. During



placement the mentioned spacer structures avoid an excessive squeezing of the solder paste and prevent the fluid openings from clogging. The fluidic interposer and the microfluidic chip are soldered together by a vapor phase soldering process with a peak temperature of 231 °C. Finally, a solvent based cleaning process is done to remove solder flux and further process residues. The inside of the fluidic interconnections are cleaned by pumping the cleaner through the system. After soldering, the ring shaped metallization around the fluid in- and outlets on the mounting area of the fluidic interposer and on the microfluidic chip realize a sealed fluidic interconnection. Tubes are plugged manually to the fluidic interposer to supply a fluid to the system. Figure 5 shows an assembled device.

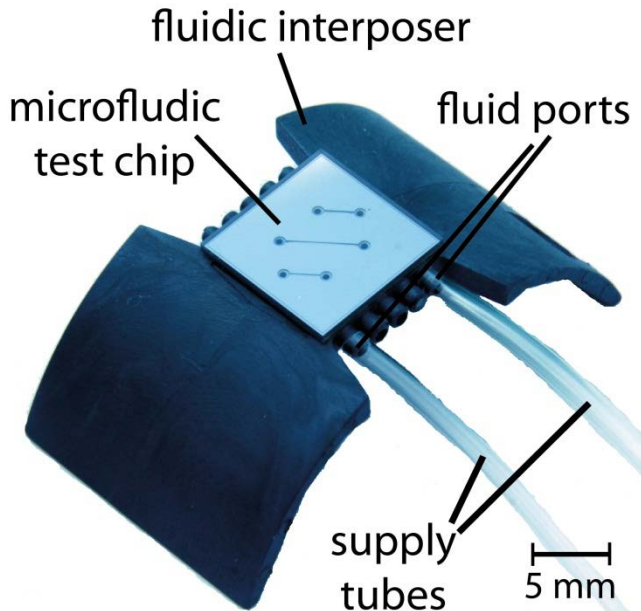


Figure 5: Assembled fluidic system. The microfluidic test chip is mounted to the fluidic interposer by a flip-chip solder process.

### DEVICE CHARACTERIZATION

For many packaging solutions the achievable inlet pressure is an important attribute [1]. To characterize the proposed system, a fluidic daisy-chain structure is realized. Similar to an electrical daisy-chain set up, a fluidic daisy-chain allows the testing of multiple fluidic interconnections. The realized fluidic daisy-chain test structure consists of three microfluidic channels in the microfluidic test chip and three fluidic channels in the fluidic interposer. Thus, in total six fluidic interconnections are implemented in one device. A schematic view is shown in Figure 6 and X-ray images of the realized samples are given in Figure 7.

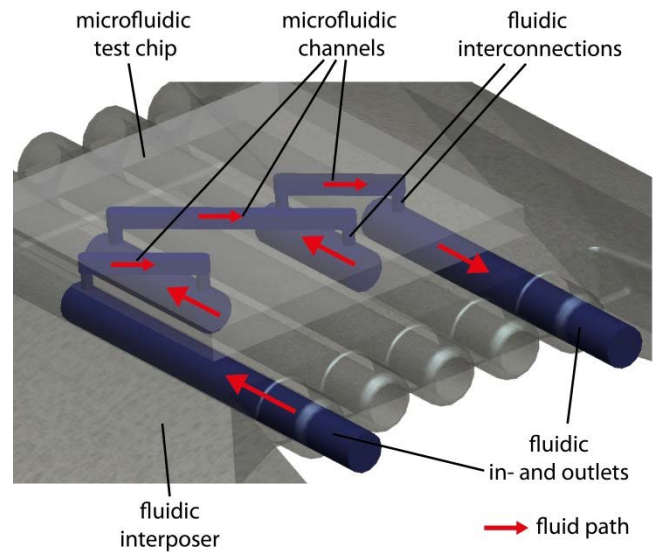


Figure 6: Concept of a fluidic daisy-chain test structure.

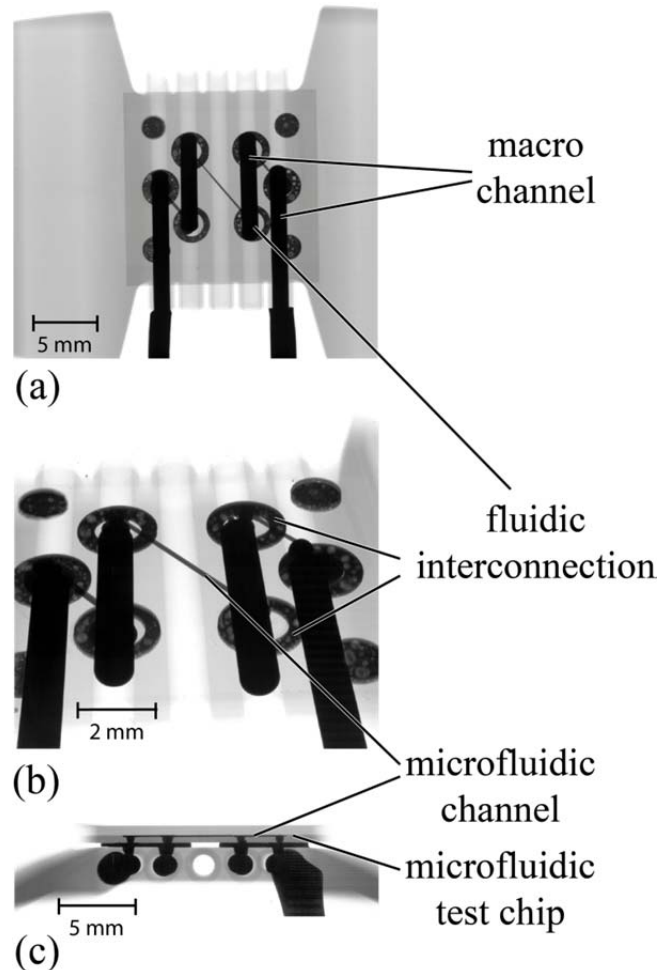


Figure 7: X-ray images of the tested fluidic daisy-chain structures. Mercury is used to visualize the fluid path. Part (a) shows the top view, part (b) an oblique view and part (c) the side view.

A cross section of the respective sample is depicted in Figure 8. Besides two ring-soldered fluid interconnections and the injection molded spacer structures one can see the microfluidic channel in the microfluidic test chip and the fluid channels in the fluidic interposer.

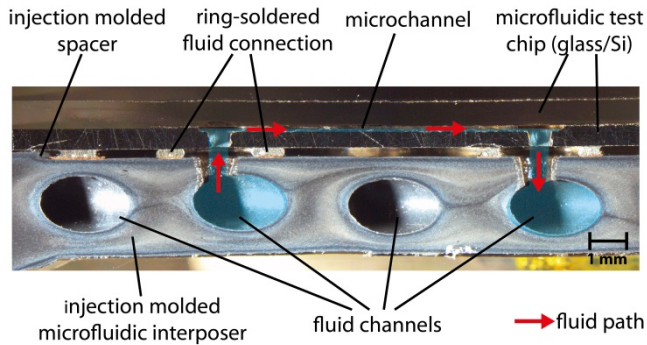


Figure 8: Cross section of the interposer with an assembled microfluidic chip.

Five interposers with daisy-chain features were prepared for characterization. Water was pumped through the system and the pressure at the inlet was measured with a manometer. A maximum pressure of 200 kPa was generated by the used pump. The five samples were tested for 120 minutes. During and after testing no visual failure could be detected. The disadvantage of the fluid daisy-chain approach is the pressure drop across the fluid path. This means that the first fluid interconnection will be stressed most and the last one will be stressed least. To test a single fluid interconnection dummy test chips without microfluidic features have been used. These dummy chips have the same metallization as the microfluidic chips but no openings or channels. Thus, the fluid path will be blocked by such chips and applied test pressures of a gaseous media will equable stress the respective fluid interconnection. For leakage detection the set-up is immersed into a water bath. The respective schematic of the test set-up is given in Figure 9. The air pressure was increased in steps of 100 kPa up to 800 kPa for testing. For pressures above 800 kPa bursting of the supply tubes occurred. Each pressure step was tested for 120 minutes. All 20 samples passed the tests without any failure.

## CONCLUSION AND OUTLOOK

In this paper a fluidic interposer has been presented that enables the transformation from the macro to the micro world for fluid supply to microfluidic systems. The interposer allows the flip-chip assembly of microfluidic chips and the fluid supply to the embedded fluid structures of the microfluidic chip.

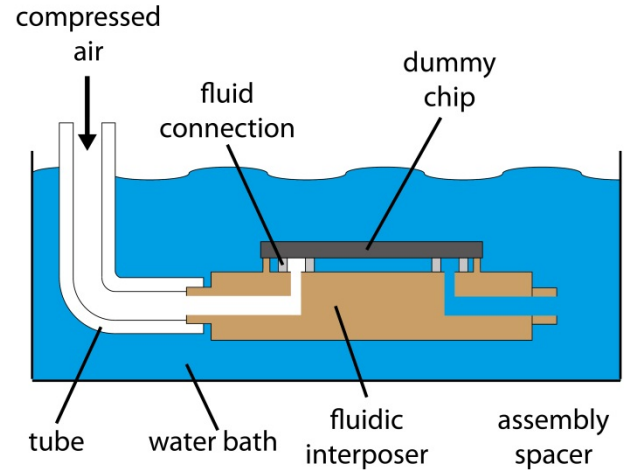


Figure 9: Leakage test set-up. A dummy chip is assembled on the fluidic interposer and tested in a water bath.

A demonstrator, based on molded interconnect device technology, was fabricated by the laser direct structuring method. Assembled systems were characterized by two different test set-ups regarding maximum pressurization abilities of the fluidic interconnections. Since only standard fabrication and assembly technologies were used, the proposed solution is compatible to full automated mass production equipment and allows a rather low-priced packaging of microfluidic devices.

Even though results look promising, further characterization and optimization is necessary. The performed pressure experiments did not determine the pressure limits of the fluid interconnections. An improved test set-up that enables higher test pressures is preferable.

## REFERENCES

- [1] C. Fredrickson, Z. Fan, "Macro-to-micro interfaces for microfluidic devices", *Lab Chip*, Vol. 4, pp. 525-533, 2004.
- [2] W. Xu, W. Cui, J. Bo, "Manufacture process of molded interconnect device (MID)", *Proc. of the 2nd International Conference on Modelling and Simulation, Manchester, UK*, May 21-22, 2009.
- [3] H. Wißbrock, "Laser direct structuring of plastics. A new addition to MID technologies", *Kunststoffe Plast Europe*, Vol. 92, Issue 11, 2002.
- [4] D. Webb, D. Hutt, N. Hopkinson, P. Conway, P. Palmer, "Packaging of Microfluidic Devices for Fluid Interconnection Using Thermoplastics", *Journal of Micromechanical Systems*, Vol. 18, No. 2, 2009.
- [5] S. Canumalla, P. Viswanadham, "Portable Consumer Electronics", *PennWell*, 2010.
- [6] D. Hutt, et al., "Electroless Nickel Bumping of Aluminum Bondpads – Part I", *IEEE Trans. Components Pack. Tech.*, Vol. 25, No. 1, 2002.

## POLYMER-BASED MICRO FLOW SENSOR WITH ALTERNATIVE ELECTRONIC SIGNAL INTERFACES FOR LOW AND HIGH FLOW RATES

*Thomas Schönstein*

Innovative Sensor Technology AG

CH-9630 Wattwil, Schweiz

Industriestrasse 2

### ABSTRACT

The qualitative and quantitative assessment of gas flow has become increasingly relevant in the use of everyday systems. The Microflow sensor, developed by Innovative Sensor Technology AG (Switzerland), is by principle a calorimetric flow sensor produced as a micro system on a glass substrate by means of photolithography and glass etching technology. These structures are arranged as a platinum micro heater and sensors in a Wheatstone bridge. The subsequent etching process produces an exposed area of polyimide membrane that is only a few microns thick and includes the resistive sensor structure as the active area.

In addition, the RTD technology included on the sensor allows for the implementation of a variety of electronic biasing and signal processing modes. Since the sensor can be powered and the bridge can be measured in both CTA and calorimetric mode, new possibilities are presented for both low and high flow rates with regard to temperature compensation, self-calibration and self-monitoring

### KEYWORDS

Calorimetric flow sensor, pick & place assembly  
CTA- Mode, low and high flow rates

### INTRODUCTION

The sensors are characterized by a very small time response and low power consumption, achieved through the principle of MEMs hot film anemometry. Despite an extremely thin membrane, the glass carrier produces a robust sensor and provides easy handling. The heater/sensor structure, in combination with the full bridge circuitry “on chip”, ensures simple signal evaluation and offers the ability to detect the flow direction. The thin film sputtering and etching processes of IST allow for low initial development costs for application-specific, custom sensor designs and support cost effective volume production. A wide range of sensor dimensions, resistance values, structural formations and mounting configurations are possible. As a result, cost effective solutions including a sensor on PCB with electronic signal processing and flow channel can be easily developed in a timely manner.

### SENSOR ADVANTAGES

Compared with its silicon-based counterparts, the micro flow sensor from IST AG offers major advantages relating to dynamic measuring range and assembly of the sensing element into customer systems for design-in processes. Due to the sensor's ability to operate in a combination of CTA and calorimetric mode, the flow signal saturation can be shifted from 1 m/s (only calorimetric mode) to 50 m/s (both modes combined). These flow velocities translate to a volumetric flow range from 0.001 L/min full scale to 10 L/min full scale (depending on the flow channel cross-sectional area) with a possible resolution of 1% of the full scale value.

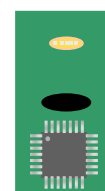
The response time of 10 ms and warm up time of 100 ms allows for time-based low power heater management. With the platinum technology of all resistive structures, a heater temperature regulation loop can be realized in order to maintain a constant temperature and to protect the sensor against damage from overheating. Especially during power down cycles, the resistive structures can be used to measure the gas temperature. As a result, it is possible to maintain active temperature compensation by tracking the heating power of the sensor's micro heater.

### SENSOR ASSEMBLY

The sensors can be produced economically and are well-suited for pick & place assembly. It can be handled similar to an IC - die or SMD component, assembled by standard pick & place machines or by hand. Electronic connections to a PCB can be achieved through wire bonding or flip chip technology. The sensor can be assembled over a milled PCB channel or directly embedded into a PCB cavity. The goal of IST's sensor/electronic interface development is to provide customers with an easy-to-use measurement concept for realizing their own proprietary solutions down to the component level of flow measurement technique.



Figure 1: Assembly example  
of Microflow sensor





### CALORIMETER MODE

The most common used measuring mode for micro machined flow sensors is the calorimetric mode. Here the temperature distribution along a sensor – heater- sensor- structure depending on gas flow is used to provide an electrical differential signal by thermal imbalance of upstream and downstream sensor elements (e.g. thermopiles)

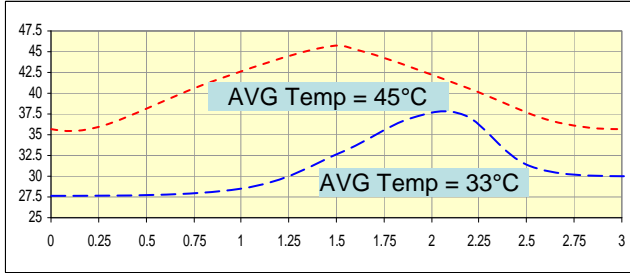


Figure2: Example of symmetrical and imbalanced temperature distribution on a 3mm sensor area

In case of a flow rate near by 200ml/min a temperature difference of some degree centigrade (°C) between up- and down stream sensor appears and causes a bridge signal of about 40....50 mV. Here the user is faced with premature saturation effects, preventing high flow applications. This can be eliminated by using both flow measuring modes at one sensor structure. (Calorimetric and Anemometric mode). The anemometric mode, especially the CTA-mode, is responsible for compensating the loss of heating power caused by gas flow. So an extended measuring range of calorimetric mode can be achieved. And additionally the output of the CTA can be used up to flow rates of 10 liter / min.

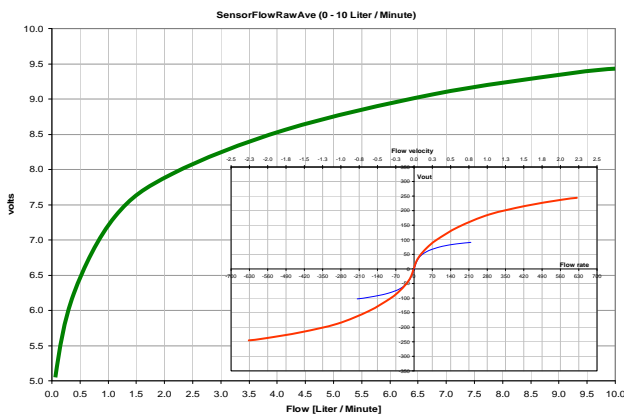


Figure 3: Example of extended flow range by using CTA- output

### CTA- Mode

The most popular anemometer is the Constant Temperature Anemometer (CTA). It's function is well described by the King's Law:

$$P_H = I_H^2 \cdot R_H = (A + B \cdot \dot{v}^n) \cdot \Delta T$$

$$n = 0.3...0.5 \quad (1)$$

By converting and simplifying this equation we obtain this formula:

$$U = U_0 \cdot \sqrt{1 + k \cdot \dot{v}^n} \quad (2)$$

$U$  = CTA-output  
 $U_0$  = free convection offset  
 $k$  = fluidic depend constant  
 $\dot{v}$  = fluid velocity

Thus, the output is determined by an offset ( $U_0$ ), an offset dependant slope of the curve, and the fluidic dependant gain value ( $k$ ).

Here,  $U_0$  represents the value of constant temperature difference ( $\Delta T$ ) between the heater and fluid. Strictly speaking, the controller of a CTA keeps the resistive structure at a constant temperature. So, different passivation thicknesses and flow element surfaces impact the CTA characteristics, even a deviation in the heat transfer coefficient ( $\alpha$ ). The characteristics depend not only on sensor alignment/orientation and fluid type, but also on fluid temperature and sensor contamination (such as dust). So the equation for a still fluid is:

$$\alpha_0 \cdot A \cdot \Delta T \sim U_0^2 (1 + k \cdot \dot{v}^n) \quad (3)$$

$$\alpha_0 \cdot A \cdot \Delta T \sim U_0^2$$

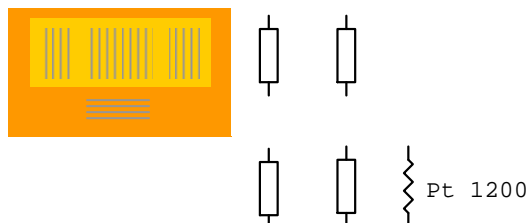
That means each deviation of CTA-characteristic, caused by free convective parameters like  $\alpha_0$  can be compensated by a  $U_0$ -adjustment at  $\dot{v} = 0$ . In order to calibrate the  $k$ -value (fluidic-caused errors) more than one point is necessary. But, fluidic-caused errors mostly depend on mechanical alignment deviations of the sensor mounting. If mounting errors can be determined by module construction, a one point calibration provides good results for many applications.



## CHIP DESIGN AND CIRCUIT

To get a high flow rate sensor circuit a microflow sensor has to be implemented into a CTA- bridge.

4-resistors + Temp. sensor



Using as full bridge  
in a CTA ; Flow direction sensitive

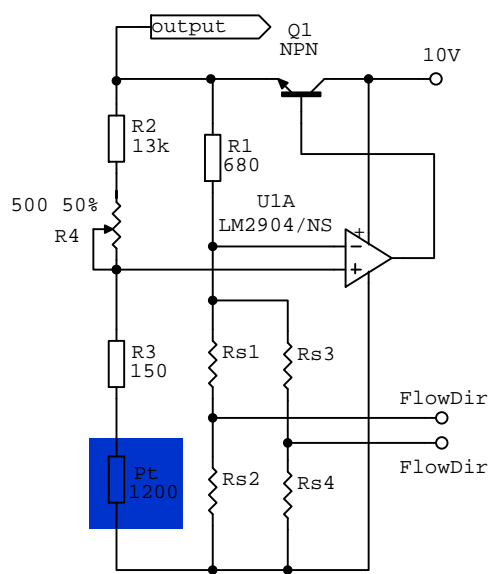


Figure 4: Sensor layout and CTA circuit

The complete 4 resistor sensor bridge acts as the heater of the CTA (Rs1....Rs4). The outputs “FlowDir” provide once the calorimetric mode and also the signal for flow direction.

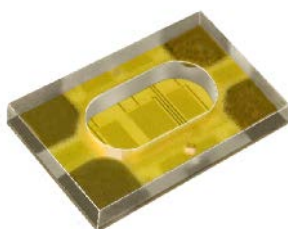


Figure 5: Microflow sensor element  
3mm x 5mm x 0,5mm

## REFERENCES:

- [1] Brokmann, U.: Beitrag zur Mikrostrukturierung von fotostrukturierbarem Glas mittels UV-Strahlung. Ilmenau: TU, 2005, Diss.
- [2] Mrotzek, S.; Hülsenberg, D.; Hesse, A.: Kristallisation eines fotostrukturierbaren Glases im System Li2O- Al2O3- SiO2. Ilmenau: TU
- [3] Technische Glaswerke Ilmenau: Fotostrukturierbares Glas für mikrotechnische Anwendungen. fuko\_flyer.pdf, Ilmenau

## CONTACT

Thomas Schönstein,  
thomas.schoenstein@ist-ag.com

# WAFER-THROUGH ACCESS TRENCHES FOR SURFACE CHANNEL TECHNOLOGY

J. Groenesteijn<sup>1</sup>, M.J. de Boer<sup>1</sup>, T.S.J. Lammerink<sup>1</sup>, J.C. Lötters<sup>1,2</sup> and R.J. Wiegerink<sup>1</sup>

<sup>1</sup>MESA<sup>+</sup> Institute for Nanotechnology, University of Twente, Enschede, The Netherlands

<sup>2</sup>Bronkhorst High-Tech BV, Ruurlo, The Netherlands

**Novelty:** We have designed a new method to integrate fluidic access to devices made by surface channel technology. The method uses a high aspect-ratio DRIE process for etching wafer-through trenches to allow access to the front side of the surface channel device. LPCVD of TEOS is used as etch-stop and to define a reliable connection between channel and access trench during fabrication. The resulting connection is robust and increases design freedom for the surface channel technology. The complete fluid path has only one wetted material, allowing for high chemical inertness.

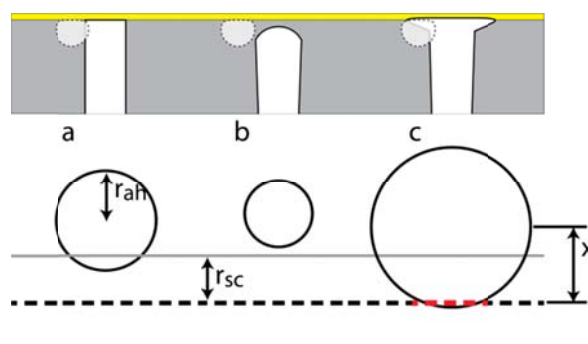
**Previous work:** In [1], surface channel technology was introduced as a universal technology for a wide range of fluidic devices. With the technology, micro channels with a diameter of a few  $\mu\text{m}$  up to over 100  $\mu\text{m}$  can be made. The channels can be released so they are freely suspended. The technology was introduced with front-side access holes. Problems with relation to robustness, scalability and fabrication freedom led to the introduction of back-side access holes in [2]. This method provided a more robust connection and leaves the front side of the device open for post-processing, vacuum sealing and (optical) read-out by external equipment. While this method solved several problems, it also introduced new ones. The high aspect-ratio DRIE etch, required to etch through the wafer, introduced wafer-scale non-uniformities making the method mainly suitable for large channels. Figure 1 shows a schematic overview of the etch-profiles of the DRIE process with the channels shown right underneath the surface (top) and the resulting connection to the surface channel (bottom). The ideal result is shown in Figure 1a. The access hole and surface channel overlap slightly. Figure 1b shows the case where the process etched slightly slower, the bottom of the hole is rounded and has not yet reached the channel: no connection is made. Figure 1c shows the case where the process etched slightly faster, notching causes the hole to increase in diameter at the end. When the hole becomes large enough that it overlaps with the etch-slits for the channels, it will disrupt the channel fabrication, resulting in leaky channels. Both etch-profiles are observed on the same wafer during processing.

**Back-side access trenches:** To make the process more reliable, more tolerant to wafer-scale non-uniformities and less dependent on the diameter of the channels, two changes were made. First, non-uniformities are reduced due to the use of rectangular trenches instead of round holes [3]. Second, the channels are fabricated first and then the access

trenches as shown in the outline in Figure 2. This makes sure that the trench cannot interfere with channel fabrication. To protect the channels during the trench etch, a layer of tetraethylorthosilicate (TEOS) oxide is deposited inside the channels using LPCVD (Figure 2b). This functions as an etch-stop for the trench etch and makes sure that the connection is properly defined. Due to this layer, the access trench can completely overlap with the channel, ensuring a connection between channel and trench as shown in Figure 3. It also allows for an over-etch for the complete height of the channel before causing a problem, allowing for compensation of wafer-scale non-uniformities. Figure 4 shows images of an access trench successfully connected to five parallel surface channels. Figure 4a shows a top view. The five channels are dark red. The etch-slits used to etch the channel are still visible as dark dots. The trench is outlined by the dotted line and can be seen as a darker area inside the channels. Figure 4b and c show SEM images of cross-sections along the vertical and horizontal red lines respectively in Figure 4a.

**Word Count: 600**

**Submitting author:** J. Groenesteijn, MESA<sup>+</sup> Institute for Nanotechnology, University of Twente, P.O. Box 217, 7500 AE Enschede, The Netherlands, phone: +31-53-4894373, e-mail: [j.groenesteijn@utwente.nl](mailto:j.groenesteijn@utwente.nl).



*Figure 1: Schematic overview of a high aspect-ratio DRIE process. Top: cross-section of the wafer. Bottom: top-view of the connection between access hole and surface channel. A) ideal result. B) etched too short: the access hole does not reach the surface channel, no connection is made. C) etched too long: notching causes the diameter of the access hole to increase. When it increases too much, it will disrupt channel fabrication resulting in leaky channels*

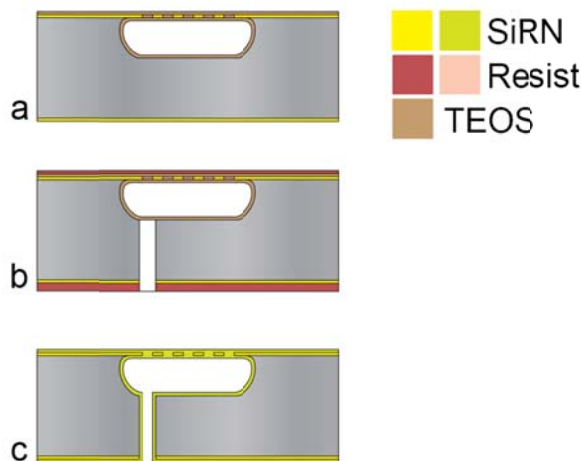


Figure 2. Schematic view of the fabrication process of back-side access trenches. A) surface channel fabrication. B) TEOS LPCVD and high aspect-ratio DRIE. C) TEOS removal and SiRN LPCVD to seal the channels and form the channel wall.

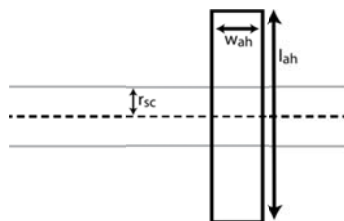


Figure 3. Top-view of the design for back-side access trenches. The trench crosses the channel, ensuring a proper connection.

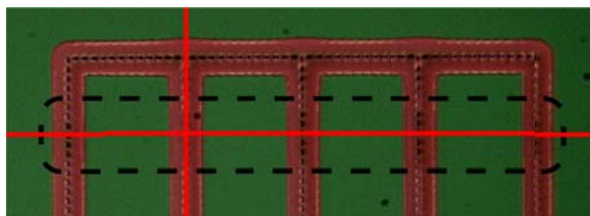


Figure 4a. Photograph of a successful connection between access trench and five parallel surface channels with a cross-channel. The trench is outlined by the dashed line and can be seen as a darker area in the surface channels. The red lines indicate the locations of the cross-sections in Figure 4.

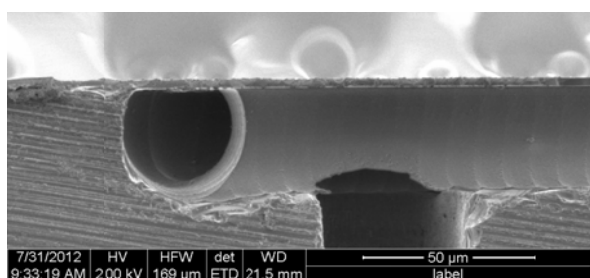


Figure 4b. SEM image of a successful connection between surface channel and access trench along the vertical red line in figure 4a. The trench crosses the channels, ensuring that it always 'hits' the channel.

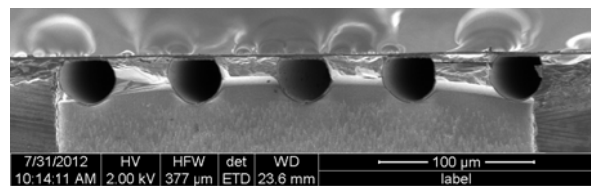


Figure 4c. SEM image of a successful connection between five parallel surface channels and an access trench along the horizontal red line in figure 4a. All five channels are connected while there is still silicon left at the top, allowing for over-etching if required due to wafer-scale non-uniformities.

## REFERENCES:

- [1] M. Dijkstra, M.J. De Boer, J.W. Berenschot, T.S.J. Lammerink, R.J. Wierink and M.C. Elwenspoek, "A versatile surface channel concept for microfluidic applications.", *Journal of Micromechanics and Microengineering*, 17:1971, 2007.
- [2] J. Haneveld, T.S.J. Lammerink, M.J. de Boer and R.J. Wierink, "Micro coriolis mass flow sensor with integrated capacitive readout", *Micro Electro Mechanical Systems, 2009. MEMS 2009. IEEE 22nd International Conference on*, pages 463–466, jan. 2009
- [3] H.V. Jansen, M.J. De Boer, S. Unnikrishnan, M.C. Louwerse and M.C. Elwenspoek, "Black silicon method x: a review on high speed and selective plasma etching of silicon with profile control: an in-depth comparison between bosch and cryostat drier processes as a roadmap to next generation equipment", *Journal of Micromechanics and Microengineering*, 19:033001, 2009.

# PRECISE FLUID HANDLING SYSTEM BASED ON PRESSURE REGULATION

Charles-André KIEFFER<sup>1</sup>, Stéphane RITTY<sup>1</sup>, Thomas BOUDOT<sup>1</sup>, Nicolas PETIT<sup>2</sup>,  
Jérémy WEBER<sup>1</sup>, Anne LE NEL<sup>1</sup>

<sup>1</sup> Fluigent, Paris, France

<sup>2</sup> Centre Automatique et Systèmes, ARMINES-ENSM, Paris

Contact author: anne.le-nel@fluigent.com

## ABSTRACT

We present a new algorithm which enables the flow-rate control of a microfluidic system using pressure actuators. Our algorithm combines the pressure control benefits with a direct flow-rate control of the system. Our algorithm can control a complex system with coupling effects or a mass parallel system with independent channels, whatever the number of channels.

We tested the performances of the algorithm on a coupled microsystem and compared them to the performances of a high precision syringe pumps solution on the same microsystem.

We also present the behavior of a system controlled by our algorithm and submitted to an external perturbation.

## KEYWORDS

Microfluidic, pressure control, flow-rate control, algorithm, regulation, fluid handling system, coupling effects, mass parallel system.

## INTRODUCTION

Conventional flow control systems, such as syringe pumps and peristaltic pumps, are not well adapted to the control of flows in microchannels. It often leads to long equilibration time, hysteresis and highly dependence on the elasticity of the system and the materials. We present here a new method to control the flows in microchannels based on pressure regulation.

## PRESSURE REGULATION

The approach proposed here is based on a pneumatic pressurization of reservoirs filling with liquid to be injected in the microsystem. An original pneumatic path combined with a very fast regulation algorithm has been developed to deliver regulated pressure from a pressure source, the FASTAB<sup>TM</sup> technology.

The use of pressure regulation in microfluidic systems is explained in figure 1 and the benefits of this technology listed in table 1.

Thanks to this patented technology, the

different instruments (MFCS<sup>TM</sup> series) can operate over a wide pressure range (from -800 mbar to 7000 mbar) to control flows from sub nL/min to thousands mL/min depending on the hydrodynamic resistance.

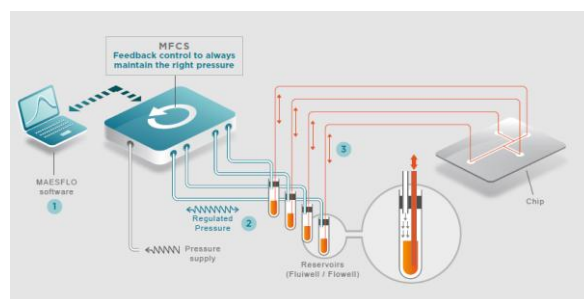


Figure 1: Principle of pressure regulation. 1: pressure values are ordered with the Maesflo software. 2: thanks to Fastab<sup>TM</sup> patented technology, the MFCS<sup>TM</sup> immediately and automatically provides the requested pressures. 3: By connecting the MFCS<sup>TM</sup> pressure channels to reservoirs, Fluiflow, the pneumatic pressure allows to precisely and smoothly control the flow into the application.

Table 1: Pressure regulation benefits.

Parameter	Value	Remark
Settling time	< 1s usually between 0.1 to 0.2 s	Output volume dependent. No dependent on the elasticity of the system
Response time	< 16 ms	
Pressure stability	0.1 %	Precision of the flow. No dependent on the elasticity of the system.
Pressure resolution	0.1 % full scale	Down to 25 µbar.
Flexibility	Up to 8 independent channels. Adaptable to any kind of pressure source	Ability to control complex fluidic set-up



## FLOW RATE CONTROL WITH PRESSURE REGULATION

### Single flow-rate channel

Because for some applications flows need to be controlled by flow-rate, a flow-rate control was developed keeping pressure benefits. To achieve this, a precise flow sensor is implemented in the fluidic system. A feedback algorithm has been developed and integrated in the software. Thanks to this algorithm the pressure is adapted to get the target flow-rate. An autocalibration step is made in order to define the characteristics of the system and adapt the algorithm.

A first algorithm has been created to control the flow-rate on one channel. The results in terms of settling time and stability are given in figure 2 and 3 and compared to highly precise syringe pump. In the conditions of figure 2 (channel diameter 50  $\mu\text{m}$ , length 50 cm), the settling time with our system is much shorter: 3 s vs 90 s with syringe pump. The stability, at low flow-rates, of the flow (figure 3) is much higher with our system, 0.2%, and not dependent of the duration of the experiment (not volume dependent). With syringe pumps, users have to find a good compromise between the volume to be injected and the precision of the flow. With our system, users do not need to make compromise as they can have very high stability (around 0.2%) even with high volumes up to 50 mL.

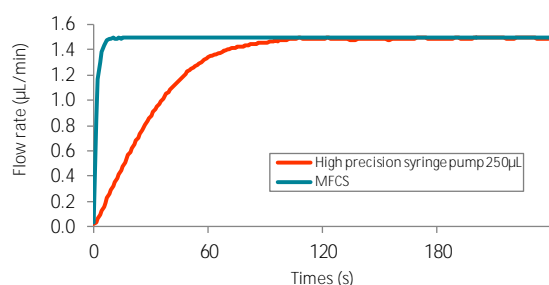


Figure 2: Comparison of the settling time at 1.5  $\mu\text{L}/\text{min}$  between highly precise syringe pump ( $\sim 90\text{s}$ ) and our system ( $\sim 3\text{s}$ ).

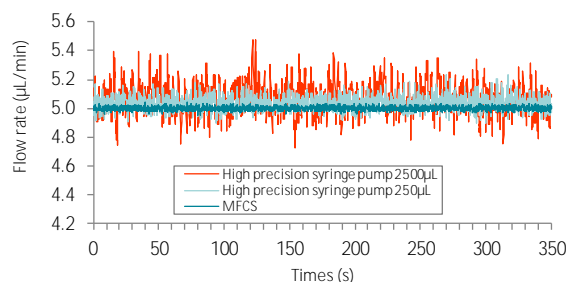


Figure 3: Comparison of the stability at 5  $\mu\text{L}/\text{min}$  between highly precise syringe pump and our system. Due to the mechanical movement of the motor (to push the piston of the syringe), decreasing the volume of the syringe from 2500  $\mu\text{L}$  to 250  $\mu\text{L}$  increases the stability from more than 2% to 1% (CV).

### New algorithm for several flow-rate channels

Usually, people need to control the flow-rate of several channels at the same time. Due to coupling effects, characteristic of the microsystem architecture, the flow-rate control of several channels using a pressure actuator could need a sharp understanding of the microsystem and the microfluidic laws. Basically, the user needs to find the right combination of pressure values which leads to the flow-rates needed. If this combination could easily be determined in basic microsystems, it could be harder for more complex systems.

The algorithm proposed here automatically calculates the pressures needed to obtain the desired flow-rate(s). It enables the flow-rate control of any microfluidic system with all the pressure control benefits (table 1).

## FEATURES AND BENEFITS OF THE NEW FLOW-RATE ALGORITHM

This new flow-rate algorithm highly helps the user to precisely control its system. The user can directly control its system with flow-rate order(s) while keeping the pressure control benefits, such as very low settling time, high accuracy and stability.

Besides, the algorithm proposed here can be used on an unknown system and will help the user to empirically understand the system's behavior. For example, the algorithm is able to point-out non-reachable flow-rate order(s) to the user, meaning that the system is working on the MFCS<sup>TM</sup> limits (maximum/minimum pressure reached) or meaning that the fluidic design of the system is incompatible with the requested flow-rate(s).

The algorithm proposed here is able to

control a large type and number of microfluidic systems, from a single channel with one input pressure to a mass parallel system with independent channels or single complex chip with several coupling effects between the channels. Only the relevant pressure channels will be activated to reach the flow-rate(s) wanted. This feature highly improves the flow-rate channels independence: even on a complex and coupled system, a new flow-rate order on a specific channel will not (or marginally) impact the other channels.

Besides, the algorithm handles positive or negative flow-rates and stop-flows. This feature means that a reverse-flow or a stop-flow is obtained with the responsiveness of a pressure control.

The new algorithm deals with perturbations (such as atmospheric pressure variation, fluid level variation into the tanks) and/or system modifications during the experiment (up to 20% variation of the main fluidic parameters) without consequences on the flow-rate control and accuracy. An example of a system controlled with our algorithm under perturbation is shown in figure 7.

Finally, as the algorithm always knows the pressure(s) and the flow-rate(s) used to control the microsystem, it provides an easy way to determine the microsystem main parameters such as the fluidic resistivity and the fluid viscosity or to identify any physical modifications in the device such as clogging or bubbles (volume and localization in the microsystem).

## ALGORITHM PERFORMANCES

### Comparison to high precision syringe pump on microchip with coupled channels

The new flow-rate algorithm, implemented with Fluigent instrumentation devices, has been tested with an IMT glass chip (ref. ICC-SY05), as shown in figure 4, and compared to high precision syringe pumps on the same chip.

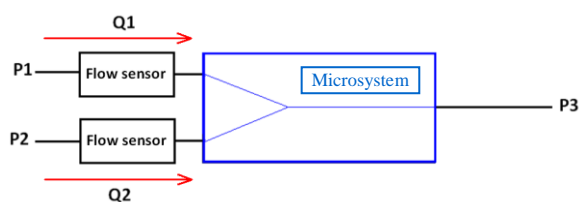


Figure 4: Scheme of the microfluidic system used to test the performances of the new flow-rate regulation. A Y microchip is connected to 3 pressure sources, 2 flow sensors are implemented on the inlets of the microchip.

The following Fluigent devices have been used for the flow-rate algorithm test: one (1) MFCS<sup>TM</sup> FLEX 1000 mbar, three (3) Fluigent 2 mL and one (1) Flowell (2 flow-rates channels, range of 7  $\mu\text{L}/\text{min}$ ).

The MFCS<sup>TM</sup> FLEX and the three (3) Fluigent have been replaced by two (2) high precision syringe pumps with a 250 mL syringe each for the comparative test.

The response time and the flow-rate behavior of these two experiments have been compared when a flow-rate order from  $-4\mu\text{L}/\text{min}$  to  $4\mu\text{L}/\text{min}$  is ordered for Q1 while the flow-rate order of Q2 stays constant at  $2\mu\text{L}/\text{min}$ .

The figure 5 shows the measured flow-rates Q1 and Q2 in the conditions described above for the two experimental conditions. The solution proposed with Fluigent devices leads to a shorter settling time compared to the high precision syringe pumps solution. The settling times are respectively 1.7s compared to 8.5s (Q1).

Besides, the solution exposed highly limits the interaction between Q1 and Q2. As shown in the figure 5, the coupling due to the chip design leads to a modification of the flow-rate Q2 when the flow-rate order of Q1 is changed. With our solution, this modification on Q2 stays punctual and limited: it leads to an over-dispensed volume of  $0.01\mu\text{L}$ . The maximal difference between flow-rate order on Q2 ( $2\mu\text{L}/\text{min}$ ) and measured Q2 is  $+0.49\mu\text{L}/\text{min}$ . With the syringe pumps solution the perturbation on Q2 leads to an under-dispensed volume of  $0.07\mu\text{L}$ . The maximal difference between flow-rate order ( $2\mu\text{L}/\text{min}$ ) and measured Q2 is  $-0.87\mu\text{L}/\text{min}$ .

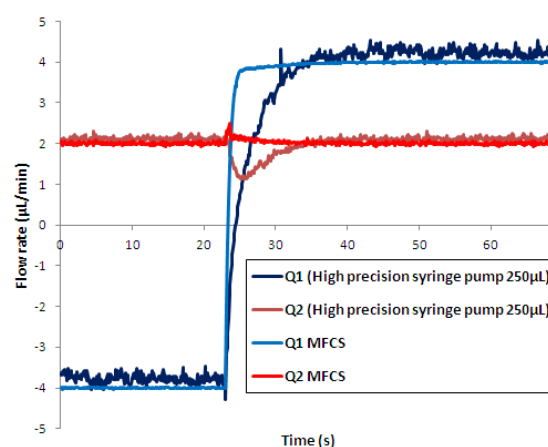


Figure 5: Flow-rates measured during the comparison test between high precision syringe pumps and our system on a Y microchip.

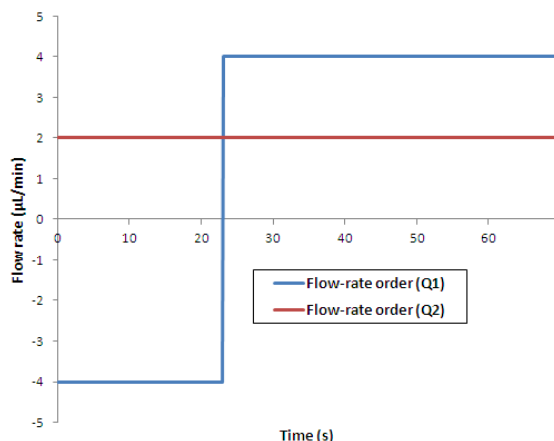


Figure 6: Flow-rate orders during the comparison test between high precision syringe pumps and our system on a Y microchip.

### Performances with a system submitted to external perturbation

Flow-rate orders of 2  $\mu\text{L}/\text{min}$  and -2  $\mu\text{L}/\text{min}$  have been sent to the algorithm presented above to control the system presented in figure 4. Then, the system is submitted to an external perturbation: the value of the pressure channel P3 has manually been decreased and increased, respectively from 200 mbar to 50 mbar and from 50 mbar to 250 mbar. The figure 7 shows the flow-rate responses regarding to the perturbation in P3.

The table 2 quantifies the performances of the flow-rate control and shows that the algorithm presented here maintains its performances even on a system submitted to external perturbations. The maximal value of the standard deviation is 0.03  $\mu\text{L}/\text{min}$ .

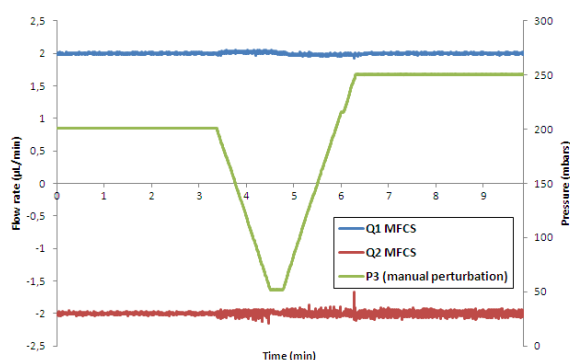


Figure 7: Flow-rates (Q1 and Q2) and output pressure (P3) measured on a Y microchip with our new flow-rate regulation. Between 3.5 minutes and 6.5 minutes, the system is submitted to an external perturbation (variation of P3).

Table 2: Flow-rates measured (Q1 and Q2) during the experiment of a Y microchip submitted to an external perturbation (variation of P3). Before perturbation: from 0 min to 3.5 min. During perturbation: from 3.5 min to 6.5 min. After perturbation: from 6.5 min to 9.5 min.

	Flow-rate Q1 ( $\mu\text{L}/\text{min}$ )	Flow-rate Q2 ( $\mu\text{L}/\text{min}$ )
<b>Before perturbation</b>	$2,00 \pm 0,01$	$-2,00 \pm 0,01$
<b>During perturbation</b>	$1,99 \pm 0,02$	$-1,99 \pm 0,03$
<b>After perturbation</b>	$2,00 \pm 0,01$	$-2,00 \pm 0,03$
<b>Flow rate order</b>	2	-2

## CONCLUSION

We present here a new method based on pressure regulation to control flows in microfluidic systems. Thanks to the flow-rate control option we show the ability to control and monitor the relevant parameters of the flow: both pressure and flow-rate with very fast settling time, excellent stability and repeatability.

With the measurement of both pressure and flow-rate, users are able to well characterize their fluidic systems and to detect any modification (presence of bubble, clogging and/or variation of the viscosity of the system...). This benefit can't be provided with a syringe pump solution due to the fact that the only available parameter is the flow-rate order, neither the pressure nor the flow-rate are measured.

## REFERENCES

- [1] C. Futterer N. Minc, V. Bormuth, J.H. Codarbox, P. Laval, J. Rossier, J.L. Viovy, Lab Chip, 2004, 4, 351-356
- [2] [www.fluigent.com](http://www.fluigent.com)

## Acknowledgements

This work was partially supported by the European FP7 project 'NADINE'.

## 4. Fluidic control systems

### NOVEL GRAVIMETRIC CALIBRATION METHOD FOR NANO LITER LIQUID HANDLING DEVICES

*D. Liang<sup>1</sup>, L. Tanguy<sup>2</sup>, A. Ernst<sup>2,3</sup>, R. Zengerle<sup>1,2,4</sup>, P. Koltay<sup>2,3</sup>*

<sup>1</sup> HSG-IMIT - Institut für Mikro- und Informationstechnik, Georges-Koehler-Allee 103, 79110 Freiburg, Germany

<sup>2</sup> Laboratory for MEMS Applications, IMTEK - Department of Microsystems Engineering, University of Freiburg, Georges-Koehler-Allee 103, 79110 Freiburg, Germany

<sup>3</sup> BioFluidix GmbH, Georges-Koehler-Allee 103, 79110 Freiburg, Germany

<sup>4</sup> BIOS - Centre for Biological Signalling Studies, University of Freiburg, Germany

#### ABSTRACT

A novel and simple liquid calibration method based on the gravimetric principle is presented. This method employs an ultra-microbalance and involves the gravimetric regression method (GRM) [1] for mass calculation as well as uncertainty analysis. The prefilled liquid in the weighing capsule is covered by a silicon oil layer to reduce the evaporation. In comparison to the GRM method with numerical compensation of evaporation this gravimetric regression method works with reduced evaporation and improves the expanded uncertainty ( $U(V_{20}), k = 2$ ) from 12.5 nl to 2.6 nl. In 384 dispensing experiments over 16 volumes between 4.6 nl and 70 nl have been tested and a good repeatability ( $1\% < CV < 15\%$ ) has been observed depending on the volume.

from the measured value, the GRM method can therefore not deliver highly precise measurement results for the volume below 100 nl.

The gravimetric regression method with reduced evaporation (GRM-R) presented here employs a silicon oil layer to reduce the evaporation from the liquid prefilled in the weighing capsule. GRM-R still involves the GRM method to numerically compensate the possible evaporation and makes reference to the ASTM-E542 standard. But due to the reduced evaporation this approach achieves an expanded uncertainty of  $U(V_{20}), k = 2$  of about 2.6 nl in the volume range from 5 nl to 70 nl. Besides the description of the measurement setup and the GRM-R method, we also presented a full uncertainty analysis and experimental evaluation of this method in the following.

#### KEYWORDS

Gravimetric regression method, gravimetric volume measurement, volumetric calibration

#### INTRODUCTION

Gravimetry has been recognized as a standard method over half a century for laboratory and industrial liquid volume calibration. Adapted from the well-known standards ASTM-E542 and ISO8655-6 we have established in our previous work a gravimetric regression method (GRM) for gravimetric volume calibration [1]. Our previous work has shown a comprehensive uncertainty analysis of the GRM and proved that the gravimetric liquid calibration standard can be extended down to the sub- $\mu$ l range. However, due to inevitable evaporation of liquid from the weighing capsule the balance never reaches equilibrium, thus generating an error that dominates in the uncertainty estimation. The expanded uncertainty of a measured volume referred to 20°C ( $U(V_{20}), k = 2$ ) of the GRM is as high as 12.5 nl at 40 nl dosage volume. As the uncertainty describes how the true value deviates

#### SETUP OF GRM-R

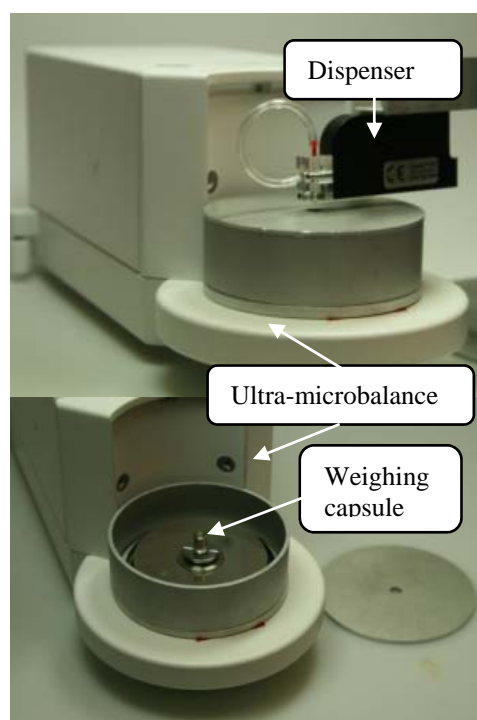


Figure 1: Gravimetric measurement setup.



The GRM-R employs an ultra-microbalance with a readability of 0.1  $\mu\text{g}$  as central measuring equipment. Such an ultra-microbalance provides currently the smallest readability among all the commercial available analytical balances. In our setup an ultra-microbalance XP2U/M (Mettler Toledo Inc, Switzerland) is placed directly under a PipeJet P9 (BioFluidix, Germany) non-contact micro dispenser, as shown in Figure 1. The dispensed nanoliter droplet enters through a 6 mm-diameter hole in the windshield and hits an aluminum weighing capsule (ID x H 6mm x 8mm, elemental Microanalysis). The setup is shielded from the surrounding with a transparent plastic cover and placed on one vibration isolated granite table (Johann Fischer Aschaffenburg DIN876-126 hardstone surface plate and Newport VH3660W-OPT vibration isolated workstation).

The presented GRM-R method employs DOW Corning® 200-Fluid 50-cs silicon oil to build an oil layer on top of the liquid in the weighing capsule (Figure 2). The initial preparation of the weighing capsule is shown in Figure 2. It begins with pipetting about 50  $\mu\text{l}$  test liquid into weighing capsule with contact to the capsule bottom, then goes on with the slow pipetting of about 100  $\mu\text{l}$  silicon oil in contact with the capsule wall on top of the test liquid. This preparation procedure avoids contamination of liquid on the capsule wall that could result in evaporation and drift of the balance signal. The dispensed liquid droplet can pass the oil layer and merges with the prefilled test liquid (Figure 3). The prefilled liquid ensures that with increasing liquid volume the oil layer can always stay on top. Therefore, the density of the measured liquid always has to be larger than the applied oil (0.96  $\text{g}/\text{cm}^3$ ) which is the case for most liquids in life-science and diagnostic applications.

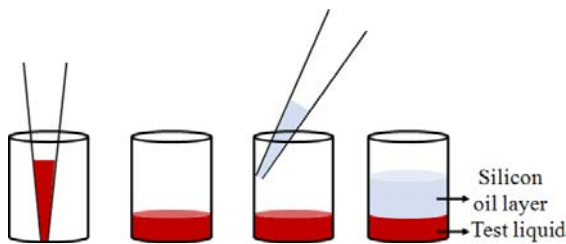


Figure 2. Initial preparation of weighing capsule.

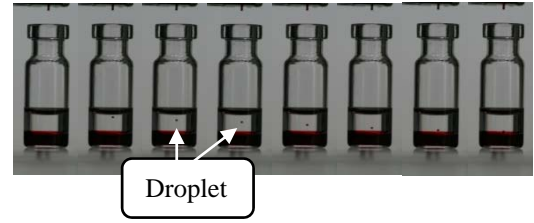


Figure 3. Image sequence (from left to right) of the transition and the merging of a dispensed droplet into a glass vessel (this vessel was used for visualization only, because the used weighing capsule is not transparent). The vessel was prefilled with test liquid and silicon oil layer like shown in Figure 2. The test liquid is a red dyed water solution.

The measurement procedure of the GRM-R including dispensing control is carried out automatically by the Software GraviDrop (BioFluidix, Germany). GraviDrop calculates the dispensed mass with the linear regression method to compensate the possible evaporation loss numerically and provides an estimation of uncertainty based on the prognosis interval [1]. A typical measurement procedure is shown in Figure 4. Thanks to the silicon oil layer almost no evaporation occurs.

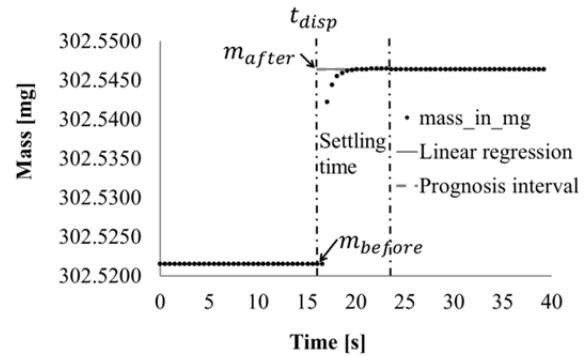


Figure 4. Typical balance readouts of one dispense measured with the GRM-R method.  $m_{\text{before}}$  and  $m_{\text{after}}$  : denote regression values “before” and “after” the liquid is dispensed onto the balance.  $t_{\text{disp}}$  : is the time when the dispense occurs.

## UNCERTAINTY ESTIMATION

The GRM method as described in [1] employs similar equations as used in the well-known ASTM E542 standards to calculate liquid volumes at reference temperature 20 °C  $V_{20}$ :

$$V_{20} = m \cdot \frac{1}{\rho_w(T) - \rho_a} \cdot \left(1 - \frac{\rho_a}{\rho_c}\right) \cdot [1 - \gamma(T - 20)] \quad (1)$$

Where  $T$  is temperature during measurement,  $\rho_w$  is the density of the measured liquid at measurement temperature  $T$ .  $\rho_a$  is air density and  $\rho_c$  is the density of the weights used to calibrate the balance.  $\gamma$  is the thermal coefficient of expansion of the measured liquid and  $m$  the mass of the dispensed liquid which is equal to  $m_{after} - m_{before} + \delta m$ .  $m_{after}$  and  $m_{before}$  are regression values “before” and “after” the liquid is dispensed onto the balance.  $\delta m$  is the correction to the statistical random weighing errors from the used balance.

The standard uncertainty of  $V_{20}$  is then calculated as [1]:

$$u(V_{20})^2 = \left(\frac{\partial V_{20}}{\partial m}\right)^2 u^2(m_{after}) + \left(\frac{\partial V_{20}}{\partial m}\right)^2 u^2(m_{before}) + \left(\frac{\partial V_{20}}{\partial m}\right)^2 u^2(\delta m) + \left(\frac{\partial V_{20}}{\partial \rho_w}\right)^2 u^2(\rho_w) + \left(\frac{\partial V_{20}}{\partial \rho_a}\right)^2 u^2(\rho_a) + \left(\frac{\partial V_{20}}{\partial \rho_c}\right)^2 u^2(\rho_c) + \left(\frac{\partial V_{20}}{\partial \gamma}\right)^2 u^2(\gamma) + \left(\frac{\partial V_{20}}{\partial T}\right)^2 u^2(T) \quad (2)$$

$u(m_{after})$  and  $u(m_{before})$  are estimated according to the prognosis interval to the regression line based on the data acquisition “before” and “after” dispensing. In case of using only the regression method to compensate the evaporation like the normal GRM [1],  $u(m_{after})$  and  $u(m_{before})$  are dominating in the calculation of  $u(V_{20})$  because of evaporation and the oscillations of weighing readouts.

Thanks to the silicon oil layer the evaporation in the GRM-R is strongly reduced. The ultramicrobalance can therefore more easily reach force equilibrium, which results in smaller values for  $u(m_{after})$  and  $u(m_{before})$ . The calculation of  $u(V_{20})$  and  $U(V_{20}), k = 2$  based on the data in Figure 4 is shown in Table 1.

The estimated  $u(V_{20})$  of the GRM-R by measuring about 25 nl liquid volume is about 1.3 nl. From Table 1 it can be obviously deduced that  $u(V_{20})$  is mainly determined by  $u(\delta m)$ , which is related to the conventional weighing process and the accuracy of the used balance. In contrast to the GRM, the  $u(m_{after})$  and  $u(m_{before})$  values can be neglected.  $u(\delta m)$  in the calculation was determined by Deutscher Kalibrierdienst (DKD-K-14701) for the used balance. “The DKD calibration certificate documents the traceability to national standards, which realize the units of measurement according to the International System of Units (SI)” [2].

Table 1. Uncertainty calculation for the data in Figure 4.

Input Quantity (*)	Unit	Value	Standard Uncertainty u(*)	Sensitivity Coefficient
$m_{before}$	µg	302521.5	0.0195	1.0029
$m_{after}$	µg	302546.4	0.0265	1.0029
$\delta m$	µg	0	1.30	1.0029
$\rho_w$	µg/nl	0.997391	1.52E-06	-25.0683
$\rho_a$	µg/nl	0.0012	2.89E-07	21.6161
$\rho_c$	µg/nl	8.006	0.01	0.0005
$\gamma$	°C <sup>-1</sup>	0.000207	2.89E-07	-89.9693
$T$	°C	23.6	0.05	-0.0052
$V_{20}$	nl	25.0		
$u(V_{20})$	nl	1.3		
$U(V_{20}), k = 2$	nl	2.6		

## EVALUATION

To evaluate the GRM-R procedure a nanoliter dispenser (PipeJet P9, BioFluidix GmbH, Germany) is positioned above an ultramicrobalance (XP2U, Mettler Toledo, Switzerland) (Figure 4). The testing liquid is double distilled water as recommended in ASTM-E542 and ISO8655-6. The weighing capsule stays in the center of the weighing cell of the balance. The inlet hole of the balance’s windshield is about 5 mm below the nozzle. The whole setup is covered by an additional wind shield and isolated from vibrations like described before. The data acquisition during the experiments as well as the volume calculations are automatically executed by the software GraviDrop (BioFluidix GmbH, Germany).

The results of the 384 experiments performed in the range from 5 nl to 70 nl are shown in Figure 5. The CV of each 24 measurements at volumes down to 5 nl remains below 10% (except for the smallest value of 4.6 nl) and the value of  $U(V_{20}), k = 2$  remains below 10% for volumes larger than 24 nl. Therefore, GRM-R is able to deliver a reliable measurement precision down to 5nl volumes and a reliable absolute accuracy down to 24 nl.

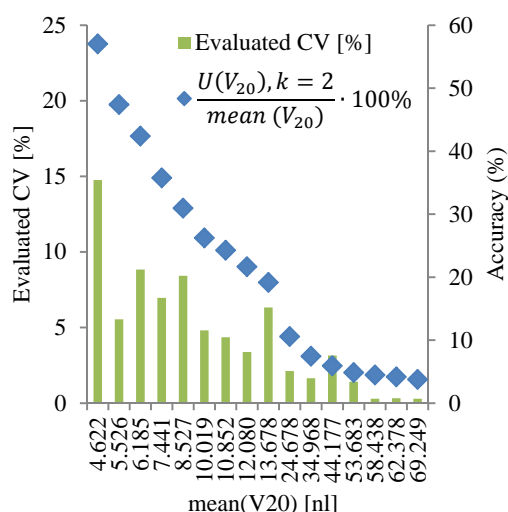


Figure 5. GRM-R evaluation results. The mean  $V_{20}$  of each of 24 dispensing experiments at 16 different droplet sizes is shown on the x-axis in [nl]. The coefficient of variation in [%] of each 24 dispenses is shown as green bars and the relative expanded uncertainty ( $\frac{U(V_{20}), k=2}{\text{mean}(V_{20})} \cdot 100\%$ ) is shown as blue diamonds.

## CONCLUSION

An improved method, the gravimetric regression method with reduced evaporation (GRM-R), for precise and accurate gravimetric low volume calibration has been presented. It is derived from the ASTM E542 standard and prevents evaporation errors by averaging balance readings before and after the droplet impact as well as by applying an oil layer to the weighing capsule to significantly reduce errors caused by evaporation. In contrast to our previous work the GRM-R improves the expanded uncertainty ( $U(V_{20}), k=2$ ) from 12.5 nl to 2.6 nl at volumes of 40 nl. Thus, the gravimetric liquid calibration methods and standards can be extended to the lower nanoliter range with high precision.

## ACKNOWLEDGMENT

The authors gratefully acknowledge financial support from the German Federal Ministry for Science and Education (BMBF) through the project “Smart Reagent Dosage” (SFK 16SV5119).

## REFERENCES

- [1] D. Liang, C. Steinert, S. Bammesberger, L. Tanguy, A. Ernst, R. Zengerle, P. Koltay, Novel gravimetric measurement technique for quantitative volume calibration in the sub-microliter range, Journal of Measurement Science and Technology, (2012) submitted
- [2] Deutscher Kalibrierdienst DKD Calibration certificate, 350DE83, DKD-K-14701, 2012-07

## CONTACT

Dong Liang, HSG-IMIT - Institut für Mikro- und Informationstechnik, Georges-Koehler-Allee 103, 79110 Freiburg, phone: +49-761-203-73254, fax: +49-761-203-73299, email: dong.liang@hsg-imit.de.

## TOWARDS A MICROVALVE FOR PROPORTIONAL CONTROL OF MASS FLOW

*M.S. Groen<sup>1</sup>, D.M. Brouwer<sup>2,3</sup>, J.C. Lötters<sup>1,4</sup> and R.J. Wiegerink<sup>1</sup>*

<sup>1</sup> MESA+ Research Institute, University of Twente, Enschede, The Netherlands

<sup>2</sup> Mechanical Automation and Mechatronics, University of Twente, Enschede, The Netherlands

<sup>3</sup> DEMCON Advanced Mechatronics, Oldenzaal, The Netherlands

<sup>4</sup> Bronkhorst High-Tech BV, Ruurlo, The Netherlands

### ABSTRACT

Precise mass flow control is an essential requirement for novel, small-scale fluidic systems. However, a small-volume, low-leakage proportional control valve for minute fluid flows has not yet been designed or manufactured. We have therefore identified and evaluated the most basic valve operating principles with respect to functionality and technology, and have reviewed several basic actuation schemes. Proceeding from these analyses, we have identified the design concepts and actuation schemes that we think are best suited for the fabrication of the intended microvalve.

### KEYWORDS

Microvalve; flow control; low leakage; mass flow controller; micro actuator; MEMS

### INTRODUCTION

Precise fluid flow control is a key requirement in many reaction, production or analytical processing systems. Over the past decade, miniaturization of complex fluidic systems has led to many new and potential applications, including microreactor assemblies [1], microscale chemical analysis systems [2] and medical systems such as rapid DNA sequencers [3] and drug micro-dosers [4]. However, the need for a small-volume, high-precision mass flow controller for minute fluid flows has not yet been fulfilled.

#### Applications and requirements

A typical mass flow controller consists of a mass flow sensor and a proportional control valve, connected in a closed control loop. In recent research a new micromachined mass flow sensor has been developed based on the Coriolis principle, capable of measuring mass flows up to 1.2 g/h with an accuracy of 10 mg/h [5]. To apply this sensor in a low-throughput mass flow controller, a microvalve capable of proportionally controlling such tiny flows is required. The potential applications of such a miniature mass flow controller include the following:

- Lab-on-a-chip, requiring high levels of miniaturization and integration;
- Chemical microreactors, demanding chemical

resistance and low leakage for safety;

- Gas and liquid chromatographs, requiring a very stable flow rate and a large dynamic control range to facilitate both high-pressure and low-pressure flows;
- Portable medical equipment and point-of-care test systems, requiring very high reliability;
- Dosing systems for the food production and pharmaceutical industries, demanding high dosing precision and easily cleanable or replaceable components.

Based on the functional demands following from these applications, we have analyzed the requirements and challenges associated with fabricating a low-throughput microvalve. Detailed specifications of the demands have been derived in [6]. A valve's capability to control flow with a short response time is deemed the most important specification, but the leakage performance is also given high weight as good closure is difficult to obtain at the micro scale.

### VALVE DESIGN ANALYSIS

Existing microvalve designs have been reviewed to evaluate the basic valving concepts with respect to functionality and technology. Given a certain differential pressure, controlling fluid flow requires control over the flow resistance of at least one element in the flow circuit. In most cases, this resistance change is achieved by changing the mechanical geometry.

Some non-mechanical alternatives have been reported, such as electro-capillary [7] or diffuser microvalves [8], but since there is no actual closure these systems cannot guarantee low leakage. They are therefore not considered in our review.

#### Basic operating principle

A basic design of a mechanical control valve is shown in Figure 1, consisting of an orifice in a fixed plate (the valve seat) which is covered by a vertically translating plunger. The maximum flow supported by the valve is defined by the structural dimensions – specifically, the diameter of the orifice and the separation between the two plates.

The maximum separation that can be achieved is called the stroke. The leakage performance of a valve



is determined by the closing surface area, the relative surface roughness and flatness of seat and plunger and the force by which the plunger is pressed against the seat.

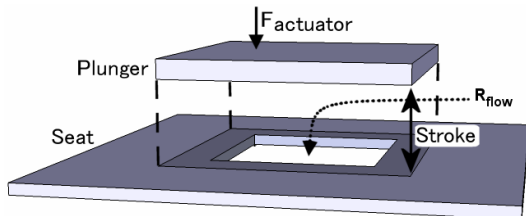


Figure 1: Basic operating principle of a translating plate microvalve

#### Designs for low leakage

A vertically translating plate is the most commonly used design concept as it offers very broad design freedom. When applied as a hard plate valve, it is commonly fabricated in silicon or silicon-derivative materials. The disadvantage to using these high Young's modulus materials is poor closure performance, as the plates will not readily deform to match each other's surface topography. Similarly, hard plate valves are very sensitive to lodging of particle contaminations.

A common modification of the translating plate concept is therefore to replace the rigid plate by a flexible membrane that wraps over the valve seat(s), as shown in Figure 2. A translating membrane can elastically deform to match the precise shape and curvature of the valve seat, improving the seal and so reducing leakage flow at the cost of improved stiction in the closed state. The greatest improvement can be obtained using materials with low Young's modulus. Compared to rigid materials however, elastomers typically have a reduced chemical resistance and higher permeability to moisture and gases.

Another modification of the translating plate concept is to fix one side of the plunger to the surrounding bulk. This turns a translating motion into tilting motion, as shown in Figure 3. With an appropriately chosen pivot point, this geometry can supply an amplification of actuator stroke (or force). Alternatively, it can be used to create a large ratio between actuator stroke and flow resistance, which increase flow control precision.

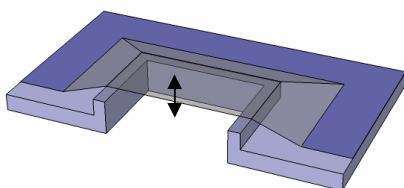


Figure 2: Flexible membrane microvalve.

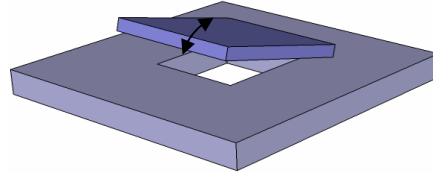


Figure 3: Tilting plate microvalve.

#### Designs for precise control

A concept intuitively well suited to flow control applications is the use of a horizontally translating or sliding plate to vary the overlap between two orifices, shown in Figure 4. Apart from straight-forward control, a big advantage of such a design is that it can be made to require zero power in the steady state, for example using stepper motors for actuation.

In contrast to its good control properties, the sliding or rotating plate concept suffers from very poor leakage performance. This is because the sliding movement takes place in the same plane as that in which the channel closure needs to be achieved. This means there is an inherent tradeoff between plate friction, which influences control precision, and valve closure.

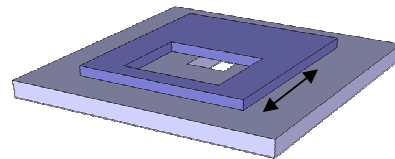


Figure 4: Sliding plate microvalve.

Another design with good control is the needle valve concept, shown in Figure 5. It uses a tapering plunger, commonly implemented as a sharp needle, moving into a tapered valve seat. The defining attribute is the large ratio between the needle's length and its diameter: A large axial translation leads to only a small change in radial closure, allowing for very precise flow control. These valves can also be made to have low leakage, by using the large closing area between the needle and the tapered seat.

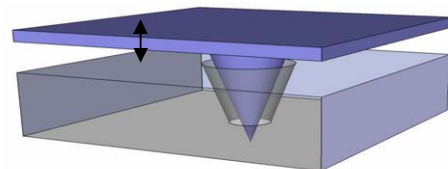


Figure 5: Needle microvalve.

A third concept for improved control precision is using an array of valves with scaling orifice dimensions. Using for example binary valve switching would give a straight-forward improvement of control precision, at the cost of increased footprint

requirements and increasing leakage for every valve added to the system.

### ACTUATOR DESIGN ANALYSIS

Mechanical microvalves are commonly divided into active and passive systems, meaning with and without a powered actuator. Passive valve designs are not evaluated in our study, because they are either one-way flow rectifiers [11], or designed to control a single, specific flow [12].

In order to achieve precise control over a range of flows, a powered actuator is required. The maximum actuator force determines the maximum differential pressure across the valve, as the actuator needs to be able to counteract the fluid force acting on the plates. The maximum actuator stroke limits the valve stroke, unless a mechanical amplification scheme is applied. The actuator also defines the power dissipation of a control valve, as well as its open-loop response time.

Because the maximum stroke, force, actuator size and power consumption are strongly dependent on each other, we have chosen the obtainable work density as a more objective metric for actuator performance. The work density is defined as the product of the maximum force and maximum stroke, divided by the total volume of the actuator. Coupled with response time and ease of integration, the work density allows a convenient comparison between different actuator types. Approximate expressions for the work density and response times of different types of actuators have been derived in [6], the results of which are reproduced in Table 2.

#### Thermal actuation

Thermal expansion actuators are based on Joule heating of materials, usually applying bilayer strain mismatch or other forms of stroke amplification. Thermal expansion actuators can be relatively easy to integrate, and they can offer a high work density. The operating speed is however limited to the thermal conductivity, so material choice is critical.

Shape memory alloy (SMA) is a special type of thermal actuator that applies a specific material phase change which occurs in some metal alloys, such as NiTi, under influence of temperature. SMA actuators are known for offering higher work densities than any other MEMS actuator [13], but the reported response times range from tens of milliseconds to several seconds. Another major disadvantage is that the performance of SMA actuators significantly decreases after thousands of cycles [14], while proportional controllers require several orders more actuator cycles during their lifespan.

#### Electric actuation

Compared to thermal actuators, more direct electric actuation typically offers higher operating speeds at lower work performance. The work density of electromagnetic actuators decreases with increasing level of integration [15], meaning a certain minimum volume is required to reach a certain force and stroke. This typically makes micromachined electromagnetic solutions too weak for flow control use.

Electrostatic actuators are very fast but either suffer from the pull-in effect (gap-closing structures) or can only deliver very small forces (lateral comb-drive designs). Because of this, the work density of electrostatic actuators is relatively low. They can however be fabricated using standard microfabrication materials.

Piezoelectric actuation, finally, uses the strain of piezoelectric materials that is induced when they are submitted to an electric field. This strain is limited to approximately 0.1% of the original size, but it can be delivered with very large forces of the order of kilonewtons. The limited stroke is commonly amplified using bimorph membranes or a leverage mechanism, or by creating stacks of actuators. Integration of piezoelectric actuators at the micro scale however remains a major challenge, especially since micromachined piezoelectric films are typically only on the order of one micrometer thick.

### CONCLUSIONS

We have analyzed the basic operating principles of a number of basic microvalve designs with regards to their suitability for precise, continuous flow control with low closed-state leakage. The results are summarized in Table 1. The needle valve concept offers good flow control properties while imposing relatively few design constraints. To obtain low leakage, an (elastomer) membrane is advantageous, while for inflexible materials a very closely fitting seat/plunger combination is required.

We have also surveyed the most common micro-actuator schemes, focusing on their work performance and response times. Given its high work density, high speed and low power usage, piezoelectric actuation is considered the best candidate for the envisioned proportional control valve, provided a solution can be found for integrating it in a microfabrication process.

### ACKNOWLEDGEMENTS

The authors thank the Point-One Phase2 innovation program of the Dutch ministry of economic affairs for funding this ongoing work. We also thank the people at DEMCON and Bronkhorst High-Tech for their help and support.

Table 1. Summary of the basic valve designs analyzed in this work (from [6]).

	Flow control		Leakage performance		Design freedom	
Translating plate		○		○	+	Many designs reported
Translating membrane		○	+	Matches seat topography, may be permeable to gases	-	Limited to thin or elastic materials
Tilting plate	+	Large $Stroke : \Delta R_{flow}$ ratio		○		○
Sliding plate	++	Plate position directly determines $R_{flow}$	--	Tradeoff between friction and closure		○
Needle	++	Very large $Stroke : \Delta R_{flow}$ ratio	○	Large contact surface, but needs high conformity		○
Scaling array	++	Resolution scales with number of sub-valves	--	Demands scale with number of sub-valves		○

Table 2. Summary of the actuator types described in this work (from [6]).

	Work density [ $J/m^3$ ]	Response time		Integration	
Thermal expansion	$< 10^5$	○	Strongly material-dependent	+	Standard materials supported
Shape memory alloy	$< 10^7$	--	$>10$ ms – 10 s		○
Electrostatic	$< 10^4$	+	$<1$ ms	+	Standard materials supported
Electromagnetic	$< 10^3$ at microscale	○	Limited by drive current electronics		○
Piezoelectric	$< 10^5$	+	$<1$ ms	-	Volume limitations, low thermal budget

## REFERENCES

- [1] V. Hessel, C. Knobloch, H. Lowe, "Review on patents in microreactor and micro process engineering", *Recent Patent Chem. Eng.* Vol. 1, pp.1-16, 2008.
- [2] P.S. Dittrich, K. Tachikawa, A. Manz, "Micro Total Analysis Systems. Latest Advancements and Trends", *Anal. Chem.*, Vol. 78, pp.3887-3908, 2006.
- [3] K.M. Horsman, J.M. Bienvenue, K.R. Blasier, J.P. Landers, "Forensic DNA Analysis on Microfluidic Devices: A Review." *J. Forensic Sci.*, Vol. 52, pp.784-799, 2007.
- [4] N.-C. Tsai, C.-Y. Sue, "Review of MEMS-based drug delivery and dosing systems", *Sens. Actuators, A*, Vol. 134, pp. 555-564, 2007.
- [5] J. Haneveld et al, "Modeling, design, fabrication and characterization of a micro Coriolis mass flow sensor", *J. Micromech. Microeng.*, Vol. 20, pp. 125001.1-125001.10, 2010.
- [6] M.S. Groen, D.M. Brouwer, R.J. Wiegerink, J.C. Lotters, "Design Considerations for a Micromachined Proportional Control Valve", *Micromachines*, Vol. 3, pp.396-412, 2012.
- [7] J. Lee et al, "Electrowetting and electro-wetting-on-dielectric for microscale liquid handling", *Sens. Actuators, A*, Vol. 95, pp.259-268, 2002.
- [8] E. Stemme, G. Stemme, "A valveless diffuser/nozzle-based fluid pump", *Sens. Actuators, A*, Vol. 39, pp.159-167, 1993.
- [11] E.H. Yang, S.W. Han, S.S. Yang, Fabrication and testing of a pair of passive bivalvular microvalves composed of p+ silicon diaphragms. *Sens. Actuators, A* 1996, 57, 75-78.
- [12] P. Cousseau et al, "Improved micro-flow regulator for drug delivery systems", *Proc. 14th IEEE Int. Conf. on Micro Electro Mech. Syst.*, Interlaken, Switzerland, 21-25 Jan 2001, pp. 527-530.
- [13] R.H. Wolf, A.H. Heuer, "TiNi (shape memory) films silicon for MEMS applications", *J. Microelectromech. Syst.*, Vol. 4, pp.206-212, 1995.
- [14] S. Miyazaki, K. Otsuka, "Development of Shape Memory Alloys", *Iron Steel Inst. Jpn. Int.*, Vol. 29, pp. 353-377, 1989.
- [15] D.M. Brouwer, "Design principles for six degrees-of-freedom MEMS-based precision manipulators", Ph.D. Thesis, University of Twente, 2007.

## CONTACT

\* M.S. Groen, M.S.Groen@utwente.nl

## 2. Fluidic control systems

## PROBING RED BLOOD CELL DYNAMICS

R.C.H. van der Burgt<sup>1,\*</sup>, P.D. Anderson<sup>2</sup> and F.N. van de Vosse<sup>1</sup><sup>1</sup> Eindhoven University of Technology, Department of Biomedical Engineering, Eindhoven, The Netherlands<sup>2</sup> Eindhoven University of Technology, Department of Mechanical Engineering, Eindhoven, The Netherlands

## ABSTRACT

For the characterization of red blood cell dynamics, we propose a ‘contactless’ experiment in which the cell is deformed by elongational flow in a cross-slot geometry. For this end, a microfluidics chip with integrated valves combined with a feedback system is required to keep the cell into the stagnation point.

First, finite element simulations with fluid-structure interaction are presented to perform parameter studies on which the design of the experimental setup is based. Next, an overview of the designed setup is given, including a pulsatile microfluidics pump, with which it is possible to study dynamic deformations of the cell. Finally, a demonstration of the setup is given.

## KEYWORDS

Feedback control, pulsatile pump, microvalve, positioning, red blood cell, piezo-electric actuator, deflecting membrane, dynamics

## INTRODUCTION

Because of the high volume contents of red blood cells (RBCs), mechanics of a single RBC plays a large role in the rheological description of blood. Moreover, RBC dynamics drive plasma mixing and transport of its components, which are both involved in blood coagulation. Therefore, a characterization of the dynamical parameters of RBCs under different flow conditions is needed.

Experimental methods, like pipette aspiration [1] or optical trapping [2], seem are not ideal to accurately capture RBC dynamics, due to contact of a solid with the cell membrane. This contact results in a more complex analysis, as the solid-cell interaction must be modeled accurately to extract mechanical parameters correctly. In addition, extra friction forces are introduced, which need to be taken into account during dynamic deformations. Finally, the cell deformations are inhomogeneous and local, while global quantities are measured like a global force-length relationship. Therefore, only global material parameters can be derived. For studying a complex material like the RBC membrane, this seems to be inadequate.

Our strategy involves estimation of mechanical properties of the RBC using an inverse analysis which combines both numerical and experimental tools and hereby provides local information about the cell.

## MATERIALS &amp; METHODS

Similar to earlier studies on droplet deformation [3] we designed a contactless experiment where a RBC is deformed in elongational flow as shown in Figure 1. Close to the stagnation point a hyperbolic velocity field will be present, described by

$$\dot{v}_y = \varepsilon y \quad \dot{v}_x = -\varepsilon x, \quad (1)$$

which is in principle a 2D potential flow with no rotational components.

To apply a well-controlled deformation state, the RBC must be kept in the center, which is an unstable situation: the cell will always flow towards the horizontal asymptote because the stagnation point acts as a potential minimum in that direction, while it will always flows away from the center in outflow direction. Therefore, continuous correction has to be performed by an automated system. Cell positioning is achieved by controlling the outflow ratio  $Q_1/Q_2$  as a function of the position of the cell ( $x$ ).

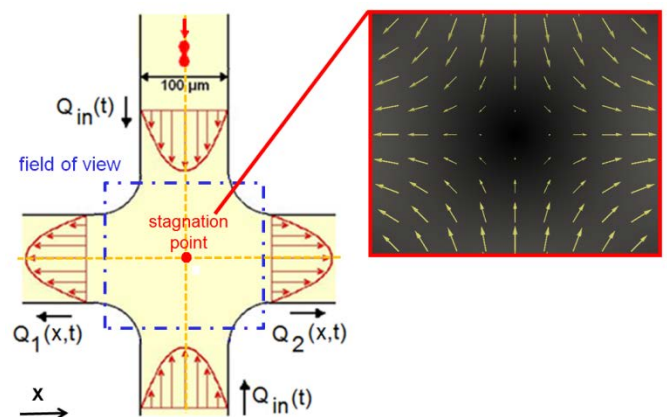


Figure 1: Schematic overview of the cross-slot geometry. In the center a hyperbolic velocity profile is present around the stagnation point, as shown at the right. The inflow  $Q_{in}$  is a function of time to enable dynamic deformations. The outflows are a function of cell position  $x$  to displace the stagnation point, enabling repositioning. Asymptotes are shown as dashed orange lines, the field of view of the microscope as the blue dash-dotted rectangle.



First, we numerically addressed the question whether the control system will be able to keep the cell at the preferred position. Parameter studies are performed with 2D fluid-structure interaction (FSI) simulations, using a fictitious domain technique [4]. Fluid and solid are coupled using Lagrangian multipliers by a weak constraint on the interface. For the fluid the Stokes equations are solved, whereas for the cell a Neo-Hookean model is prescribed. The control system dynamics is put as boundary conditions on the outflow channels.

A microfluidics chip with optical access containing the cross-slot geometry and valves is required. All structures on the chip are rigid to avoid compliance that would delay feedback or damp the inflow pulses. Therefore, using lithography, the structures are directly made in a 100 micron thick photoresist (SU-8). Valve chambers are micro-milled into the chip and covered with a PDMS membrane, that also seals the channels. The membrane can be deflected into the valve chamber by a piezo-electric actuator, resulting in a higher hydraulic resistance. In that way the outflow ratio  $Q_1/Q_2$  can be controlled in closed loop (Figure 2). The encasing aluminum frame clamps all layers together and holds 4 heating elements and heat sensor that enable the temperature to be controlled at 37° C.

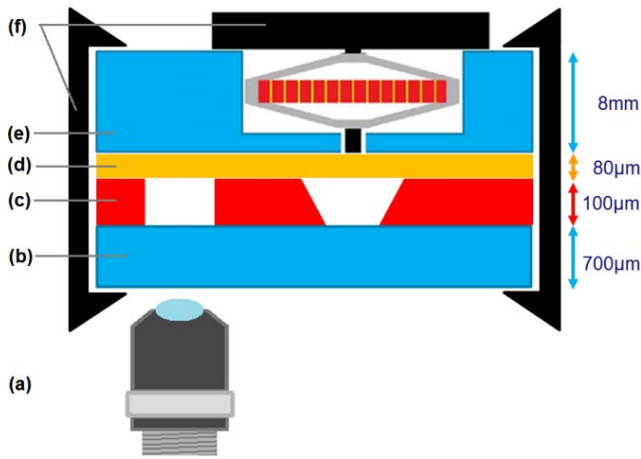


Figure 2: Overview of the cross-slot setup with: (a) microscope objective, (b) glass slide, (c) SU-8 photoresist layer containing the milled valve chambers, (d) PDMS membrane, (e) polycarbonate block containing fluid connectors, and (f) an encasing aluminum frame, holding the piezo-electric actuators, heating elements, and temperature sensor.

By varying  $Q_1/Q_2$  as a function of cell position ( $x$  in Figure 1, taking the center of the cross-slot as origin), the stagnation point is displaced, moving the cell to the desired location. Cell position is determined by image analysis software (Matlab realtime

workshop). Raw camera images are background subtracted and thresholded to track the cell. With the extracted position the error is calculated which enters a proportional controller.

To characterize RBC dynamics the inflow has been made tunable in time. For that purpose a pump that drives pulsatile flow with a frequency of 10's of Hz, and amplitudes down to 10 nl/s is designed and built. By periodically deflecting a steel plate into a rigid fluidic chamber using a voice coil, an oscillatory flow is produced. Plate deflection is in the bending regime, such that the volume displacement is proportional to the current through the voice coil, enabling open loop control.

Because of linearity of the system, the oscillatory flow is superimposed to the steady flow of the syringe pump, see Figure 3. The pump system is characterized by  $\mu$ -PIV measurements (GPIV) under a spinning disk confocal microscope, which are translated to flow.

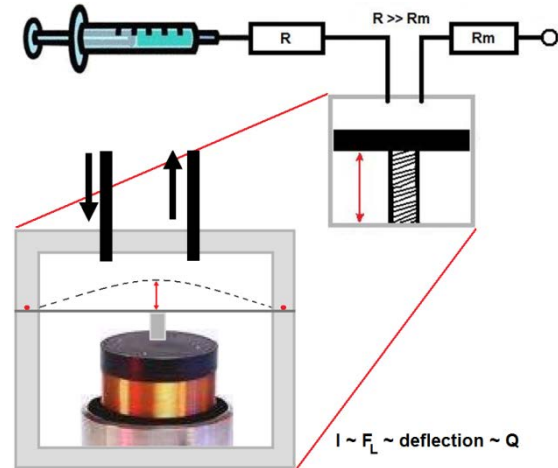


Figure 3: Overview of the pulsatile pump system. A syringe pump is placed in series with the oscillatory displacement pump. Although a glass syringe is used, compliance upstream of the oscillatory pump will be high. By ensuring that the resistance  $R$  is an order of magnitude larger than the downstream resistance  $R_m$ , most of the flow pulse will go downstream.

## RESULTS

### FSI parameter studies

An incoming deformable cell enters the cross-slot off-center and is being positioned at the center. Next, flow is increased to stretch the cell. Results of a simulation where a cell is dynamically deformed while actively controlled are shown in Figure 4(a) to (c). The feedback frequency is 32 Hz, which is the maximum frequency the image software can cope with. All dynamics for valve actuation and delay caused by image acquisition are added to the boundary conditions at the outflow boundaries. Found is that to capture most of the cells, the outflow ratio  $Q_1/Q_2$  is needed to vary between 0.1 and 10.

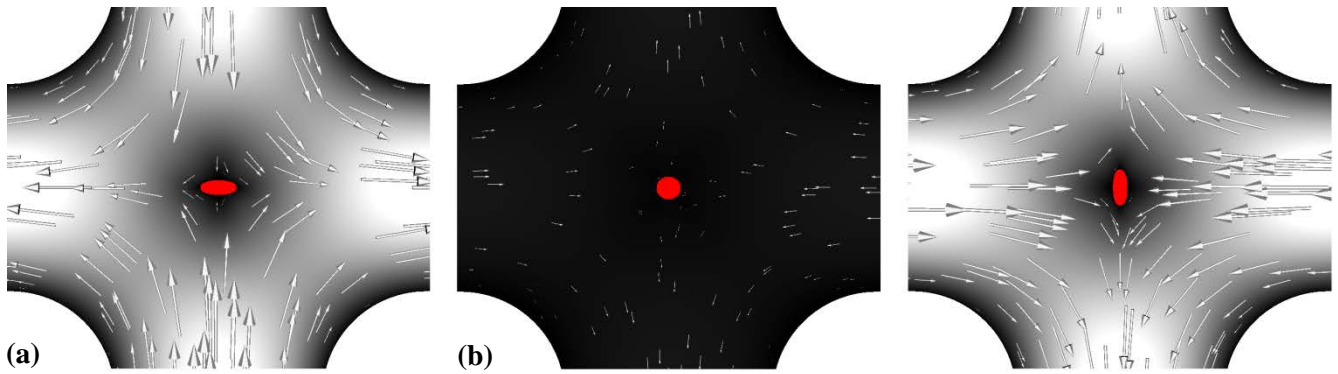


Figure 4: Circular cell in stagnation point with feedback control. Flow is a cosine in time:  $f = 0, 0.5\pi$ , and  $\pi$  rad for (a) to (c), respectively.

### Testing the setup

The function of the valve is visualized by seeding the flow with polystyrene beads with a diameter of  $1\ \mu\text{m}$  (Figure 5a and b). While the piezo-electric actuator goes from minimum to maximum displacement (0-140V), the stagnation point is displaced from top

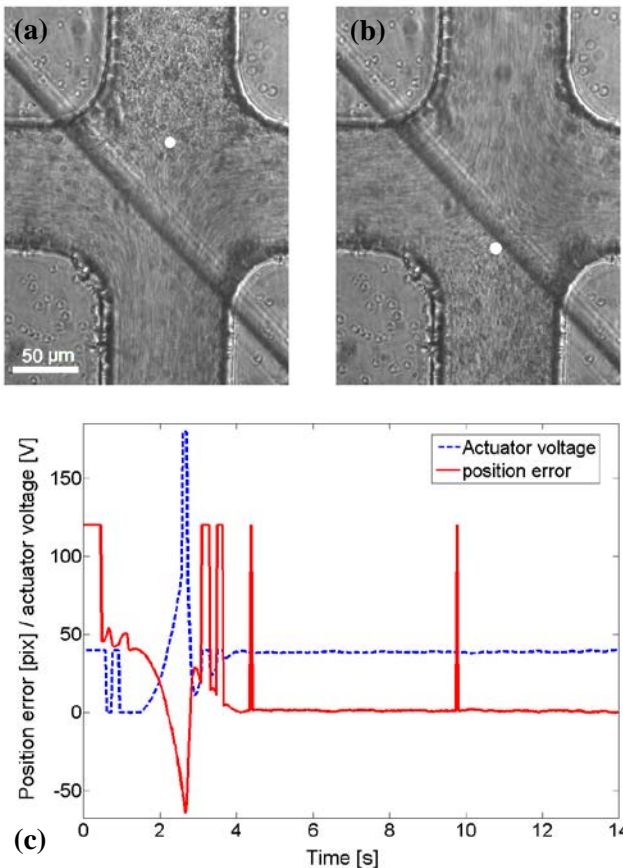


Figure 5: the beads in (a) and (b) show the position of stagnation point that shift as a response to the actuator. The white circles show the stagnation point at the minimum (a) and maximum actuator voltage (b). The diagonal stripe is a scratch in the top of the PDMS membrane. In (c) the tracked position of a hollow glass sphere in time (red solid line). The actuator, driven by the feedback controller (blue dashed line is voltage), displaces the stagnation point such that the bead is pushed towards the center. The spikes are caused by loss of tracking by the software.

to bottom, indicated with the white circles. The graph in Figure 5c shows the position of a hollow glass sphere ( $10\ \mu\text{m}$  diameter) in time (solid line) which follows the actuator voltage (dashed line).

### Pulsatile microfluidics pump performance

A range of frequencies (0.1-10Hz) and pulse magnitudes (10-100 nl/s) have been tested in a straight channel (cross-section  $2 \times 0.1\ \text{mm}$ ). Result of a typical pulsatile flow measurement is shown in Figure 6. The PIV measurement volume is in the center of the channel in order to capture the maximum in the fluid velocity. The measured maxima compared well to the expected absolute maximum ( $<10\%$ , the former always underestimated), considering a Poiseuille profile. However, because the cross-section of the measurement volume ( $1.2 \cdot 10^{-3}\ \text{mm}^2$ ) is smaller than the channel cross-sectional area ( $0.2\ \text{mm}^2$ ), the averaged velocity fields that are obtained with GPIV software are scaled by the applied constant flow of the syringe pump to calculate the flow in time.

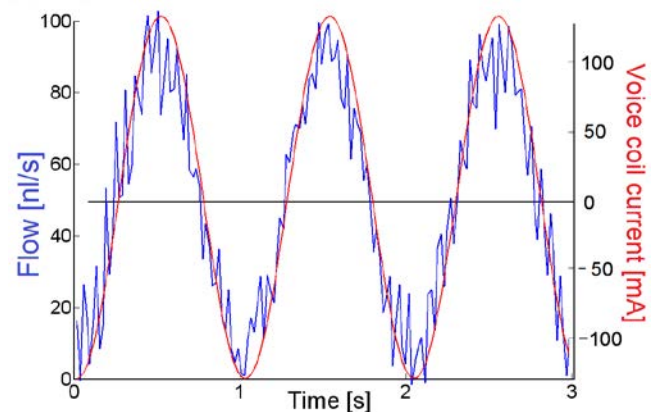


Figure 6: the velocity fields measured with PIV are averaged and scaled to flows. Results of one measurement is shown (spiky blue curve), which fits the applied current through the voice coil (smooth red curve). By making use of a current source, there is no phase shift between driver input and plate displacement due to inductance of the coil.

## DISCUSSION

With the setup described above we are able to perform step-wise loading and unloading experiments in which membrane relaxation, plasticity, and remodeling are investigated. Moreover, a full frequency sweep from 0.1-10 Hz at different amplitudes can be performed.

An inverse analysis with the constitutive model under investigation matching the deformation state in the experiment, in which the local stress is known, will give new insights in the rheological behavior of the RBC.

Concerning the response of a for example visco-elastic material, it is of importance to check for the stress state that is applied to the cell. Therefore,  $\mu$ PIV measurements inside the field of view should be performed during the deformation experiments. These measurements might not give the direct stress, but with a numerical model membrane shear stresses can be calculated, given velocity fields elsewhere in the cross-slot as a boundary condition.

Although a bead can be trapped contactlessly with the current setup, some problems have to be overcome before a RBC can be mechanically probed in a controlled manner. First, the actuation of the valve does not only change channel resistance, but also causes fluid displacement upstream (approximately 0.1  $\mu$ l at maximum stroke). Because the actuator is fast (order ms), this causes a spike in backflow, which destabilizes control. Therefore, another proportional controller is implemented on the actuator, which acts as a low-pass filter. Another problem is the onset of sedimentation of the RBC, caused by a density difference between cell and medium. This is solved by placing the microscope on its side. Gravity is working in the direction of inflow now, such that sedimentation is counteracted by feedback control in that direction.

When no particle is present yet, the image for feedback control is focused in the symmetry plane of the channel. However, the RBC does not necessarily enter the cross-slot in that plane, though it is being forced to the centerline by hydrodynamic forces. Second, the image for feedback should be low in resolution for sake of keeping computational power low and it is acceptable that the cell is out of focus, if only it is traceable. On the other hand, the image that registers cell deformation demands a high lateral resolution and perfect focusing of the RBC. This is

solved by using two cameras and multifocal plane microscopy. The infinity focused light travels from the objective through a tube lens and is split in two. A low resolution camera is used for feedback control, the other camera has high resolution and is focused in a plane of choice by changing the image distance, without disturbing feedback control.

## CONCLUSION

A microfluidics setup is designed and built in which a RBC is dynamically deformed using elongational flow. The cell is held in the center by a feedback system consisting of a microvalve with piezo-electric actuator and image analysis software. A pulsatile micropump controls the flow magnitude in time to vary fluid stresses on the RBC membrane.

## ACKNOWLEDGMENTS

The author likes to thank Johan 't Hart (Philips Research) and Menno van Baardwijk (Technomask), and Gerber van der Graaf (TU Delft) for the manufacturing of the fluidic chip, milling of the valve chambers, and PIV software, respectively.

## REFERENCES

- [1] Evans, E.A., "New membrane concept applied to the analysis of fluid shear- and micropipette-deformed red blood cells", *Biophysical Journal*, Vol. 13, pp. 941-954, 1973.
- [2] Henon, S., Lenormand, G., Richert, A., Gallet, F., "A new determination of the shear modulus of the human erythrocyte membrane using optical tweezers", *Biophysical Journal*, Vol. 76, pp. 1145-1151, 1999
- [3] Janssen, J., Peters, G., and Meijer, H., "An opposed jets device for studying the breakup of dispersed liquid drops", *Chemical Engineering Science*, Vol. 48, pp. 255-265, 1993.
- [4] van Loon, R., Anderson, P.D., de Hart, J., and Baaijens, F.P.T., "A combined fictitious domain/adaptive meshing method for fluid-structure interaction in heart valves", *International Journal for Numerical Methods in Fluids*, Vol. 46, pp. 533-544, 2004.

## CONTACT

\*R.C.H. van der Burgt, r.c.h.v.d.burgt@tue.nl



**A LOW-COST, NORMALLY CLOSED, SOLENOID VALVE FOR NON-CONTACT DISPENSING IN THE SUB- $\mu$ L RANGE**

*S. Bammesberger<sup>1</sup>, S. Kartmann<sup>1</sup>, L. Tanguy<sup>1</sup>, D. Liang<sup>3</sup>, K. Mutschler<sup>1</sup>, A. Ernst<sup>1,2</sup>, P. Koltay<sup>1,2</sup> and R. Zengerle<sup>1,3</sup>*

<sup>1</sup> University of Freiburg, IMTEK - Department of Microsystems Engineering, Freiburg, Germany

<sup>2</sup> Biofluidix GmbH, Freiburg, Germany

<sup>3</sup> HSG-IMIT - Institut für Mikro- und Informationstechnik, Freiburg, Germany

**ABSTRACT**

We present a disposable, normally closed, non-contact dispensing valve for the sub- $\mu$ l range. The miniaturized solenoid valve (diameter: 8 mm, height: 27.25 mm) is compatible to standard Luer-Lock interfaces. The experimentally determined minimal dispensing volume was 163 nl (CV 1.6%) for water and 123 nl (CV 4.5%) for 66% (w/w) glycerol/water. Its modular design allows the reuse of components and actuators that are not contaminated by the reagent. Low-cost polymer components in contact with the reagent during the dispensing process can be considered as disposables, rendering expensive washing steps unnecessary and reducing risk of cross-contamination.

**KEYWORDS**

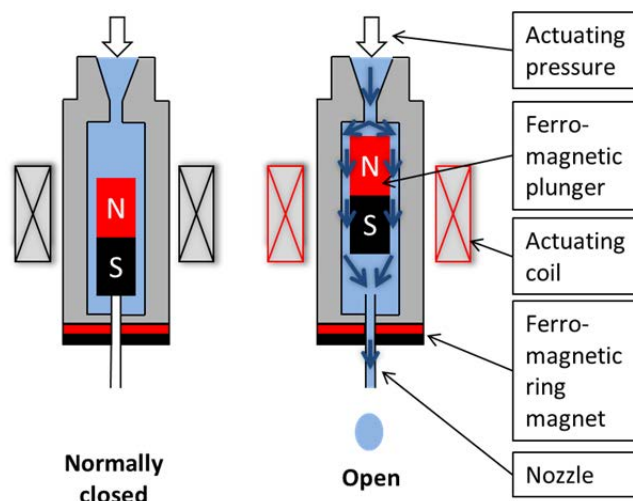
Non-contact dispensing, low-cost, disposable, solenoid valve, normally closed

**INTRODUCTION**

Dispensing valves for biomedical applications are facing demanding requirements in terms of minimal volume, precision and accuracy [1]. For most applications, dispensing valves need to be normally closed requiring rather complex closing or return mechanisms. Additionally, the avoidance of cross-contamination is crucial giving preference to non-contact dispensing systems. Piezo actuated or solenoid dispensing valves are the preferred technologies to address these requirements due to their highly dynamic and precise behavior [2,3]. Most of the commercially available systems feature complex and expensive designs, materials and mechanisms and therefore need to be washed and reused. These washing procedures decrease throughput and increase the risk of cross-contamination. Due to the simple design and the low-cost materials, the valve presented here could be used as a disposable enabling carry-over free reagent dispensing without expensive and time consuming washing steps.

**WORKING PRINCIPLE**

Fig. 1 depicts the working principle of the dispensing valve. The inlet of the valve is pressurized at a constant pressure level. This actuating pressure is



*Figure 1: Working principle of the dispensing valve. Left: In its normally closed state, the ring magnet attracts the plunger and the valve seat is closed. Right: The actuating coil overcomes the attractive force between the ring magnet and the plunger to open the valve.*

released when the valve is being opened. Opening is achieved by a movable ferromagnetic plunger that is pushed upwards by electromagnetic actuation to open the upper end of a metal capillary which forms the valve seat. The solenoid valve is normally closed, i.e. a ferromagnetic ring magnet attracts the plunger and pulls it downwards if the actuating electrical coil is not energized. If the actuating coil is energized, a magnetic field is induced which overcomes the attractive force of the two permanent magnets to open the valve and to release the pressure.

The coil is energized by an electrical current in form of a “peak-and-hold” square-wave, i.e. the signal starts with a peak current of 10 A which is reduced to a hold current level of 2.7 A after 5 ms. Applying a higher current especially at the beginning of the actuation pulse, where the inductivity of the solenoid and the attractive force of the permanent magnet needs to be overcome, allows for a dynamic movement of the plunger. The lower hold current reduces heat coupling effects that can lead to heating of the reagent decreasing its viscosity, which results in higher flow rates and thus a reduced accuracy and precision.



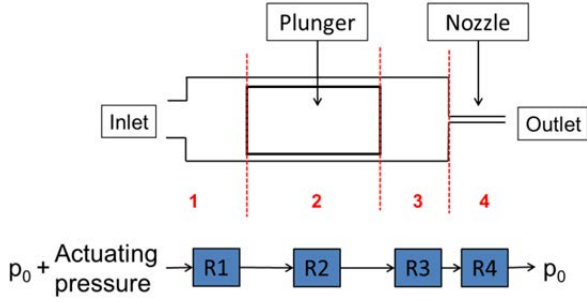


Figure 2: Scheme of the different subsections of the dispensing valve and the corresponding fluidic resistances. The total fluidic resistance equals the sum of the individual resistances  $R1$  to  $R4$ .

The fluidic resistances of the various subsections inside the valve are outlined in Fig. 2. Due to the small radius of the nozzle of  $100\ \mu\text{m}$ , the total fluidic resistance of the dispensing valve is dominated by the fluidic resistance of the nozzle  $R4$  [4],

$$R_4 = \frac{8\eta h}{\pi r^4}. \quad (1)$$

Where  $l$  and  $r$  represent the length and the radius of the nozzle and  $\eta$  represents the viscosity of the reagent. The flow rate  $q$  is inversely proportional to the fluidic resistance

$$q \propto (R)^{-1} \propto r^4, \quad (2)$$

which indicates a very strong effect of geometrical tolerances of the radius of the nozzle to the flow rate and therefore to the volumetric dispensing accuracy.

## DESIGN

The valve's modular low-cost design consists of "dry parts" which are not in contact with the reagent and "wet parts" which are contaminated by the liquid to be dispensed. The dry parts comprise the actuation solenoid ( $2.2\ \Omega$ ,  $0.47\ \text{mH}$ ) and the ring magnet (hard ferrite,  $380\text{--}400\ \text{mT}$ ), which functions as a normally closing magnetic attraction mechanism (see Fig. 1, 3 and 4).

The wet parts consist of a metal capillary ( $\text{ID} \times \text{h} = 0.2 \times 5.5$  (to  $16.5$ ) mm), the valve body and the ferromagnetic plunger ( $\text{OD} \times \text{h} = 2 \times 10$  mm, NdFeB,  $1170\text{--}1250\ \text{mT}$ ) which is coated with Parylene C to ensure biocompatibility. The metal capillary simultaneously forms the valve seat (upper end) and the nozzle of the valve (lower end). The valve body is fabricated by 3D printing (material "Visijet EX 200") but is designed to be injection-moldable. A circular piece of silicone or EPDM ( $\text{OD} \times \text{h} = 1.8 \times 1$  mm) is attached to the lower end of the plunger forming the sealing layer at the valve seat.

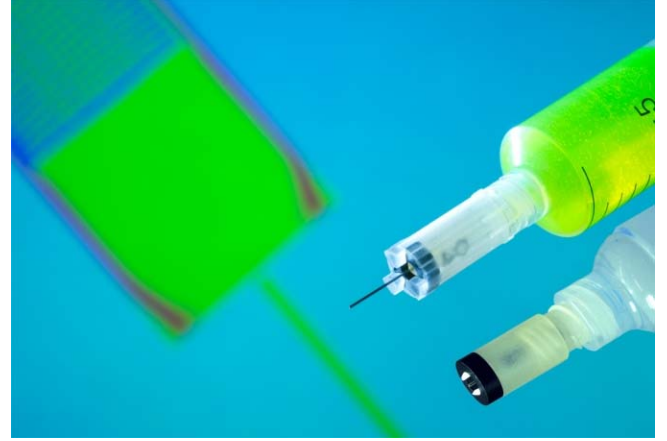


Figure 3: The dispensing valve with its black ring magnet attracting the inner plunger to its normally closed position. Foreground: Two valves mounted on commercial syringes. Upper valve: Long nozzle ( $16.5\ \text{mm}$ ) and external ring magnet fixture. Lower valve: Short nozzle ( $5.5\ \text{mm}$ ) and ring magnet attached by clamping fixture. Background: A screenshot of numerical simulations of the fluid dynamics within the valve.

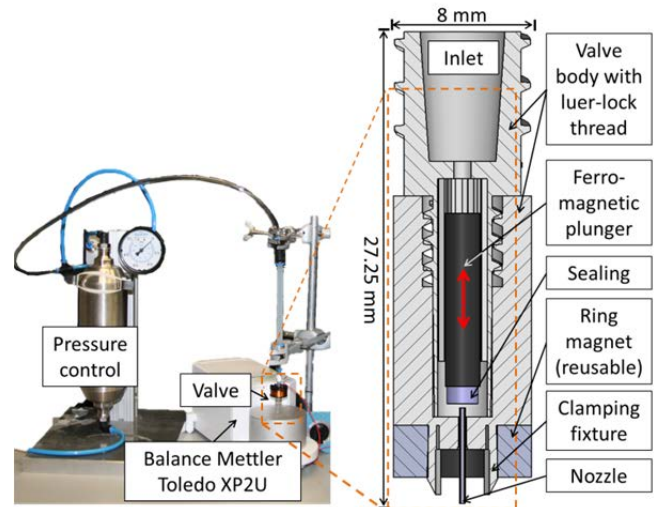


Figure 4: Left: The experimental measurement set-up. Right: Cross-section through the dispensing valve with the movable plunger (red arrow).

## EXPERIMENTS

Experiments presented hereafter were performed with a nozzle of the length  $h = 5.5\ \text{mm}$  and with EPDM as sealing material. The dispensing performance has been characterized with water ( $\eta = 1.03\ \text{mPas}$ ) and 66% (w/w) glycerol/water solution ( $\eta = 16.98\ \text{mPas}$ ). The actuation pressure was set to  $200\text{--}400\ \text{mbar}$  for water and  $800\ \text{mbar}$  for glycerol to compensate for the higher viscosity. The dispensed volume was measured gravimetrically using an evaporation compensating measurement method as described by Liang et al. [5]. Each data point of Fig. 5

and 6 represents the mean volume  $\bar{V}$  of one run of  $N = 24$  individually measured aliquots  $V_n$ :

$$\bar{V} = \frac{1}{N} \sum_{n=1}^N V_n. \quad (3)$$

The “Intra-Run CV” [6] of the respective run,

$$\text{Intra-Run CV} = \frac{\sqrt{\frac{1}{N-1} \sum_{n=1}^N (V_n - \bar{V})^2}}{\bar{V}}, \quad (4)$$

represents the coefficient of variation (CV) of the volume of  $N$  aliquots of a run. The variation across  $L = 4$  different dispensing valves was evaluated and is denoted by the “Tip-to-Tip CV” defined as [6]:

$$\text{Tip-to-Tip CV} = \frac{\sqrt{\frac{1}{L-1} \sum_{l=1}^L (\bar{V}_l - \bar{V}_{T2T})^2}}{\bar{V}_{T2T}}, \quad (5)$$

Whereby  $\bar{V}_l$  represents the mean volume of one run with one valve  $l$  and  $\bar{V}_{T2T}$  represents the mean volume of all  $L = 4$  valves. The *Tip-to-Tip CV* measures the volumetric precision of the different valves’ mean volume if all parameters (actuation time and pressure) are kept constant. Thus, it evaluates the influence of the fabrication tolerances, in particular variations of the inner diameter of the nozzle, on the dispensing accuracy of the individual valves.

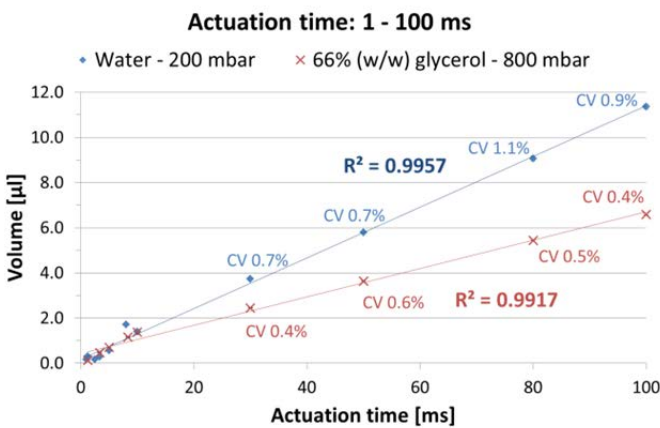


Figure 5: The dispensed volume in dependence of the actuation time for water (blue squares) and glycerol (red crosses). Each data point represents one run of 24 individual measurements. Percentages and corresponding error bars (too small to be visible in this figure) state the respective Intra-Run CV.

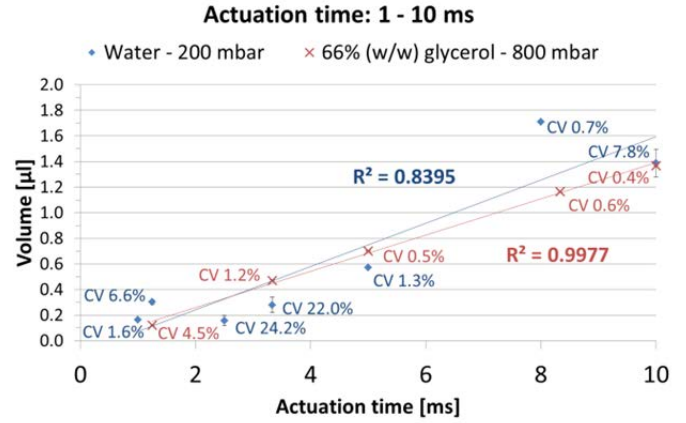


Figure 6: Detail of Fig. 5 for actuation times  $\leq 10$  ms. The measured minimum volume was 163 nl for water (Inter-Run CV 1.6%) and 123 nl for glycerol (Inter-Run CV 4.5%).

## RESULTS

### Volume range and linearity

The actuation time of the solenoid was varied between 1 to 100 ms. The measured volume ranged between 163 nl to 11.4  $\mu$ l for water and 123 nl to 6.6  $\mu$ l for 66% (w/w) glycerol. The correlation of the measured volume to the actuation time was very linear for the complete volume range with  $R^2 = 0.9957$  for water and  $R = 0.9917$  for glycerol, as shown in Fig. 5. For very small volumes  $< 2 \mu$ l (see Fig. 6) coefficient of determination was  $R^2 = 0.8395$  for water and  $R^2 = 0.9977$  for glycerol. The flow rate, calculated from the measurements at 100 ms, was 113.61  $\mu$ l/s (water) and 65.95  $\mu$ l/s (glycerol).

### Intra-Run CV

The dispensing valve showed a highly precise dispensing performance with *Intra-Run CVs* prevalently below 1.0% for volumes  $> 2 \mu$ l (see Fig. 5) and prevalently below 8% for volumes in the range of 0.1 to 2  $\mu$ l (see Fig. 6 and Tab. 1).

Two outliers in terms of a high *Intra-Run CV* at 280 nl (*Intra-Run CV* = 22.0%) and at 157 nl (*Intra-Run CV* = 24.2%) can be explained by the absence of the very first aliquot for the respective runs i.e. no liquid was ejected in these first dispenses at all.

The *Intra-Run CVs* at the smallest volumes were 1.6% for water at 163 nl and 4.5% for glycerol at 123 nl. Hence, the dispensing valve enables the high precision dispensing of liquid volumes down to the lower end of the sub- $\mu$ l range.

### Tip-to-Tip CV

The *Tip-to-Tip CV* of four different tips was 14.7% or 150 nl (at a mean volume of 1.02  $\mu$ l, see Tab. 1), revealing considerable variations of the flow rate for different valves due to fabrication tolerances.

Table 1: Tip-to-tip experiments with  $L = 4$  different valves. The runs were performed with water at an actuating pressure of 400 mbar with an actuating time of 5 ms. The mean volume of all four valves is 1020  $\mu\text{l}$  with a Tip-to-Tip CV of 14.7%.

	Valve 1 = 1	Valve 1 = 2	Valve 1 = 3	Valve 1 = 4	<b>T2T CV</b>
Volume $\bar{V}_i$ [ $\mu\text{l}$ ]	1.16	1.07	0.83	1.02	<b>1.02</b>
Intra- Run CV	1.9%	2.4%	5.7%	2.2%	<b>14.7%</b>

The diameter of the used nozzles is specified with fabrication tolerances of  $\pm 10 \mu\text{m}$ . According to equation 2, this corresponds to an expected variation of flow rate in-between  $q_{\min} = -18.6\%$  to  $q_{\max} = +21.6\%$ , which matches well with the experimental Tip-to-Tip CV of 14.7%. Thus, the volumetric variation across different valves is mainly attributed to the nozzle. It could be improved e.g. by injection molded nozzles with low tolerances or by individual calibration of each valve.

#### Variation of nozzle length

For some applications, e.g. for the aspiration of reagents out of micro titer plates, an elongated nozzle length can be necessary. Equations 1 and 2 imply that the flow rate  $q$  is expected to be inversely proportional to the nozzle length  $h$ . In Tab. 2, the flow rate of water for a nozzle length of  $h = 16.5 \text{ mm}$  is compared to a nozzle having a third of the length ( $l = 5.5 \text{ mm}$ ). The experiments are in good accordance with the theory. Hence, the nozzle length can be changed in order to adapt the flow rate and the functionality of the dispensing valve to specific applications.

Table 2: Experimental evaluation of the flow rate  $q$  of water at different nozzle lengths.

	$h = 16.5 \text{ mm}$	$h = 5.5 \text{ mm}$
Pressure: 0.2 bar	$q = 48 \mu\text{l/s}$	$q = 125 \mu\text{l/s}$
Pressure: 0.4 bar	$q = 88 \mu\text{l/s}$	$q = 232 \mu\text{l/s}$

It should be noted, that due to the linear increase of the fluidic resistance for a longer nozzle, the required minimal actuating pressure for dispensing high viscous liquids increases also. For 66% (w/w) glycerol solution the minimal actuating pressure increased from 0.7 to 1.3 bar when the nozzle length was increased from 5.5 mm to 16.5 mm.

## CONCLUSION

We have presented a normally closed, non-contact, solenoid dispensing valve for the sub- $\mu\text{l}$  range. The Intra-Run CV primarily was below 1% for volumes  $> 2 \mu\text{l}$  and below 8% for volumes in the range of 0.1 to  $2 \mu\text{l}$ . The Tip-to-Tip CV was 14.7% at  $1.0 \mu\text{l}$  indicating a strong influence of fabrication tolerances on the flow rate of the valve and the necessity to calibrate the valve for a specific application.

Its modular injection moldable design allows for low-cost fabrication and disposable use of all liquid contaminated components. Thus, elaborate washing procedures are obsolete and cross-contamination is prevented effectively. Its compact design ( $8 \times 27.25 \text{ mm}$ ) and the standard Luer-Lock interface enable straightforward micro dispensing with high precision up to the sub- $\mu\text{l}$  range.

## REFERENCES

- [1] D. A. Dunn, I. Feygin, Challenges and solutions to ultra-high-throughput screening assay miniaturization: submicroliter fluid handling, *Drug Discovery Today*, vol. 5, pp. 84-91, 2000
- [2] W. D. Niles, P. J. Coassin, Piezo- and solenoid valve-based liquid dispensing for miniaturized assays, *Assay and Drug Development Technologies*, vol. 3, pp. 189-202, 2005
- [3] K. Fanwei, Y. F. Zheng, C. Weidong, Automatic liquid handling for life sciences - A critical review of the current state-of-the-art, *International Conference on Robotics and Biomimetics*, pp. 480-486, 2009
- [4] Encyclopedia of Microfluidics and Nanofluidics, *Springer*, 2008,
- [5] D. Liang, C. Steinert, S. Bammesberger, L. Tanguy, A. Ernst, R. Zengerle, P. Koltay, Novel gravimetric measurement technique for quantitative volume calibration in the sub-microliter range, *Journal of Measurement Science and Technology (submitted)*, 2012
- [6] S. Bammesberger, A. Ernst, N. Losleben, L. Tanguy, R. Zengerle, P. Koltay, Quantitative characterization of non-contact microdispensing technologies for the sub-microliter range, *Drug Discovery Today (submitted)*, 2012

## CONTACT

\*S.Bammesberger, [stefan.bammesberger@imtek.de](mailto:stefan.bammesberger@imtek.de)

#### 4. Fluidic control systems

### A MICROFLUIDIC PASSIVE BATCH MIXING CHIP FOR RECOMBINASE POLYMERASE AMPLIFICATION UTILIZING PHASEGUIDE TECHNOLOGY

*S. Hakenberg<sup>1</sup>, M. Hügler<sup>1</sup>, G. Dame<sup>1</sup> and G.A. Urban<sup>1</sup>*

<sup>1</sup> Laboratory for Sensors, Department for Microsystem Engineering (IMTEK), University of Freiburg, Georges-Köhler-Allee 103, 79110 Freiburg, Germany

A simple but efficient passive micromixer is the choice for many applications in chemical and biochemical analyses<sup>1</sup>. In microfluidics so far all passive pressure driven mixing structures require additional space on the chip in order to realize efficient mixing<sup>2,3</sup>. In this novel approach that space is omitted by conjoining the mixing section and the destination chamber for the mixed species. Mixing structures aiming for efficiency and negligible chip space often require complex fabrication technologies<sup>4</sup>. Here a simple and cost saving fabrication method is used<sup>5</sup>.

Herewith a passive microfluidic batch mixing chip is presented which is based on the recently introduced phaseguide technology<sup>6</sup>. Thus complete control over the way of filling and emptying of any type of microfluidic structures is given<sup>6</sup>. This allows for the first time to directly integrate passive mixing elements into a target chamber. The applicability of this system is demonstrated with isothermal recombinase polymerase amplification<sup>7</sup> (RPA) on chip including its necessary mixing step.

Fabrication method is dry film resist technology with subsequent direct Pyrex wafer bonding described elsewhere in detail<sup>5</sup>. The used dry film resist is 30 µm thick Ordyl SY330. The first laminated layer forms phaseguides after a lithography step. Three more layers build channel and chamber walls. The chip is syringe pump actuated and liquids are colored with methylene blue and neutral red.

RPA is an isothermal oligonucleotide amplification method operated at low temperature<sup>7</sup>. Therefore no thermal cycling device is needed anymore for target molecule amplification and detection. A primer probe system is used similar to the polymerase chain reaction. All reagents were purchased from *TwistDx*. The RPA signal is detected with a *Nikon Eclipse TE2000-U* inverted fluorescence microscope while maintaining the chip temperature at 39°C. The measurement is shown in figure 3.

Layout of the chip is illustrated in figure 1 while the fluidic mixing sequence is shown on chip in figure 2. Phaseguides are forming continuous pinning barriers thus allowing precise segmented and sequenced filling. In the parallel filling chamber two 6.5 µl liquid volumes are filled side by side of each other in an unmixed state. Under actuation liquids advance along the mixing structure within the destination chamber. Once it is filled the two liquids are in a mixed state within 1 min. Mixing of this type is also successfully tested with two liquids clearly differing in viscosity. As in any other laminar flow micromixer the mixing principle is to shorten the diffusion length between the

liquids. *COMSOL Multiphysics* simulations with chip dimensions result in complete diffusive mixing within 1 min after the mixing step while from the unmixed state it would take more than 1 h.

The mixing chip setup was tested with RPA as one possible application. Fundamentally this chip allows to introduce a liquid next to another one in a very defined and reproducible way and to subsequently mix the two species. This can be crucial in any microfluidic assay where it is necessary to introduce one or more components successively. Mixing appears possible for liquids differing in viscosity, but the range of this difference still needs to be determined. In combination with this mixing chip and our earlier presented on-chip electrophoretic RNA extraction module<sup>8</sup> this opens up the way towards a rapid and low cost pathogen detection system in lab-on-a-chip format.

**Word Count: 544**



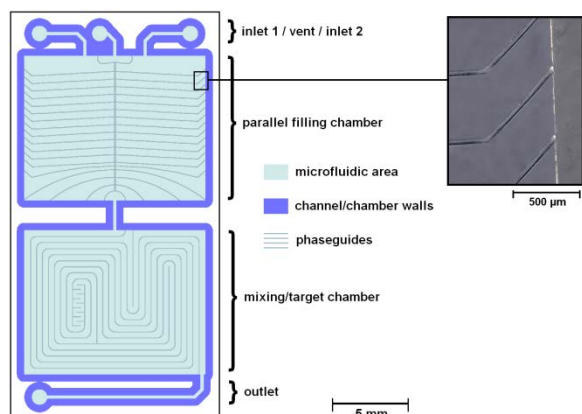


Figure 1: Layout of the microfluidic mixing chip. Top right picture shows a microscopic enlargement of phaseguides from a fabricated chip.

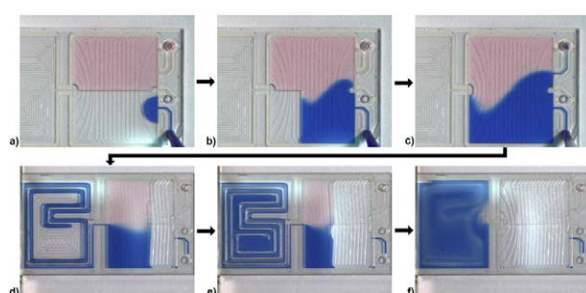


Figure 2. Mixing sequence on chip demonstrated with food coloured water. Chronological order is indicated by arrows from parallel filling towards mixed state.

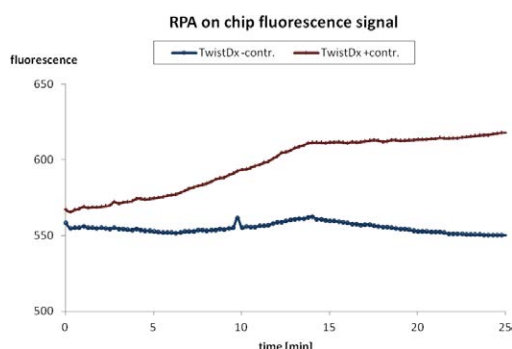


Figure 3. Fluorescence microscope RPA signal measurement.

## REFERENCES:

1. N.-T. Nguyen and W. Zhigang, "Micromixers - a review", *J. Micromechanics and Microengineering*, 2005, **15**, R1-R16.
2. C.-C. Hong, J.-W. Choi and C. H. Ahn, "A novel in-plane passive microfluidic mixer with modified Tesla structures", *Lab Chip*, 2004, **4**, 109-113.
3. S. Hardt, K. Drese, V. Hessel and F. Schönfeld, "Passive Micro Mixers for Applications in the Micro Reactor and  $\mu$ TAS Field", *ASME Conference Proceedings*, 2004, **2004**, 45-55.
4. H. Chen and J.-C. Meiners, "Topologic mixing on a microfluidic chip", *Applied Physics Letters*, 2004, **84**, 2193-2195.
5. P. Vulto, T. Huesgen, B. Albrecht and G. A. Urban, "A full-wafer fabrication process for glass microfluidic chips with integrated electroplated electrodes by direct bonding of dry film resist", *J. Micromechanics and Microengineering*, 2009, **19**, 5pp 077001.
6. P. Vulto, S. Podszun, P. Meyer, C. Hermann, A. Manz and G. A. Urban, "Phaseguides: a paradigm shift in microfluidic priming and emptying", *Lab Chip*, 2010, **11**, 1596-1602.
7. O. Piepenburg, C. H. Williams, D. L. Stemple and N. A. Armes, "DNA Detection Using Recombination Proteins", *PLoS Biol*, 2006, **4(7)**: e204, 1115-1121.
8. P. Vulto, G. Dame, U. Maier, S. Makohliso, S. Podszun, P. Zahn and G. A. Urban, "A microfluidic approach for high efficiency extraction of low molecular weight RNA", *Lab Chip*, 2010, **10**, 610-616.

## FLOW STOPPING USING A 3D-STRUCTURED MICROFLUIDIC T-JUNCTION

*T.J. Chen<sup>1</sup>, F.G. Tseng<sup>2</sup> and C.C. Chieng<sup>2,3</sup>*

<sup>1</sup> National Tsing Hua University, Institute of NanoEngineering and Microsystems, Taiwan

<sup>2</sup> National Tsing Hua University, Engineering and System Science, Hsinchu, Taiwan

<sup>3</sup> City University of Hong Kong, Mechanical and Biomedical Engineering, Hong Kong

### ABSTRACT

This study proposed a 3D-structured T-junction for valving and chopping liquid slug in microchannel systems. The liquid flow stopped sharply and held liquid in coming channel without leakage to other microchannels. An integrated microfluidic passive valves system, one wall with a hydrophobic polydimethylsiloxane (PDMS) surface and the other walls with hydrophilic PDMS surfaces had been fabricated and tested. Numerical models with experimental validation were applied to analyze and to demonstrate the operating ranges of the present design, including the choices with microchannel surfaces, diffuser/nozzle and sudden changes of the channel levels at the 3-D structured T-junction.

### KEYWORDS

T-junction, microchannel, capillary valve

### INTRODUCTION

Microfluidic systems have been widely applied in biology, medicine, drug screening, and portable device. Operations of microfluidic systems include fluid mixing, metering, transport, valving, separation, incubation [1], and etc. by the use of flow channels, micro-valves, pumps, and other devices. [2], [3]. The active components such as valves and pumps are usually the main cause of complicating the process, raising the cost and reducing reliability in microfluidic systems, while the microfluidic system using passive components makes the device or chip design simpler, reliable and cheap [4]. It has been an attractive and the important research that to replace the active pump driven by the surface tension, and to replace the active valve by passive valve for fluid systems operating. Passive valves, such as diffuser valves [5], pH-sensitive valves [5], hydrophobic valves [6], [7], and capillary valves [8], [9], have no moving parts and are especially attractive because they are not sensitive to the physicochemical properties of liquids and are simple to fabricate. Different valves have different functions in controlling the flow of fluids, and they can be grouped accordingly, such as stop valves and check valves.

Stop valve is a common capillary valve that can be used to conduct procedure or timing control in fluidic systems. In most studies, the stop valve is often

connected to a wide groove or a long straight channel that allow it to have a stronger ability to against the burst pressure or avoid leakage [10]. However the stop valve may be required to work in small space, like a T-shape channels junction which is a common component of pipe networks that re-distributes or merging flow. The dynamic tracking process and analysis of capillary stop valve with different design are important and basic for fluidic systems.

The use of a numerical model can provide a detailed demonstration of the stopping process of a stop valve in a T-junction configuration using a complete set of fluid dynamics equations representing the inertial effect, viscous dissipation and the surface tension force at the gas-liquid interface; the use of these equations is known as the computational fluid dynamics (CFD) technique. Numerical simulations have previously been conducted on other valve designs, such as Moroney et al. [11] performed two-dimensional computations of the capillary flow in their initial valve design, Cho et al. [12] computed the transient evolution of the meniscus in hydrophilic and hydrophobic cases, and Zeng et al. [13] performed three-dimensional computations based on Navier-Stokes equations using a Volume of Fluids method for multiphase flows.

In this study, the demonstrating fluidic network connects microchannels by the T-junctions as a ladder (Fig.1a) and one section of the ladder consisting two proposed T-junctions at opposite ends is shown in the SEM image (Fig.1b). The microfluidic chip which made by polydimethylsiloxane (PDMS) molding and bonding was fabricated for biomedical applications. Based on the premise of simple and reliable fabrication process, a microfluidic chip that consists of 3D ladders, different hydrophilic materials and different channels size was designed to demonstrate the fluid stopping at T-junctions. In addition, numerical simulations are performed to illustrate the detailed dynamics of liquid in different size channels and the parameters of the design.

### EXPERIMENTAL TESTS

The detailed (enlarged) structure of T-junction is shown in the SEM image (Fig.1c), which include a nozzle of sharp change cross section and a step height in front of the nozzle opening. The step height

indicates the level change from the incoming (straight) channel to the side channel at T-junction. It is the 3D-structured T-junction. In order to quantify the fluid stopping, parameters are labeled in Fig.1d. The liquid is colored in blue, the extrusions of the liquid are labeled by Y-axis, i.e. extrusions at center cutting plane, on top surface and bottom surface  $Y_{top,ctr}$ ,  $Y_{bot,ctr}$ , or at bottom corner  $Y_{top,cor}$ . In the present study, the same aspect ratio but different widths of the flow channels are analyzed using numerical simulations. Refer Fig. 1d, there are 6 groups of configuration dimensions with different width of Straight Channel width ( $W_{str}$ ), Straight Channel height, Side Channel width ( $W_{si}$ ), and Ladder height: All contact angles of sidewalls and bottom are set to 55 degrees, while the contact angle of top plate was set to 85 degrees. In the numerical simulation, the grid system consists of 25,644 cells with grid-independent results

## RESULTS AND DISCUSSION

Figure 2 shows a typical process of liquid flowing toward the T-junction. The velocity is all zero (in blue color) as the initial condition for computation on the mid-elevated horizontal plane (Fig.2a). The interface of liquid and air is outlined with yellow lines. In Figure 2b, a curved liquid-gas interface is formed by the surface tension forces inclined on the channel surfaces for various degrees of hydrophilicity. The velocity profile at any constant Y (i.e. vertical, perpendicular cutting plane) is of a parabolic shape, with the highest velocity occurring at the center cutting plane of the channel as expected. As the liquid surface approaches the nozzle inlet of the 3D-structured T-junction, the liquid-air interface at the bottom corner reaches the nozzle first with a faster speed because the corner flow effect due to the higher hydrophilic degree of bottom and sidewalls surface (Fig. 2c). The red color in Fig. 2d shows that flow proceeds through the nozzle with acceleration and a higher velocity until it reaches the intersection edges of the straight and side channels. Earlier arrival was observed for the liquid fluid at the bottom corner than other parts as the liquid surface approaches the edge of T-junction. The free surface of the liquid slug has a convex shape and extends from the straight channel to side channel. Because there is an abrupt increase in flow area as the liquid slug leaves the straight channel, the flow resistance is increased, causing the fluid flow to stop. Figure 2e also shows the stopping of the fluid with a reversed direction and very low velocity. The ladder height structure slows down the change in the flow area and moderates the change in the flow velocity, thus preventing leakage from the straight channel. After oscillating motions inside the liquid slug and the interface subside, the liquid remains

stable at the edge of T-junction, with no leakage (Fig. 2f).

Figure 3 shows the meniscus movement with different width of the straight channels. If the liquid is extruded to the opposite wall of the side channel, is bound to leak. Therefore, the width of the side channel corresponds to 100% of the displacement in Y direction. The extrusion of liquid front extends farther as the channel is wider and oscillates in longer time span before stabilizing as comparing blue solid lines ( $Y_{top,ctr}$ ) in each group. When the liquid front reaches stabilized, the smaller channel size, the top edge than the bottom edge of the liquid surface is closer to the inner side. The larger the channel size, liquid surface stagnation is more prominent. In these six groups simulation, the  $Y_{top,ctr}$  of E group shows its liquid front surface has started to retracted and balanced, however the leakage occur at bottom in the vertical direction occurred. And the group F shows, before  $Y_{top,ctr}$  reaches maximum, it has been to achieve a 100% distance, that means, liquid surface touch the other side of the side channel and leak.

The maximum extrusion  $Y_{top,ctr}$  versus the width of Straight channel is summarized and plotted in Fig.4. The extrusion distance is increased faster when the channel size is greater than 90 $\mu$ m.

The effects of nozzle size of Straight Channel and can be summarized by non-dimensional parameters such as Weber number ( $We$ ) and Euler number ( $Eu$ ). Since Weber number is the ratio of inertia force and surface tension and Euler number is the ratio of pressure force and surface force. The product of  $We$  and  $Eu$ , denoted by  $\alpha$ , represents the ratio of pressure force and surface force; and can be expressed as in the following form:

$$\alpha = Eu \cdot We = \frac{P_{inlet} \cdot W_{Str} \cdot H_{Str}}{\sigma \cdot \cos \theta_{Bot/Side} \cdot (W_{Nozzle} + 2 \cdot H_{Str})}$$

Where  $\sigma$  is surface tension coefficient,  $\theta_{Bot/Side}$  is the contact angle of the channel at bottom and side wall surfaces and  $P_{inlet}$  is the Inlet pressure applied (N/m<sup>2</sup>).

Based on the above equation,  $\alpha$  is linearly related to width of the Straight Channel in our cases. Figure 5 shows that the protrusion distance is increased with the size of nozzle opening and  $We$ . If  $We$  is less than a value of 1.295, or the inertia force less than surface tension force, the protrusion of the liquid front will not touch the opposite wall of Side Channel ( $Y_{Prot} < W_{si}$ ) and the liquid slug will stop at the rim of Straight Channel, i.e. the T-junction. (Figure 5)

Figure 6 demonstrates the successful stop in the experiments of the group D. All the liquid surfaces are stopped at the capillary valve position in a slightly protruding as the simulation results.

## CONCLUSION

In this study, a 3D-structured T-junction was successfully functioned as a valveless stop valve with no leakage and to chop flow in one direction by surface forces at the liquid-gas interface in the microchannel system, both in experiments and numerical simulations. The design parameters include key elements of a nozzle structure, a height structure, channel size and surface hydrophobicities.

## FIGURE AND TABLE

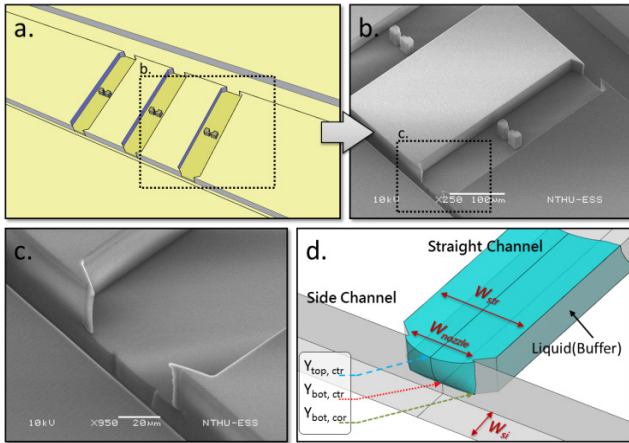


Figure 1: (a) Fluidic system diagram. (b),(c) The SEM image of Ladder Microchannel Networks. (d) Labeling the variables characterizing the moving histories for liquid slug (in blue color) filling with Straight channel.

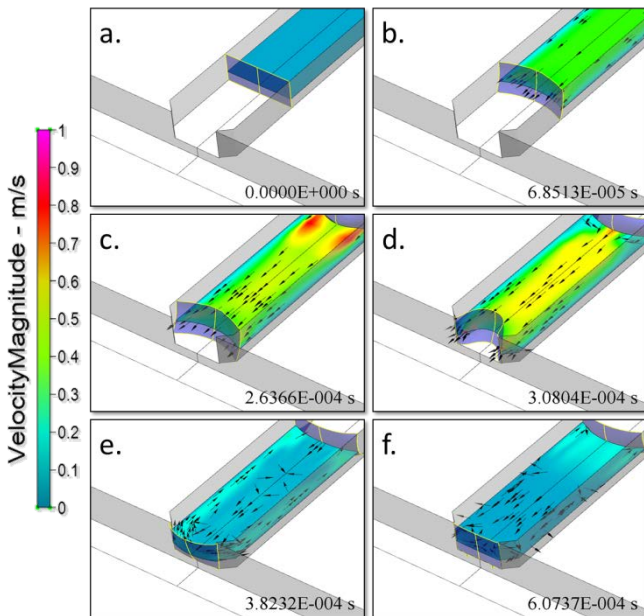


Figure 2: Liquid front surface (in blue color) and Snapshots of velocity contours (colorful) and vectors on horizontal cutting plane as the liquid slug moving toward 3-dimensional structured T-junction of Straight channel and Side channels.

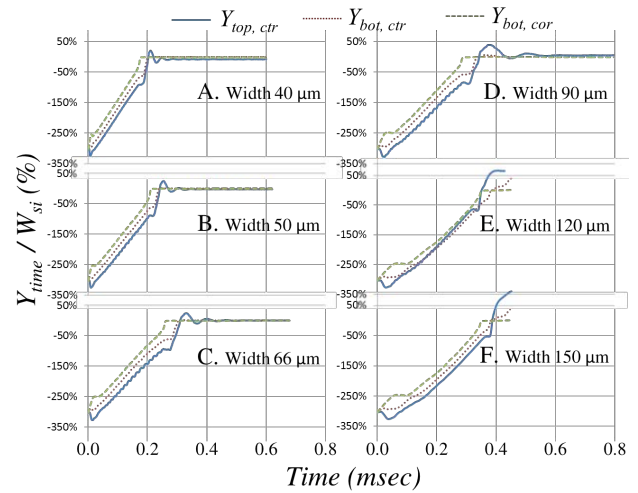


Figure 3: The moving histories of liquid front registered by representing loci of points  $Y_{bot,cor}$ ,  $Y_{bot,ctr}$ , and  $Y_{top,ctr}$  for width of Straight Channel as 40 ~ 150  $\mu\text{m}$ .

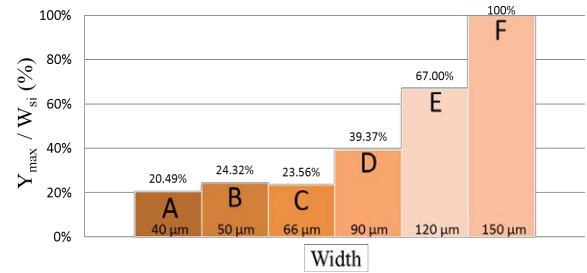


Figure 4: Liquid Front Extrusion Ratio by different Straight Channels Width.

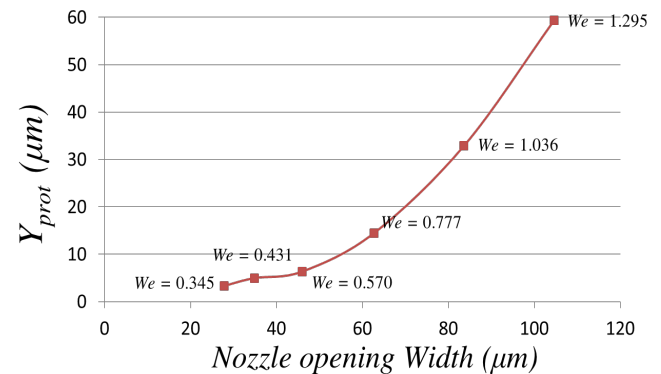


Figure 5: Liquid Front Extrusion vs Nozzle Opening Width. ( $\theta_{Top}=85^\circ$ ;  $\theta_{Bot/Side}=55^\circ$ ; Back Pressure = 2000 pa)



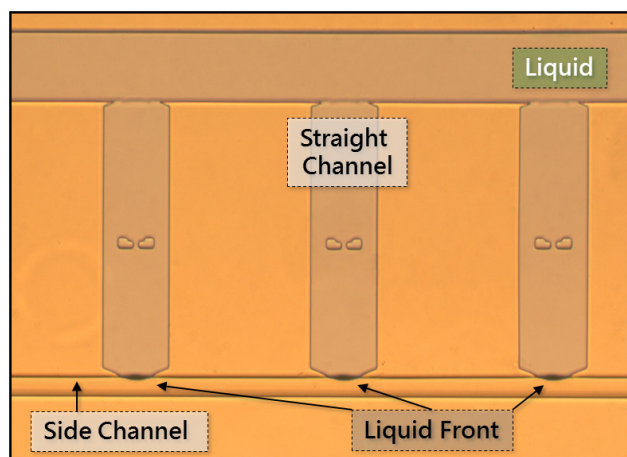


Figure 6: Experimental demonstration of the stopping of liquid slug front at T-junctions for a parallel T-junction microfluidic system.

## ACKNOWLEDGMENTS

The authors would like to thank support from National Science Council (NSC) of Taiwan under grant numbers NSC 100-3113-E-007-001 and NSC 99-2623-E-007-009-ET.

## REFERENCES

- [1] D. Mark, S. Haeberle, G. Roth, F. von Stetten, and R. Zengerle, "Microfluidic lab-on-a-chip platforms: requirements, characteristics and applications.," *Chemical Society reviews*, vol. 39, no. 3, pp. 1153–82, Mar. 2010.
- [2] N. Jeon, D. Chiu, C. Wargo, and H. Wu, "Microfluidics section: design and fabrication of integrated passive valves and pumps for flexible polymer 3-dimensional microfluidic systems," *Biomedical Microdevices*, vol. 4, no. 2, pp. 117–121, May 2002.
- [3] M. Zimmermann, P. Hunziker, and E. Delamarche, "Valves for autonomous capillary systems," *Microfluidics and Nanofluidics*, vol. 5, no. 3, pp. 395–402, Jan. 2008.
- [4] K. W. Oh and C. H. Ahn, "A review of microvalves," *Journal of Micromechanics and Microengineering*, vol. 16, no. 5, pp. R13–R39, May 2006.
- [5] E. Stemme and G. Stemme, "A valveless diffuser/nozzle-based fluid pump," *Sensors and Actuators A: physical*, 1993.
- [6] H. Andersson and W. V. D. Wijngaart, "Hydrophobic valves of plasma deposited octafluorocyclobutane in DRIE channels," *Sensors and Actuators B: Chemical*, vol. 75, pp. 136–141, 2001.
- [7] C. Lu, Y. Xie, Y. Yang, M. M.-C. Cheng, C.-G. Koh, Y. Bai, L. J. Lee, and Y.-J. Juang, "New

valve and bonding designs for microfluidic biochips containing proteins.," *Analytical chemistry*, vol. 79, no. 3, pp. 994–1001, Mar. 2007.

[8] T. Leu, "Pressure barrier of capillary stop valves in micro sample separators," *Sensors and Actuators A: Physical*, vol. 115, no. 2–3, pp. 508–515, Sep. 2004.

[9] H. Cho, H. Y. Kim, J. Y. Kang, and T. S. Kim, "How the capillary burst microvalve works.," *Journal of colloid and interface science*, vol. 306, no. 2, pp. 379–85, Feb. 2007.

[10] J. M. Chen, P. C. Huang, and M. G. Lin, "Analysis and experiment of capillary valves for microfluidics on a rotating disk," *Microfluidics and Nanofluidics*, vol. 4, no. 5, pp. 427–437, Jul. 2007.

[11] R. Moroney, R. Amantea, and S. McBride, "A Passive Fluid Valve Element for a High-density Chemical Synthesis Machine," *2nd International Conference on Modeling and Simulation of Microsystems, San Juan, PR*, Apr 19-21, 1999.

[12] H. Cho, H. Kim, J. Kang, and T. Kim, "Capillary passive valve in microfluidic systems," *Nanotechnology Conference, Boston, USA*, Mar 7–11, 2004.

[13] J. Zeng, "Fluidic capacitance model of capillary-driven stop valves," *MEMS proceedings of ASME international mechanical engineering congress and exposition, Orlando*, pp. 1–7, 2000.

## CONTACT

- \* T.J. Chen, peterchen810@gmail.com
- \* C.C. Chieng, cchieng@ess.nthu.edu.tw

## THE APPLICATION OF MICRO-AND NANOFLUIDICS IN WOBBE INDEX METERS

*R.J. Wiegerink<sup>1</sup>, J.C. Lötters<sup>1,2</sup>, T.S.J. Lammerink<sup>1</sup>, M.G. Pap<sup>1</sup>, A.J. Mouris<sup>3</sup>*

<sup>1</sup> University of Twente, Enschede, The Netherlands

<sup>1</sup> Bronkhorst High-Tech BV, Ruurlo, The Netherlands

<sup>1</sup> Hobr  Instruments BV, Purmerend, The Netherlands

### ABSTRACT

A new concept for Wobbe Index, Heating Value and Air Demand analysis of gaseous fuels is introduced. This technology enables the analysis of fuel gas properties at a fraction of the current costs. Applications include monitoring of gas grid entry specifications (for example biogas) and optimization of small gas fired combustion processes.

### KEYWORDS

Wobbe Index, Calorific Value, Gas analyser, Combustion.

### INTRODUCTION

Natural gas is an important source of energy for industrial and domestic applications worldwide and its' share in the energy mix continues to grow. Applications include boilers, stoves, process heaters, furnaces and gas turbines for power generation. As global consumption of natural gas is growing and at the same time "easy" gas reservoirs are depleted, sources and quality of fuel gas are becoming more diverse and composition variations are increasing. These new gas sources include biogas from landfills or digesters, shale gas and coal bed methane. Also, LNG carriers and new long range pipelines take gas to new markets, thereby changing the composition in the gas grid of their destinations.

Accurate and fast continuous analysis of gas quality is important as it will allow gas suppliers controlling the quality within specifications by blending streams with different compositions. In case gas quality can not be controlled for instance because the supply is single source, "on-line" gas analyzers can help users to control combustion processes by adjustment of flow or other process variables. This paper describes a miniature multi-parameter gas quality analyzer based on MEMS (Micro-Electro-Mechanical-System) technology.

For safe, environmentally responsible and economic operation of small and large gas fired installations variations in gas quality need to stay within well defined limits.

### WOBBE INDEX

Important gas quality parameters are calorific

value, specific gravity and Wobbe Index. The calorific value is the amount of heat produced when a unit volume or mass of fuel is burned stoichiometrically. Gas specific gravity is the density of a gas over the density of air at reference conditions. The Wobbe Index (defined as the heating value of a gas divided by the square root of its' specific gravity) is a measure of the interchangeability of fuel gases when introduced into a heater over a burner with a fixed differential pressure. Two gases with the same Wobbe Index will deliver the same amount of heat into a combustion process per unit of time regardless of the composition. Consider for example two fuel gas cases:

Case 1: 100% natural gas, calorific value 32.65 MJ/Nm<sup>3</sup> and specific gravity 0.6

Case 2: Propane/Air mixture, calorific value 47.54 MJ/Nm<sup>3</sup> and specific gravity 1.28

Whereas both gas mixtures have very different calorific values and densities, the Wobbe Index is exactly the same: 42.00 MJ/Nm<sup>3</sup>. This means that the amount of heat delivered per unit of time through the same burner will be exactly the same for both mixtures. This example is not hypothetical: when LPG is used as a back-up fuel for natural gas the Wobbe Index of vaporized LPG is controlled by blending with air. Gas quality specifications in national grids are typically very tight to ensure safe operations of domestic appliances like boilers and stoves. In The Netherlands for example the limits are 43.46-44.41 MJ/Nm<sup>3</sup>.



Fig 1: Hobr  Instruments Wobbe meter

## FUEL GAS ANALYSERS

The latest generation Wobbe Index analysers (Fig. 1), based on the residual oxygen principle, typically deliver Wobbe Index, calorific value and specific gravity of gaseous fuels in less than 10 seconds. Also air demand (defined as the volume of air needed for complete combustion of a unit volume of gas) is available as an additional output. Whereas these analysers are typically very rugged and reliable, the investment cost and total cost of ownership are inhibitive for their application in small scale combustion processes. Costs of ownership include instrument air and power consumption, installation and maintenance costs and gas consumption for the analysis.

The University of Twente, Bronkhorst High-Tech BV and Hobré Instruments have partnered to develop a so called Integrated Wobbe Meter. The project aims to deliver a Wobbe Index meter on a chip with overall dimensions of 20x20x20 mm. Benefits of this Integrated Wobbe Meter include:

- Cost price enables utilization in small scale installations
- Low sample flow and minimal emissions
- Simultaneous availability of calorific value, Wobbe Index, specific gravity and air demand signal
- Very low utility consumption and easy installation
- No need for trained analyser maintenance engineers on site, no user serviceable parts
- Redundancy possible at low cost

## INTEGRATED WOBBE METER

The basic principle of the Integrated Wobbe Meter is calorimetry: the heat evolved in the combustion process of the sample gas is measured. MEMS surface channel technology is applied for the fabrication of the tubes, sensors and heater elements on a silicon chip (Fig. 2).

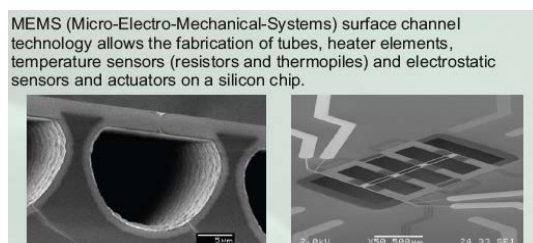


Fig 2: MEMS surface channel technology

Combustion air and fuel gas are metered into the combustion section using micro Coriolis sensors (Fig. 3).

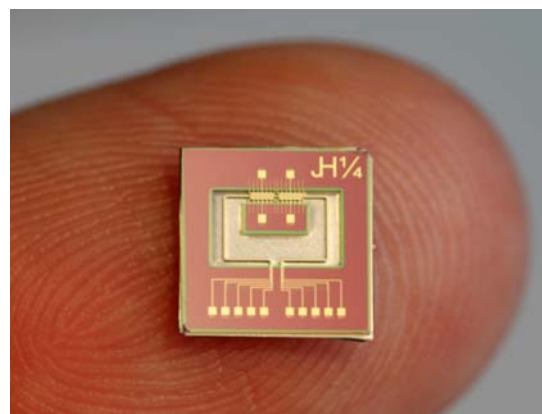


Fig 3: Micro Coriolis Sensor

In addition to mass flow the Coriolis sensor also delivers gas density which enables calculation of the specific gravity. The air demand can be determined by controlling the air/fuel mixing ratio so that the highest temperature is delivered. Typical gas flow through the Integrated Wobbe Meter is less than 0.1 l/hr.

First tests have proven the principle, the project will now focus on a range of challenges:

- Meeting accuracy and repeatability specifications
- Overall response time minimization
- Heat management
- Long term stability
- Potential corrosion issues by combustion products
- Potential clogging of the micro channels

## CONCLUSIONS

MEMS surface channel technology and the possibility to integrate a micro Coriolis flow and density meter are the key to realize a completely new integrated Wobbe Meter with minimal dimensions and gas and utility consumption. The much lower costs in comparison with existing technologies can potentially enable small scale biogas and green gas projects. Also better control of smaller gas fired installations will be facilitated, thereby reducing emissions, optimizing energy efficiency and increasing the lifetime of equipment.

## CONTACT

\* R.J. Wiegerink, [r.j.wiegerink@utwente.nl](mailto:r.j.wiegerink@utwente.nl)

## 2. Actuators

(please choose category from list)

## Poster or Presentation

(if requesting poster)

# MICROREACTORTECHNOLOGY: REAL-TIME FLOW MEASUREMENTS IN ORGANIC SYNTHESIS

S.A.M.W. van den Broek<sup>1</sup>, P.J. Nieuwland<sup>1</sup>, K. Koch<sup>1</sup>

<sup>1</sup> FutureChemistry Holding BV, Nijmegen, The Netherlands

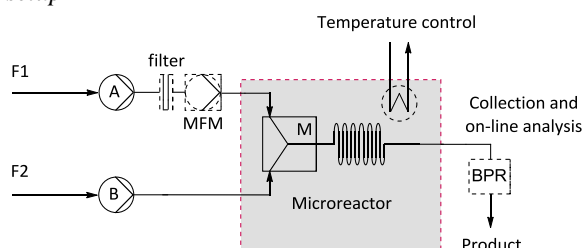
**OBJECTIVES:** With the commercial availability of integrated microreactor systems, the numbers of chemical processes that are performed nowadays in a continuous flow is growing rapidly. The control over mixing efficiency and homogeneous heating in these reactors allows industrial scale production that was often hampered by the use of large amounts of hazardous chemicals. Accurate actuation and in line measurements of the flows, to have a better control over the chemical reaction, is of added value for increasing reproducibility and a safe production. In this research we investigated the opportunities of flow metering in flow chemistry on microliter scale using FutureChemistry's FlowStart Evo, depicted in figure 1.

Figure 1: FlowStart Evo



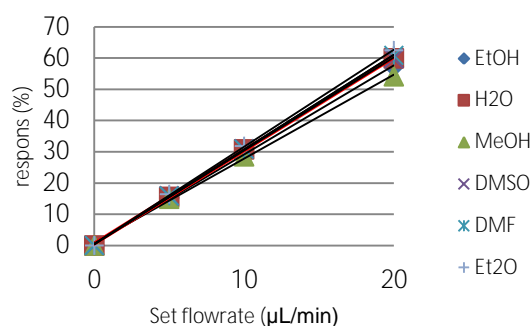
**Methods:** A flow meter (Liquiflow mini, Bronkhorst Technology), based on a thermal measuring principle, was intensively tested on accuracy and robustness with a diversity of organic solvents frequently used in organic processes, using the setup depicted in figure 2. In addition, a model reaction was chosen, using the FM as an external feedback on actual flowrate. Measurement of volatile solvents however appeared not possible with this meter. A more general applicable measuring principle, based on mass flow, was therefore ought to broaden the use flow metering. Applicability of this flow meter was investigated with a variety of organic solvents.

Figure 2: Schematic drawing of the microreactor-setup



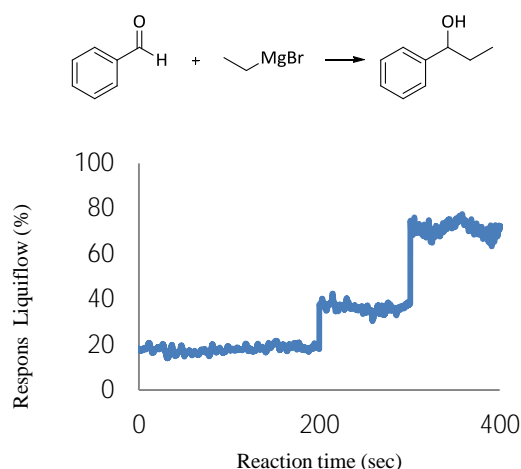
**RESULTS:** The Liquiflow and the mass flow meter were both tested with Syringe A filled with the solvent of choice and Syringe B blocked. Respons was measured with different flowrates. The Liquiflow showed large deviations in respons even when corrected for difference in heat capacity of the solvent. The mass flow meter on the other hand showed a linear correlation with small deviations when normalized with the density of the solvent (figure 3).

Figure 3: Normalized flowrate by mass flow measuring



With the flowrate successfully measured, a model reaction, a Grignard reaction, was chosen to optimise the product formation with different flowrates using the Liquiflow for external feedback. Figure 4 nicely shows the fast respons of the flow meter on changing the flowrate. Full conversion was obtained with a flowrate of 6.0 uL/min, which equals an average respons of 41.3% of the flow meter.

Figure 4: Real-time flow measuring





**CONCLUSIONS:** Positive displacement metering pumps with a high resolution stepper motor provide for excellent flow rates within the submicroliter dispensing of solvents and the Liquiflow provides a very useful tool to accurately measure these flow rates and therefore provide for an external feedback. Using the Liquiflow, differences in heat capacity of the solvents of choice have to be taken into account. Respons onto volatile solvents (e.g. diethyl ether, dichloromethane) is highly fluctuating, making this type of metering only applicable for non volatile solvents. The mass flow meter on the other hand, provides accurate flow rate in low microliter range for both non volatile and volatile solvents.

**RESEARCH SUPPORT:** Supported by the PICOLI program which is part of the “Pieken in de delta” funded by the Ministry of Economic affairs.

**REFERENCE:**

[1] S.A.M.W. van den Broek, R. Becker, K. Koch and P.J. Nieuwland, *Micromachines* **2012**, 3, 244-254.

## PRESSURE DROP REDUCTION IN ONCE-THROUGH MICRO EVAPORATORS

*Cor Rops<sup>1</sup>, Giaco Oosterbaan<sup>1</sup> and Cees van der Geld<sup>2</sup>*

<sup>1</sup> TNO, De Rondom 1, 5612 AP Eindhoven, The Netherlands

<sup>2</sup> Eindhoven university of Technology, PO Box 513, 5600 MB Eindhoven, The Netherlands

### ABSTRACT

The present investigation explores the possibilities to reduce the pressure drop of a single channel micro evaporator. Flow boiling relations for small diameter tubes are studied and showed a general form of the empirical correlations. Using this formulation, we were able to deduce reduction factors for the momentum pressure drop and friction pressure drop in case of a conical channel. These theoretical derived reduction factors show that the total pressure drop can be reduced significantly. The momentum pressure drop completely vanishes for outflow/inlet diameter ratio of 6.3 in case of water. The friction pressure drop is reduced by a factor of ten at an outflow/inlet diameter ratio larger than 4. Experimental comparison using a five time diameter increase shows that the estimated reduction factor approaches the theoretical derived value for higher water supplies.

### KEYWORDS

Flow boiling, Microfluidics, Pressure drop reduction, Microchannels.

### INTRODUCTION

In the 1980's production techniques became available for MEMS (Micro Electro Mechanical Systems). This allowed the mass production of small sized fluidic systems having a better control of process conditions and faster response times [1]. The significantly reduced cost price allows that crucial parts of the system may become disposable units. This gives opportunities to improve the controllability and the serviceability of high-tech systems. For example, in ALD (Atomic Layer Deposition) and CVD (Chemical Vapor Deposition) processes micro evaporators could have added value, given their controllability and serviceability.

Process miniaturization possesses some inherent drawbacks as well. In industry, many processes such as gas production or evaporation contain a change in product phase. Especially in these phase change processes, the pressure drop may become large due to the expansion, and notably so in small sized channels. The rapid expansion in a confined microchannel induces pressure fluctuations and flow instabilities [2]. The relatively large pressure drop of phase-

transitional flows in a microchannel makes a micro system rather unsuitable for low pressure applications. Over the last decade, two-phase flow and flow boiling in small diameter channels has been investigated offering valuable insights regarding pressure drop characteristics [3-5].

This investigation explores possibilities to reduce the pressure drop of a straight micro evaporator. First, flow boiling relations for small diameter tubes are studied, generating ideas how to lower the pressure drop. Widening the channel, and thus giving additional space to the expansion, is found to have much potential. An experimental setup is made to examine some of these ideas further, see section 3. In section 4 the results are given and discussed. Finally, in the last section conclusions are drawn and recommendations are given.

### THEORETICAL BACKGROUND

Many empirical pressure drop models exist for a two-phase flow of phase-transitional flow passing through a small diameter channel. In general three different contributions to the total pressure drop are recognized:

$$\Delta P_{tot} = \Delta P_{static} + \Delta P_{mom} + \Delta P_{fric} , \quad (1)$$

where  $\Delta P_{tot}$  is the total pressure drop over the channel,  $\Delta P_{static}$  is the hydrostatic pressure drop induced by a height difference,  $\Delta P_{mom}$  is the momentum pressure drop generated by the acceleration of the fluid, and  $\Delta P_{fric}$  is the frictional pressure drop. If the slip velocity, i.e. the ratio of the gas velocity over the liquid velocity inside the channel, is known at each axial position, the first two pressure drops are straightforward to be estimated. The frictional component is more complex.

### General two-phase flow frictional pressure drop models

The correlations offered by Friedel (1979), Gronnerud (1972), Chrisholm (1973), Bankoff (1960) and Chawla (1967) , see [6], multiply the liquid pressure drop using an empirical factor, which brings into account the additional energy dissipation occurring inside a two-phase flow. This multiplier is in general dependent on the vapour quality,  $x$ , the

density ratio,  $\rho_{gas}/\rho_{liq}$ , the viscosity ratio,  $\mu_{liq}/\mu_{gas}$  and the total mass flux,  $G_{tot}$ .

Diameter reduction leads to a change in two-phase flow patterns inside the channel. Therefore, the additional energy dissipation inside a small diameter channel will be different than for a regular sized channel. Various investigators [7-10] have proposed new empirical correlations to estimate the two-phase pressure drop. Most of these models are similar to the Lockhart-Martinelli two-phase pressure drop model using an adapted Martinelli parameter. The typical form of a pressure drop model for a small diameter channel is therefore:

$$\Delta P_{fric} = \Phi_{CorrLiq}^2 \Delta P_{liq}, \quad (2a)$$

$$\Delta P_{liq} = \frac{a}{Re_{liq}} \frac{\Delta l}{D_h} \frac{((1-x)G_{tot})^2}{2\rho_{liq}}, \quad (2b)$$

$$\Phi_{CorrLiq}^2 = 1 + \frac{C}{\chi} + \frac{1}{\chi^2}, \quad (2c)$$

$$\chi^2 = \left( \frac{1-x}{x} \right)^{n_1} \left( \frac{\rho_{gas}}{\rho_{liq}} \right)^{n_2} \left( \frac{\mu_{liq}}{\mu_{gas}} \right)^{n_3}, \quad (2d)$$

where  $\Phi_{CorrLiq}$  is the two-phase flow multiplier applied to the liquid pressure drop,  $\Delta P_{liq}$ . Next,  $a$  is the numerical value depending on the channel shape,  $Re_{liq}$  is the Reynolds number based on the liquid mass flux (ie.  $(1-x)G_{tot}$ ),  $L$  is the length of the channel,  $D_h$  is the (hydraulic) diameter of the channel,  $G_{tot}$  is the total mass flux,  $\chi$  is the Martinelli parameter and  $C$  is some model dependent constant, as well as  $n_1$ ,  $n_2$  and  $n_3$ .

Due to the relative ease of use these multiplier models are widely used. However, their applicability is rather limited to the kind of fluids they were developed for. Even if applied within their development field, still typical errors like 30-50% should be taken into account [6].

### Two-phase flow pressure drop in conical widening channel

Usually a straight channel with a constant diameter is used. However, on continuously enlarging the channel diameter downstream the momentum pressure drop can be lowered. Assuming all liquid in, and all vapour (gas) coming out the momentum pressure drop becomes for a channel with a constant diameter

$$\Delta P_{mom} = G_{tot}^2 \left[ \frac{1}{\rho_{gas}} - \frac{1}{\rho_{liq}} \right]. \quad (3)$$

In case of a continuously widening channel with an inlet diameter,  $D_i$ , and an outlet diameter,  $D_o = \alpha D_i$ , the momentum pressure drop becomes:

$$\begin{aligned} \Delta P_{mom} &= \left[ \frac{m_{tot}^2}{\alpha^4 \frac{\pi^2}{16} D_i^4 \rho_{gas}} - \frac{m_{tot}^2}{\frac{\pi^2}{16} D_i^4 \rho_{liq}} \right], \\ &= G_{tot,i}^2 \left[ \frac{1}{\alpha^4 \rho_{gas}} - \frac{1}{\rho_{liq}} \right], \end{aligned} \quad (4)$$

where  $m_{tot}$  is the total mass flow through the widening channel and  $\alpha$  is the ratio of the outflow diameter over the inlet diameter. This implies that the momentum pressure drop can be annihilated by a sufficient widening of the channel ( $\alpha = [\rho_{liq}/\rho_{gas}]^{1/4}$ ). This annihilation of the momentum pressure drop can only be achieved by a widening channel. In case of a channel with a constant diameter, the momentum pressure drop term remains to be present regardless of its diameter.

Similarly the friction pressure drop is lowered by a continuously widening channel. Equations (2a-d) show the typical channel diameter dependency of the two-phase friction pressure drop. Rearranging these equations yields:

$$\frac{\Delta P}{\Delta l} = \frac{\Phi_{CorrLiq}^2 a}{\frac{(1-x)G_{tot}^2}{D^5 \mu_{liq}}} \frac{1}{D} \frac{((1-x)G_{tot})^2}{2\rho_{liq}} = c(l) \cdot D^{-4} \quad (5)$$

Where  $c(l)$  comprises all terms which are assumed to have no dependency on the channel diameter. The constant  $c$  does vary over the length of the channel since the vapour quality changes over the evaporation length. For a conical channel the vapour quality can most likely be approximated by some power fit depending on  $l$ . Similarly such a power fit can be made using the diameter of the conical channel instead of the axial position  $l$ . The constant  $c(l)$  can then be redefined as:  $c(l) = const \cdot D^b$ . The power  $b$ , most likely between -1 and 1, will influence the currently assumed minus 4th power. However, given the variety and inconsistency of the empirical models at this level, no indirect diameter dependency ( $b=0$ ) is assumed for reasons of simplicity. The final estimated error due to this assumption is shown as an error bar in Figure 1. Next, the friction pressure drop over the channel is calculated by the integral over the length of the widening channel. On assuming a linearly changing diameter the following can be derived:

$$\begin{aligned} \Delta P &= const \int_0^L D^{-4} dl \\ &= const \int_0^L \left[ \frac{D_o - D_i}{L} l + D_i \right]^{-4} dl \\ &= \frac{const \cdot L}{3(D_o - D_i)} \left[ D_i^{-3} - D_o^{-3} \right] \end{aligned} \quad (6)$$

and therefore by using  $D_o = \alpha D_i$ , the first order approximation friction pressure drop can be written as:

$$\Delta P = \frac{\text{const} \cdot L}{D_i^4} \cdot \frac{-1}{3} \left( \frac{1-\alpha^{-3}}{1-\alpha} \right) \quad (7)$$

Equation (7) shows that the pressure drop for a widening channel equals the constant diameter channel drop multiplied by a reduction factor depending on the ratio of the exit and entry diameter. Increasing this ratio will reduce the additional term coming from the conical shape, see Fig1.

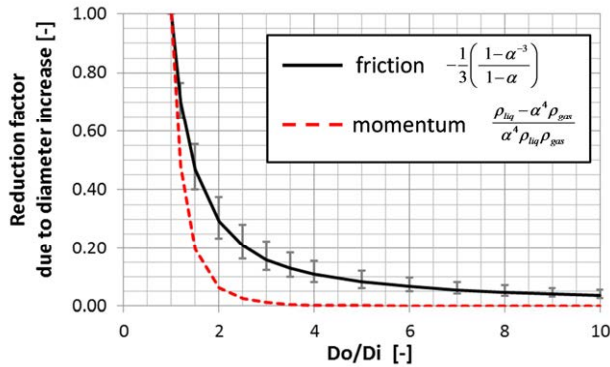


Figure 1: The factor reducing the friction pressure drop (black solid line) and the momentum pressure drop (red dashed line) over a conical channel compared to a channel with constant diameter equal to the initial diameter of the conical channel.  $D_o$  is the outflow channel diameter,  $D_i$  is the inlet channel diameter.  $\rho_{\text{liq}}=960 \text{ kg/m}^3$ ,  $\rho_{\text{gas}}=0.6 \text{ kg/m}^3$

This investigation aims on estimating the above mentioned reduction factors from a dual set of flow-pressure drop measurements.

## EXPERIMENTAL SETUP

To investigate the effect of the linear increase of the channel diameter two test sections have been made:

1. a stainless steel reference channel with a constant diameter of 0.6mm
2. a stainless steel conical channel with an inlet diameter of 0.6mm and an outlet diameter of 3mm

The theoretical friction reduction factor for a 5 time diameter increase is 0.083, and the momentum reduction factor is 0.001. Therefore, momentum induced pressure drops are neglected for the conical setup.

### Schematic setup overview

Two measurement setups have been made to investigate the effect of channel widening. A reference channel and a conical channel. Both have the same (heated) length of 50 mm combined with an entrance length of 14.75mm results in a total length of 64.75mm, see Fig.2

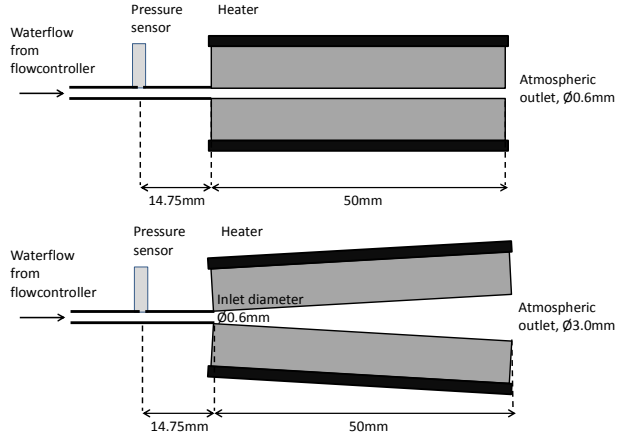


Figure 2: Schematic drawing of the reference channel and the conical channel. The heated length: 50mm.

Demineralised water (no specific degassing procedure, 21°C) flows from the flow controller past the differential pressure sensor, which measures the pressure difference between the upstream location and the ambient pressure. This sensor is placed near the interchangeable heated channel, however still allowing the detection of the backflow. Boiling starts at the heated section. Therefore, in the heated section a two-phase flow occurs. This heated channel has an atmospheric outlet, which ensures that the pressure measured by the pressure sensor equals the two-phase pressure drop of the channel. For comparison reasons the length of the conical channel is exact the same as the reference channel.

For both measurement setups the heat is supplied using a heating wire tightly spun around the outside wall. A temperature sensor is placed 4mm after the inlet of the heated section and 0.8mm from the channel interior wall. This temperature serves as an input for the electronic control system, and will be referred to as the wall temperature,  $T_{\text{wall}}$ . The water is supplied using a Bronkhorst flowcontroller (type mini-coriflow, M12).

### Measurement method

The measurements have been performed using the following procedure. First the heater is turned on and the wall is brought to the desired temperature. Typically, the wall temperature is set at approximately 130 °C. For water this temperature is close to the critical heat flux temperature, which is 126 °C for pool boiling. Next, the water is turned on and set to 1, 3, 5, 10, 15, 20, 30 and 40gr/hr. After a stabilizing period the pressure sensor is logged (read-out frequency 4Hz) for at least 2-5 minutes. This data is used to obtain the average pressure drop and its variations. It is ensured that no gaseous phase is present in the tubing from channel to the sensor.



## RESULTS AND DISCUSSION

Figure 3 shows the measured pressure drop for the reference channel and the conical channel for various water flow rates.

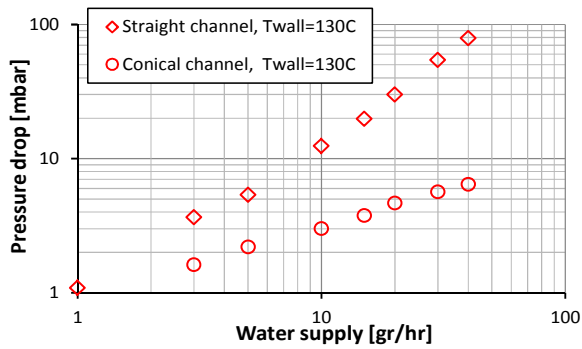


Figure 3: Total pressure drop results 0.6mm straight channel and 0.6-3.0mm conical channel.

Figure 3 shows that the measured pressure drop is about 80 mbar for the reference channel and 7 mbar for the conical channel at 40 gr/hr water supply. For larger water supplies the pressure drop reduction factor obtained by the conical channel is increased. The reduction factor ranges from about 2 at low water supply to about 10 at high water supplies.

The estimated momentum pressure drop for the constant diameter channel is about 25mbar at 40gr/hr, less than 2mbar at 10 gr/hr and thus negligible for the lower water supplies. This implies that the two-phase friction pressure drop has a rather linear (power 1) behavior with respect to the water supply. The estimated momentum pressure drops for the conical channel are all less than 0.1 mbar and thus negligible compared to the total pressure drop. Therefore, the measured pressure drop is approximately equal to the two-phase friction pressure drop. The measured reduction factor of the friction pressure drop ranges from about 1/2 at 3gr/hr water supply to about 1/8 at 40gr/hr water supply. For higher supply flows the reduction factor seems to approach the theoretical value, 0.083, corresponding to a five time diameter increase. see Fig.4.

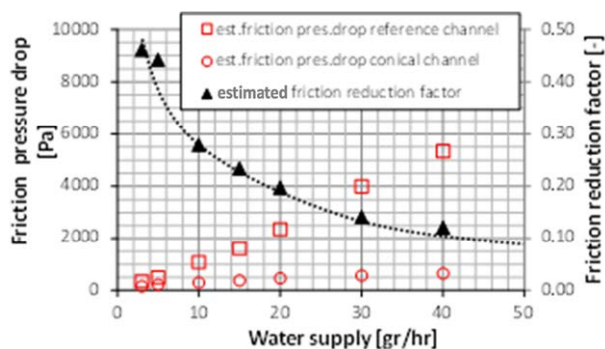


Figure 4: Left axis: Estimated friction pressure drop, red squares and circles. Right axis: the resulting reduction factor.

## CONCLUSIONS

A survey over two-phase flow pressure drop correlations showed a general form of the empirical correlations. Using this formulation, we were able to deduce reduction factors for the momentum pressure drop and friction pressure drop in case of a conical channel. The length of the channel is no parameter in these theoretical reduction factors. These reduction factors show that the total pressure drop can be reduced significantly. The momentum pressure drop completely vanishes for outflow/inlet diameter ratio of 6.3 in case of water. The friction pressure drop is reduced by a factor of ten at an outflow/inlet diameter ratio larger than 4.

Experimental comparison using a five time diameter increase shows that the estimated reduction factor approaches the theoretical derived value for higher water supplies. This indicates that the momentum pressure drop (which is negligible in our conical channel and significant in our straight channel) has no influence on the friction pressure drop correlation.

## REFERENCES

- [1] Tabeling, P. *Introduction to microfluidics*. Oxford university press, 2005.
- [2] Bergles, A.E., Lienhard, J.H., Gail, V., Kendal, E., and Griffith, P. Boiling and evaporation in small diameter channels. *Heat transfer eng.*, pp. 18–40, 2003.
- [3] Kandlikar, S. G. Fundamental issues related to flowboiling in minichannels and microchannels. *Exp. Thermal and Fluid Science*, pp. 389–407, 2002
- [4] Kawahara, A., Chung, P.M.-Y., and Kawaji, M., Investigation of two-phase flow pattern, void fraction and pressure drop in a microchannel. *Int. J. of multiphase flow*, pp. 1411–1435, 2002.
- [5] Brutin, D., and Tadrist, L. Pressure drop and heat transfer analysis of flow boiling in a minichannel: influence of the inlet condition on two-phase flow stability. *Int. J. of heat and mass transfer*, pp. 2365–2377, 2004.
- [6] Thome, J.R. *Wolverine engineering data book III*. Wolverine Tube Inc., Electronic distribution, 2004.
- [7] Qu, W., Mudawar, I. Measurement and prediction of pressure drop in two-phase micro-channel heat sinks. *Int. J. of Heat and Mass Transfer*, pp. 2737–2753, 2003.
- [8] Lee, H.J., Lee, S.Y. Heat transfer correlation for boiling flows in small rectangular horizontal channels with low aspect ratios. *Int. J. Multiphase Flow*, pp. 2043–2062, 2001.
- [9] Mishima, K., Hibiki, T. Some characteristics of air–water two-phase flow in small diameter vertical tubes. *Int. J. Multiphase Flow*, pp. 703–712, 1996.
- [10] Rops, C.M., Geers, L.F.G., Westerweel, J. Explosive bubble growth during flow boiling in micro-channels. *Proceedings of 5<sup>th</sup> European Thermal-Sciences Conference*, Eindhoven, The Netherlands, 2008.

## TOWARDS SINGLE CELL LEVEL HEAT SHOCK PROTEIN EXPRESSION BY MEANS OF HYDRODYNAMIC TRAPPING AND LOCAL HEATING

Maurizio R. Gullo<sup>1</sup>, Ryohei Ueno<sup>2</sup>, Yuan Pang<sup>2</sup>, Nobuyuki Takama<sup>2</sup>, Yasuyuki Saka<sup>2</sup>,  
Beomjoon Kim<sup>2</sup> and Jürgen Brugger<sup>1</sup>

<sup>1</sup> Microsystems Laboratory, Ecole Polytechnique Fédérale de Lausanne (EPFL), 1015 Lausanne, Switzerland

<sup>2</sup> Institute of Industrial Science (IIS), The University of Tokyo, Japan

### ABSTRACT

This paper reports on the design, fabrication and experimental assessment of a microfluidic device aimed for the study of temperature induced heat shock proteins expression at the single cell level. A simple analytical design rule has been developed and numerically verified. The device was able to trap fluorescent micro beads and NIH-3T3 fibroblast cells.

### KEYWORDS

Microfluidic, Single Cell Tapping, Micro Heater, Heat Shock Protein

### INTRODUCTION

#### Heat Shock Protein

Heat shock proteins (HSPs) are essential in the cells own repair mechanism [1]. The expression of HSPs is increased when the cells are exposed to environmental stresses; e.g. high temperature, infections or toxins [2]. Currently biomedical researchers are investigating the use of HSPs for highly efficient anticancer vaccinations and anticancer inhibitor agents [3]. Most studies of HSPs expression are based on a temperature induced stress, i.e. heating of the entire cell cultures [2]. However, to better understand the reaction pathway of HSPs expression at the single cell level, local and short time heating experiments are necessary. Laser heated nanoparticles have recently allowed to locally heat cells [4]. However, it proved to be difficult to predict the amount of absorbed energy and thus temperature. Micro thermocouples integrated in membranes might be used for single cell heating. Yet, the fragility of the submicron structures seems to be incompatible with biological experiments [5]. Recently, Ginet et al. [6] proposed to locally heat cells by using joule heated microelectrodes. Controlled positioning of single cells on the heater has however not yet been achieved.

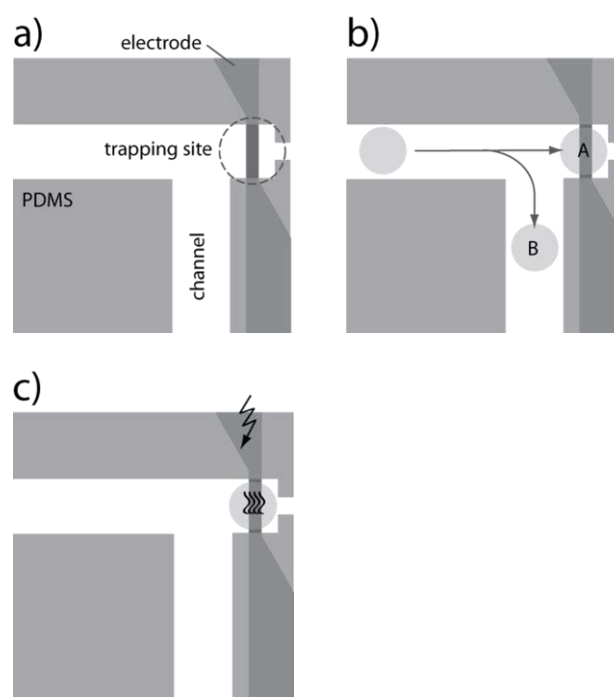


Figure 1: a) Top view of the microfluidic device showing the channel, the trapping site and the micro electrode heater. b) Principle of the hydrodynamic trap: When the trap is empty the first cell arriving (A) will be trapped due to the higher flow along path A. Once the trap is filled the flow will be higher along path B, thus all following cells (B) will bypass the trap. c) Once the cell is trapped it can be locally heated in order to express HSPs.

We propose to approach this challenge by combining a hydrodynamic trap and microelectrode heater for trapping cells and conduct local heat experiments. A schematic view of the device and its working principle is given in figure 1.

#### Hydrodynamic Trap

The hydrodynamic trap is based on a previous developed system aimed to trap MEMS components [7]. The design has been adapted to be used with soft materials such as biological cells.

The trapping principle as shown in figure 1b is based on equilibrating the volumetric flow rate along the two paths of the trap as proposed by Tan et al. [8]. Although Tan et al. describe the trapping principle analytically; the geometrical dimensions of the trap are not straight forward. Therefore numerical simulations are necessary to optimize the trap [9]. We designed a simple T-shaped trap with precise design constraints as shown in figure 2. The channel cross section is restraint onto a square shape with side width  $W$ . The trapping site has a channel length which is also given by  $W$ . The escape channel length ( $B$ ) is a multiple of  $W$ . In this configuration it is possible to analytically solve and simplify the governing equations: The pressure drop in a microfluidic channel is given by

$$\Delta p = \frac{C(\alpha)}{32} \mu L Q \frac{P^2}{A^2} \quad (1)$$

Where  $C$  is a constant that depends on the micro channel aspect ratio  $\alpha$ , the Darcy friction factor and the Reynolds number of the liquid [9],  $\mu$  is the viscosity of the liquid,  $L$  the channel length over which the pressure drop occurs,  $Q$  the volumetric flow rate,  $P$  the perimeter of the micro channel and  $A$  the cross section area of the micro channel. With the design constraints shown in figure 2 and described above, equation (1) can be simplified to

$$\Delta p = \frac{C(\alpha)}{2} \mu L Q \frac{1}{W^4} \quad (2)$$

At equilibrium state the pressure drop along the trapping path (A) and the escape channel path (B) must be the same as along path 2.

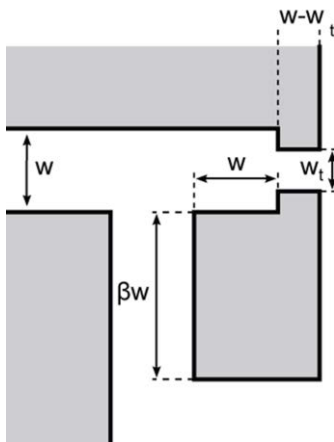


Figure 2. Dimensions and design rule for the hydrodynamic trap, where  $W$  is the width and height of the micro channel  $W_t$  the width of the trap and  $\beta$  defines the length of path B.

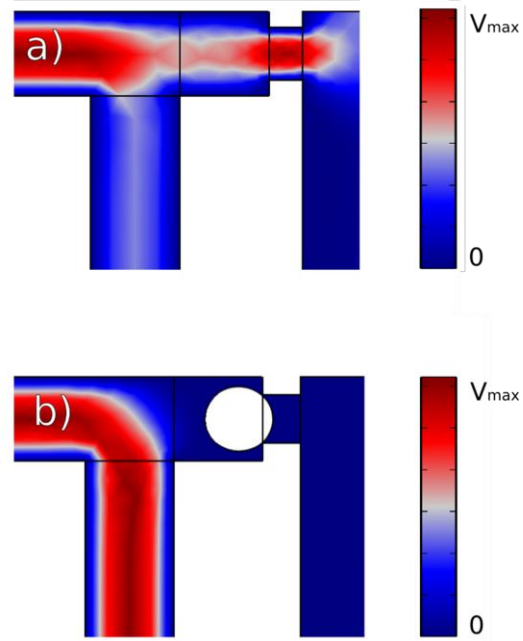


Figure 3. Numerical simulation results of the hydrodynamic trap showing the velocity magnitude ( $V_{max}$  is the maximum velocity). a) While no part is trapped, the velocity along path A is the highest. b) However after a part was trapped, the velocity is maximum along path B (see figure 1b).

$$\Delta p_A = \Delta p_B \quad (3)$$

The length  $L$  will be replaced with the corresponding length of channel A and B respectively. It is important to note that path B is a multiple of  $W$ , where  $\beta$  is the multiplication factor. The constant  $C$  can be calculated following [9] where the aspect ratio in our simplified design is  $1 < \alpha < 0.8$ . Equation (3) can be thus be written as

$$\frac{Q_A}{Q_B} = \frac{\beta}{\frac{W^3}{W_t^3} + 3} \geq 1 \quad (4)$$

where  $W_t$  is the width of the trapping site (figure 2). To ensure a successful trapping of the parts it is mandatory that the flow rate  $Q$  trough path A is bigger than trough path B as long as no target is trapped. This relation is already shown on the right hand side of equation (4) and can be further simplified to

$$\beta \leq \left( \frac{W}{W_t} \right)^3 + 3 \quad (5)$$

With this simple equation it is now possible to easily design a hydrodynamic trap adapted to a given biological cell size. Typically for a given cell the channel size  $W$  will be chosen in order to

accommodate the cell and the trap size  $W_t$  should be designed small enough to hinder the transition of the cell. N.b.  $W_t$  should also be selected narrow enough to avoid the elastically deformable cell to slip through the trap. Therefore a good gap size is the diameter of the cell core.

## RESULTS AND DISCUSSION

### Numerical Validation

Numerical simulations have been performed using COMSOL™ to assess the flow velocities inside the device with the goal verify the analytical design rule and to prove the trapping efficiency of device. The design principle was applied for three different micro channel sizes ( $W = 6\mu\text{m}$ ,  $11\mu\text{m}$  and  $16\mu\text{m}$ ). The microfluidic trap was modeled in three dimensions using the laminar flow module (spf). The linear velocity magnitudes in the case of an empty and filled trap were simulated. The boundary conditions at the channel inlet were set to a perpendicular inflow velocity of  $10\mu\text{m/s}$ , whereas at the channel outlet was let open with the “no viscous stress” condition imposed. All walls of the channel were set to the “no slip” boundary condition.

Figure 3 shows a cut along the channel horizontal center plane of the simulated velocity magnitude along path A and path B for the empty (figure 3a) and occupied trap (figure 3b). It is clearly visible that in the case of the empty trap the highest flow magnitude is along path A (into the trap). In the case of an occupied trap the flow is mainly along path B (bypassing the trap). A residual flow in the corners of the trap's cross section could be seen. This is due to the fact that the cross section of the trap is square shaped and the part designed to block the trapping site is round. The residual flow always stayed minimal compared to the main flow. However it is an indication to work at low flow rates when trapping biological cells, such to avoid shear stress induced harm.

Based on previous work [6] in liquid (DI water) thermal simulations by COMSOL™ (figure 4c) were used to tune the geometry of the gold micro heater electrode.

### Fabrication

The devices were fabricated by state of the art PDMS molding techniques. The mold is micro machined from a standard silicon wafer. First the convex structure of the micro channels was patterned by photolithography and deep reactive ion etching. The silicon mold was then silanized by fluorosilane to

reduce the adhesion of PDMS and facilitate the release of the molded device.

The PDMS was mixed 10:1 with hardener and degassed for 1h. After pouring onto the silicon mold, the PDMS was degassed again and left to crosslink at room temperature for 8h, in order to avoid stress and shrinking of the replica. To permanently bond the microfluidic chip to a glass cover slide containing the heater electrodes, the two parts were cleaned in ethanol, activated by  $\text{O}_2$  plasma and immediately put into contact. To enhance the sealing the bonded devices were cured in at  $80^\circ\text{C}$  for 3 minutes. Traps with the characteristic dimension  $W = 6\mu\text{m}$ ,  $11\mu\text{m}$  and  $16\mu\text{m}$  and trap size of  $W_t = 1\mu\text{m}$ ,  $3\mu\text{m}$  and  $5\mu\text{m}$  were fabricated, respectively.

The micro heater consists of a  $8\mu\text{m}$  wide planar gold micro electrode fabricated by conventional lithography methods. It was designed in order to be operated at the required temperature range (between  $40^\circ\text{C}$  and  $50^\circ\text{C}$ ) using bias voltages below the hydrolysis limit. Figure 4d shows a micrograph of the trap combined with a micro heater. The system was validated and calibrated by thermal imaging [6].

### Trapping beads

The trapping functionality was validated with  $5\mu\text{m}$  diameter green fluorescent PMMA beads suspended in DI water and surfactant (Octoxinol-9, Triton® X-100). The parts were fed into the micro channel

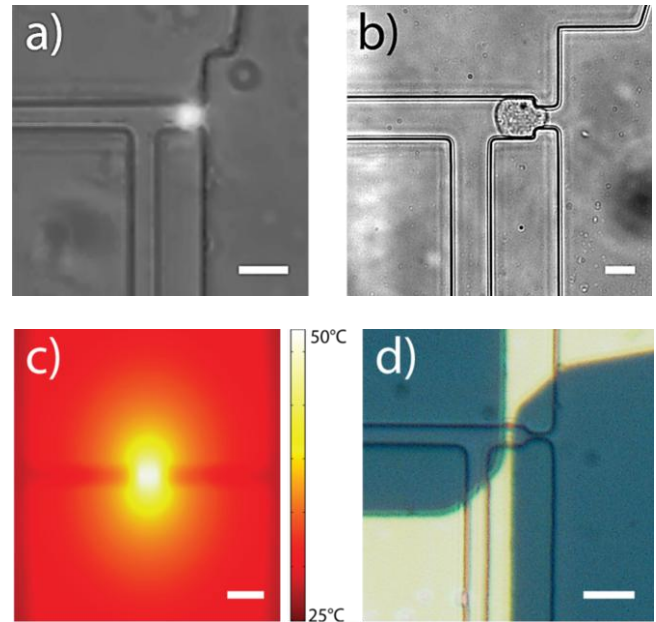


Figure 4: a) Top view optical micrograph of  $5\mu\text{m}$  fluorescent micro bead hydrodynamically trapped. b) Top view optical micrograph of trapped NIH-3T3 fibroblast cell. c) Thermal simulation results of micro heater operated at  $100\text{mV}$ . d) Hydrodynamic trap combined with micro heater. All scale bars are  $10\mu\text{m}$ .



system ( $W = 6\mu\text{m}$  design) by a syringe pump through an injection valve system at a speed of  $0.1\mu\text{l}/\text{min}$ . The beads were continuously injected into the device until the first bead was trapped (figure 4a). All successive beads did bypass the trap as expected. To test the bypass efficiency after trapping a bead we injected a mix of,  $2\mu\text{m}$  and  $1\mu\text{m}$  beads. No smaller beads were trapped in the residual flow but all successfully bypassed the trap, which proves the high efficiency of the trap design.

### Trapping cells

The cells used for trapping were NIH-3T3 fibroblasts genetically modified to express a green fluorescent HSPs upon heating [6]. The cells were grown in cell culture medium inside an incubator for 3 days. Thereafter they were released into suspension by adding trypsin to the medium. Once the cells were released the trypsin was rinsed and replaced with fresh medium. The cells stayed non adherent for a duration of 2h which was long enough to carry out the trials. The typical diameter of investigated NIH-3T3 is  $15\mu\text{m} \pm 5\mu\text{m}$ , therefore the  $W = 16\mu\text{m}$  device was used for the trapping experiments.

Prior to the cell trapping experiments the device was cleaned and primed by sequentially rinsing with 7% ethanol, phosphate buffered saline and cell culture medium. As the experiments were performed outside the incubator the medium had to be modified, in order to keep its neutral pH in ambient atmosphere. During the experiment the device was kept at  $37^\circ\text{C}$  by a heater stage. The cells could be kept alive for 6h once trapped.

To avoid harmful shear stress on the fragile and elastic cells or squeezing them through the trap it is necessary to work at minimal flow speeds. The overall flow rate was controlled by a high precision syringe pump and additionally reduced to  $0.01\mu\text{l}/\text{min}$  by a micro-metering pressure valve. At these flow rates successful trapping of fibroblast cells has been achieved under optical control (figure 4b).

For flow speeds  $> 0.01\mu\text{l}/\text{min}$  the cells were squeezed through the trap and thus the trap efficiency decreased.

### CONCLUSION AND OUTLOOK

We present a hydrodynamic trap based on simple analytical design rules. Therefore the necessity of computer simulations to design these kind of traps has been rendered obsolete. The trap has been verified numerically and experimentally by trapping fluorescent micro beads. Moreover, the trap was used

to successfully trap NIH-3T3 cells at flow rates around  $0.01\mu\text{l}/\text{min}$ . The ultimate goal is to conduct single cell HSPs expression experiments. Therefore a gold micro heater electrode has been machined on the cover slide of the micro channel device. However, the HSPs expression process takes about 8h and the cells could only be kept alive for 6h, even when putting the devices back in the incubator after trapping. The main reason is the lack of nutrients in the cell culture medium after 6h. For successful HSPs trials it is necessary to redesign the trap in order to offer a bigger liquid reservoir, to keep a constant culture medium flow in the channels and to further miniaturize the system in order to perform the experiments inside an incubator.

### REFERENCES

- [1] A. Sharma et al., "Hyperthermia-associated carboplatin resistance: Differential role of p53, HSF1 and Hsp70 in hepatoma cells", *Cancer Sci.* 101, pp. 1186, 2010
- [2] I. Shamovsky et al., "New insights into the mechanism of heat shock response activation", *Cellular and Molecular Life Sciences* 65, pp. 855, 2008
- [3] C. Didelot et al., "Anti-Cancer Therapeutic Approaches Based on Intracellular and Extracellular Heat Shock Proteins", *Curr Med Chem* 14, pp. 2839, 2007
- [4] Y. Kamei et al., "Infrared laser-mediated gene induction in targeted single cells in vivo", *Nat Methods* 6, pp. 79, 2009
- [5] A. A. Minakov et al., "Ultrafast thermal processing and nano calorimetry at heating and cooling rates up to  $1\text{ MK/s}$ ", *Rev Sci Instrum.* 78, pp. 73902, 2007
- [6] P. Ginet et al., "Towards single cell heat shock response by accurate control on thermal confinement with an on-chip microwire electrode", *Lab Chip*, 11, pp. 1513, 2011
- [7] M. R. Gullo et al., "Hydrodynamic Trap for Directed Self-Assembly of MEMS", *IEEE NEMS*, in press, 2012
- [8] W.-H. Tan et al., "A trap-and-release integrated microfluidic system for dynamic microarray applications", *PNAS*, 104, pp. 1146, 2007
- [9] S. Kobel et al., "Optimization of microfluidic single cell trapping for long-term on-chip Culture", *Lab Chip*, 10, pp. 857, 2010

### CONTACT

\* M. R. Gullo, maurizio.gullo@epfl.ch